

Studying soil-structure interaction effects: Advanced joint analysis of borehole and building seismic data

**vorgelegt von
Dipl.-Phys. Bojana Petrovic
geb. in Zagreb (Kroatien)**

**von der Fakultät VI - Planen Bauen Umwelt
der Technischen Universität Berlin
zur Erlangung des akademischen Grades**

**Doktor der Naturwissenschaften
-Dr.rer.nat.-**

genehmigte Dissertation

Promotionsausschuss:

Vorsitzender: Prof. Dr. Frank Rackwitz
Gutachter: Prof. Dr. Yuri Petryna
Gutachter: Prof. Dr. Ümit Dikmen (Bogazici University Kandilli)
Gutachter: Prof. Dr. Stefano Parolai

Tag der wissenschaftlichen Aussprache: 20. Juli 2017

Berlin 2018

Eidesstattliche Erklärung

Hiermit erkläre ich an Eides statt, dass ich die Dissertation selbständig verfasst habe. Die von mir benutzten Hilfsmittel und Quellen sind aufgeführt. Die Arbeit hat in gleicher oder ähnlicher Fassung noch keiner anderen Prüfungsbehörde vorgelegen.

Berlin den 05.03.2017

Bojana Petrovic

Acknowledgements

First of all, I would like to express my very special thanks to my supervisor Prof. Stefano Parolai. I would like to thank him for encouraging my research and for allowing me to grow as a research scientist. I would like to thank him for all his support during these years, for his disposability in every moment and for always believing in me. I can hardly imagine a better advisor. Grazie mille per tutto!!

I would like to thank Prof. Yuriy Petryna for accepting to act as my TU supervisor and reviewer, and for his very useful critical remarks. Special thanks go also to my external reviewer Prof. Ümit Dikmen.

Moreover, I am deeply grateful to Dr. Dino Bindi, my co-supervisor in the first part of my PhD studies, my first year office mate, my travel companion during field trips especially to Bishkek, the person who taught me not only the secrets of being a scientist but also the ones of being an artist and above all a good friend. Grazie Dino!

I would like to thank Dr. Kevin Fleming for proof reading not only of this thesis, but of all my publications, abstracts, posters, presentations, reports and proposals. Thank you for taking always the time, especially for all the last minute issues.

I would like to send my thanks to Istanbul to my colleagues and friends from the Kandilli institute, Bogazici University, especially to Prof. Ümit Dikmen and Prof. Erdal Safak for their hospitality and scientific support during the two very productive months of my PhD studies that I spent there. Teşekkürler!

Furthermore, I would like to say thank you to Prof. Roberto Paolucci and Giovanna Pianese from Politecnico di Milano for the great collaboration that we had, it was really a pleasure to work with you. Alla prossima!

My sincere thanks also go to Greece, to the working group of Prof. Kyriazis Pitolakis at the Aristotle University Thessaloniki, especially to Dr. Sotiria Karapetrou, Dr. Maria Manakou and Dr. Zafeiria Roumelioti for the sound collaboration. Ευχαριστώ!

Moreover, I would like to thank the colleagues from the CAIAG institute, especially Sagynbek Orunbaev and Temirlan Seraliev for their support during the measurements in Bishkek, Kyrgyzstan.

Finally, my thanks go to my colleagues and friends from our working group for their contribution to the pleasant working environment, especially to Max, Shahid, Tobi, Marc, Michael, Marco, Kostas, Ana-Luisa, Alina and Elisa. Thank you all!

Last but not least, I would like to express my deep sense of gratitude to my parents and Davide for all their support during all these years. Hvala mama i tata za vašu podršku u svakom pogledu! Grazie mille Davide!



Preface

This thesis is a cumulative dissertation composed of eight chapters and the following five publications containing all details.

Bindi, D., B. **Petrovic**, S. Karapetrou, M. Manakou, T. Boxberger, D. Raptakis, K. D. Pitilakis, and S. Parolai (2015). Seismic response of an 8-story RC-building from ambient vibration analysis, *Bull. Earthq. Eng.*, 13, 2095-2120. <https://dx.doi.org/10.1007/s10518-014-9713-y>

Petrovic, B., Dikmen, S. U., Parolai, S. (2017a). A real data and numerical simulations-based approach for estimating the dynamic characteristics of a tunnel formwork building: preliminary results, *Bulletin of Earthquake Engineering*. <https://dx.doi.org/10.1007/s10518-017-0250-3>

Raub, C., M. Bohnhoff, B. **Petrovic**, S. Parolai, P. Malin, K. Yanik, R. F. Kartal, and T. Kilic (2016). Seismic-wave propagation in shallow layers at the GONAF-Tuzla site, Istanbul, Turkey, *Bull. Seismol. Soc. Am.*, 106, no. 3, 912-927. <https://dx.doi.org/10.1785/0120150216>

Petrovic, B., and S. Parolai (2016). Joint deconvolution of building and downhole strong-motion recordings: evidence for the seismic wave field being radiated back into the shallow geological layers, *Bull. Seismol. Soc. Am.*, 106, no. 4, 1720-1732. <https://dx.doi.org/10.1785/0120150326>

Petrovic, B., Parolai, S., Pianese, G., Dikmen, S. U., Moldobekov, B., Orunbaev, S., Paolucci, R. (2017b). Joint deconvolution of building and downhole seismic recordings: An application to three test cases, *Bulletin of Earthquake Engineering*. <https://dx.doi.org/10.1007/s10518-017-0215-6>



Table of Contents

Eidesstattliche Erklärung	i
Acknowledgements	iii
Preface	v
Table of Contents	vii
Abstract	ix
Zusammenfassung	xi
Glossary	xiii
Abbreviations	xv
1 Motivation	1
2 Overview	3
3 Theoretical background	5
3.1 Wave propagation through media	5
3.2 Dynamic behavior of buildings	7
4 Methods	9
4.1 Deconvolution approach	9
4.2 Constrained deconvolution	10
4.3 Joint deconvolution and estimation of energy being radiated back from buildings to the soil ...	12
5 The test sites	19
5.1 The AHEPA test site in Thessaloniki, Greece	19
5.2 The Tuzla Peninsula in Turkey	20
5.3 The Bishkek vertical array in Kyrgyzstan – CAIAG and downhole installation	21
5.4 The Istanbul vertical array in Turkey – the B22 building and downhole installation	21
5.5 The Mexico City vertical array in Mexico – the Jalapa building and downhole installation	22
6 Application of the considered methods	25
6.1 Studies dealing with velocity in buildings and soil	25
6.1.1 The AHEPA test site	26
6.1.2 The B22 building	28
6.1.3 The Tuzla Peninsula	30
6.2 Attenuation studies in buildings and soil	31
6.2.1 The AHEPA test site	32
6.2.2 The Tuzla Peninsula	33
6.3 Joint analysis of building and downhole seismic data - estimation of energy being radiated back from buildings to the soil	35

6.3.1 Validation of the method by the use of synthetic seismograms	35
6.3.1.1 Reconstructing the real seismic input	35
6.3.1.2 Reconstructing the wave field being radiated back from the building to the soil	36
6.3.2 Building site interaction assessment: Application to three different test cases.....	38
7 Conclusions and outlook.....	47
8 References.....	49
Appendices: Publications.....	55
Appendix a): Seismic response of an 8-story RC-building from ambient vibration analysis.....	57
Appendix b): A real data and numerical simulations-based approach for estimating the dynamic characteristics of a tunnel formwork building: preliminary results	89
Appendix c): Seismic-wave propagation in shallow layers at the GONAF-Tuzla site, Istanbul, Turkey	121
Appendix d): Joint deconvolution of building and downhole strong-motion recordings: evidence for the seismic wave field being radiated back into the shallow geological layers	151
Appendix e): Joint deconvolution of building and downhole seismic recordings: An application to three test cases.....	175

Abstract

Since earthquakes can neither be prevented nor predicted, in order to reduce damage to the built environment and human losses, the fundamental goal is to improve the design of buildings. For this purpose, variations in ground motion over short distances during earthquakes arising from both site effects (modifications of the ground motions due to changes in the shallow geological layers) and soil-structure interaction (SSI, influence of built structures in modifying the ground motion during earthquake shaking) have to be better understood and integrated in seismic hazard and risk assessment. In urban areas, SSI is not limited to interactions between a single building and the soil, but is extended to interactions between the city as a whole and the soil, the so-called site-city interactions (SCI).

Until now, these effects were mainly studied by 2D and 3D numerical simulations, which are usually based on very simplified representations of the distribution of the buildings and their coupling with the soil, with only a limited number of analyses based on real data sets being carried out in order to investigate this topic. Studies of the wave propagation in buildings and through the soil based on real data sets were usually carried out separately. Studying and understanding the wave propagation through building-soil layers and investigating the interactions that take place is possible only if real data recorded simultaneously by sensors installed in a building and borehole are analyzed jointly.

In this thesis, in order to tackle the problem of understanding soil-structure interactions (i.e., modifications of the wave field generated actively through structural vibrations and passively through scattering and diffraction by the presence of a built structure) in more detail, first, the wave propagations through the soil and buildings are analyzed separately in order to identify their main influences on the wave field and to help with the interpretation of the results derived from the innovative joint analysis proposed here. Note that this analysis is shown to provide a more comprehensive view of the wave propagation through the building and soil and the effects of their interaction.

The novel approach outlined in this study, the so-called joint deconvolution, analyzes jointly recordings of sensors installed in a borehole and a nearby building. It makes it possible to study the wave propagation through the soil to the building and back under different levels of shaking. In particular, it allows the real seismic input and the wave field being radiated back from a building to the soil to be reconstructed and thus, the energy that is released back from the building to the soil to be quantified. This capacity to extract correctly both the incoming energy and that radiated back using the joint recordings inside the soil and in the building is, amongst others, the main theoretical contribution of this work.

After a validation of the novel approach using synthetic data, three studies (in Bishkek, Kyrgyzstan; Istanbul, Turkey and Mexico City, Mexico) of real data sets recorded by downhole installations and building sensors have been carried out and the results are presented in this thesis. These three test cases include different soil conditions and building construction types. Since the impedance contrasts between the buildings and the soil are different, as well as the wave propagation velocities in the subsurface and through the built structures, different building-soil couplings should be expected. For all three test cases, the energy radiated back from the building to the soil was estimated by the new method, and the estimated amount of energy radiated back was found to be not negligible (e.g., for the Bishkek case, at 145 m depth, 10-15% of the estimated real input energy is expected to be from the building, for Istanbul

at 50 m depth, this value is also 10-15%, while for Mexico City at 45 m depth, it is 25-65% of the estimated real input energy).

The presented study shows the influence of buildings in modifying ground motion during earthquake shaking. If energy is radiated back from a building into the soil, it will also affect the behavior of the buildings located nearby. The potential of the method in analyzing the interactions between individual buildings and the soil by real data sets was demonstrated. The presented method and its appropriate modifications in the future also appear promising for studying more complicated cases, from building-building interactions through the soil up to site-city interactions. This offers the possibility to investigate how the waves generated by each individual built structure can interfere with each other, resulting in increased/decreased hazard. This can depend on the positions of the buildings and the urban geometry, therefore, offering the opportunity to optimize them in order to reduce seismic risk in the future. Furthermore, once the full physical mechanism of soil-structure interactions is understood, if included and integrated in a statistical framework consistent with probabilistic seismic hazard and risk assessment, improved estimations of seismic hazard and risk would be possible.

Zusammenfassung

Da Erdbeben weder verhindert noch vorhergesagt werden können, besteht das grundlegende Ziel darin, das Design von Gebäuden zu verbessern, um somit den Schaden an Bauwerken und die Anzahl an Menschenopfern zu verringern. Daher müssen Änderungen der Bodenbewegung über kurze Strecken während Erdbeben, die sowohl aufgrund von Standorteffekten (Modifikationen der Bodenbewegungen aufgrund von Änderungen der oberflächennahen geologischen Schichten) als auch aufgrund von Boden-Bauwerk-Interaktion (soil-structure interaction, SSI, Einfluss von Bauwerken auf die Bodenbewegung während Erdbeben) entstehen, besser verstanden und in die Abschätzung von seismischer Gefährdung und Risiko integriert werden. In städtischen Gebieten ist die SSI nicht auf Wechselwirkungen zwischen einzelnen Gebäuden und dem Boden beschränkt, sondern auf die Wechselwirkungen zwischen der Stadt als Ganzes und dem Boden, die sogenannte Standort-Stadt-Interaktion (site-city interaction, SCI), erweitert.

Bisher wurden diese Effekte überwiegend durch 2D und 3D numerische Simulationen untersucht, die in der Regel auf sehr vereinfachten Darstellungen der Gebäudeverteilung und ihrer Kopplung mit dem Boden beruhen. Nur eine begrenzte Anzahl von Untersuchungen wurde bisher basierend auf Messdatensätzen durchgeführt, um dieses Thema zu erforschen. Analysen der Wellenausbreitung in Gebäuden und durch den Untergrund basierend auf Messdatensätzen wurden bisher in der Regel separat durchgeführt. Die Wellenausbreitung durch Gebäude-Untergrund-Schichten, sowie die auftretenden Wechselwirkungen zu untersuchen und zu verstehen, ist nur dann möglich, wenn Messdaten von Sensoren, die in einem Gebäude und einem Bohrloch installiert sind, gemeinsam analysiert werden.

In dieser Arbeit wird, um das Problem des Verständnisses von Boden-Bauwerk-Interaktion (d.h. Modifikationen des aktiv durch Schwingungen des Bauwerks und des passiv durch Streuung und Diffraktion durch das Vorhandensein des Bauwerks erzeugten Wellenfeldes) näher zu erläutern, zunächst die Wellenausbreitung durch den Untergrund und das Gebäude separat analysiert, um ihren Haupteinfluss auf das Wellenfeld zu identifizieren und somit später bei der Interpretation der Ergebnisse zu helfen, die sich aus der hier vorgeschlagenen innovativen gemeinsamen Analyse ergeben. Man beachte, dass diese Untersuchung gezeigt hat, dass sie eine umfassendere Betrachtung der Wellenausbreitung durch das Gebäude und den Untergrund sowie die Auswirkungen ihrer Wechselwirkung liefert.

Der in dieser Arbeit entworfene neue Ansatz, die sogenannte „joint deconvolution“, ermöglicht es, Aufzeichnungen von Sensoren, die in einem Bohrloch und einem nahe gelegenen Gebäude installiert sind, gemeinsam zu analysieren. Die Wellenausbreitung durch den Untergrund zu dem Gebäude und zurück kann somit unter verschiedenen Erschütterungsniveaus untersucht werden. Insbesondere ermöglicht die neue Methode, den realen seismischen Eingang und das Wellenfeld, das von einem Gebäude an den Untergrund zurückgestrahlt wurde, zu rekonstruieren, und somit die Energie, die vom Gebäude wieder an den Boden zurückgegeben wurde, zu quantifizieren. Die Fähigkeit, sowohl die eingehende Energie als auch die vom Gebäude abgestrahlte, anhand gemeinsamer Auswertung von Aufzeichnungen der Boden- und Gebäudebewegung korrekt zu extrahieren, ist einer der wichtigsten theoretischen Beiträge dieser Arbeit.

In dieser Arbeit wurden nach einer Validierung der neuartigen Methode mit synthetischen Daten, drei Studien (in Bischkek, Kyrgyzstan; Istanbul, Türkei und Mexiko City, Mexiko) basierend auf

Messdatensätzen von Bohrloch- und Gebäudesensoren, durchgeführt. Diese drei Testfälle umfassen unterschiedliche Bodenverhältnisse und Bauformen. Da die Impedanzkontraste zwischen den Gebäuden und dem Untergrund unterschiedlich sind, sowie die Wellenausbreitungsgeschwindigkeiten, sind unterschiedliche Bauwerk-Untergrund-Koppelungen zu erwarten. Für alle drei Testfälle konnte die von dem Gebäude in den Untergrund zurückgestrahlte Energie durch die neue Methode abgeschätzt werden und diese abgeschätzte Menge der zurückgestrahlten Energie ist nicht vernachlässigbar (z.B. für Bishkek entspricht auf 145 m Tiefe 10-15% der bestimmten Energie des realen Inputs der vom Gebäude abgestrahlten Energie, für Istanbul entspricht dieser Wert auf 50 m Tiefe ebenso 10-15%, während für Mexico City dieser auf 45 m Tiefe 25-65% der Energie des realen Inputs entspricht.

Die vorliegende Studie zeigt den Einfluss von Gebäuden auf die Veränderung der Bodenbewegung während Erdbeben. Wenn Energie von einem Gebäude in den Boden zurückgestrahlt wird, wird dies auch das Verhalten der Gebäude, die sich in der Nähe befinden, beeinflussen. Das Potenzial des Verfahrens zur Analyse der Wechselwirkungen zwischen einzelnen Gebäuden und dem Untergrund wurde anhand von Messdatensätzen gezeigt. Die hier vorgestellte Methode und entsprechende Modifikationen dieser, die in Zukunft durchgeführt werden sollten, scheinen vielversprechend, um auch kompliziertere Fälle, von der Gebäude-Gebäude-Interaktion durch den Untergrund bis hin zu Standort-Stadt-Interaktion, zu untersuchen. Dies bietet die Möglichkeit, zu ermitteln, wie die Wellen, die durch jedes einzelne Bauwerk erzeugt werden, interferieren können, was zu erhöhter/verminderter Gefährdung führt. Dies kann von den Positionen der Gebäude und der Geometrie der Stadt abhängen und bietet daher die Möglichkeit, diese zu optimieren, um künftig seismisches Risiko reduzieren zu können. Sobald der vollständige physikalische Mechanismus der Boden-Bauwerk-Interaktion verstanden werden kann, wäre eine verbesserte Abschätzung der seismischen Gefährdung und des Risikos möglich, wenn diese Informationen in einen statistischen Rahmen einbezogen werden, der mit der probabilistischen seismischen Gefährdungs- und Risikobewertung konsistent ist.

Glossary

Acausal part of the deconvolved wave field

The part of the deconvolved wave field where time $t < 0$ (using the reference location to define $t = 0$).

Causal part of the deconvolved wave field

The part of the deconvolved wave field where time $t > 0$ (using the reference location to define $t = 0$).

Deconvolution (approach/interferometry)

The deconvolution approach is based on the comparison of recordings of the same impulse at different locations and provides the propagator between the two locations. It is sometimes also called deconvolution interferometry or seismic interferometry (especially when wave propagation in buildings is considered).

Deconvolved wave field

In the time domain the deconvolution provides the so-called deconvolved wave field. When buildings are considered, it is usually called the Impulse Response Function, in borehole seismology it is usually called the Green's Function.

Down-going waves

In the deconvolved wave field, the down-going waves are the waves propagating downwards after reflection at either the top of the building, the Earth's surface or at interfaces between different (soil or building) layers.

Impulse Response Function (IRF)

When wave propagation in buildings is considered, IRF is usually used in the same way as deconvolved wave field.

Joint deconvolution

The joint deconvolution is the application of the deconvolution approach to borehole and building seismic data jointly.

Phases

The different components of the deconvolved wave field in the time domain.

Real seismic input

The real seismic input is the part of the recorded wave field after removing all downward propagating waves.

Seismic interferometry

Same as deconvolution (approach/interferometry)

Site-city interaction (SCI)

Interactions taking place between the entire city and the soil.

Soil-structure interaction (SSI)

Interactions taking place between individual buildings and the soil.

Up-going waves

In the deconvolved wave field, the up-going waves are the waves propagating upwards (through the soil to the Earth's surface and the roof of the building).

Virtual source

When the deconvolution approach is applied, different locations can be considered as references. If we do not consider the deepest sensor, but a sensor located at a higher level as reference, it is called a virtual source.

Abbreviations

CAIAG	Central Asian Institute for Applied Geophysics
FAS	Frequency Amplitude Spectrum
GONAF	Geophysical Observatory of the North Anatolian Fault
IRF	Impulse Response Function
SCI	Site-City Interaction
SOSEWIN	Self-organizing Seismic Early Warning Information Network
SSI	Soil-Structure Interaction



1 Motivation

Numerous regions worldwide are prone to high levels of seismic hazard due to their locations near active faults, and hence close to zones where earthquakes occur. If these faults are additionally located within or near highly populated regions (i.e., representing the exposure of dense urban areas), in combination with poor building design and construction (i.e., high vulnerability of the built structures), as is the case in many parts of the world, then the population in such areas is exposed to high seismic risk. Reducing the seismic risk is only possible if the seismic risk assessment has been properly carried out. So far, this assessment is based on the estimation of hazard (i.e., the probability of exceeding a level of ground motion) at the surface. The probability of exceeding a given damage state of a building (i.e., using the appropriate fragility curves) is estimated based on this hazard assessment. However, interactions between individual buildings and the soil, as well as those between buildings, are not taken into account in seismic risk assessment.

Since earthquakes can neither be prevented nor predicted, reducing damage to the built environment and human losses can only be achieved by adapting and improving the design of buildings in the long term, which involves a detailed knowledge of the variability of ground shaking over short distances during an earthquake. Not only the changes in the shallow geological layers contribute to modifications in the ground shaking (the so-called site effects, on which a great deal of research have been done so far), but also the interactions of individual buildings with the soil (the so-called soil-structure interaction, SSI, e.g. Bard et al. 1996). Understanding these effects is one of the most challenging tasks for the seismological and engineering communities. Interactions of the soil with the built environment itself might lead to modifications of the amplitude and duration of the shaking of both the building and the soil if the fundamental frequencies of the building and soil are similar, as observed e.g., during the 1985 Michoacán Mexico earthquake (e.g., Wirgin and Bard 1996; Kham et al. 2006). Furthermore, waves generated by built structures emitted into the ground will also affect the behavior of nearby buildings, which would include interactions between ensembles of built structures (the city) and the soil layers during seismic events, leading to the so-called site-city interactions (SCI, e.g., Gueguen et al. 2002; Kham et al. 2006).

Although the influence of structures located at the surface on seismic wave propagation (both passively influencing the input wave field through scattering and diffraction and actively generating a wave field through structural vibrations) have been investigated for several decades, only a very limited number of studies based on the analysis of empirical data has been undertaken until now (e.g., Jennings 1970; Kanamori et al. 1991; Gueguen et al. 2000). In fact, the analysis of soil-structure and site-city interactions have mainly been carried out by 2D and 3D numerical simulations (e.g., Wirgin and Bard 1996; Semblat et al. 2004; Kham et al. 2006), focusing mainly on the study of the effects of buildings on the free-field ground motion. Usually, in order to limit the computation time and the number of governing parameters within the model, simplified representations of the SCI are considered, and hence, they give only a limited insight into the real ongoing SCI effects.

The main objective of this thesis is therefore to propose a novel approach which makes it possible to study the soil-structure interactions (herein referring to the modifications of the wave field generated by the active and passive presence of the built structure) in more detail based on real data sets. Studying seismic wave propagation through buildings (e.g., Snieder and Safak 2006) or the soil (e.g., Mehta et al. 2007a, b) during earthquake shaking has been carried out through separate studies until now.

However, while in order to analyze soil-structure interaction effects, first the dynamic characteristics of the building and soil have to be understood in detail, an overall comprehension of SSI effects can only be achieved if data from buildings and downhole recordings are analyzed jointly. For this purpose, earthquake recordings collected in a building and a nearby borehole simultaneously (Fig. 1), are analyzed jointly in order to allow a comprehensive investigation of wave propagation through building-soil-layers under different levels of shaking. Moreover, the behavior of different buildings due to the coupling of the structure with different types of soil is investigated. Finally, the considered approach makes it possible to reconstruct the real seismic input and the wave field being radiated back from the building to the soil, and thus, to quantify the energy being released back from the building to the soil.

The proposed method has been found to be very promising for improving our understanding of the interactions taking place between built structures and the soil during earthquake shaking using real data sets. It is the first step for improving not only our understanding of the interaction between individual buildings and the soil, but to investigate also interactions taking place between ensembles of buildings and the soil in the future. In fact, understanding the interactions taking place between ensembles of buildings and the soil might help on the short term to identify areas of higher seismic risk within urban centers, industrial areas, etc., and thus, to improve the preparations for the case of an emergency. Furthermore, understanding the physical phenomenon of the interactions taking place could allow its inclusion in statistical frameworks (as is done for now in a simplified way for standard probabilistic seismic hazard assessment, PSHA, and probabilistic risk assessment), making its practical application possible (e.g., land use planning, design etc.). Moreover, improving the comprehension of SSI and SCI effects in detail would allow the improvement of the structural design not only of individual buildings, but of entire urban areas on the long term. Finally, it would lead to improvements in seismic risk assessment and mitigation. Especially these final goals have motivated the investigations presented in this thesis.

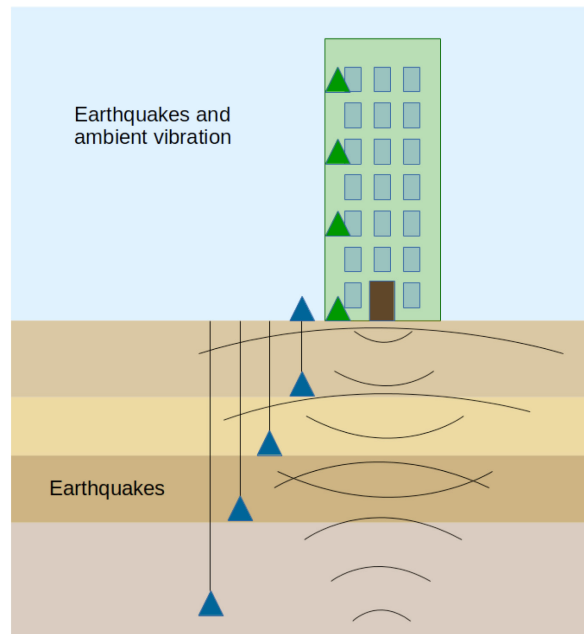


Figure 1. Schematic representation of a vertical array (consisting of a building equipped with sensors, green triangles and a downhole sensors installation, blue triangles) for the investigation of the wave propagation through the building-soil layers.

2 Overview

Monitoring built structures makes it possible to improve the understanding of their dynamic behavior under seismic loading. The seismic response of a building can be estimated by two different techniques, namely the vibrational (e.g., Chopra 1996) and the waveform approaches (e.g. Kanai 1965; Todorovska and Trifunac 1990; Snieder and Safak 2006). The vibrational approach aims for the estimation of natural frequencies and normal modes (e.g., by the frequency domain decomposition, FDD, Brincker et al. 2001) of a building-foundation-soil system (system frequencies) and, thus, provides the global properties of the built structure (related to the whole built structure). Alternatively, the waveform approach aims at the estimation of the properties of the seismic wave propagation by the deconvolution approach (e.g., Snieder and Safak 2006; Kohler et al. 2007; Picozzi et al 2009; Todorovska 2009; Nakata et al. 2013; Rahmani and Todorovska 2013; Bindi et al. 2015; Petrovic et al. 2017a). Different from the vibrational approach, the application of the deconvolution approach removes the coupling with the ground, i.e., the soil-structure interaction effects (Snieder and Safak 2006; Todorovska 2009) and hence, provides the fixed-base frequencies (frequencies related only to the built structure, which would exist if it were constructed on a base of infinite mass and stiffness). If data from a dense network of stations installed in a building at different floors is available, the deconvolution approach provides the local characteristics of the building, i.e., the wave propagation velocity between two sensors. For this reason, the deconvolution approach has also found its application in the field of damage detection (e.g., Todorovska and Trifunac 2008a, b, c; Pianese et al. 2018).

Moreover, the deconvolution approach is often used in downhole seismology in order to estimate wave propagation velocity and attenuation structures in near-surface layers by the analysis of earthquake data recorded by downhole sensors (e.g., Trampert et al. 1993; Mehta et al., 2007a, b; Assimaki et al. 2008; Parolai et al. 2009, 2010, 2012, 2013; Oth et al. 2011; Raub et al. 2016). This makes it possible to improve the understanding of the dynamic behavior of the near-surface geology.

In 1970, waves generated by structural vibrations were recorded for the first time in seismic ground motions in urban areas by Jennings, followed by studies e.g., by Kanamori et al. (1991), Erlingsson and Bodare (1996) and Gueguen et al. (2000), Mucciarelli et al. (2003), Ditommaso et al., (2010a). Chavez-Garcia and Cardenas-Soto (2002) investigated interactions between two tall buildings through soil by the use of the H/V spectral ratio method. The impact of structure-soil-structure interactions on the dynamic response of structures was furthermore experimentally analyzed by Kitada et al. (1999). A reduced scale centrifuge experiment was carried out by Chazelas et al. (2001) in order to study the interactions between structures through soil.

Several 2D and 3D numerical studies have been carried out in order to investigate the seismic wave field modifications (compared to the free-field case) due to surface structures that behave as secondary seismic sources and local interactions between structures through soil, namely the site-city interactions (e.g., Wirgin and Bard 1996; Bard et al. 1996; Gueguen et al. 2002; Semblat et al. 2002, 2004, 2008; Kham et al. 2006). In addition, attempts for a semi-analytical description of the site-city effects were made by, e.g., Gueguen et al. (2000) and Boutin et al. (2004). As mentioned before, numerical simulations are an additional, very useful tool, but are generally a simplified representation of the ongoing processes and may, due to the simplifications employed, not show all aspect of SSI and SCI expected in a real city.

All of these studies provide only a limited insight into soil-structure and site-city effects. In order to better understand the wave propagation through building-soil layers and to investigate the phenomena of energy being radiated back from the building to the soil, real data sets made up of recordings from building and downhole installations have to be analyzed jointly.

3 Theoretical background

3.1 Wave propagation through media

When an earthquake occurs, different types of waves are generated, namely the so-called body and surface waves. Body waves are composed of compressional P and shear S-waves (with the two shear wave components SH and SV: SH-waves are polarized in the horizontal plane and SV-waves in the vertical plane) and travel through the body of Earth. Surface waves (i.e., Rayleigh and Love waves) travel at the Earth's surface. P and S-waves velocities in turn provide information about the mechanical properties of the Earth's interior.

The Earth's interior is not composed of one homogenous layer, but can be approximated by a layered structure (for example, in the shallow part by unconsolidated sediments and bedrock) where the seismic wave velocity and the density of the material changes vertically, but not laterally with depth (although this is an approximation as there are lateral variations in the mechanical properties, especially in the upper-most layers). At each of the interfaces between two different layers with differing properties, refraction (change in the propagation direction when passing the interface due to different properties of both media) and reflection (at the interface between two media) take place, analogous to light passing through different media. Note that in the case of P or SV wave incidence, wave conversion (P to SV-wave or SV to P-wave) also takes place (e.g., Shearer 1999).

Each layer of a medium is characterized by its impedance Z defined as

$$Z = \rho v, \quad (1)$$

which is the product of the material density ρ and the wave propagation velocity v . For example, if two soil layers with different mechanical properties (layer 1: ρ_1, v_{p_1}, v_{s_1} and layer 2: ρ_2, v_{p_2}, v_{s_2} , with v_p being the P-wave velocity and v_s the S-wave velocity) are considered, the impedance contrast between these two layers is defined as

$$c = \frac{\rho_1 v_1}{\rho_2 v_2}, \quad (2)$$

v_i being v_{p_i} or v_{s_i} .

Figure 2 presents the refraction and reflection of an incoming SH wave.

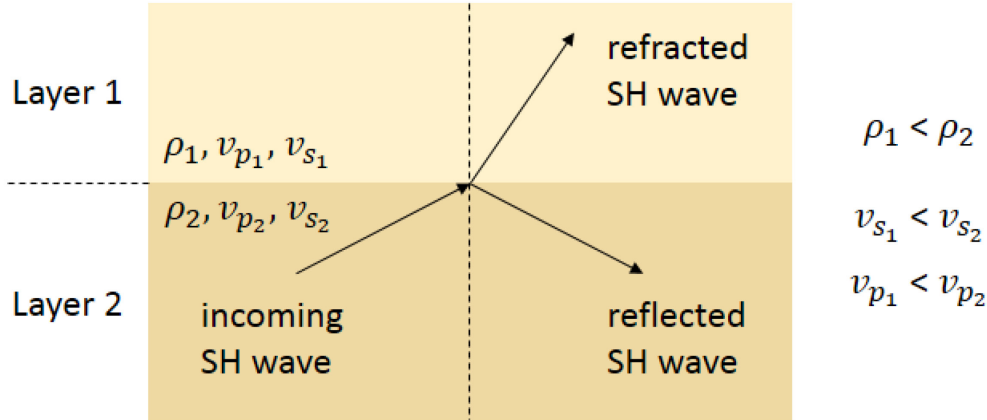


Figure 2. SH wave propagation through two layers with different densities and velocities, showing the reflection and refraction of the incoming SH wave at an interface between the two layers.

The amount of energy that is reflected or transmitted (refracted) at the interface between two different media can be estimated by the reflection and the transmission coefficients (r and t , respectively). The amplitude of the waves propagating through the two layers and reflected at the interface between the two layers is defined by the reflection coefficient r

$$r = \frac{\rho_2 v_2 - \rho_1 v_1}{\rho_2 v_2 + \rho_1 v_1} = \frac{Z_2 - Z_1}{Z_2 + Z_1} = \frac{1 - c}{1 + c}, \quad (3)$$

while the transmission coefficient t is given as

$$t = \frac{2\rho_1 v_1}{\rho_2 v_2 + \rho_1 v_1} = \frac{2Z_1}{Z_2 + Z_1} = \frac{2c}{1 + c} = 1 - r. \quad (4)$$

Seismic waves that are propagating through the soil lose energy due to attenuation mechanisms. Three main effects contribute to the attenuation effects, namely intrinsic attenuation, scattering attenuation, and geometrical spreading.

Elastic wave propagation is defined by a permanent exchange between potential and kinetic energy. Since these processes are not completely reversible, energy losses take place due to heat and internal friction, this process is called the intrinsic attenuation. The intrinsic attenuation, which is generally frequency independent, is given by the quality factor Q_s . The relationship between the quality factor Q_s and the viscous damping ratio γ is given by

$$\gamma = 1/(2 Q_s) \quad (5)$$

Scattering attenuation, which is generally frequency dependent, takes place due to changes in the material and leads to amplitude decay and dispersive effects, where the energy of the wave field is scattered in different phases. Depending on the wavelengths (related to the frequency content) in the considered wave field, different scattering regimes can take place.

Geometrical spreading refers to the general decrease in amplitude due to propagation from a point source over a spherical surface with increasing radius.

3.2 Dynamic behavior of buildings

As mentioned before, the dynamic behavior of a building can be described either by the wave propagation velocities (see Section 3.1) or by the normal modes and the corresponding frequencies. The vibration of a building is described by a superposition of all contributing normal modes. These modes can be either bending or torsional modes. A bending mode defines the behavior of a building under an external load perpendicular to the vertical axis, a torsional mode the twisting of a building due to an applied torque. The mode shapes of the first three bending modes are shown schematically in Figure 3.

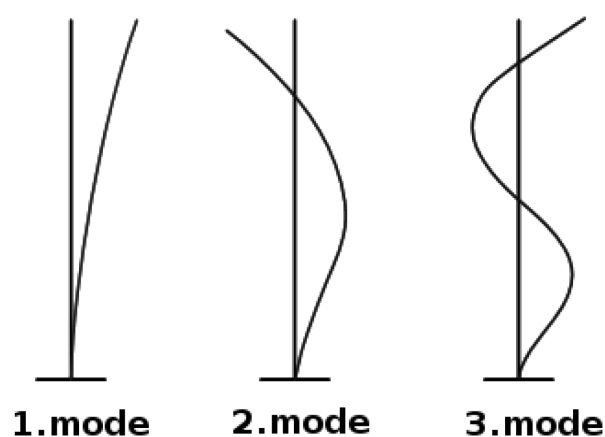


Figure 3. Scheme of the first three bending modes.

4 Methods

The new methodology which was developed within the framework of this thesis is based on the waveform approach, which involves the deconvolution and constrained deconvolution methods. In this chapter, the main characteristics of the deconvolution and constrained deconvolution approaches are first summarized. Second, the new methodology, namely the joint deconvolution, including a novel procedure for estimating energy being radiated back from the building to the soil, is presented step by step.

4.1 Deconvolution approach

The deconvolution of a signal $u(t)$, recorded at a generic location, by a signal recorded at a reference location $u_{ref}(t)$ (both being generated by the same source) is defined in the frequency domain as (e.g., Snieder and Safak 2006)

$$D(\omega) = \frac{u(\omega)}{u_{ref}(\omega)} \quad (6)$$

where $u(\omega)$ and $u_{ref}(\omega)$ are the Fourier transforms of the motions recorded at generic and reference locations, respectively, and $\omega = 2\pi f$ is the angular frequency. Usually, the sensor installed at the top or the bottom of either a building or a downhole installation is used as the reference. Since this problem is ill-conditioned, the regularized Tikhonov deconvolution (Tikhonov and Arsenin 1977; Bertero and Boccacci, 1998)

$$D(\omega) = \frac{u(\omega)u_{ref}^*(\omega)}{|u_{ref}(\omega)|^2 + \varepsilon} \quad (7)$$

is used to avoid instabilities, where ε is a regularization parameter. ε controls the degree of filtering in order to stabilize the deconvolution and is defined as a percentage of the average spectral power. The deconvolution approach using the recording at the roof as the reference (virtual source) is shown exemplarily for three different locations within a building in the frequency domain (as given in equation (7), Figure 4, left) and in the time domain (after calculating the inverse Fourier transform, Figure 4, right). The deconvolved wave field in the time domain is dominated by up (Fig. 4, right, red line) and down-going waves (Fig. 4, right, blue line) in the acausal and causal part, respectively. The time lag τ between the peaks of the up and downward propagating waves, together with the distance between two sensors, is used to estimate the slowness, and hence, the propagation velocity, between the two sensors.

When the deconvolution approach is applied, the horizontal components of ground motion are expected to be mainly related to the S-wave propagation, and the vertical component to the P-wave propagation (Mehta et al. 2007a, b; Parolai et al. 2009). In this thesis, the studies dealing with recordings of building sensors (both using the building sensor's recordings alone and the joint analysis of building and downhole sensor's recordings) are focused on the analyses of the horizontal components, and hence the S-wave propagation. This is due to the fact that the modes of buildings (both bending and torsional

modes) are mainly visible in the horizontal components. The analysis of the wave propagation through shallow geological layers is based on both, that is the investigation of S and P-wave propagation.

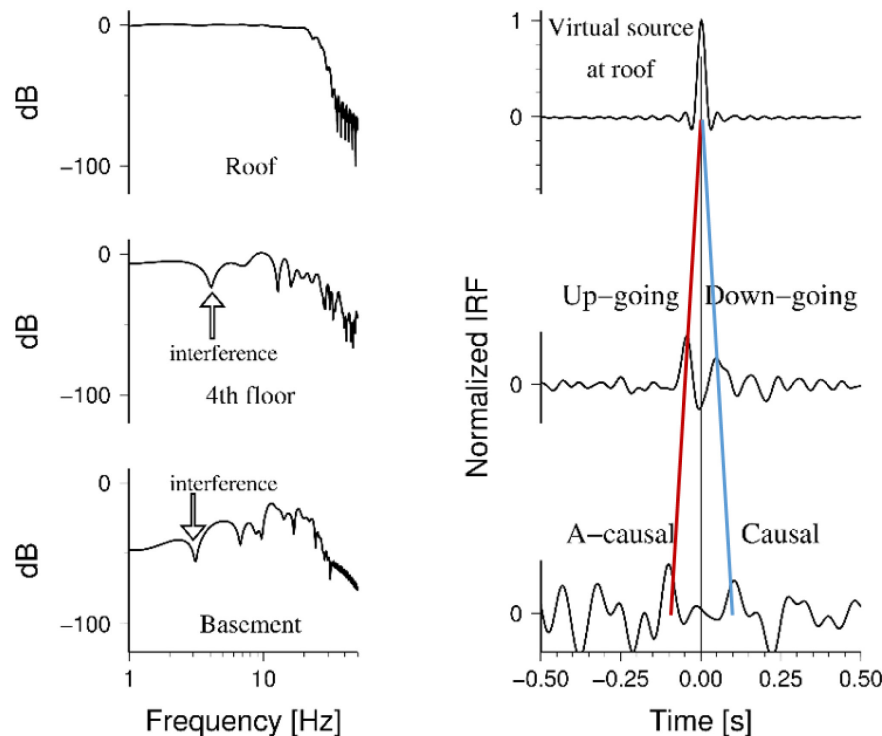


Figure 4. Examples of deconvolved wave fields calculated using the recording at the roof as the reference for three different locations within a building (basement, 4th floor and roof). Left: Frequency domain; right: time domain. Figure from Bindi et al. (2015).

4.2 Constrained deconvolution

Recordings from downhole sensors do not only include the upward propagating wave field, but also all down-going waves reflected at the interfaces of shallower layers (between the sensors' locations and the Earth's surface). In order to estimate the real seismic input (the shaking at a certain depth level), the downward propagating waves (in the space between the surface and considered depth) have to be removed to obtain the part of the wave field related only to the upward propagating waves. Bindi et al. (2010) proposed a method, the constrained deconvolution approach, which makes it possible to determine the seismic input motion by using the recordings of a surface-downhole pair of sensors. If this approach is applied to sensors that are installed in a nearly homogeneous medium (small impedance contrast between the layers), no information on the soil properties, i.e., the velocity structure and the quality factor Q , which is usually difficult to estimate, are needed. The discussed problem is shown in Figure 5a, where $S(t)$ and $B(t)$ are the ground motions (accelerations) recorded at the surface and the downhole sensors, respectively. $I(t)$ is the seismic input motion, which is the part of the wave field of interest. Bindi et al. (2010) used an iterative method (Landweber method, e.g., Bertero and Boccacci

1998; Bertero et al. 1997) which constrains a priori the solution and hence, filters out the down-going waves. The method has been validated using synthetic seismograms (shown in Fig. 5b) calculated using an impulse source at depth for a layered subsoil velocity model derived for the Ataköy (Istanbul, Turkey) vertical array (Parolai et al. 2009). The synthetic seismograms calculated for the bottom and the top sensors and the results of the unconstrained deconvolution (dominated by an up and a downward propagating pulse) are shown in Figure 5b, left. The results of the constrained deconvolution approach are presented in Figure 5b, right. The reconstructed input (black curve) and the target recording (gray curve) are shown in the top panel and are almost identical. The recording at the surface and the constrained deconvolution results (obtained by selecting the time domain of the solution and considering only the positive part of the deconvolved wave fields, i.e., time domain and positivity constraints), are depicted in the middle and bottom panels, respectively.

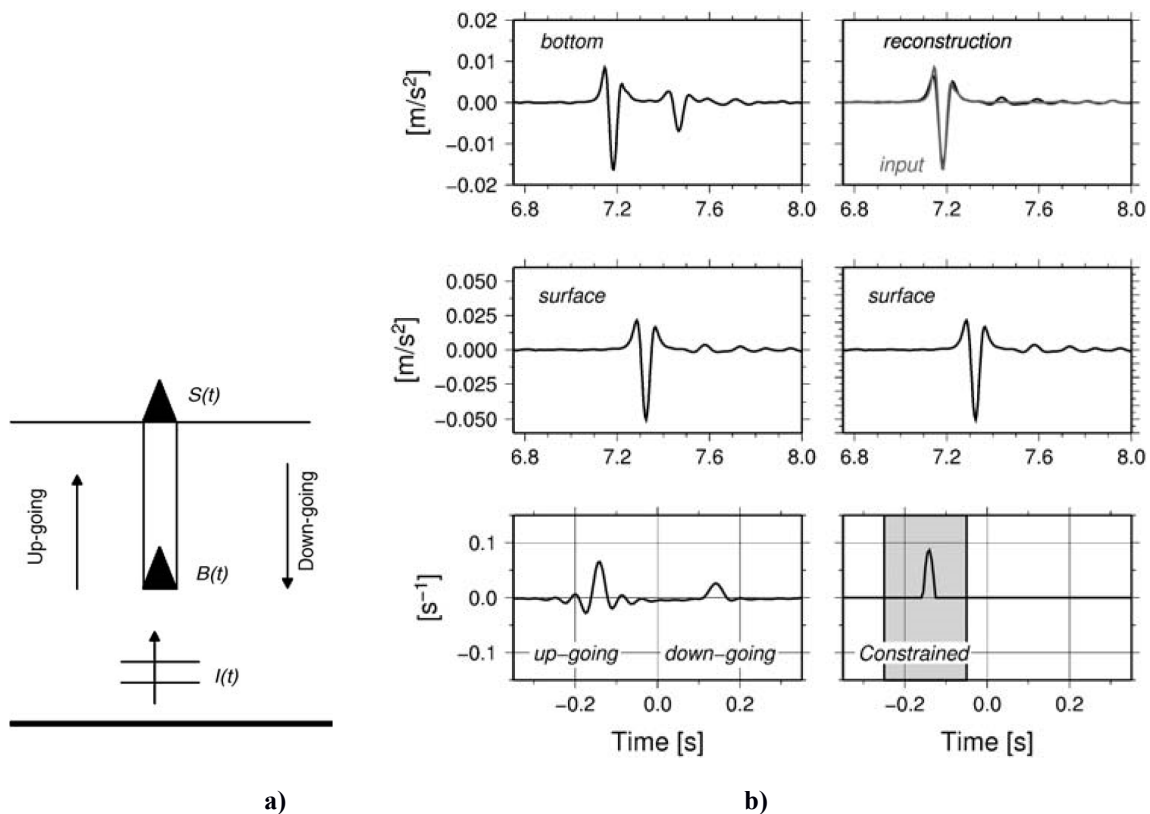


Figure 5. a) Scheme of the discussed problem: surface recording $S(t)$ and downhole recording $B(t)$ are used to estimate the seismic input motion $I(t)$. b) Validation of the constrained deconvolution with synthetic seismograms. Left: Unconstrained deconvolution; downhole recording (top), surface recording (middle), downhole to surface deconvolution (bottom). Right: Constrained deconvolution; top: comparison between estimated seismic input motion (black curve) and the target recording (gray curve), surface recording (middle), constrained deconvolution, positivity and time domain constraints applied to deconvolution (bottom). Figures from Bindi et al. (2010).

4.3 Joint deconvolution and estimation of energy being radiated back from buildings to the soil

A new methodology for the joint analysis of building and downhole sensor recordings and for separating the contribution of different refracted/reflected phases in the wave field, was developed within the framework of the research undertaken as part of this thesis and is described in Petrovic and Parolai (2016). The main advantage of the proposed procedure is that it also makes it possible the estimation of the energy being radiated back from the building to the soil through four main steps that are described in the following.

The methodology is summarized in Figure 6 and schematically shown in Figure 7, exemplarily for the recordings of three sensors, one installed at the building's roof, one at the Earth's surface, and one downhole sensor installed in the soil.

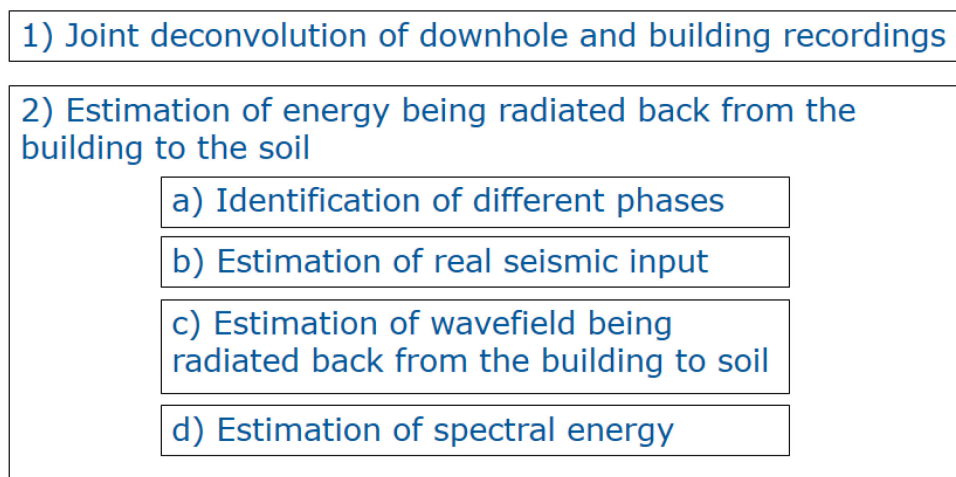
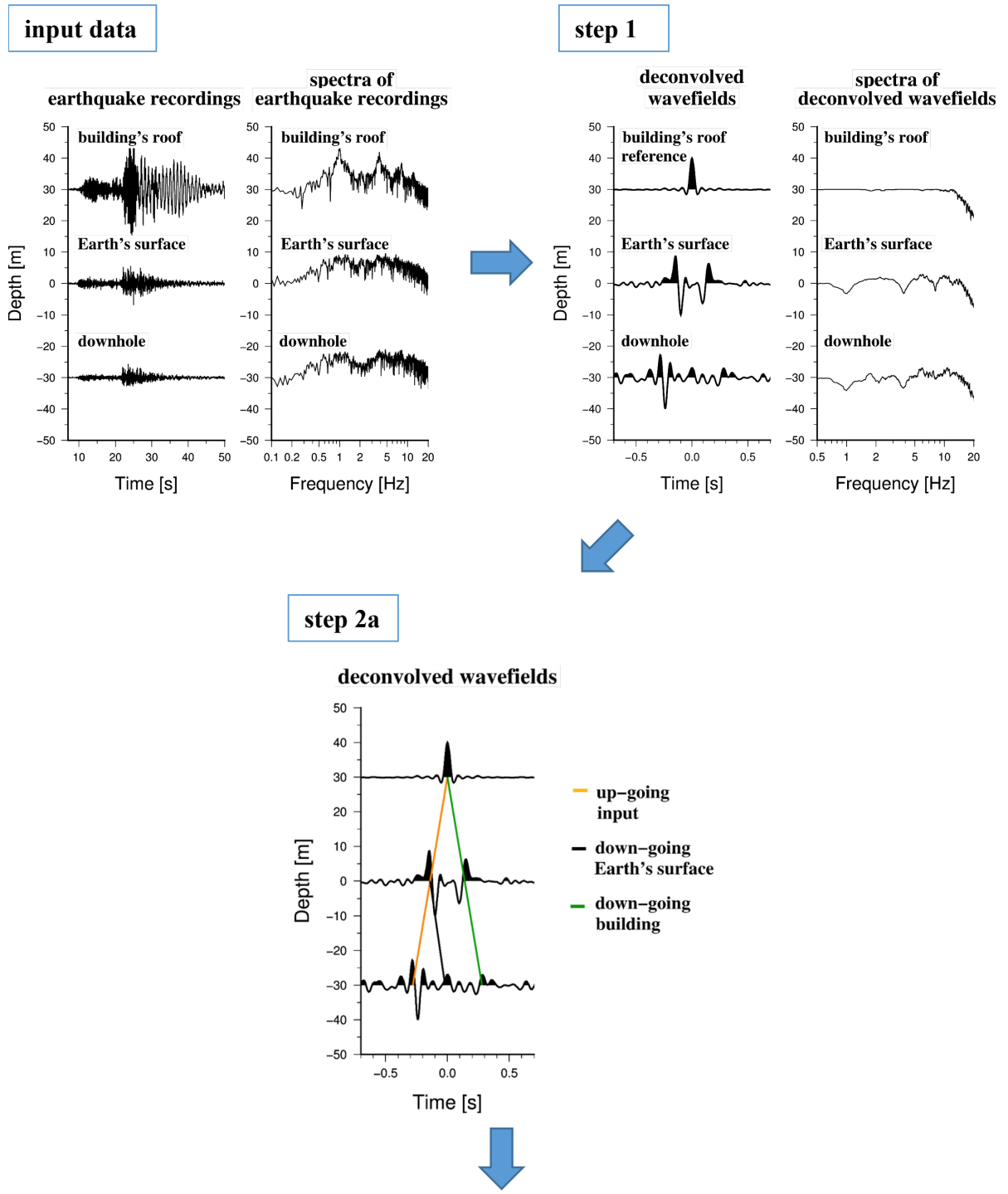
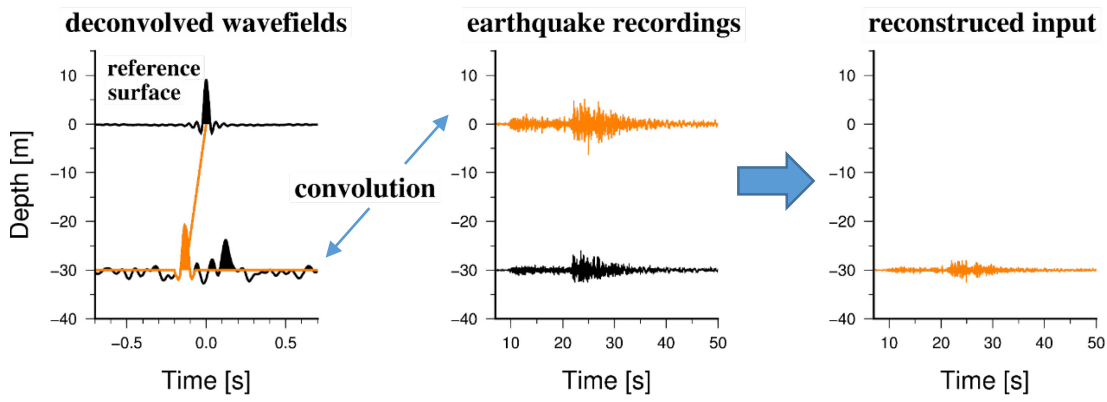


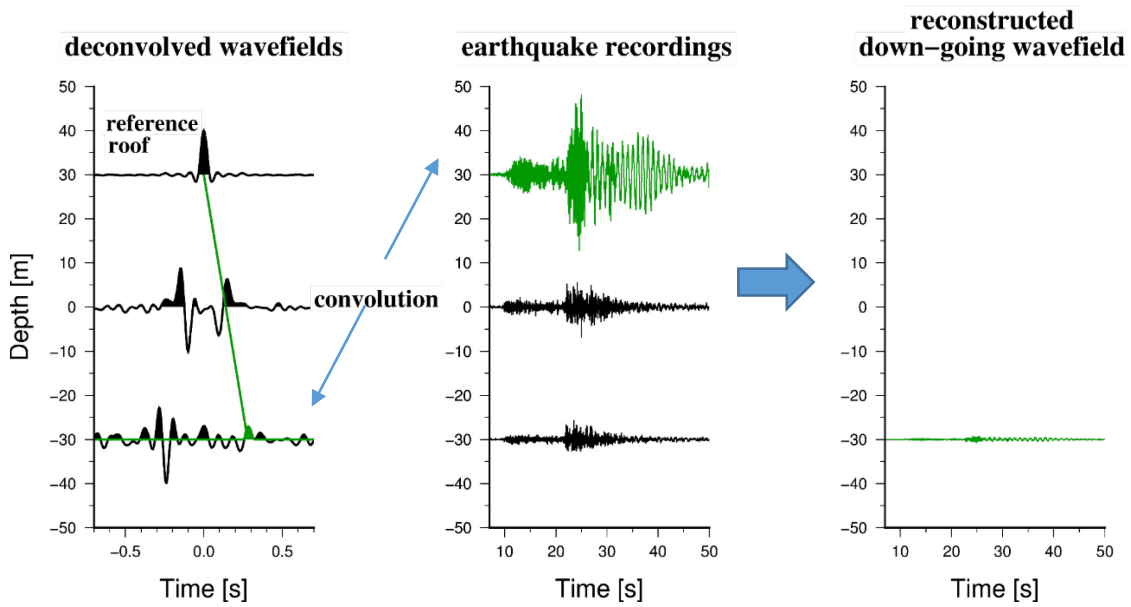
Figure 6. Scheme describing the steps 1)-2d) of the methodology developed as part of the research undertaken for this thesis. Figure from Petrovic et al. (2017b).



step 2b



step 2c



step 2d

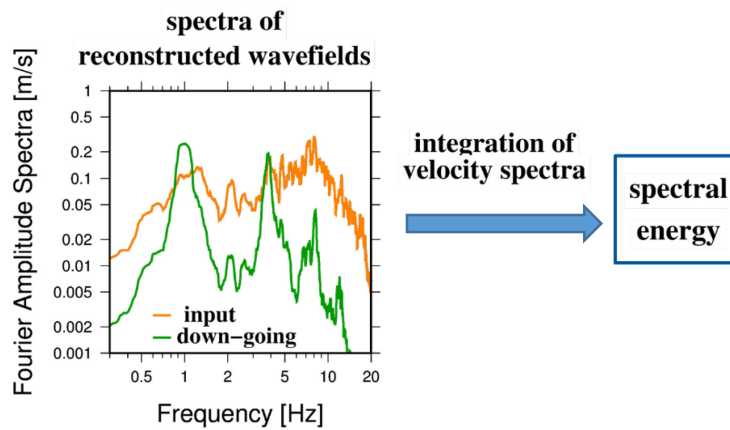


Figure 7. Scheme showing the methodology steps (as listed in Figure 6). On the left top the earthquake recordings (at the building's roof, the Earth's surface and in the soil) and the corresponding Fourier amplitude spectra are shown. **Step 1)** Joint deconvolution (reference: roof) in time (left) and frequency domain (right). **Step 2a)** Identification of the different phases of the deconvolved wave field (orange lines: up-going waves, black lines: down-going waves, reflected at the Earth's surface, green lines: down-going waves, reflected at the buildings' roof). **Step 2b)** Reconstruction of real seismic input. Left: deconvolved wave fields (ref.: Earth's surface), orange: part of deconvolved wave field that belongs to the upward propagating waves; center: earthquake recordings, orange: recording needed for reconstruction; right: reconstructed real seismic input after convolving the part of the deconvolved wave field of the interest and recording (both shown in orange). **Step 2c)** Reconstruction of the wave field being radiated back from the building to the soil. Left: deconvolved wave fields (ref: roof), green: part of deconvolved wave field that belongs to the wave field reflected at the roof; center: earthquake recordings, green: recording needed for reconstruction; right: reconstructed down-going wave field after convolving the deconvolved wave field of interest and recording (both shown in green). **Step 2d)** Spectra of wave fields reconstructed in step 2b (orange) and 2c (green). The spectral energy is obtained after integration of the velocity spectra.

Step 1) First, the joint deconvolution of borehole and building sensor recordings, based on the application of the deconvolution approach to building and downhole recordings simultaneously, is carried out (Fig. 6 and 7, step 1). For this purpose, the station at the top of the building is used as the reference. Differently from the simple nearly homogeneous case (e.g., when considering the wave propagation through a homogenous soil layer), where the deconvolved wave field is dominated by one upward and one downward propagating wave, for the case of several layers (including the building and soil layers), the deconvolved wave field is more complex due to reflections/refractions at each interface (between the sensor's location and the Earth's surface), dominated by several up and downward propagating peaks.

Step 2a) Since the deconvolved wave field of a multi-layer system is dominated by several upward and downward propagating peaks, first, the different peaks have to be assigned to the different phases (upward propagating waves, downward propagating waves reflected at the Earth's surface, reflections at impedance contrasts and the top of the building, etc., Fig. 6 and 7, step 2a). A comparison of results obtained for synthetic data (calculated by numerical simulations) and real data, as well as the results of the analytical transfer functions for layered media, help in the assignment of the peaks.

Step 2b) Then, the real seismic input, i.e., the ground motion at a certain depth related only to the upward propagating waves from below, is reconstructed by removing all downward propagating waves (reflections from the building's roof, the Earth's surface and the impedance contrasts existing in the geological layers between the surface and the depth at which the sensor is located) using an approach similar to the constrained deconvolution proposed by Bindi et al. (2010) as shown in Figures 6 and 7, step 2b (not applying the Landweber method as Bindi et al. 2010, but a direct convolution). In order to reconstruct the real seismic input, either the building-downhole or only the downhole sensors can be used, with the roof sensor or the one at 0 m serving as the reference when deconvolution is carried out. Therefore, the part of the deconvolved wave field that is associated with the upward propagating waves (differs for the two cases with different reference stations) is convolved with the recording at the reference sensor (either at 0 m or at the roof).

Step 2c) Furthermore, the part of the wave field that is associated with the waves being radiated back from the building to the soil (down to different depths) is separated by using the same approach (constrained deconvolution) as the one used to reconstruct the real seismic input (Figures 6 and 7, step

2c). The part of the wave field associated with the downward propagating waves (radiated back from the building to the soil) in the deconvolved wave field (the reference being the roof sensor) is convolved with the recording at the roof of the building. Please note that several peaks assigned to different phases might arrive at the same time and hence, overlap (Petrovic and Parolai 2016). In order to correctly reconstruct the downward propagating wave field, the relative importance of the contribution of the different phases arriving at the same time, is needed. For this reason, the analytical transfer function is calculated (Petrovic and Parolai 2016, Appendix). The relative importance can then be calculated when information on the velocity structure (obtained from the deconvolution approach) and the densities (mainly of importance for the building, the equivalent density of the building can be estimated by multiplying the percentage of the filled volume with respect to the total volume, by the density of the building material used) are given. No a priori information on the quality factor Q (intrinsic attenuation) is needed.

Step 2d) Finally, the spectral energy being radiated back from the building to the soil is estimated by the integration of the velocity spectra of the wave field associated with the real seismic input (b) and with the downward propagating waves (c) over a certain frequency band (the same frequency band as used for the joint deconvolution and dependent upon the frequency band of the spectra recorded at the roof of the building) as shown in Figures 6 and 7, step 2d. The estimated energy corresponding to the wave field being radiated back from the building to the soil is compared to the reconstructed real seismic input energy.

As mentioned in step 2c, considering a media consisting of more layers (such as, for example, one building and at least one soil layer), the wave field associated with the waves being radiated back from the building to the soil can be reconstructed correctly when the relative importance of the contributing different phases is taken into account. For this purpose, information about the velocity structure (obtained directly from the deconvolution approach) and equivalent densities of the building (in this case the average density) and soil layers are needed. Usually these quantities are approximately known for the soil, and can be estimated for the building. Information about the quality factor Q , which is usually difficult to estimate, is not needed.

Assuming the building's behavior can be described by a shear beam model and hence modeled as one building layer over a soil layer (as shown in Fig. 8), the analytical transfer function $x(f)/y(f)$ for the sensor in the soil layer is obtained for a two-layer media (Petrovic and Parolai, 2016) as

$$\frac{x(f)}{y(f)} = \underbrace{\frac{1}{2(1+r)} e^{-i2\pi f(-\frac{\tau_1}{Q_1} - \frac{\tau_2}{Q_2})}}_{(a)} + \underbrace{\frac{r}{2(1+r)} e^{-i2\pi f(\frac{\tau_1}{Q_1} - \frac{\tau_2}{Q_2})}}_{(b)} + \underbrace{\frac{r}{2(1+r)} e^{-i2\pi f(\frac{\tau_2}{Q_2} - \frac{\tau_1}{Q_1})}}_{(c)} \quad (8)$$

$$+ \underbrace{0.5(1-r)}_{(d)} e^{-i2\pi f(\frac{\tau_1}{Q_1} + \frac{\tau_2}{Q_2})} + \underbrace{\frac{r^2}{2(1+r)}}_{(e)} e^{-i2\pi f(\frac{\tau_1}{Q_1} + \frac{\tau_2}{Q_2})}.$$

where f is the frequency, τ_1 and τ_2 are the travel times for wave propagation from the top of the building to the impedance contrast (building-soil discontinuity) and from the impedance contrast to the sensor in the soil, and Q_1 and Q_2 are the quality factors of the building and soil layers, respectively, and r is the reflection coefficient (equation (3)). The derivations of the analytical transfer functions for both a two-layer and a three-layer media can be found in Petrovic and Parolai (2016, Appendix).

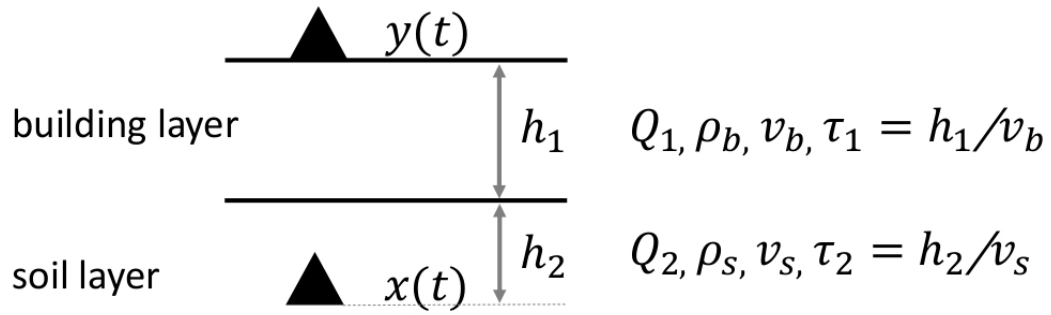


Figure 8. The two layer model, consisting of one building layer overlying the soil layer (a half-space), with recordings $y(t)$ at the top of the building and recordings $x(t)$ in the soil layer. h_1 and h_2 are the building height and the distance from the building-soil discontinuity to the location of the sensor in the soil, respectively. Q_1 and Q_2 are the quality factors, ρ_b and ρ_s are the densities and v_b and v_s the shear wave velocities of the building and soil layers, respectively. τ_1 and τ_2 are the travel times for wave propagation from the top of the building to the impedance contrast (building-soil discontinuity) and from the impedance contrast to the sensor in the soil. Figure from Petrovic and Parolai (2016).

5 The test sites

In this thesis, the data from 5 test sites (the different analyses performed for each test site are listed in Table 1) are used either to investigate the velocity and/or attenuation in buildings or soil separately, or to analyze the wave propagation through building-soil layers jointly and to estimate the energy being radiated back from the building to the soil (three test cases). A short description of each test site is given in the following paragraphs.

Table 1. Test sites and analyses performed for each test site.

Test site	Type of analysis	Section
AHEPA building	○ study dealing with velocity in building	6.1.1
	○ study of the wave attenuation in the building	6.2.1
Tuzla Peninsula	○ study dealing with velocity in soil	6.1.3
	○ study dealing with the wave attenuation in soil	6.2.2
Bishkek vertical array	○ joint analysis of building and downhole seismic data	6.3.2
Istanbul vertical array	○ study dealing with velocity in building	6.1.2
	○ joint analysis of building and downhole seismic data	6.3.2
Mexico City vertical array	○ joint analysis of building and downhole seismic data	6.3.2

5.1 The AHEPA test site in Thessaloniki, Greece

The AHEPA hospital is an 8-story RC-building in Thessaloniki (Greece), belonging to one of the largest hospitals in northern Greece (Bindi et al. 2015). It is composed of two units connected via a seismic joint (Fig. 9). This building has been selected as a test site¹ for developing a structural health monitoring system and is instrumented with a permanent strong motion network (Self-organizing Seismic Early Warning Information Network, SOSEWIN, Fleming et al. 2009). Two events recorded by the SOSEWIN network are analyzed in this study. In addition, temporary measurements with a dense network of stations (39 short period L4C-3D Mark sensors connected to Earth Data Logger 24bit digitizers) were performed in order to register ambient vibration and to investigate the dynamic properties of the building in detail, including both the velocity (Section 6.1.1) and attenuation (Section 6.2.1).

¹ <https://lhotse21.gfz-potsdam.de/nagvis/frontend/nagvis-js/index.php?mod=Map&act=view&show=ahepa>

5.3 The Bishkek vertical array in Kyrgyzstan – CAIAG and downhole installation

The Central Asian Institute for Applied Geosciences (CAIAG, Figures 11a and 12a) in Bishkek (Kyrgyzstan) is a three story reinforced masonry structure which was equipped with seven SOSEWIN units² in 2012. In its courtyard, a 150 m deep downhole was drilled and equipped with borehole sensors at 0, 10, 25, 45, 85 and 145 m depth (e.g., Parolai et al. 2013). The S-wave velocity (v_s) profiles (obtained after the inversion of the spectra of the deconvolved wave fields, from Parolai et al. 2013) and the stratigraphy at this site are also shown in Figure 11a. Four events recorded by the Bishkek vertical array (building and downhole sensors) were used to develop a novel approach (Section 4.3) to study the wave propagation through building-soil layers and to estimate the energy being radiated back from a building to the soil, published in Petrovic and Parolai (2016). A comparison with results obtained by the same approach to the data sets of two other vertical arrays (the Istanbul vertical array and the Mexico City vertical array) is presented in Section 6.3.2 and Petrovic et al. (2017b).

5.4 The Istanbul vertical array in Turkey – the B22 building and downhole installation

The B22 building (Fig. 11b and 12b) is a 16 story residential reinforced concrete building constructed by tunnel formwork technology in Istanbul, Turkey (Petrovic et al. 2017a). Due to their expected high seismic resistance, millions of buildings with this construction type have been built over the last decades, especially in regions prone to high seismic hazard. However, only a very limited number of real data analyses has been performed. For this reason, but also due to its close location (50 m distance) to the Ataköy vertical array (borehole sensors at 0, 25, 50, 70 and 140 m depth; e.g., Parolai et al. 2009, 2010, 2012), the B22 building has been instrumented since summer 2013 by SOSEWIN units in the basement, on the 8th floor and the roof, and since September 2015 by a dense SOSEWIN station network³ consisting of 15 stations, installed at two different locations within the building at seven floors. The Istanbul vertical array, consisting of the instrumented building and the downhole installation, is one of the three test sites used to study the wave propagation through the building-soil structure (see Section 6.3.2 and Petrovic et al. 2017b). In addition, in September 2015, a thumper truck experiment was performed, which involved installing 36 4.5 Hz Geophones connected to CUBE digitizers⁴ within the building (two instruments per floor and four additional ones on the roof). Both ambient vibration and earthquake recordings are used to study the building's dynamic behavior in detail (see Section 6.1.2 and Petrovic et al. 2017a).

² <https://lhotse21.gfz-potsdam.de/nagvis/frontend/nagvis-js/index.php?mod=Map&act=view&show=caiaag>

³ <https://lhotse21.gfz-potsdam.de/nagvis/frontend/nagvis-js/index.php?mod=Map&act=view&show=istanbul>

⁴ <https://www.omnirecs.de/dc3.html>

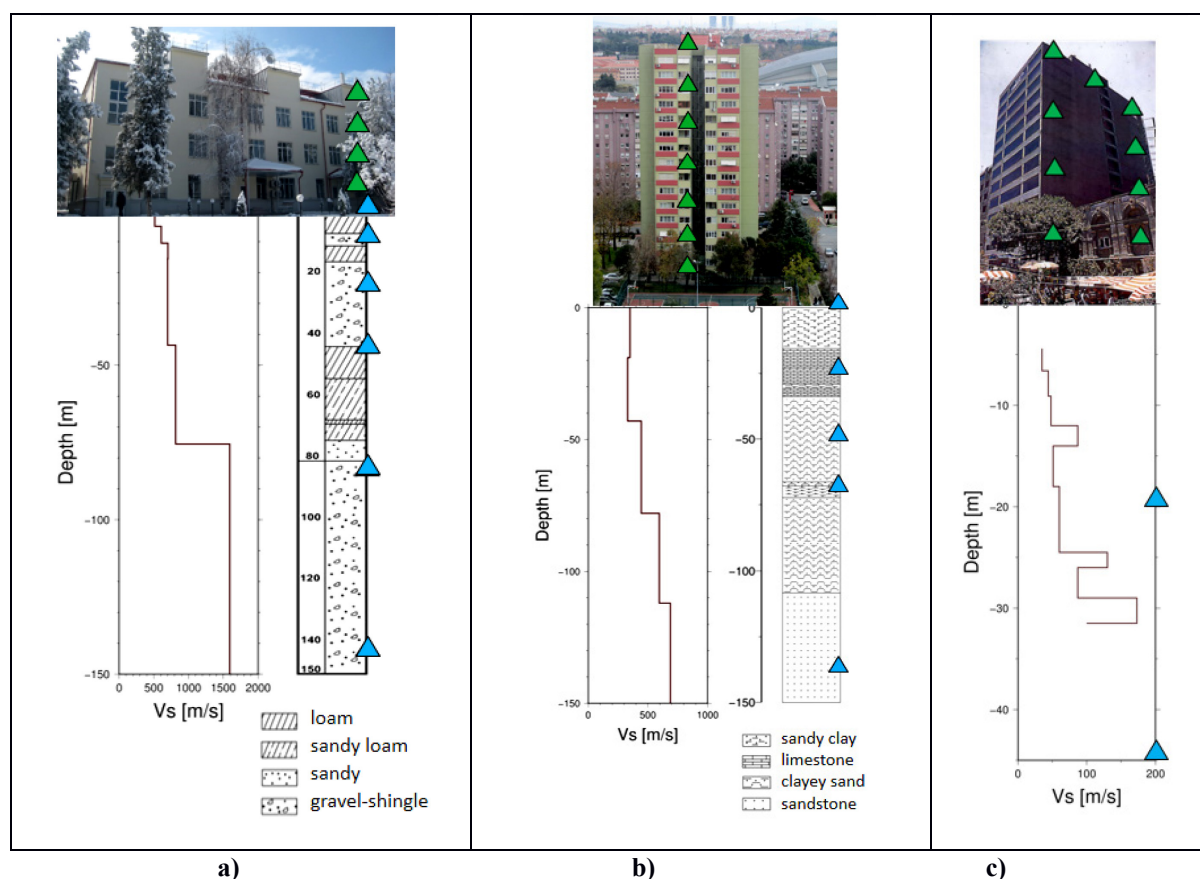


Figure 11. Three of the test sites considered in this work (including pictures of the buildings) for studying soil-structure interaction effects. Networks of sensors are installed in buildings (green squares or triangles) and boreholes (blue triangles). The shear wave velocity profile and the stratigraphy are shown for **a)** Bishkek, Kyrgyzstan, and **b)** Istanbul, Turkey. For Bishkek, the best fitting v_s models obtained after the inversion of the spectra of the deconvolved wave field are shown in different colors. For Istanbul, the best fitting v_s models (different colors) and the results obtained from P-S logging (gray line) are shown. For **c)** Mexico City, Mexico, the results of the P-S logging are presented. Figure from Petrovic et al. (2017b).

5.5 The Mexico City vertical array in Mexico – the Jalapa building and downhole installation

The Jalapa building is a 14 story reinforced concrete building (Fig. 11c and 12c) which was instrumented (1992-2004) with 11 units at different locations on 4 floors (basement, 6th and 11th floor, and roof). In the first three stories of the Jalapa building, a parking lot is situated, with offices located on the other stories. In addition, a borehole installation (two accelerographs at 20 and 45 m depth) was located underneath the basement of the building. The Jalapa building is one of the few well-instrumented buildings in Mexico that was damaged several times and retrofitted twice during its lifetime (Murià-Vila et al. 2001). For this reason, it has found great interest in the earthquake engineering community. The dynamic behavior of the Jalapa building has been studied e.g., by Meli et al. (1998) and Murià-Vila et al. (2001), soil-structure interaction effects have been observed by e.g., Paolucci 1993; Faccioli et al. 1996; Murià-Vila et al. 2004. A data set of events recorded by the Mexico

City vertical array (building and downhole installation) is used to study the wave propagation through the building-soil layers (Section 6.3.2 and Petrovic et al. 2017b).

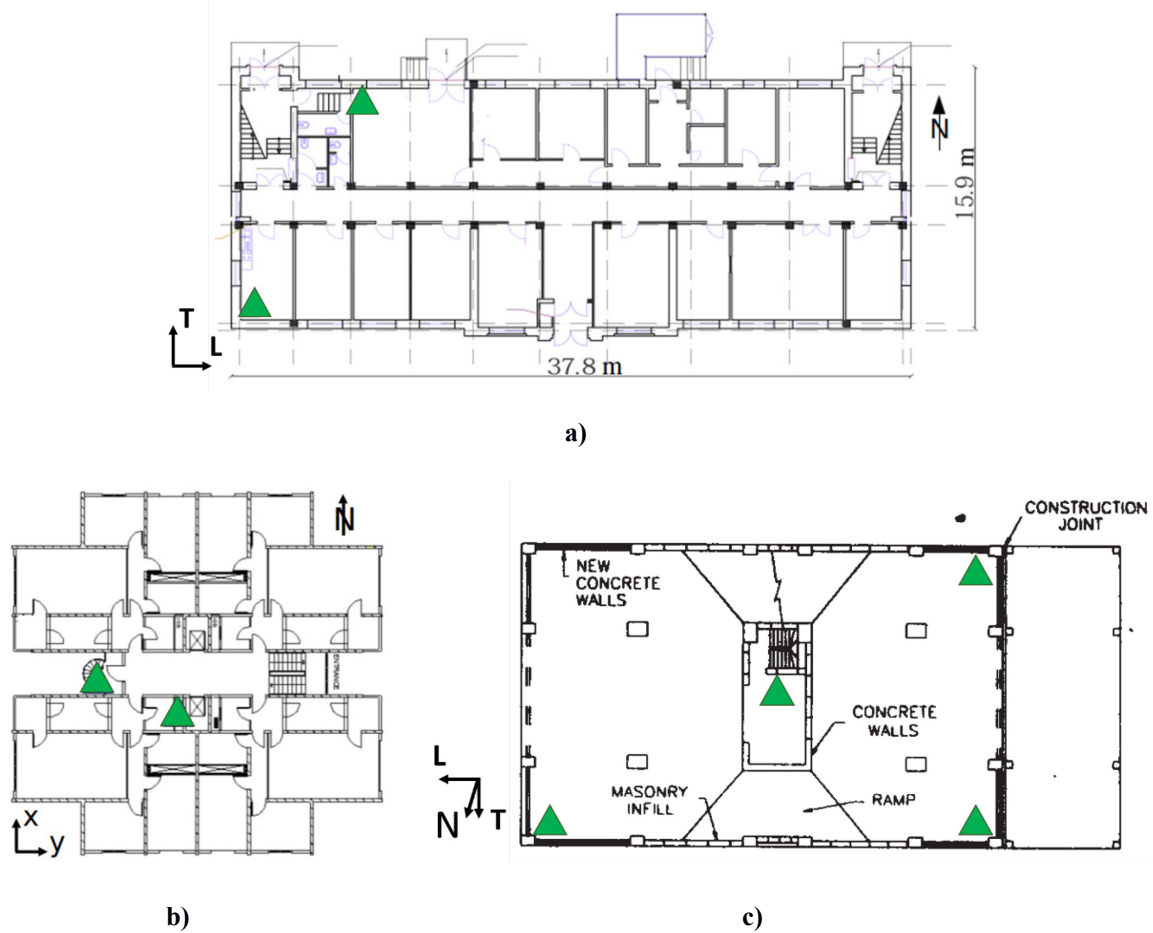


Figure 12. Floor plans of the three investigated buildings **(a)** CAIAIG institute, Bishkek, Kyrgyzstan, **(b)** B22 building, Istanbul, Turkey, **(c)** Jalapa building, Mexico City, Mexico). The locations of the sensors are shown by green triangles, their orientations by arrows at the left corner of each footprint showing either the longitudinal (L) - transverse (T) or the x-y orientation of the sensors. Figure from Petrovic et al. (2017b).

6 Application of the considered methods

6.1 Studies dealing with velocity in buildings and soil

Studying and understanding the wave propagation through buildings and soil, first separately, will simplify the interpretation of the complex deconvolved wave field obtained by the joint deconvolution, due to information retrieved for some of the phases (related either only to the building or to the soil). Nevertheless, identifying and quantifying the energy being radiated back from the building to the soil is only possible if building and downhole sensor data are analyzed jointly.

On the one hand, when recordings from buildings are analyzed by the deconvolution approach (waveform approach), the building's dynamic behavior is decoupled from that of the soil. When data from buildings and boreholes are analyzed jointly by the deconvolution approach, and the recordings at the roof of the building are used as the reference, the characteristics of the building will be projected also to the deconvolved wave fields of the downhole sensors. For this reason, understanding first the building's characteristics is essential. On the other hand, considering only the soil layers separately will make it easier to understand the different phases of the deconvolved wave field, and hence the velocity structure of the soil layers before extending the study to the more complicated case of the building-soil structure and thus, the more complex deconvolved wave field.

Analyzing ambient vibrations, active source signals or earthquake recordings helps the investigation of dynamic behavior of buildings. Ambient vibration measurements have the advantage that a large number of buildings can be monitored in detail under weak dynamic loading in a short time at a relatively low cost by the installation of dense sensor networks (e.g., Ivanovic et al. 2000; Michel et al. 2008; Prieto et al. 2010; Bindi et al. 2015). Thus, the dynamic behavior, i.e., the shear wave velocity which is proportional to the stiffness, of a large number of buildings can be estimated. Nevertheless, if different sources of ambient vibration are located inside a building, the deconvolved wave field may not be defined by clear upward and downward propagating peaks, as in the case of earthquake recordings, but may show a more complex pattern. Moreover, studies based on ambient vibrations are not adequate for estimating the wave propagation through shallow geological layers due to the low sensitivity of the downhole strong motion sensors. Since the core of this thesis is to investigate wave propagation through building-soil layers and to estimate the amount of energy that is radiated back from the building to the soil during a seismic event, earthquake recordings are used for the joint analysis. Ambient vibration recordings are analyzed as an additional tool to investigate the dynamic behavior of buildings in more detail by data recorded by dense temporary networks.

Two studies dealing with velocities in buildings are shown first (the AHEPA test site, Thessaloniki, Section 5.1, and the B22 building, Istanbul, Section 5.4), followed by a study on the wave propagation in shallow geological layers at the Tuzla Peninsula (Section 5.2).

6.1.1 The AHEPA test site

The shear wave propagation through the AHEPA building (Section 5.1) is investigated by applying the deconvolution approach to both ambient vibration measurements and earthquake recordings (Bindi et al. 2015). The comparison of the results obtained by using the recordings at the top of the building as the reference, applied to both ambient vibration measurements (blue, one hour of data) and earthquake recordings (red) are shown in Figure 13. The deconvolved wave fields obtained from the earthquake recordings are in good agreement with the ambient vibration results for the first and fourth floors, but not for the basement. The deconvolved wave fields of the earthquake recordings are dominated by a clear upward and downward propagating wave for all floors. However, for the results obtained from the dense ambient vibration measurements, the deconvolved wave fields of the higher floors show clear upward and downward propagating phases, whereas the deconvolved wave fields of the lower floors show a more complex pattern. The complex pattern of the deconvolved wave field in the first three floors is ascribed to the complex distribution of internal sources within these floors (several entrances to the first and second floors). This example shows that ambient vibration measurements are a useful tool, but might also lead to difficulties in interpretation if several internal noise sources exist (e.g., Bindi et al. 2015). In order to overcome these limitations in the interpretation of real data due to such complex patterns, comparisons with results obtained from numerical simulations are required.

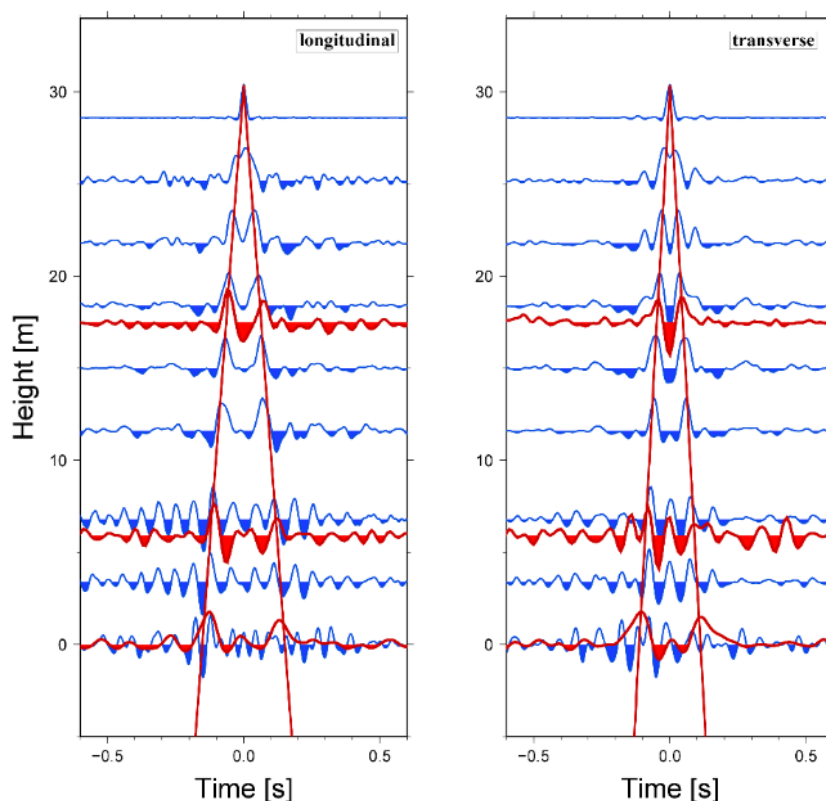


Figure 13. Deconvolved wave fields obtained by the analysis of ambient vibration (blue) and earthquake recordings (red) for both horizontal directions (left: longitudinal, right: transverse) of the AHEPA hospital. Recordings of two different earthquakes (Volvi earthquake of 11 October 2013, M_w 4.2 and 38 km distance, and the Cephalonia earthquake of 26 January 2014, M_w 6.1 and 350 km distance) are used. Figure from Bindi et al. (2015).

The vertical propagation of SH waves in a layered medium is calculated by an approach which was developed by Wang (1999). This approach is based on a matrix propagator method which is stabilized numerically by inserting an additional numerical procedure into the matrix propagation loop. The simulations are carried out using sampling rates and generate a signal frequency band similar to that used with the real data. The building is herein modeled as a shear beam, consisting simply of three overlying layers with different shear wave velocities. The aim was not to find the best model for this building, but to use a simple model to estimate the velocity structure of the building by a comparison of the deconvolved wave fields of the real and synthetic data sets (obtained from the model). For the first three floors (first layer: basement to 2nd floor, second layer: 2nd floor to third floor), the shear wave velocities are estimated by varying the characteristics of the model until a model was found that best fits the real data results. For the higher floors, the shear wave velocities are calculated by considering the time lags and the height differences between the floors and using a least squares fit.

The comparison of the deconvolved wave fields of the real data (green) and the best fitting model (blue) are shown in Figure 14. For the AHEPA building, the velocities of the lower floors were estimated to be much higher (from basement to second floor: $v_{\text{transverse}}=1000$ m/s and $v_{\text{longitudinal}}=500$ m/s) than those of the higher floors (2nd floor to third floor: $v_{\text{transverse}}=400$ m/s and $v_{\text{longitudinal}}=200$ m/s, 3rd floor to roof: $v_{\text{transverse}}=276$ m/s and $v_{\text{longitudinal}}=200$ m/s). Since the distribution of the shear wave velocity is linked to the stiffness of the structure, for the AHEPA building, the velocity and hence, also the stiffness, is much higher at the basement and lower floors. The increased stiffness at the base building is expected due to the fact that the basement is partially embedded (along one side only) and because the dimensions of the reinforced concrete elements (columns) are progressively decreasing with the height.

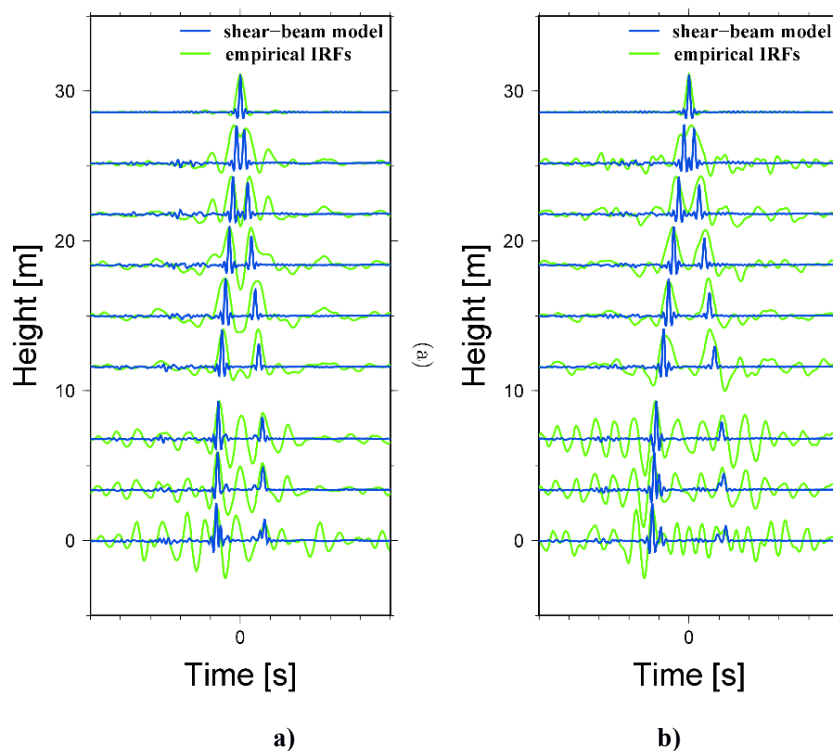


Figure 14. Comparison between the deconvolved wave field obtained from ambient vibration measurements (green lines) and those from synthetic data (blue lines) for the longitudinal (a) and the transverse (b) directions. Figure from Bindi et al. (2015).

6.1.2 The B22 building

Both ambient vibration/active source measurements and earthquake recordings are used in order to investigate the dynamic properties of the B22 building (Section 5.4 for building information, with results presented in Petrovic et al. 2017a).

In Figure 15, the deconvolved wave fields of ambient vibration/active source measurements using the recordings at the bottom of the building as the reference are shown for the x (Fig. 15a, c) and y-directions (Fig. 15b, d, see Fig. 12b for the orientation of the components). Interestingly, apart from the upward and downward propagating waves (magenta lines), from the bottom to the roof and back in both the acausal and causal parts, the oscillation of the building with the frequencies of the first and second bending modes ($f_{x_1}=1.02$ Hz, $f_{y_1}=1.37$ Hz, green lines, $f_{x_2}=3.85$ Hz, $f_{y_2}=5$ Hz, red lines) are clearly visible for both directions (Fig. 15 a, b). Please note that the second mode is characterized by a polarity change between the 11th floor and the roof (Fig. 15 c, d, marked with orange circles) which is due to the crossing of the zero point at this height (see Fig. 3). The excitation also of the second mode is probably connected to the frequency content of the input signal (where the dominant frequency band lies between 0.5 and 15 Hz).

Moreover, in order to better understand the dynamic characteristics of the B22 building and to be able to interpret later the deconvolved wave field of the building-downhole-installation, the deconvolution approach using the recording at the top as the reference (the same as for the joint deconvolution) is applied to both ambient vibration/generated source measurements (Fig. 16a and 16b for x and y-direction, respectively) and earthquake recordings (Fig. 16c and 16d for x and y-direction respectively, blue lines). The deconvolved wave fields of both are dominated not only by the upward and downward propagating waves (orange lines), but also by peaks with inverted polarity (green lines) that propagate with the same velocity. These peaks are again related to the second mode and the inverted polarity around the 13th floor.

In addition, a comparison of the deconvolved wave field of real data with the results of the synthetic seismograms usually helps in the interpretation. In this case, the building was not modeled as a simple layer, since it was observed that not all characteristics of the building's behavior could be captured by this simple model, that is, none of the characteristics in the deconvolved wave field due to the higher bending modes or torsional modes will be seen if a simple layer model is used. A Finite Element Modeling (FEM) was carried out, where synthetic seismograms were calculated as the building's response to an event recorded at the basement of the building and given as an input to the Finite Element Model.

The deconvolved wave fields of the synthetic seismograms (gray) are shown in Figure 16 for the x (Fig. 16c) and y (Fig. 16d) directions, together with the results of the earthquake recordings (blue). When comparing the deconvolved wave fields of real and synthetic data for the x-direction, the deconvolved wave fields are almost identical. For the y-direction, there are some discrepancies between the results of real and synthetic data, due to some differences in the fundamental frequencies obtained from real data and the FEM. The comparison of synthetic data results obtained by FEM with real data results is very useful for understanding better the deconvolved wave field of the real data set. Finally, it was confirmed that the two peaks with inverted polarity propagating with the same velocity as the upward and downward propagating waves, between the basement and the 10th floor, are due to the strong

excitation of the second mode. In fact, the excitation of different modes, in this case the second mode, might depend also on the input used for the study (e.g., Ditommaso et al. 2010b).

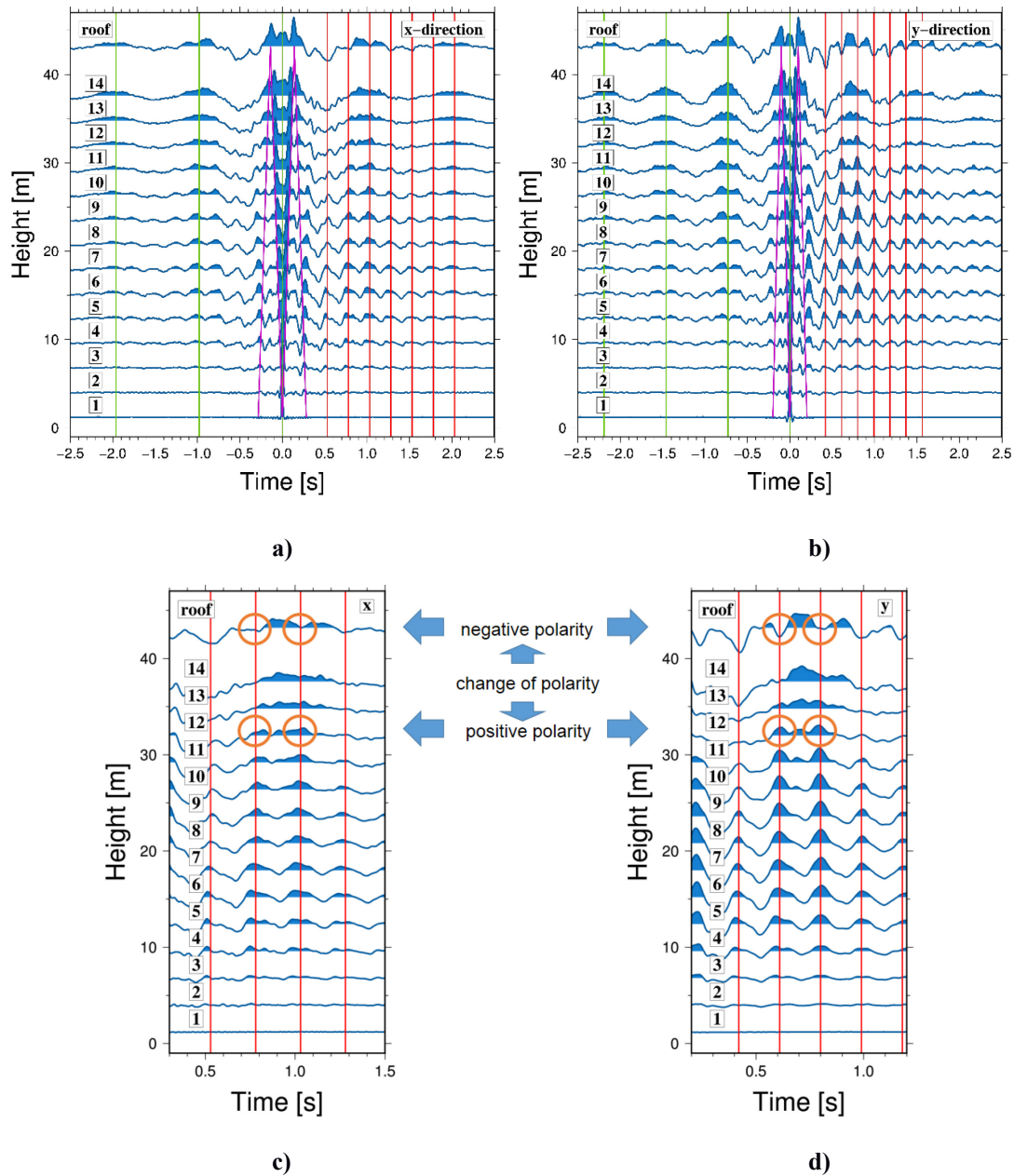


Figure 15. **a, b)** Deconvolved wave fields (acausal and causal parts) using station at the ground floor as the reference (**a**): x-direction, **b**): y-direction). Magenta lines show the upward and downward propagating waves, oscillations of the building are shown by green (first mode) and red lines (second mode). **c, d)** Deconvolved wave fields, causal part, (changed time scale), showing the change of polarity between the 11th floor and the roof for the x (**c**) and the y (**d**) direction. Figure from Petrovic et al. (2017a).

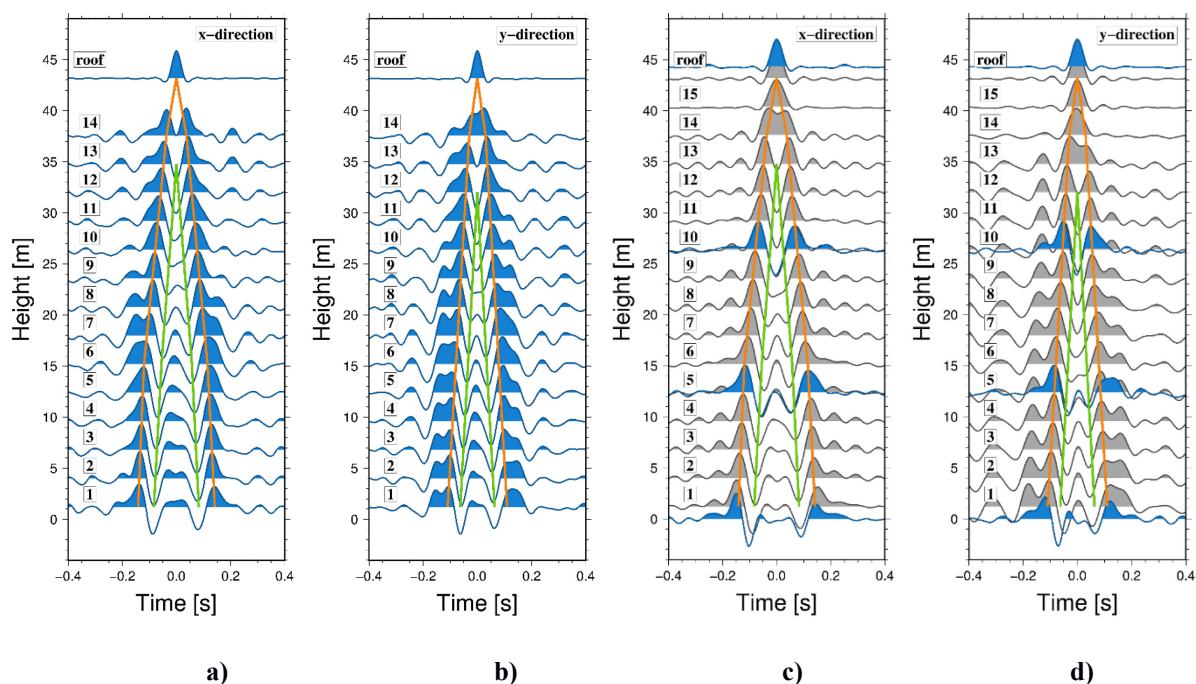


Figure 16. a), b) Deconvolved wave fields of the ambient vibration/generated source recordings, using the recording at the top as reference. Orange lines show the upward and downward propagating waves, green lines show the upward and downward propagating waves with inverted polarity due to the influence of the second mode. a) x-direction, b) y-direction. c), d) Comparison of the deconvolved wave fields (reference: recording at the roof) of synthetic seismograms (gray) and the real data earthquake results after stacking (blue) for the x (c) and y-directions (d). Figure from Petrovic et al. (2017a).

6.1.3 The Tuzla Peninsula

A study on the seismic wave propagation in shallow geological layers was performed for the Tuzla Peninsula (Section 5.2) in Raub et al. (2016). Deconvolved wave fields were calculated for 26 events and the stacked results are presented for all three components in Figure 17, using the recordings at the surface (top) and at 288 m depth (bottom) as the references. Three-component sensors were installed only at the surface and 288 m depth hence, only an average shear wave velocity could be estimated (~ 1800 m/s). Considering the deconvolved wave fields for the vertical component using both the recording at the top and at the bottom as references, two reflected P (gray dashed lines) waves with velocities of (~ 4000 - 4500 m/s) can be seen originating from an interface (e.g., a low velocity layer) between 71 and 144 m. Every additional layer, e.g., a building layer, results in a more complex deconvolved wave field. As the soil layers alone may already have a complex structure, such as the near-surface layers of the Tuzla Peninsula, it is helpful to consider first only the recordings of the downhole installation and thus, only the properties of the soil. This information on the velocity structure of the soil will in turn simplify the interpretation of the results of the joint deconvolution.

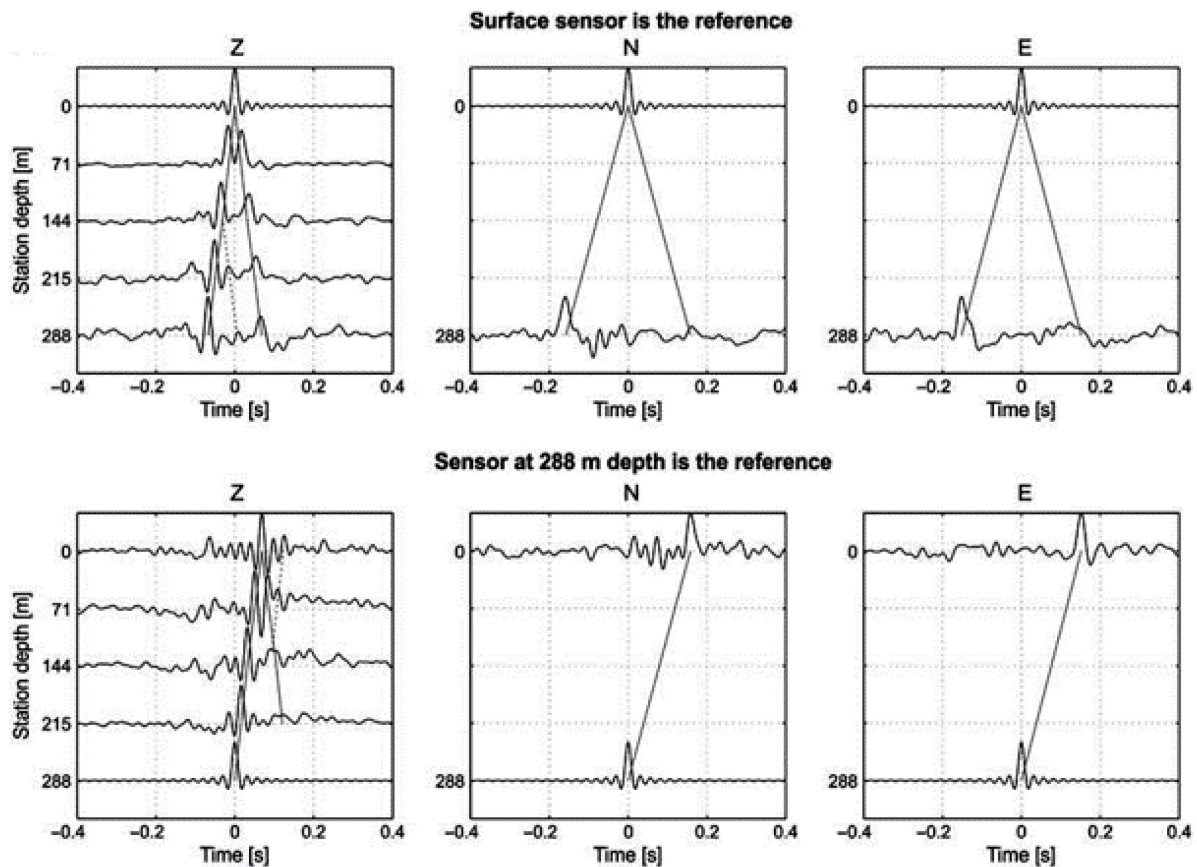


Figure 17. Deconvolved wave fields (after stacking the results for 26 events) of the vertical and horizontal components (left: Z, middle: N, right: E) using the recordings at the surface (top) and at 288 m (bottom) as the references. Figure from Raub et al. (2016).

6.2 Attenuation studies in buildings and soil

The response of a building or the soil mainly depends on its shear wave velocity and the attenuation. While studying the wave propagation velocity in buildings and soil separately is straightforward (if systems consisting of nearly homogeneous layers are considered), studying its attenuation is a much more complicated task. This is due to the fact that it might be difficult to separate the effects of scattering and intrinsic attenuation, since they depend on each other non-linearly. In fact, also for the Earth's medium, which is far from being uniform, the estimates of the separated scattering and intrinsic attenuation are generally biased (e.g., Del Pezzo et al. 2011).

In this thesis, a special focus is placed on the joint estimation of the properties of the material (building and soil) in terms of S-wave velocity, and on the assessment of the energy released back by the building to the ground when excited by seismic waves. In any case, in order to provide a better description of the dynamic characteristics of the analyzed structures, attempts were made to estimate their intrinsic attenuation, given by the quality factor Q . Although they do not represent the core of this thesis, some of the results obtained are shown in the following in order to provide a more comprehensive picture of the work carried out.

In this thesis the results of two studies aiming at assessing the intrinsic attenuation described by the quality factor Q , both in a building (for the AHEPA test site, Section 5.1) and shallow geology (for the Tuzla Peninsula, Section 5.2) are shown.

6.2.1 The AHEPA test site

When a building is considered, its geometry and its shear wave propagation velocity control its resonant frequencies, while the rate of energy dissipation is determined by the attenuation mechanisms involved. In general, it is expected that the decay of the deconvolved wave field (that according to the deconvolution approach mainly represents the ballistic / deterministic part of the propagation) over time depends principally on the intrinsic attenuation, i.e., on the quality factor Q , if the structure has only small vertical heterogeneities. The radiation losses due to quasi-homogeneities are expected to have a minor role. Snieder and Safak (2006) estimated the quality factor Q from the amplitude decay (slope equal to $-\omega/2Q$) of the natural logarithm of the envelope of the deconvolved wave field filtered with a bandpass filter around the fundamental frequency. This technique or modifications of it have found several applications in studying the quality factors of buildings (e.g., Kohler et al. 2007; Prieto et al. 2010; Newton and Snieder 2012).

Innovatively, the deconvolved wave field (obtained from ambient vibration measurements) for the AHEPA test site (Section 5.1, Bindi et al. 2015) has been analyzed in order to evaluate the intrinsic attenuation. With the approach proposed by Snieder and Safak (2006) and usually used for estimation of the quality factor Q_s in buildings, Q_s could not be estimated in a satisfactory way. This was due to the fact that it was difficult to define the part of the curve that should have been considered to estimate the slope (and hence, the quality factor), not allowing a univocal solution of the problem. For this reason, a method by Parolai et al. (2010) who estimated the quality factor Q_s in shallow layers by fitting the calculated transfer function with a theoretical transfer function (calculated analytically) was followed. In this case, the building is modeled as several overlying layers. This approach was applied to the transfer function between a generic floor and the roof (Fig. 18a, b: black lines, a: longitudinal, b: transverse) and fitted with a theoretical transfer function (Fig. 18a, b: gray lines) iteratively estimated during the inversion procedure. The travel time controls the position of the troughs in the Fourier spectra, while the quality factor controls the amplitude of the troughs and their attenuation with frequency. A grid search procedure (Fig. 18c) is applied over the quality factor Q_s and the travel time τ in order to minimize the root mean square difference between the theoretical and empirical transfer functions. For the grid search, the travel time τ is assumed to be in a $\pm 10\%$ range of the travel time estimated from the empirical deconvolved wave field, the Q_s values are fixed from 1 to 100. The quality factors for the best fitting model are estimated to be $Q_s=54$ ($\gamma=0.01$) and $Q_s=25$ ($\gamma=0.02$) for the longitudinal and transverse components, respectively. The cross section along the Q_s values for the travel time of the minimum misfit function (white line in c) is shown in Figure 18d (longitudinal) and 18e (transverse). The cost function has a steep gradient towards lower Q_s values, but an almost flat variability towards higher Q_s values. Thus, it is worth mentioning that the estimation of Q_s is not very precise due to a very flat misfit curve.

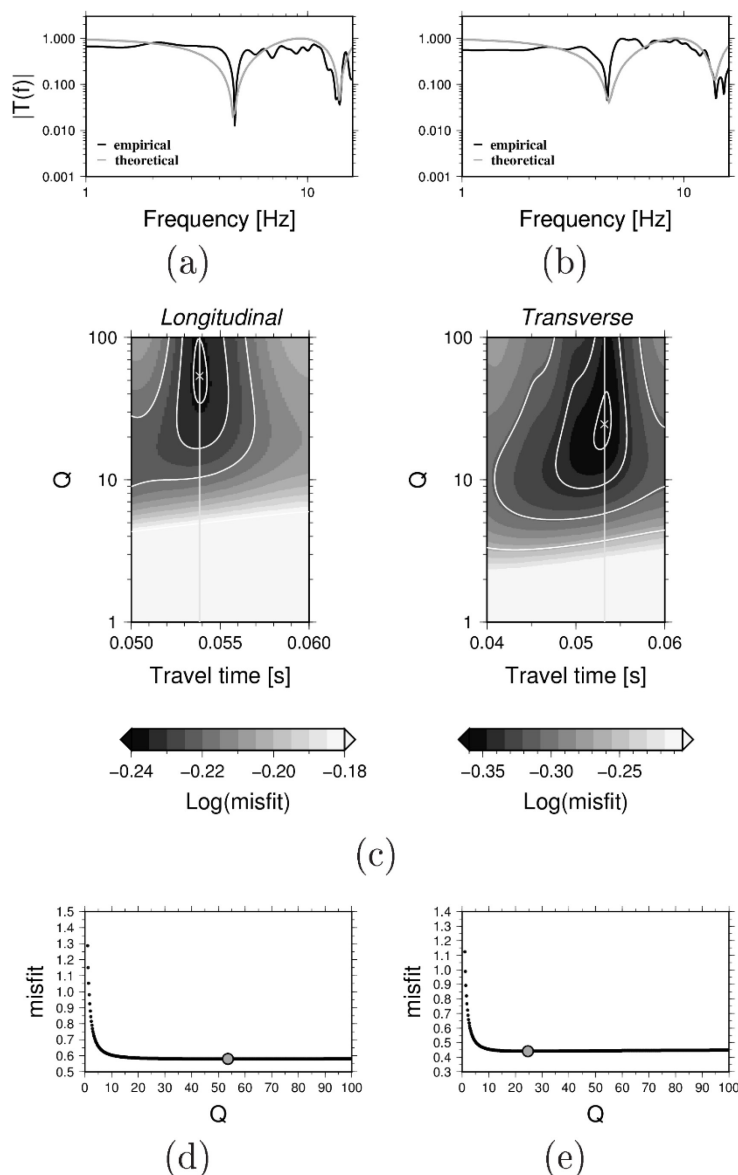


Figure 18. Results for the estimation of the quality factor Q using ambient vibration (left: longitudinal, right: transverse direction). **a**, **b**: Comparison between empirical (black) and the best fitting model transfer function (gray); **c**: grid search results for different travel times – Q values; **d**, **e**: cross section along the Q values for the travel time of the minimum misfit function (white line in **c**), the gray points indicate the minimum Q . Figure from Bindi et al. (2015).

6.2.2 The Tuzla Peninsula

Different methods have been proposed in the past to study the attenuation in near-surface geology when data from vertical arrays, i.e., earthquake recordings from different depths and at surface, are available. Methods based on spectral-ratio analysis (e.g., Gibbs et al. 1994; Safak 1997; Parolai et al. 2007) are widely used to estimate the intrinsic attenuation (i.e., quality factor Q). Moreover, e.g., matching techniques, spectral modeling, synthetic modeling, were used to determine the quality factor. In

addition, mechanical characteristics of subsoils can be investigated by the inversion of borehole weak and strong motion data (e.g., Assimaki et al. 2008, Parolai et al. 2012).

For the GONAF-Tuzla site (Section 5.2, Raub et al. 2016), due to high seismic velocities (P and S-waves velocities of ~ 3600 - 4100 and ~ 1800 m/s, respectively) and heterogeneities (a low-velocity layer between ~ 90 m and ~ 140 m) as shown in Section 6.1.3., leading to strong interference effects between up and downward propagating waves and, hence, complicated spectra, a stable determination of Q based on spectral ratio was not possible. For this reason, forward modeling of the deconvolved wave field in the time domain is performed in order to determine effective Q values and to refine the velocities' estimates. The misfit functions are shown in Figure 19 for all three components at 288 m depth and the vertical component at 215, 144 and 71 m depth. The minima of the misfit function are marked by white dots. For all three components, in the misfit functions, the effective Q values are well constrained, whereas the velocities appear less constrained. Figure 20 presents the comparison of the deconvolved wave fields obtained from real (dotted line) and synthetic data (solid line). The results for the best fitting deconvolved wave field of synthetic data are shown. In the modeling approach, the amplitudes and travel times of the upward propagating pulse and the one reflected at the Earth's surface are fitted without weighting the amplitudes. The grid search procedure to find the best fitting model was performed for homogenous layers above each sensor. Due to the assumptions made in the modeling (homogeneous layer above each sensor considered, impedance contrasts not taken into account), the effective quality factors are biased by the impedance contrasts between the observation points (locations of sensors). More complex techniques are therefore needed in order to better capture the heterogeneities in the subsurface.

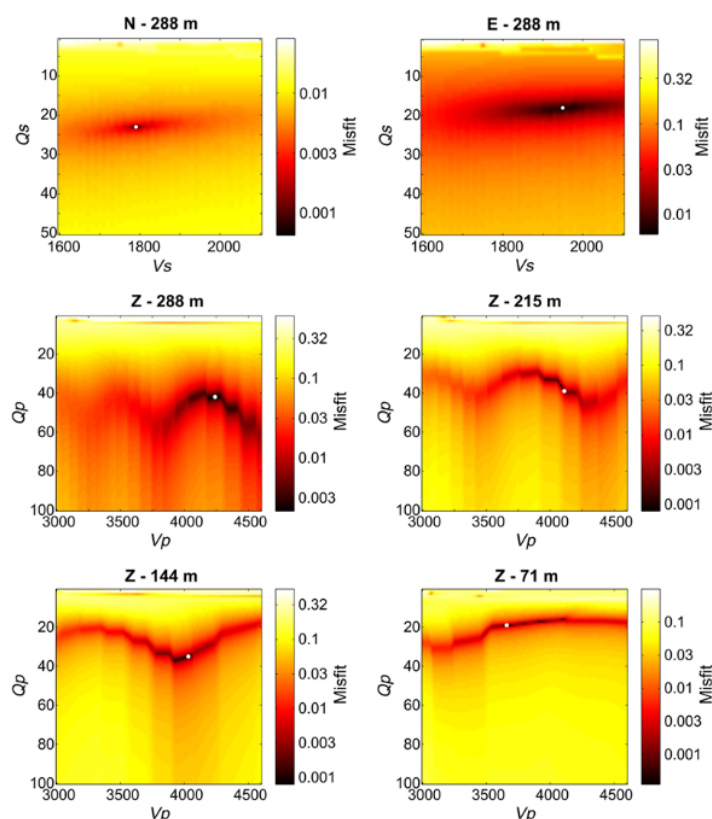


Figure 19. Misfit functions for all depths (vertical component) and at 288 m (horizontal components), used for the estimation of v_p and Q_p , and v_s and Q_s , respectively. The white dots mark the minimum of each misfit function. Figure from Raub et al. (2016).

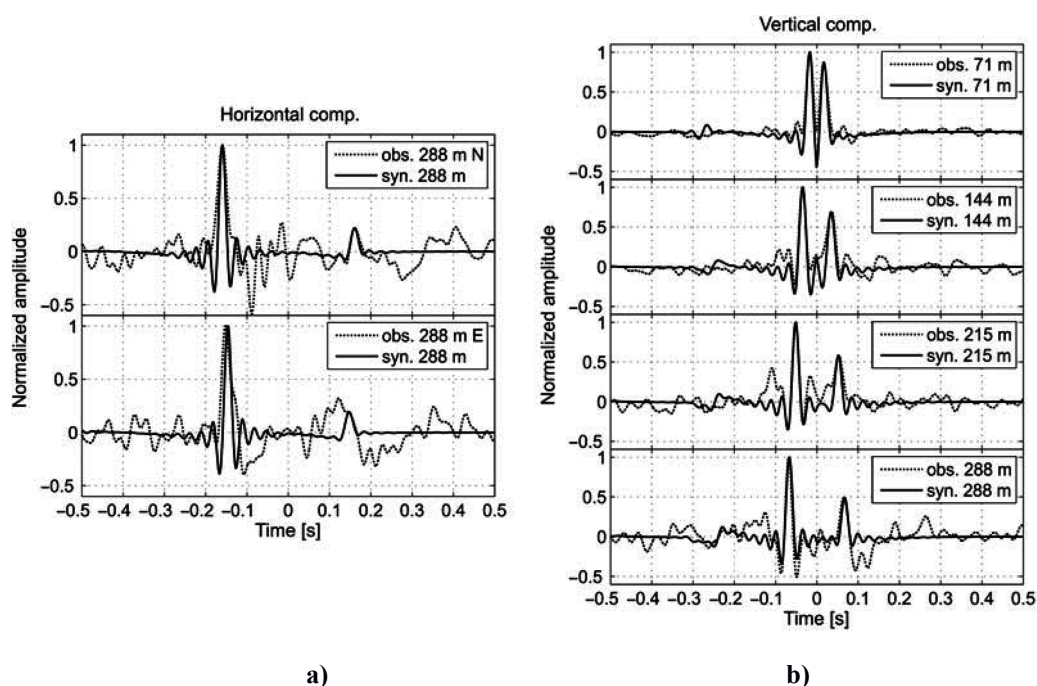


Figure 20. Comparison of the deconvolved wave fields derived from real (dotted line) and best fitting synthetic data (solid line). **a)** Horizontal, **b)** vertical component. Figure from Raub et al. (2016).

Both test studies, using either building or downhole data, presented some difficulties in estimating the quality factor. In order to be able to study a more complex structure consisting of a building and soil layers, more complex techniques will be needed in the future in order to study these attenuation effects. Analyses of the attenuation of building-soil structures are beyond the scope of this thesis, but will be an important issue for the continuation of this work in the future in order to study wave propagation in more detail.

6.3 Joint analysis of building and downhole seismic data - estimation of energy being radiated back from buildings to the soil

6.3.1 Validation of the method by the use of synthetic seismograms

6.3.1.1 Reconstructing the real seismic input

The validation of the methodology presented in section 4.3 (Petrovic and Parolai 2016, Petrovic et al. 2017b) is performed with synthetic data. For the sake of simplicity, a homogenous soil layer representing a general site is considered and the synthetic seismograms are obtained from numerical simulations (Fig. 21a) using the Wang (1999) approach. After carrying out the deconvolution using the recording at 0 m (top) as the reference (Fig. 21b), the real seismic input is reconstructed (Fig. 21c, red lines), by the application of an approach similar to the one proposed in Bindi et al. (2010) (Section 4.2), the constrained deconvolution. For this purpose, the part of the deconvolved wave field that is associated with the upward propagating wave field in the acausal part (Fig. 21d, red line) is convolved with the recording at the top. The reconstructed real seismic input (Fig. 21c, red lines) coincides with the real

seismic input (Fig. 21c, gray lines, first peak), which is known, since, in this case, synthetic data are analyzed. In the simple case of a nearly homogeneous layer, the deconvolved wave field is very simple, dominated by one upward and one downward propagating peak and hence, the input can be reconstructed without any prior knowledge of the velocity structure.

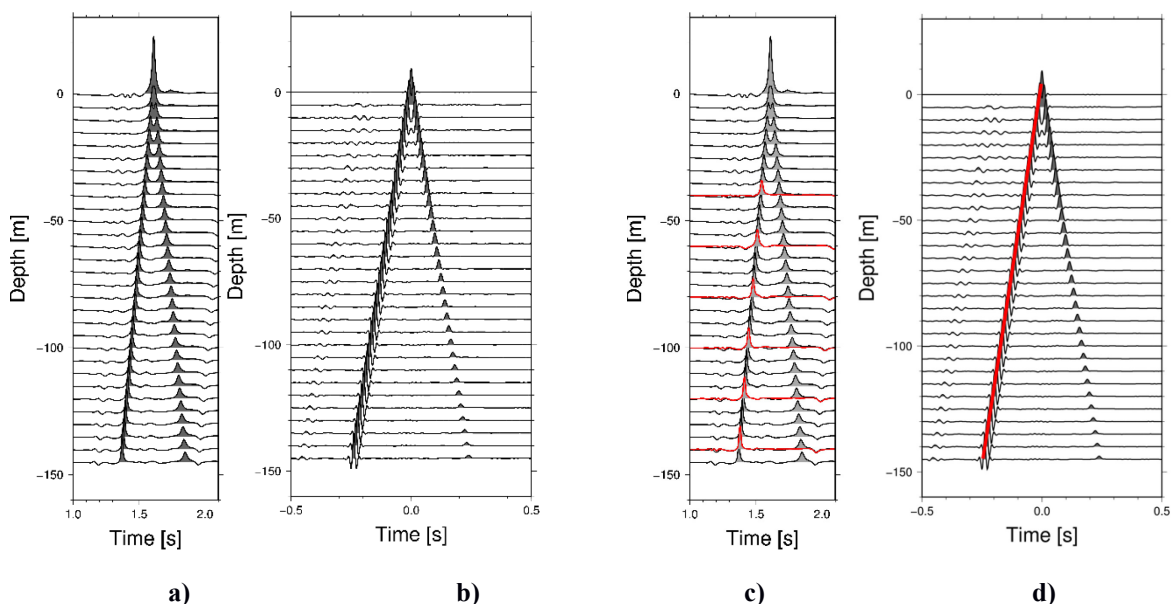


Figure 21. **a)** Synthetic seismograms for a homogenous layer; **b)** deconvolved wave field using the recordings at the top as the reference; **c)** reconstructed real seismic input (red); **d)** part of the deconvolved wave field used to reconstruct the real seismic input (red).

6.3.1.2 Reconstructing the wave field being radiated back from the building to the soil

A numerical simulation of a three-layer media is carried out using the Wang (1999) approach. The synthetic seismograms are shown in Figure 22a for the uppermost two layers. Herein, only the two uppermost layers are considered for simplicity (less different phases involved in the deconvolved wave field). Nevertheless, a three-layer media is used in order to show that deeper layers have no influence on the reconstruction of the phases in the shallower layers. This is due to the fact that when the deconvolution approach is applied, the deconvolved wave field contains information related to the layers between the sensors. No knowledge about the characteristics of the deeper layers is therefore needed. The deconvolved wave fields using the recording at the top of the building as reference are shown in Figure 22b. The deconvolved wave field is dominated by two upward propagating peaks in the acausal and two downward propagating peaks in the causal part. The first peak in the acausal part (first red line) is associated with the upward propagating waves (equation (8), term a), the second one (second red line) has to be taken also into account when back projecting the recording at the top of the building to the downhole in order to remove the effect of multiple reflections in the building (equation (8), term b). The third peak (black line) describes the wave field reflected at the Earth's surface (equation (8), term c) and finally, the fourth peak (green line) is related to the wave field of interest in this study, that is the wave field being radiated back from the building to the soil (equation (8), term d).

However, at the same time, a second phase (same green line) arrives which is associated with the wave field missing in the recording at the top of the building, since a part of the energy has already been reflected at the Earth's surface (equation (8), term e), and hence leading to the lack of energy in the roof recording. In order to correctly reconstruct the part of the wave field being radiated back from the building to the soil, and hence to separate the contribution of these two phases arriving at the same time (equation (8), terms d and e), the relative importance of the following factors, $0.5(1 - r)$ (equation (8), term d) and $\frac{r^2}{2(1+r)}$ (equation (8), term e), has to be taken into account. These two factors, and thus also the relative importance, depend only on the reflection coefficient, and hence, the shear wave velocities and densities of the two layers. By convolving the part of the deconvolved wave field that is of interest (Fig. 22b, green line) with the recording at the roof, and by taking into account the relative importance of the two factors, the wave field being radiated back from the building to the soil is reconstructed correctly (Fig. 22c, green lines), as can be seen from the comparison with the synthetic seismograms (Fig. 22c, gray lines).

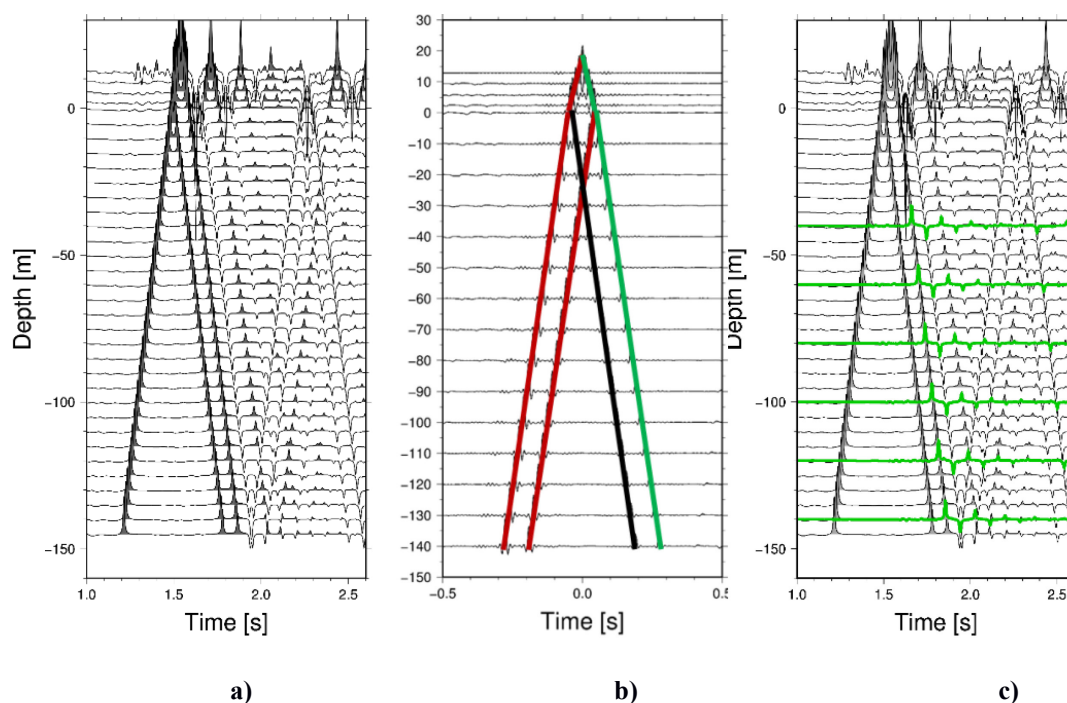


Figure 22. **a)** Synthetic seismograms for a three layer system, the uppermost two layers (representing a building and a soil layer) are shown here; **b)** deconvolved wave field using the recording at the top as reference, red: upward propagating waves, black: waves reflected at Earth's surface, green: wave field being radiated back from the building to the soil; **c)** reconstructed wave field being radiated back from the building to the soil (green).

In Figure 23, the two factors (red: equation (8), term d, blue: equation (8), term e) versus the reflection coefficient r (Fig. 23a) and the impedance contrast c (Fig. 23b) are illustrated. Since the ratio between the densities of the building (average density) and the soil is usually high, and hence also the impedance contrast c , r approaches 1 (Fig. 23a) and subsequently, the second factor (equation (8), term e, blue line) gains in importance.

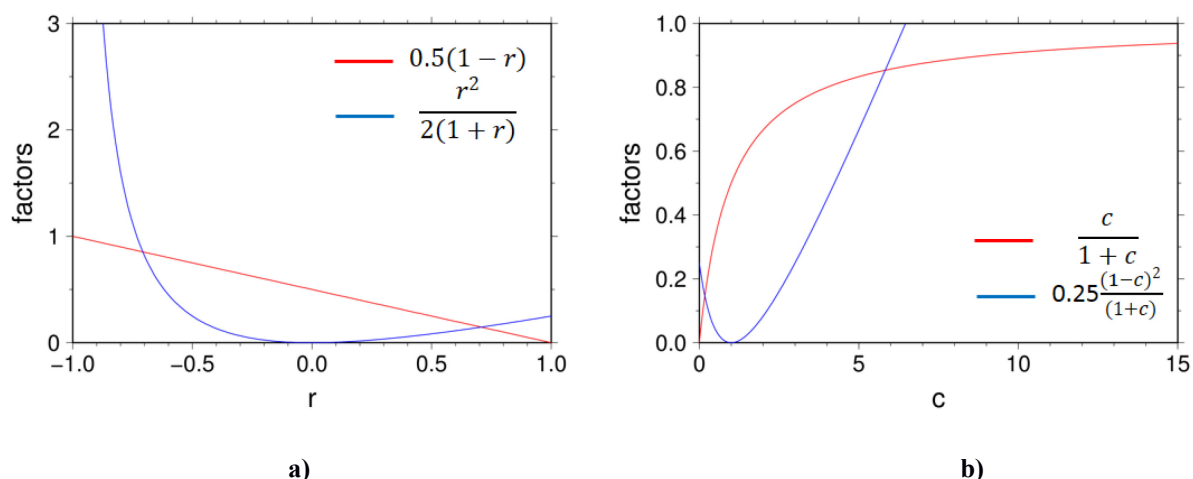


Figure 23. Contributions of the two factors (equation (8), terms d and e) as a function of the reflection coefficient r (a) and the impedance contrast c (b).

6.3.2 Building site interaction assessment: Application to three different test cases

For the three test cases for which data from downhole and building sensors are analyzed jointly (Bishkek, Istanbul and Mexico City, sections 5.3-5.5), the recordings of the downhole sensors are oriented along the two main building axes for each of the analyzed buildings (Fig. 12). If recordings of downhole and building sensors do not have the same sampling rate, as for the test cases in Bishkek (sampling rate of the downhole sensors 500 Hz; sampling rate of the building sensors 100 Hz) and Istanbul (sampling rate of the downhole sensors 200 Hz, sampling rate of the building sensors 100 Hz), the recordings with the lower sampling rate are resampled to the higher sampling rate in order to improve the resolution of the deconvolution results in the time domain (e.g., Céspedes et al. 1995; Tamim and Ghani 2010) and to make it possible to analyze the data jointly. Note that in these analyses, different soil conditions and building construction types are considered (Petrovic et al. 2017b). Hence, due to different impedance contrasts between the building and soil layers, different building-soil couplings are expected.

In Bishkek, the shear wave propagation velocity of the CAIAG building (~ 300 m/s) is lower than the shear wave propagation velocity of the soil (~ 600 m/s). In the Istanbul case, the shear wave propagation velocity in the uppermost soil layer (~ 300 m/s) is similar to the shear wave propagation velocity through the B22 building. In Mexico City, the Jalapa building with a similar/higher (before/after retrofitting) shear wave propagation velocity (70 m/s-140 m/s) is constructed on soft soil with a lower shear wave propagation velocity (~ 60 m/s). The velocity contrasts affect the impedance contrasts c and hence, the reflection coefficients r . Nevertheless, it is important to keep in mind that in the case of a building-soil structure, the impedance contrast will also be defined by the density contrast, since the equivalent densities of buildings (300 kg/m^3 - 500 kg/m^3) are much lower than the density of the soil (1500 kg/m^3 - 2100 kg/m^3). Only poor information on the construction materials of the buildings was available, therefore, the estimated equivalent density value of the building is not very accurate.

An example of the recordings and the corresponding Fourier spectra (blue lines: building sensors, magenta lines: downhole sensors) are shown for one horizontal component (Bishkek: transverse component, Istanbul: x-direction, Mexico City: transverse direction, see Fig. 12) for one event for all sensors of each vertical array in Figure 24 (a: Bishkek, b: Istanbul and c: Mexico City). For all three buildings, the fundamental frequency corresponds to the first bending mode of the shown horizontal component. For all three cases, the variation of the ground motion with the depth/height and the larger level of shaking in the building are observed. The oscillation of the buildings (extension of shaking duration and increasing of amplitude) affects the recordings of the sensors installed at different levels (in particular, on the higher floors) as can be seen especially for the Istanbul and Mexico City vertical arrays. The variation of the frequency content measured by the building and downhole sensors can be seen clearly for the Bishkek and Istanbul vertical arrays, when the Fourier spectra are considered. For the installation in Mexico City, there is only a small variation in the frequency content with depth and the frequency band is much narrower compared to the other two test cases. This is due to the fact that the soft clay acts as a narrow-band-pass filter that amplifies a very narrow frequency band (most of the energy located between 0.2 and 2 Hz). The spectra at the top of the buildings are dominated by a peak (peaks) at the frequencies that correspond to frequencies of the first vibrational mode(s). For the Bishkek vertical array, the spectrum at the roof is dominated by a clear resonant peak at 5 Hz, most likely connected to the first bending mode in the transverse direction (Petrovic and Parolai 2016). For the vertical array in Istanbul, the Fourier spectra of the recordings at the higher floors and the roof are dominated by 3 peaks at frequencies $f_1=1$ Hz, $f_2=3.84$ Hz and $f_3=7.5$ Hz. In the detailed study on the dynamic behavior of the B22 building (Petrovic et al. 2017a), the first three bending modes in the x-direction were identified at these frequencies. In the Fourier spectrum at the roof of the Jalapa building, a peak at around $f=0.4$ Hz can be assumed. This frequency corresponds to the first bending mode in transverse direction before retrofitting of the building (Petrovic et al. 2017b).

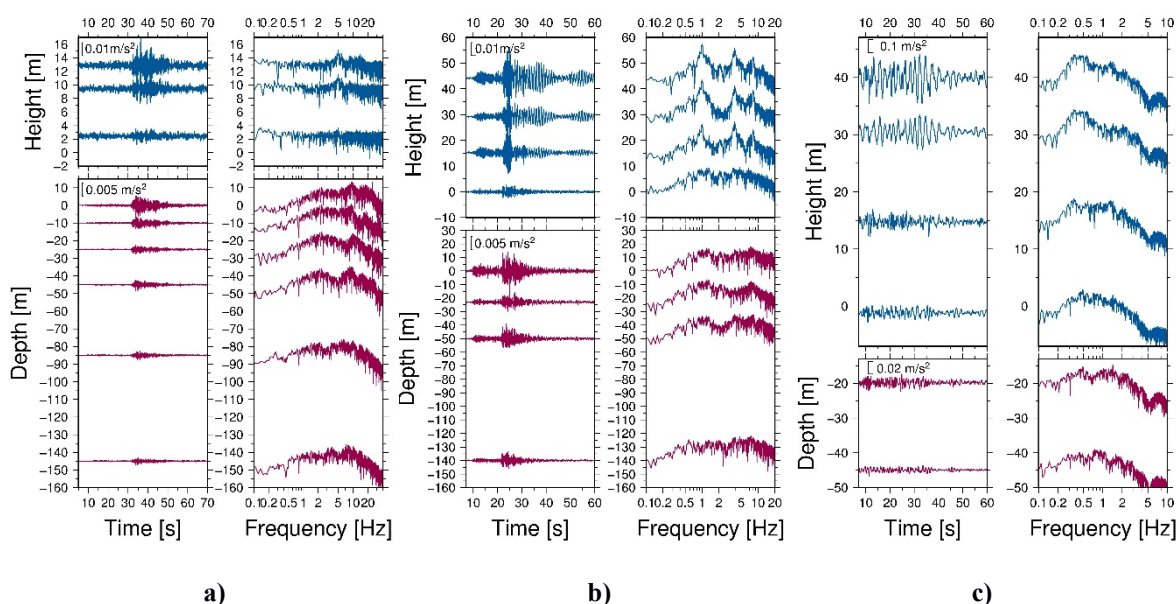


Figure 24. Recordings of one horizontal component for one example event for each building-downhole installation (blue lines: building sensors, magenta lines: downhole sensors) and the corresponding Fourier Spectra. **a)** Bishkek vertical array, transverse direction; **b)** Istanbul vertical array, x-direction; **c)** Mexico City vertical array, transverse direction. Figure from Petrovic et al. (2017b).

The joint deconvolution approach applied to one horizontal direction (Bishkek: transverse component, Istanbul: x-direction, Mexico City: transverse direction, see Fig. 12) of each building and the downhole sensors recordings by using the recordings at the roof as the reference is shown here. The results obtained after stacking the results of all single events (for each test site, 4-6 events are investigated, further information about the analyzed events can be found in Petrovic et al. 2017b) are shown in Figure 25 for Bishkek (a) and Istanbul (b). These two buildings have not suffered damage until now and hence, the dynamic behavior has not changed over time. Furthermore, it must be kept in mind that the buildings' behavior is analyzed under relatively low seismic loading. Therefore, stacking all events is feasible. It is, however, different for the test case in Mexico City, since the Jalapa building suffered some structural and non-structural damages during the analyzed time period and was even retrofitted twice during its lifetime. For this reason, the analyzed events are divided into time periods where the main characteristics of the structure did not change and are stacked for each period (Fig. 25c: 1993 events, 25d: 1997-1998 events, 25e: 1999 event). Only events inducing linear behavior in the structure, i.e., that did not produce any damage, are used for this study. Between the two analyzed time periods, including the events in 1993 and 1997/98, the building was damaged by earthquakes in 1994 and 1995 and retrofitted (e.g., Meli et al. 1998). As a consequence, the dynamic behavior of the building has changed, i.e., the shear wave velocity and hence, the fundamental frequency, has increased. Between the events shown in Fig. 25d and 25e, the building was damaged again by a M_w 6.9 event in 1998 (e.g., Murià-Vila 2001) and the shear wave velocity diminished slightly. For all three test cases, the upward propagating waves (orange lines), waves reflected at the Earth's surface (black lines) and the waves being radiated back from the building to the soil (green lines), which are the ones of interest in this work, were identified.

Numerical simulations are performed for all three test cases in order to better understand the results, and hence, the wave propagation through the building-soil structure obtained from the joint deconvolution approach applied to real data. For this reason, the forward propagation part of the inversion code employed by Parolai et al., (2012, 2013) based on the Wang (1999) approach, is used. As an example, for the test case of Bishkek, the synthetic seismograms showing the propagation of S-waves with nearly vertical incidence between the deepest downhole sensor (at -145 m) and the sensor at the roof of the building (at 13 m) are shown in Figure 26a. The corresponding S-wave velocity profile used for the numerical simulation is shown in Figure 26b. The building's behavior was modeled as a shear beam, and hence added as an additional layer ($v_s=300$ m/s, $\rho=400$ kg/m³) on top of the soil layers. It is necessary to be aware that assuming a building behaves as a pure shear beam is a simplified model. Most buildings behave as a combination of a shear and a bending beam. Nevertheless, this assumption is adequate for the aim of our studies, which is not to find the best model of the analyzed buildings. In this way, the main features observed in the real data results are analyzed and interpreted by looking at the main features observed in the simplified model.

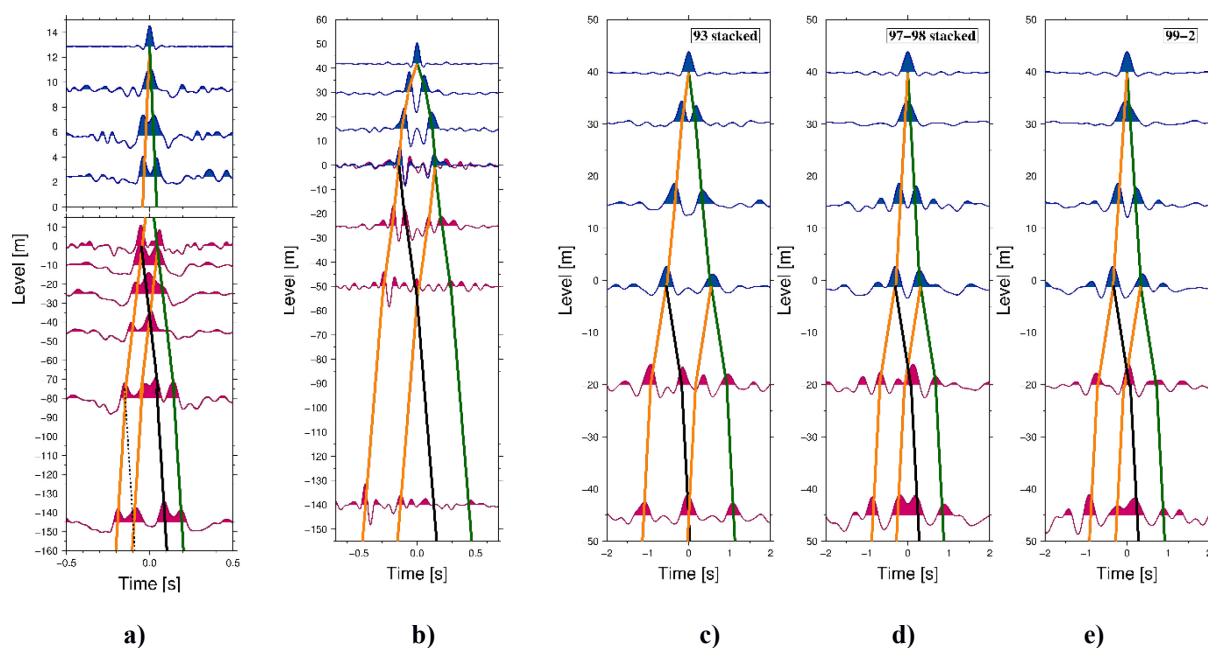


Figure 25. Deconvolved wave fields (blue lines: building sensor, magenta lines: downhole sensors) obtained after stacking the results of all analyzed events (or events of different time periods for the Mexico City vertical array) for one horizontal component using the recordings at the top of the building as the reference. Orange, black and green lines correspond to upward propagating waves, downward propagating waves reflected at the Earth's surface and the wave field radiated back from the building to the soil, respectively. **a)** Bishkek vertical array, stacking of results of all events; **b)** Istanbul vertical array, stacking of results of all events; **c)** Mexico City vertical array, events of 1993; **d)** Mexico City vertical array, events of 1997-1998 after the building was damaged (by the 1994 and 1995 events) and retrofitting, **e)** Mexico City vertical array, events of 1999 after the building suffered damage by a previous 1999 event. Please note the different vertical and horizontal scales. Figure from Petrovic et al. (2017b).

For all three test cases, the joint deconvolution was first applied to the real data, and then to the synthetic seismograms obtained by the numerical simulations, using the recordings at the top as the reference. The comparison of the deconvolved wave fields obtained for the real data (blue lines: building, magenta lines: downhole) and the synthetics (gray lines) is shown in Figure 27 for all three test cases (a: Bishkek, b: Istanbul, c: Mexico City, 1993 events after stacking, d: Mexico City: 1997-1998 events after stacking and e: Mexico City: MC-1999-2 event). For the test cases in Istanbul and Mexico City, two different numerical simulations are used, namely one including a building layer and one without a building layer (the results of both models are plotted together in Fig. 27b-27e). This is because of the fact that considering only the model that includes a building layer (like for the installation in Bishkek) leads to a large discrepancy between the synthetic and real data results since the wave field being radiated back from the Earth's surface to the soil (black line) in the real data results could not be identified in the results of the synthetic seismograms. This discrepancy is possibly due to two factors. The first is that the building is not, as assumed for the model, a continuous layer. Furthermore, the building is also often not located exactly above the downhole installation but several tens of meters away (as, e.g., for the test case in Istanbul), i.e., in reality, there is no building layer directly above the downhole installation. However the sensors in the borehole are anyway recording the wave field released back to the ground by the nearby built structure. Furthermore since the reflection is not taking place at a single point, but over a finite area (the Fresnel Zone, which describes the horizontal dimension of the seismic resolution)

whose dimension depends on the frequency (e.g., Lay and Wallace 1995), the wave field reflected at the free surface will also be recorded by the downhole sensors if located inside the Fresnel zone.

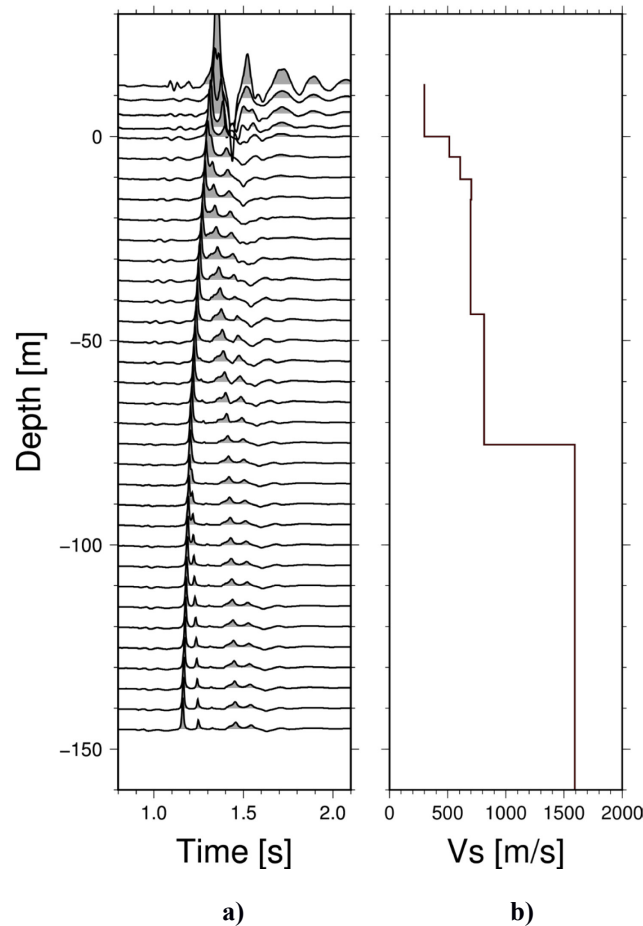


Figure 26. a) Synthetic seismograms showing the propagation of S-waves with nearly vertical incidence between the deepest borehole sensor and the sensor at the top of the building. **b)** v_s structure used for the simulation (velocity model v_s for the soil from Parolai et al., 2013, v_s for the building layer estimated by the use of the interferometric approach). Figure from Petrovic and Parolai (2016).

Nevertheless, when using a combination of the two models for the test cases in Istanbul and Mexico City, the results obtained for the real and synthetic data for all three test cases (Fig. 27) show a good correlation and it is possible to assign univocally all different phases (marked by orange, black and green lines as in Fig. 25) contained in the complex deconvolved wave fields. For the test case in Bishkek (Fig. 27a), a better separation of the individual peaks is observed for the deconvolved wave fields of the synthetic seismograms compared to the real data results. This is because for the synthetic data, a broader frequency band could be used in order to obtain better defined peaks in the time domain and hence, simplify the identification of the peaks in the real data results. For the estimation of the deconvolved wave field of the real data due to the signal to noise ratio and the spectral energy content of the analyzed events, only a narrower frequency band was used. Thus, this results in broader peaks of the deconvolved wave field in the time domain.

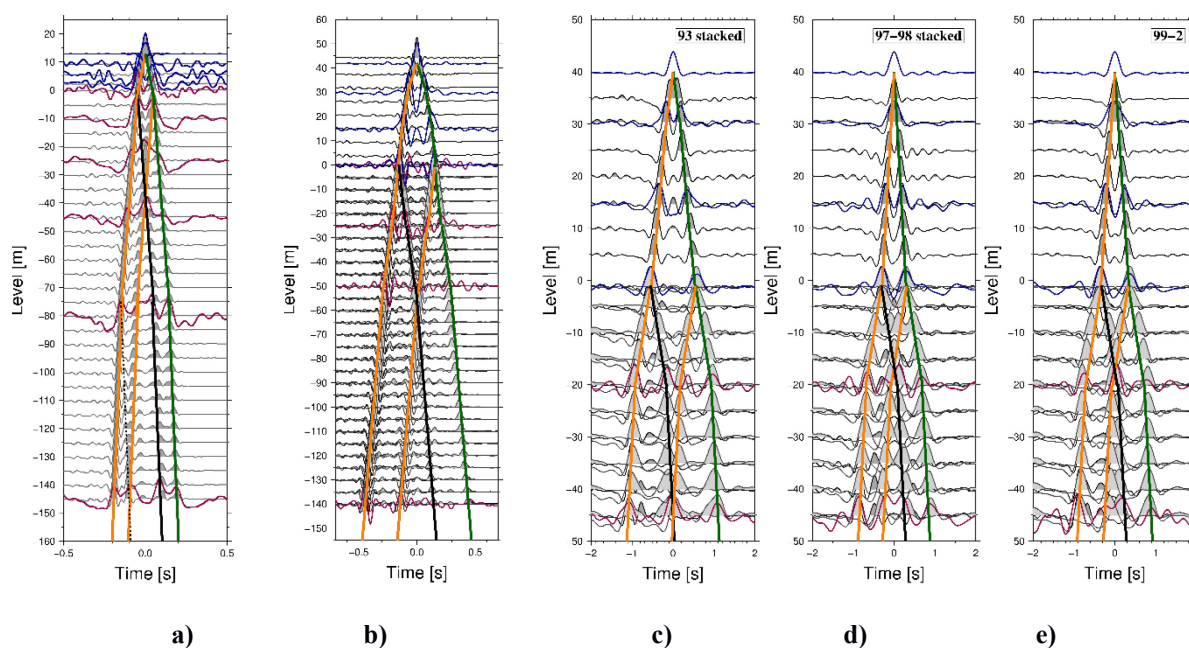


Figure 27. Comparison of deconvolved wave fields (blue lines: building sensor, magenta lines: downhole sensors) of real data obtained after stacking (as shown in Fig. 25) and synthetic data (gray lines) obtained from numerical simulations. Orange, black and green lines correspond to upward propagating waves, downward propagating waves reflected at the Earth's surface and the wave field radiated back from the building to the soil, respectively. **a)** Bishkek vertical array, stacking of results of all events; **b)** Istanbul vertical array, stacking of results of all events; **c)** Mexico City vertical array, events of 1993; **d)** Mexico City vertical array, events of 1997-1998 after the building was damaged (by 94 and 95 events) and retrofitting; **e)** Mexico City vertical array, events of 1999 after the building suffered damage by a previous 1999 event. Please note different vertical and horizontal scales. Figure from Petrovic et al. (2017b).

For the Istanbul vertical array (Fig. 27b), the deconvolved wave fields of real data are also dominated by peaks with inverted polarity, propagating from the building down to the soil with the same propagation velocity. These peaks are not observed in the deconvolved wave fields of the numerical simulations. As discussed in Section 6.1.2, these peaks are due to the second bending mode, which is not seen in the simple model of a single building layer. Since the recording at the top of the building is used as the reference, this characteristic is projected also to the downhole sensors (Petrovic et al. 2017a). For Mexico City, the agreement between synthetic and real data is very good, showing that the simplified model of building layers is sufficient in this case.

After the identification of the different phases of the deconvolved wave field, the real seismic input and the wave field being radiated back from the building to the soil are estimated by the constrained deconvolution. However, it must be kept in mind that several phases may arrive at the same time as the wave field of interest, the wave field being radiated back from the building to the soil and hence, the relative importance of the factors (see Section 6.3.1) has to be taken into account.

Exemplarily, for the Bishkek case, the real seismic input and the wave field being radiated back from the building to soil are shown for one event recorded by the Bishkek vertical array (Fig. 28). The ground motion recorded at the Earth's surface (top) and at the downhole sensor at 145 m depth (middle) are shown in Fig. 28a. Fig 28a (bottom) represents the reconstructed real seismic input at -145 m. The corresponding Fourier spectra are shown in Figure 28b. The ground motion recorded at the roof's sensor (top) and the reconstructed wave field being radiated back from the building to the soil at 10 m (middle)

and 145 m depth (bottom) are shown in Figure 28c and the corresponding spectra in 28d. A large spectral peak at the fundamental frequency of the building (~ 5 Hz) is observed in the reconstructed downward propagating wave field at both depths. The amplitude of this peak is clearly diminishing with increasing depth, and is less than that observed at the top of the building.

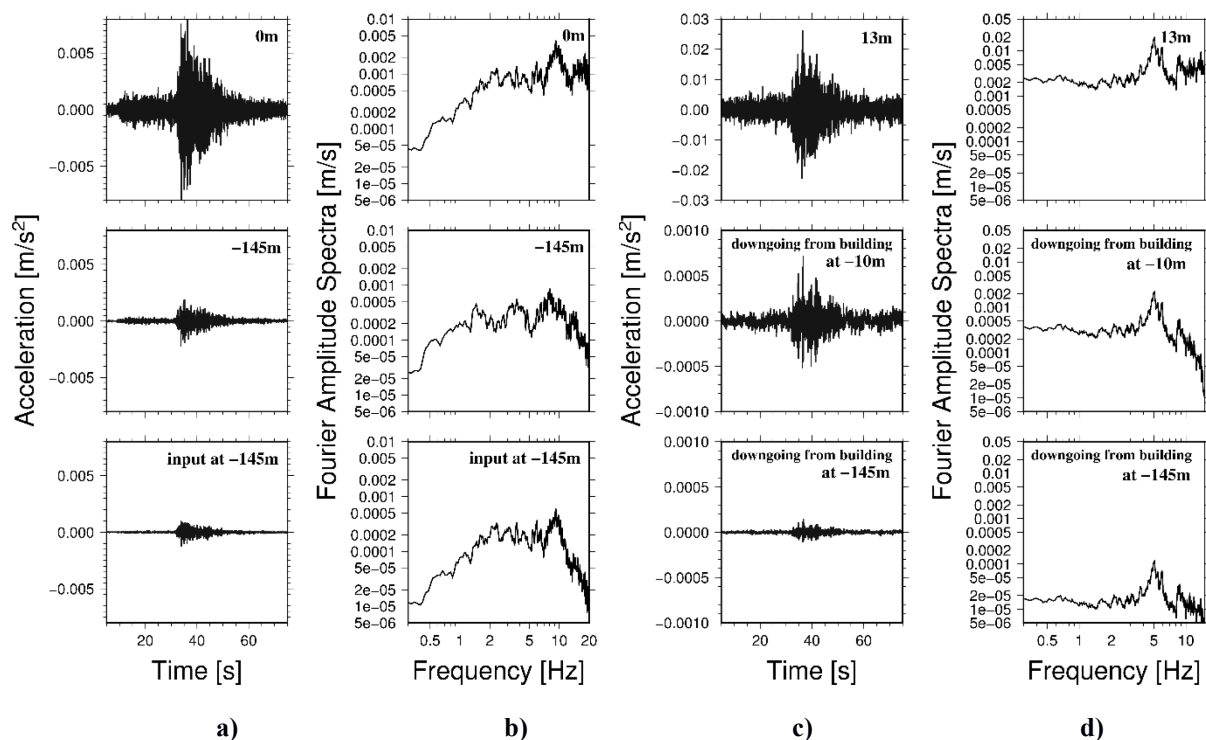


Figure 28. **a)** Ground motion recorded at the free surface (top), at 145 m depth (middle) and the reconstructed input motion at 145 m depth (bottom) for an exemplary event recorded by the Bishkek vertical array. **b)** Corresponding Fourier spectra of ground motion recorded at the surface (top), 145 m depth (middle) and of retrieved input motion (bottom). **c)** Ground motion recorded at the roof of the building (top), and the retrieved wave field radiated back from the building at 10 m depth (middle) and at 145 m depth (bottom) for the same event. **d)** Corresponding Fourier spectra of ground motion recorded at the roof (top), and of the retrieved wave field radiated back from the building at 10 m depth (middle) and 145 m depth (bottom). Figure from Petrovic and Parolai (2016).

In Figure 29a, the recorded ground motion at 50 m depth (gray) is compared with the reconstructed real seismic input at the same depth (blue) for four different earthquakes for the Istanbul test site. The comparison between the recorded ground motion (gray) at 50 m depth and the reconstructed wave field radiated back from the building to the soil (green) at the same depth is shown in Figure 29b. The Fourier amplitude spectra of the recorded ground motion at 50 m depth (gray), the reconstructed real seismic input (blue) and the reconstructed wave field radiated back from the building to the soil (green) are shown in Figure 29c for the four considered earthquakes. Interestingly, for all four earthquakes the spectra of the down-going waves (green) are dominated by three peaks at frequencies corresponding to the first three bending modes in the considered direction. The spectra of the original recordings (gray) show also peaks at these three frequencies, whereas, as expected, the spectra of the reconstructed real seismic input (i.e., the part of the wave field after removing all down-going waves) have no peaks at these frequencies.

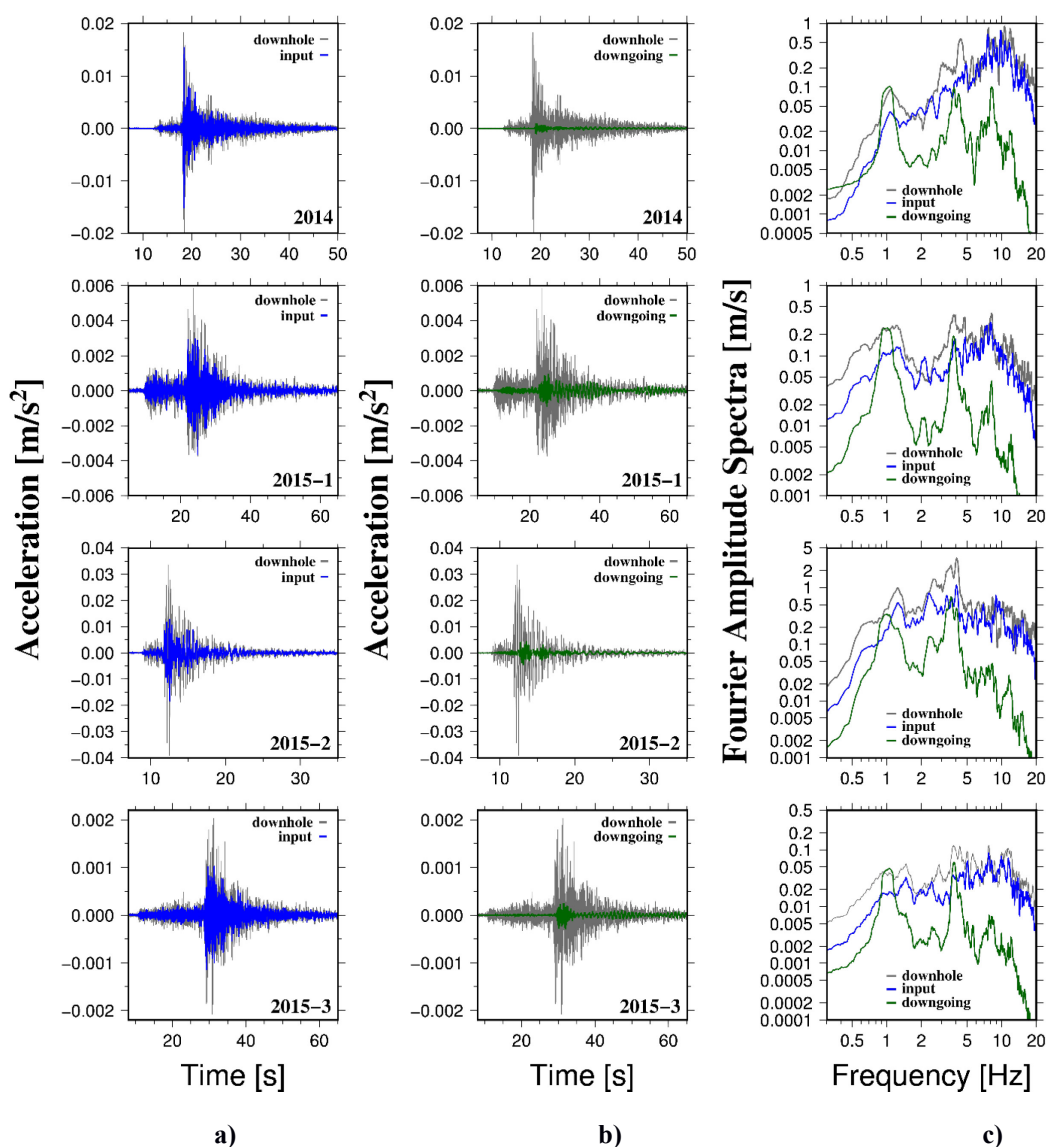


Figure 29. Istanbul vertical array. **a)** Comparison of recorded ground motion at 50 m depth (gray) and the reconstructed real seismic input (blue) at the same depth for four different earthquakes. **b)** Comparison of recorded ground motion at 50 m depth (gray) and the reconstructed down-going wave radiated back from the building to the soil (green) at the same depth. **c)** Fourier amplitude spectra of original recording (gray), the reconstructed real seismic input (blue) and the reconstructed wave field radiated from the building to the soil (green).

The spectra of the reconstructed real seismic input (blue lines, Fig. 30a: Bishkek, 145 m depth, Fig 30b: Istanbul, 50 m depth, Fig 30c,d,e: Mexico City, 45 m depth) and of the wave field being radiated back from the building to the soil at two different depths (red and green lines) are presented exemplarily for Bishkek and Istanbul, in each case for one earthquake and for one earthquake in each of the three considered time periods for Mexico City in Figure 30 (Petrovic et al. 2017b). For the test sites in Bishkek and Istanbul, the spectra of the downward propagating waves are dominated by peaks at the frequencies of the first (Bishkek) or the first three (Istanbul) bending modes. For Mexico City, the spectra of the reconstructed down-going wave show two peaks at frequencies of the first two bending modes in this direction for the shown earthquake before the retrofitting (Fig. 30c), whereas for the two

events after the retrofitting (Fig. 30d, e) show additionally also a peak at the frequency corresponding to the first torsional mode.

Finally, after the integration of the velocity spectra (of the reconstructed real seismic input and the wave field being radiated back from the building to the soil), the spectral energy is obtained. For all three test cases, it is found that the amount of energy being radiated back from the building to the soil is not negligible. For the Bishkek vertical array, the energy that is radiated back by the building to the soil corresponds on average to 10-15% (at -145 m) and 40%-50% (at -10 m) of the energy of the real seismic input at 145 m depth when estimated using the available event's recordings. For the Istanbul test case, the energy associated with the downward propagating wave field is estimated to be around 10-15% (both at 25 m and 50 m depth) of the energy of the reconstructed real seismic input at 50 m depth for both levels. In the case of the Mexico City test site, the energy belonging to the wave field radiated back from the building to the soil is estimated as 70-90% (at 20 m) and 25-65% (at 45 m) of the reconstructed real seismic input at 45 m depth. The variability of the estimated energy being radiated back from the building to the soil for the Mexico City test site might be due to two facts. On the one hand, different inputs might stimulate the structure in different ways. On the other hand, it has to be taken into account that the building has been both damaged and retrofitted between the considered events and thus, the dynamic properties have changed. Radiating back a different amount of energy to the soil for different events might be due to this fact, corresponding to considering different buildings.

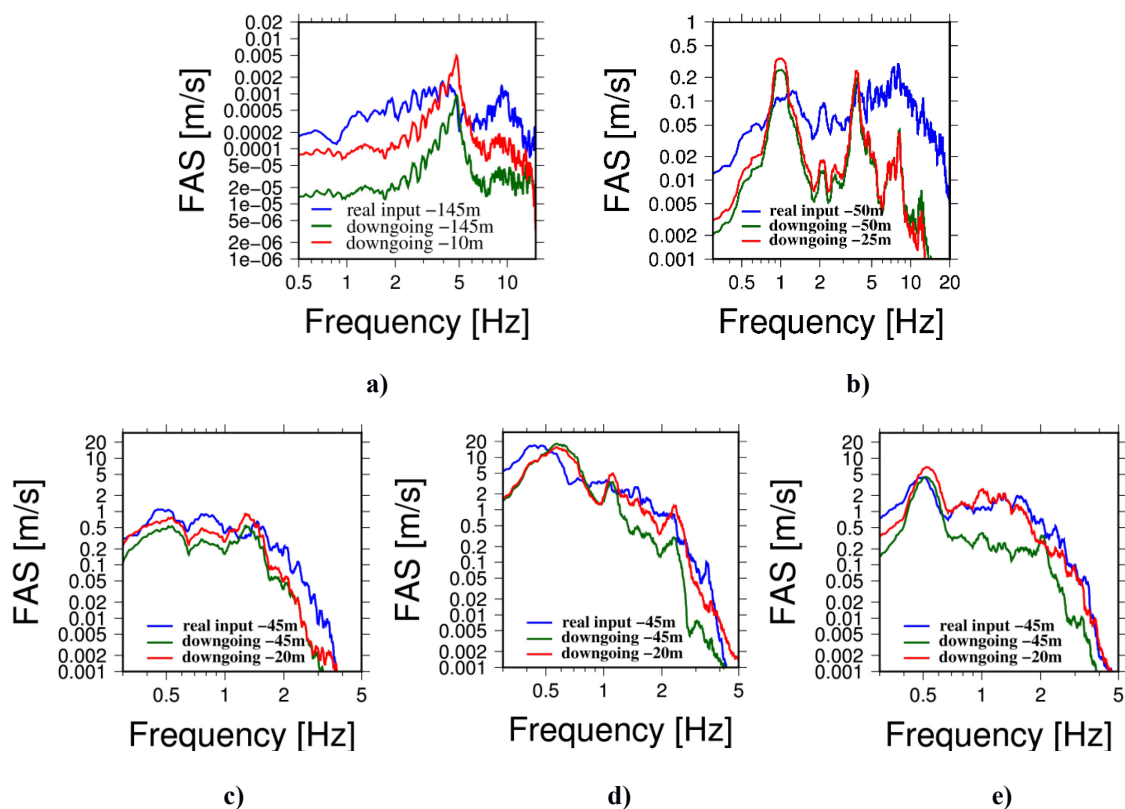


Figure 30. a) Bishkek: Input spectrum at -145 m (blue), spectrum of down-going waves radiated back from the building reconstructed at -145 m (green) and at -10 m (red) for Bi-2015-2. b) Istanbul: Input spectrum at -50 m (blue), spectrum of down-going waves radiated back from the building at -50 m (green) and at -25 m (red) for IS-2015-1. c) - e) Mexico City: Input spectrum at -45 m (blue), spectrum of down-going waves radiated back from the building at -45 m (green) and at -20 m (red) for MC-1993-2 (c), MC-1997-1 (d) and MC-1999-2 (e). Figure from Petrovic et al. (2017b).

7 Conclusions and outlook

In this thesis, the deconvolution approach was first carried out for investigating both the dynamic characteristics of buildings (applied to ambient vibrations, generated sources and earthquake recordings from sensors installed in buildings) and the velocity and attenuation profiles in shallow geological layers (applied to earthquake events recorded by downhole installations) separately. It is essential to understand first the behavior of the building and soil separately, in order to simplify the comprehension of the results obtained by the joint analysis. Information on some phases of the deconvolved wave fields, either related to the building or to the soil, facilitate later the interpretation of the deconvolved wave field of the soil-structure system. This deconvolved wave field is more complex due to the joint analysis of building and downhole sensors and thus, due to phases resulting from the soil-structure interaction. Nevertheless, if data from buildings or soil is analyzed separately, it is not possible to obtain information about the wave propagation through the building-soil-structure and to estimate the energy being radiated back from a building to the soil.

For this reason, a new approach, namely the joint deconvolution, for the analysis of wave propagation through the building-soil structure and the estimation of the energy being radiated back from the building to the soil, was developed within the framework of this thesis. After the validation with synthetic data, it was applied to three different test cases representing different soil structure couplings. It was shown that after the univocal identification of the different phases contributing to the deconvolved wave field, even in a medium that is not almost homogeneous, the estimation of ground motion associated with the real seismic input (after downward propagating waves have been removed) and of the wave field being radiated back from the building to the soil, are feasible. The different phases of the wave field can also be reconstructed correctly for complicated underground velocity structures by the application of the constrained deconvolution. No knowledge about the Q factor (intrinsic attenuation) that might be difficult to estimate is required, only information about the velocity (obtained from the deconvolution approach) and density (usually known for the soil, and equivalent density of buildings can be estimated with the information generally at hand) are needed.

For all three different test cases (different building types, velocity profiles of the soil, distances between borehole and building installations) the energy being radiated back from the building to the soil was estimated by the proposed methodology. The amount of energy being radiated back was found to be not negligible in all three test cases (e.g., for the Bishkek case, at 145 m depth, 10-15% of the estimated real input energy is expected to be from the building, for Istanbul at 50 m depth, this value is also 10-15%, while for Mexico City at 45 m depth, it is 25-65% of the estimated real input energy), and the observed wave field radiated back correlates inversely with the impedance contrast between the building and soil. This suggests that interactions between the wave fields generated by nearby buildings are also possible, and thus, should be also taken into account in design codes. The application of the methodology to higher levels of shaking is also needed to further verify the approach.

In this thesis, for all three buildings, the horizontal component corresponding to the first bending mode (of the fundamental frequency) was shown. The bending modes of the three analyzed buildings are mainly in one of the horizontal directions (parallel to the main building axes). Since buildings usually do not behave as ideal beams and thus, also combined modes are possible, taking the maximum component into account in place of the component along the main building axes separately, will be

considered in the future for buildings with more complicated building's dynamic behavior (e.g., combined bending modes).

Further studies that investigate the attenuation of waves propagating through the building-soil structure will be important in order to obtain a better, more detailed understanding of the wave propagation.

In addition to 2D and 3D numerical simulations of soil-structure and site-city interaction effects, which have found a wide application for studying these effects, but are always a simplified representation of the ongoing processes, the proposed methodology is promising for the study of these effects by the analysis of real data composed of building and downhole recordings. The application of the proposed method is the first step in order to investigate soil-structure interactions by analyzing the wave propagation through a building-soil structure and the energy being radiated back from the building to the soil. This work is in fact one of the first studies based on real data sets that has shown the influence of objects (in this case three different single buildings) located at the Earth's surface on modifying the ground motion during an earthquake shaking.

Nevertheless, in order to understand more complicated cases, including building-building interactions up to site-city effects from real data sets, more extensive 3D vertical array installations are needed. Such 3D vertical arrays should consist of several instrumented buildings and downhole installations.

Extending the studies to city-soil interaction effects might give us, in the long term, both new visions about how the construction of buildings and urban settlements can be improved, as well as information on the already existing (positive or negative) interference effects of the buildings' configurations in already existing urban areas. On the one hand, once the interactions of buildings and the soil and interactions between several buildings through the soil are understood, the design of individual buildings, as well as of urban areas in general, when planning future cities located in regions prone to high seismic hazard, might be improved by taking these interactions into account. On the other hand, the knowledge obtained about interactions taking place between cities and the soil will also be very useful to better understand and identify regions of higher seismic risk within existing urban areas and thus, the seismic risk assessment. This information will be of great value for the civil protection, making it possible to identify the parts of the city exposed to a higher risk, and therefore, to adapt and improve the emergency plans, the response and recovery actions.

8 References

- Assimaki, D., W. Li, J. H. Steidl and K. Tsuda (2008). Site amplification and attenuation via downhole array seismogram inversion: a comparative study of the 2003 Miyagi–Oki aftershock sequence, *Bull. Seismol. Soc. Am.*, 98, 301-330.
- Bard, P. Y., P. Gueguen and A. Wirgin (1996). A note on the seismic wave field radiated from large building structures into soft soils, Proceedings of *Eleventh World Conference on Earthquake Engineering*, Acapulco, Mexico, June 23-28, 1996, Elsevier Science Ltd. 1996, paper no. 1838.
- Bertero, M. and P. Boccacci (1998). Introduction to inverse problems in imaging. Bristol: IOP Publishing.
- Bertero, M., D. Bindi, P. Boccacci, M. Cattaneo, C. Eva, and V. Lanza (1997). Application of the projected Landweber method to the estimation of the source time function in seismology, *Inverse Probl.* 13, 465–486.
- Bindi, D., S. Parolai, M. Picozzi and A. Ansal (2010). Seismic input motion determined from a surface-downhole pair of sensors: a constrained deconvolution approach. *Bull. Seismol. Soc. Am.*, 100, no. 3, 1375-1380.
- Bindi, D., B. Petrovic, S. Karapetrou, M. Manakou, T. Boxberger, D. Raptakis, K. D. Pitilakis, and S. Parolai (2015). Seismic response of an 8-story RC-building from ambient vibration analysis, *Bull. Earthq. Eng.*, 13, 2095-2120.
- Boutin, C. and Roussillon, P. (2004). Assessment of the urbanization effect on seismic response, *Bull. Seismol. Soc. Am.*, 94, no.1, 251-268.
- Brincker, R., L. Zhang and P. Andersen (2001). Modal identification from Ambient Responses using Frequency Domain Decomposition, *Smart Mater. Struct.*, 10, 441-445.
- Céspedes, I., Y. Huang, J. Ophir, S. Spratt (1995). Methods for estimation of subsample time delays of digitized echo signals, *Ultrasonic Imaging*, 17, 142-171.
- Chavez-Garcia, F. J. and M. Cardenas-Soto (2002). The contribution of the built environment to the free-field ground motion in Mexico City, *Soil Dyn. Earthq. Eng.*, 22, 773-780.
- Chazelas, J. L., O. Abraham and J. F. Semblat (2001). Identification of different seismic waves generated by foundation vibration: centrifuge experiments, time-frequency analysis and numerical investigations, Proceedings of *4th International Conference on Recent Advances in Geotechnical Earthquake Engineering And Soil Dynamics*, San Diego, California, USA, March 26- 31, 2001.
- Chopra, A. K. (1996). Modal analysis of linear dynamic systems: physical interpretation. *J. Struct. Eng.*, 122, 517-527.
- Del Pezzo, E., F. Bianco, S. Marzorati, P. Augliera, E. D’Alema and M. Massa (2011). Depth-dependent intrinsic and scattering attenuation in north central Italy, *Geophys. J. Int.*, 186, 373-381.

-
- Ditommaso, R., M. Mucciarelli, M. R. Gallipoli and F. C. Ponso (2010a). Effect of a single vibrating building on free-field ground motion: numerical and experimental evidences, *Bull. Earthq. Eng.*, 8, 693-703.
- Ditommaso, R., S. Parolai, M. Mucciarelli, S. Eggert, M. Sobiesiak, J., Zschau (2010b). Monitoring the response and the back-radiated energy of a building subjected to ambient vibration and impulsive action: the Falkenhof Tower (Potsdam, Germany), *Bulletin of Earthquake Engineering*, 8, 3, 705-722.
- Erlingsson, S. and A. Bodare (1996). Live load induced vibrations in Ullevi stadium – dynamic soil analysis, *Soil Dyn. Earthq. Eng.*, 15, 171-188.
- Faccioli, E., R. Paolucci, M. Vanini (1996). Studies of site response and soil-structure interaction effects in a tall building in Mexico City. Proceedings of *Eleventh World Conference on Earthquake Engineering*, Acapulco, Mexico, June 23-28, 1996, Elsevier Science Ltd. 1996 paper no. 569.
- Fleming, K., M. Picozzi, C. Milkereit, F. Kühnlenz, B. Lichtblau, J. Fischer, C. Zulfikar, O. Özel., SAFER and EDIM working groups (2009). The Self-organizing Seismic Early Warning Information Network (SOSEWIN), *Seismological Research Letters*, 80, no. 5, 755-771.
- Gibbs, J. F., D. M. Boore, W. B. Joyner and T. E. Fumal (1994). The attenuation of seismic shear waves in quaternary alluvium in Santa Clara Valley, California, *Bull. Seism. Soc. Am.*, 84, 76-90.
- Guéguen, P., P. Y. Bard, and F. J. Chávez-García (2002). Site-City seismic interaction in Mexico City-like environments: An analytical study, *Bull. Seismol. Soc. Am.*, 92, no. 2, 794–811.
- Guéguen, P., P. Y., Bard P.Y and C.S. Oliveira (2000). Experimental and numerical analysis of soil motions caused by free vibrations of a building model, *Bull. Seismol. Soc. Am.*, 90, no.6, 1464-1479.
- Ivanovic, S. S., M. D. Trifunac, M. I. Todorovska (2000). Ambient vibration tests of structures – a review, *ISET Journal of Earthquake Technology*, 37, no. 4, 165-197.
- Jennings, P.C. (1970). Distant motions from a building vibration test, *Bull. Seismol. Soc. Am.*, 60, 2037-2043.
- Kanai, K. (1965). Some new problems of seismic vibrations of a structure. In: Proceedings of the 3rd world conference on earthquake engineering, Auckland and Wellington, New Zealand
- Kanamori, H., J. Mori, D. L. Anderson, T. H. Heaton (1991). Seismic excitation by the space shuttle Columbia, *Nature*, 349, 781-782.
- Kham, M., J.-F. Semblat, P.-Y. Bard and P. Dangla (2006). Seismic site-city interaction: main governing phenomena through simplified numerical models, *Bull. Seism. Soc. Am.*, 96, no.5, 1934-1951.
- Kitada, Y., M. Kinoshita, M. Iguchi and N. Fukuwa (1999). Soil-structure interaction effect on an Npp reactor building. Activities of Nupec: Achievements and the current status, M. Celebi and I. Okawa (Editors), *Proc. UJNR workshop on soil-structure interaction*, Menlo Park, California, 22-23 September, paper no. 18.
- Kohler, M. D., T. H. Heaton and S. C. Bradford (2007). Propagating waves in the steel, moment-frame factor building recorded during earthquakes, *Bull. Seismol. Soc. Am.*, 97, 1334-1345.
- Lay, T. and T.C. Wallace (1995). Modern global seismology, *Academic press*, 1995.

-
- Mehta, K., R. Snieder, and V. Grazier (2007a). Extraction of near-surface properties for a lossy layered medium using the propagator matrix, *Geophys. J. Int.*, 169, 2171-280.
- Mehta, K., R. Snieder and V. Grazier (2007b). Downhole receiver function: a case study, *Bull. Seism. Soc. Am.*, 97, 1396-1403.
- Meli R., Faccioli E., Murià-Vila D., Quaas R. and R. Paolucci (1998). A Study of site effects and seismic response of an instrumented building in Mexico City, *Journal of Earthquake Engineering*, 2, 89-111.
- Michel, C., P. Gueguen, P.-Y. Bard (2008). Dynamic parameters of structures extracted from ambient vibration measurements: An aid for the seismic vulnerability assessment of existing buildings in moderate seismic hazard regions, *Soil Dynamics and Earthquake Engineering*, 28, no. 8, 593-604.
- Mucciarelli, M., M. R. Gallipoli, F. C. Ponzio and M. Dolce (2003). Seismic waves generated by oscillating building, *Soil. Dyn.. Earthq. Eng.*, 23, 255-262.
- Murià-Vila, D.M., G. Rodriguez, A. Zapata, A. M. Toro (2001). Seismic response of a twice-retrofitted building, *ISET Journal of Earthquake Technology*, 38, 67-92.
- Murià-Vila, D.M., R. Taborda, A. Zapata-Escobar (2004). Soil-structure interaction effects in two instrumented tall buildings, *Proceedings of 13th World Conference on Earthquake Engineering*, Vancouver, B.C., Canada, August 1-6, 2004, paper no. 1911.
- Nakata, N., R. Snieder, S. Kuroda, S. Ito, T. Aizawa, and T. Kunimi (2013). Monitoring a building using deconvolution interferometry. I: Earth-quake-data analysis, *Bull. Seismol. Soc. Am.*, 103, no. 3, 1662-1678.
- Newton C, Snieder R (2012) Estimating intrinsic attenuation of a building using deconvolution interferometry and time reversal. *Bull. Seismol. Soc. Am.*, 5, 2200-2208.
- Oth, A., S. Parolai, and D. Bindi (2011). Spectral analysis of K-NET and KiK-net data in Japan, Part I: Database compilation and peculiarities, *Bull. Seismol. Soc. Am.*, 101, no. 2, 652-666.
- Paolucci, R (1993). Soil-structure interaction effects on an instrumented building in Mexico City. *European Earthquake Engineering VII*, 3, 895-908.
- Parolai, S., A. Ansal, A. Kurtulus, A. Strollo, R., Wang and J. Zschau (2009). The Ataköy vertical array (Turkey): insights into seismic wave propagation in the shallow-most crustal layers by waveform, *Geophys. J. Int.*, 178, 1649-1662
- Parolai, S., D. Bindi, A. Ansal, A. Kurtulus, A. Strollo and J. Zschau (2010). Determination of shallow S-wave attenuation by down-hole waveform deconvolution: a case study in Istanbul (Turkey), *Geophys. J. Int.*, 181, no. 2, 1147-1158.
- Parolai, S. D. Bindi, S. Ullah, S. Orunbaev, S. Usupaev, B. Moldobekov, H. Echter (2013). The Bishkek vertical array (BIVA): acquiring strong motion data in Kyrgyzstan and first results, *Journal of Seismology*, 17, no 2, 707-719.
- Parolai, S., M. Mucciarelli, M. R. Gallipoli, S. M. Richwalski and A. Strollo (2007). Comparison of Empirical and Numerical Site Responses at the Tito Test Site, Southern Italy, *Bull. Seism. Soc. Am.*, 97, 1413-1431.

- Parolai, S., R. Wang and D. Bindi (2012). Inversion of borehole weak motion records observed in Istanbul (Turkey), *Geophys. J. Int.*, 188, no 2, 535-548.
- Petrovic, B., S. U. Dikmen, S. Parolai (2017a). A real data and numerical simulations-based approach for estimating the dynamic characteristics of a tunnel formwork building: preliminary results, *Bulletin of Earthquake Engineering*, DOI: 10.1007/s10518-017-0250-3.
- Petrovic, B. and S. Parolai (2016). Joint deconvolution of building and downhole strong-motion recordings: evidence for the seismic wave field being radiated back into the shallow geological layers, *Bull. Seismol. Soc. Am.*, 106, no. 4, 1720-1732.
- Petrovic, B., S. Parolai, G. Pianese, S. U. Dikmen, B. Moldobekov, S. Orunbaev, R. Paolucci (2017b). Joint deconvolution of building and downhole seismic recordings: An application to three test cases, *Bulletin of Earthquake Engineering*, DOI: 10.1007/s10518-017-0215-6.
- Picozzi, M., S. Parolai, M. Mucciarelli, C. Milkereit, D. Bindi, R. Ditommaso, M. Vona, M. R. Gallipoli and J. Zschau (2009). Interferometric Analysis of Strong Ground Motion for Structural Health Monitoring: The Example of the L'Aquila, Italy, Seismic Sequence of 2009, *Bull. Seismol. Soc. Am.*, 101, no. 2, 635-651.
- Pianese, G., B. Petrovic, S. Parolai, R. Paolucci (2018). Identification of the non-linear response of buildings by a combines Stockwell Transform and deconvolution interferometry approach, *Bulletin of Earthquake Engineering*, DOI: 10.1007/s10518-018-0307-y.
- Prieto, G.A., J.F. Lawrence, A.I. Chung and M.D. Kohler (2010). Impulse response of civil structures from ambient noise analysis, *Bull. Seismol. Soc. Am.*, 100, 2322-2328.
- Rahmani, M. and M. I. Todorovska (2013). 1D system identification of buildings during earthquakes by seismic interferometry with waveform inversion of impulse responses – method and application to Millikan library, *Soil Dyn. Earthq. Eng.*, 47, 157–174.
- Raub, C., M. Bohnhoff, B. Petrovic, S. Parolai, P. Malin, K. Yanik, R. F. Kartal, and T. Kilic (2016). Seismic-wave propagation in shallow layers at the GONAF-Tuzla site, Istanbul, Turkey, *Bull. Seismol. Soc. Am.*, 106, no. 3, 912-927.
- Safak, E. (1997). Models and methods to characterize site amplification from a pair of records, *Earthq. Spectra*, 13, 97-129.
- Semblat, J.F., M. Kham, P.Y. Bard and P. Gueguen (2004). Could “site-city interaction” modify site effects in urban areas? Proceedings of 13th World Conference on Earthquake Engineering, Vancouver, B.C., Canada, August 1-6, 2004, Paper No. 1978.
- Semblat, J.F., M. Kham, P. Gueguen, P.Y. Bard and A.M. Duval (2002). Site-city interaction through modifications of site effects, Proceedings of 7th Conference of Earthquake Engineering, Boston, United States, July 21-25, 2002.
- Semblat, J.F., M. Kham and P. Y. Bard (2008). Seismic wave propagation in alluvial basins and influence on site-city interaction, *Bull. Seismol. Soc. Am.*, 86, 2665-2678.
- Shearer, P. M. (1999). Introduction to Seismology, *First Edition*, Cambridge University Press, Cambridge, 2009.

- Snieder, R. and E. Şafak (2006). Extracting the building response using seismic interferometry: Theory and application to the Millikan library in Pasadena, California, *Bull. Seism. Soc. Am.*, 96, 586-598.
- Tamim, N. S. M., F. Ghani (2010): Techniques for Optimization in Time Delay Estimation from Cross Correlation Function, *International Journal of Engineering & Technology*, 10, 69-75.
- Tikhonov, A.N. and V.Y. Arsenin (1977). Solution of ill-posed problems. Washington: Wiston/Wiley.
- Todorovska, M. I. (2009). Seismic Interferometry of a Soil-Structure Interaction Model with Coupled Horizontal and Rocking Response. *Bull Seismol Soc Am*, 99, no. 2A, 733-741.
- Todorovska, M. I. and M. D. Trifunac (1990). A note on the propagation of earthquake waves in buildings with soft first floor, *J. Eng. Mech.*, 116, 892-900.
- Todorovska, M. I. and M. D. Trifunac (2008a). Earthquake damage detection in the imperial country services building III: Analysis of wave travel times via impulse response functions, *Soil Dynamics and Earthquake Engineering*, 28, 387-404.
- Todorovska, M. I. and M. D. Trifunac (2008b). Earthquake damage detection in structures and early warning, Proceedings of 14th World Conference on Earthquake Engineering, Peking, China, October 12-17, 2008.
- Todorovska, M. I. and M. D. Trifunac (2008c). Impulse response analysis of the Van Nuys 7-story hotel during 11 earthquakes and earthquake damage detection, *Structural Control and Health Monitoring*, 15, no. 1, 90-116.
- Trampert, J., M. Cara and M. Frogneux (1993). SH propagator matrix and Qs estimates from borehole- and surface- recorded earthquake data, *Geophys. J. Int.*, 112, 290-299.
- Wang R (1999). A simple orthonormalization method for stable and efficient computation of Greens functions. *Bull. Seismol. Soc. Am.*, 89, 733-741.
- Wirgin, A., P. Y. Bard (1996). Effects of building on the duration and amplitude of ground motion in Mexico City, *Bull. Seismol. Soc. Am.*, 86, 914-920.

Appendices: Publications

Appendices a)-e) are publications which are part of this thesis, the Postprint versions are included here.

a) Bindi, D., B. **Petrovic**, S. Karapetrou, M. Manakou, T. Boxberger, D. Raptakis, K. D. Pitilakis, and S. Parolai (2015). Seismic response of an 8-story RC-building from ambient vibration analysis, *Bull. Earthq. Eng.*, 13, 2095-2120. <https://dx.doi.org/10.1007/s10518-014-9713-y>

b) **Petrovic**, B., Dikmen, S. U., Parolai, S. (2017a). A real data and numerical simulations-based approach for estimating the dynamic characteristics of a tunnel formwork building: preliminary results, *Bulletin of Earthquake Engineering*. <https://dx.doi.org/10.1007/s10518-017-0250-3>

c) Raub, C., M. Bohnhoff, B. **Petrovic**, S. Parolai, P. Malin, K. Yanik, R. F. Kartal, and T. Kilic (2016). Seismic-wave propagation in shallow layers at the GONAF-Tuzla site, Istanbul, Turkey, *Bull. Seismol. Soc. Am.*, 106, no. 3, 912-927. <https://dx.doi.org/10.1785/0120150216>

d) **Petrovic**, B., and S. Parolai (2016). Joint deconvolution of building and downhole strong-motion recordings: evidence for the seismic wave field being radiated back into the shallow geological layers, *Bull. Seismol. Soc. Am.*, 106, no. 4, 1720-1732. <https://dx.doi.org/10.1785/0120150326>

e) **Petrovic**, B., Parolai, S., Pianese, G., Dikmen, S. U., Moldobekov, B., Orunbaev, S., Paolucci, R. (2017b). Joint deconvolution of building and downhole seismic recordings: An application to three test cases, *Bulletin of Earthquake Engineering*. <https://dx.doi.org/10.1007/s10518-017-0215-6>

Appendix a): Seismic response of an 8-story RC-building from ambient vibration analysis

The final publication is available at Springer via <https://dx.doi.org/10.1007/s10518-014-9713-y>

Bindi, D., B. Petrovic, S. Karapetrou, M. Manakou, T. Boxberger, D. Raptakis, K. D. Pitilakis, and S. Parolai (2015). Seismic response of an 8-story RC-building from ambient vibration analysis, *Bull. Earthq. Eng.*, 13, 2095-2120.

Abstract

In this study, we assess the dynamic characteristics of an 8-story RC-building composed by two units connected through a structural joint. This building, belonging to one of the largest hospitals in northern Greece, has been selected in the framework of a European funded project (REAKT) as test site for developing a Structural Health Monitoring system and it is instrumented with a permanent strong motion network. The assessment of the dynamic characteristics is performed using ambient vibration recorded by a temporary seismic network installed inside the structure. Non-parametric identification methods, namely the Peak Picking and Frequency Domain decomposition, are applied to perform operational modal analysis and extract the natural frequencies and mode shapes of the structural system. Since the detection of changes in the shear wave velocity inside the building is relevant for Health Monitoring analysis, we use the ambient vibration recordings to perform a deconvolution interferometry. Moreover, a shear-beam model is considered to estimate the velocity in the first three floors, where the distribution of internal sources introduces complex patterns in the impulse response functions. The velocity for lowest part of the building is estimated by optimizing the match between the arrival times of the empirical and theoretical pulses. Finally, the velocities and quality factors estimated from ambient vibration analysis are consistent with preliminary results obtained analyzing earthquake data recorded in the same building.

1 Introduction

The rapid development of data acquisition and processing capabilities has given rise to major advances in the experimental operational studies, particularly in the field of structural health monitoring. Monitoring of civil structures becomes increasingly popular as it offers the opportunity to better understand the dynamic behavior of structures under seismic loading, measuring the structural response and monitoring the damage evolution. Therefore it is considered a significant tool for seismic protection and risk mitigation ensuring the integrity and improving the performance and reliability of structures.

The seismic response of a building can be determined looking either at the characteristics of the normal modes (vibrational approach, e.g. Chopra, 1996) or at the properties of seismic waves propagating within the building (waveform approach, e.g., Kanai, 1965; Todorovska and Trifunac, 1990; Snieder and Şafak, 2006; Todorovska, 2009; Rahmani and Todorovska, 2013; Nakata et al., 2013). Dynamic characterization of civil engineering structures (frequencies, mode shapes, damping ratios) is of major importance in a wide range of research and application fields, such as dynamic response prediction, finite element model updating, structural health monitoring and vibration control engineering. Since a limited number of moderate to strong earthquakes occur per year close to instrumented buildings, which are anyway very limited, the dynamic characteristics of civil engineering structures are generally extracted from the building response to forced vibrations, weak/moderate earthquakes and ambient vibrations, limited however to the range of linear deformation. Although the origin of using ambient vibration for building monitoring started long time ago (e.g. Davinson, 1924; Carder, 1936; Housner and Brady, 1963; Trifunac, 1972; Ivanović et al, 2000), the development of several system identification techniques in the context of modal analysis of output only systems, made this kind of monitoring approach very popular in the last two decades (e.g. Brincker et al., 2001; Van Overschee and De Moor, 1996; Peeters and De Roeck, 1999). Operational Modal Analysis (OMA) is generally preferred to forced vibration measurements due to the fact that the same modal parameters can be obtained from vibration data in operational rather than laboratory conditions (Reynders, 2012). There are several studies that have used ambient vibration testing for the identification of the dynamic behavior of civil engineering structures (Brownjohn, 2003; Ventura et al., 2003), finite element calibration and updating (Teughels, 2003; Jaishi and Ren, 2005), vulnerability assessment (Guéguen et al., 2007; Michel et al., 2008; Michel et al., 2012) and damage detection (Peeters, 2000).

In the context of the waveform approach, the application of ambient vibration has been pushed by the introduction of the deconvolution interferometry (e.g. Snieder and Şafak, 2006). Seismic interferometry (Aki, 1957; Clearbout, 1968; Snieder and Şafak, 2006) is based on the correlation of waves recorded at different receivers; under some assumptions on the source distribution, it can be used to retrieve the Green's function that accounts for the wave propagation between the two receivers (e.g. Lobkis and Weaver, 2001; Wapenaar, 2004). This technique has been applied in many seismological contexts and, in particular, to downhole seismology, where the interferometry has been used to determine the velocity and attenuation structures in correspondence of instrumented boreholes (e.g. Trampert et al., 1993; Metha et al., 2007; Assimaki, 2008; Parolai et al., 2010). The interferometric approach has been widely used to evaluate the shear wave velocity and attenuation inside the building using earthquake data (e.g. Snieder and Şafak, 2006; Kohler et al., 2007; Nakata et al., 2013; Rahmani and Todorovska, 2013). The deconvolution removes the dependency on the source excitation and, differently from the vibrational approach, the effect of the coupling with the ground (Snieder and Şafak, 2006; Todorovska, 2009). On the other hand, the application of the interferometric approach to ambient vibration is still limited (e.g.

Prieto et al., 2010; Nakata and Snieder, 2014). The presence of several internal sources of noise simultaneously acting during the acquisition is the main difference with respect to the interferometry using earthquake data, making the results depending, in general, on the radiation losses at the base of the building (Nakata and Snieder, 2014).

In this study, we apply both OMA and the interferometry approaches to an instrumented 8-story hospital (AHEPA) constructed in the seventies in Thessaloniki (Greece). This RC building has been selected as test site for the European funded REAKT project⁵. We first compute the dynamic characteristics of the hospital building to evaluate changes in its vulnerability due to all possible geometrical modifications, mass distributions and material deterioration through time. Traditionally, in seismic vulnerability assessment studies it is implicitly assumed that the structures are optimally maintained during their lifetime neglecting any deterioration effect (e.g. due to aging, pre-existing earthquake damage etc.) that may adversely affect their structural performance under dynamic (or even static) loading (Pitilakis et al., 2014). Therefore, it is of primary importance to identify the real structural conditions and potential pathology of the building. The use of ambient noise measurements for identifying the actual state of the structures is a very attractive technique for that. In the framework of REAKT, a permanent strong motion system was installed for monitoring the building and implementing an early earthquake warning system (EEW) for near real time damage assessment. Since variation in the shear wave propagation induced by an earthquake could be a useful proxy for possible damage detection, in this study we also estimate the shear wave velocity in the building by applying an interferometric approach to ambient vibrations. This waveform approach provides a spatially distribution of physical parameters playing a role in the seismic response of the structure (e.g. shear wave velocity, related to the structural rigidity). Therefore, by merging the interferometric results with the description of the building in terms of normal modes, we get a comprehensive view of the dynamic characteristics of the building.

2 AHEPA hospital: Structural description and permanent instrumentation.

The AHEPA general hospital in Thessaloniki is one of the largest hospitals in northern Greece, located in the campus of Aristotle University. It is a major teaching and research center and part of the National Healthcare System of Greece. The hospital complex consists of 40 buildings of various functions and typologies, 2 electrical substations, a gas distribution network and an underground water supply system. Many of these buildings were built before 1985 and are classified as low seismic code structures. In case of the emergency its central location in the city of Thessaloniki makes it one of the most important medical care centers for an efficient crisis management. The target building hosts both administration and hospitalization activities. It was constructed in 1971 and is considered representative of structures that have been designed according to the old 1959 Greek seismic code (Royal Decree of 1959), where the ductility and the dynamic features of the constructions are ignored. It is an eight story infilled structure and its special feature is that it is composed of two adjacent tall building units that are connected with a structural joint (Figure 1a). UNIT 1 covers a rectangular area of 29m by 16m while UNIT 2 has a trapezoidal cross section of 21m by 27m by 16m. The total height of the building with respect to the foundation level is 28.6m with a constant inter-story height of 3.4m except for the second floor where the height increases to 4.8m due to the presence of a middle floor level which covers only a part of the typical floor plan (Figure 1a). From the structural point of view the buildings force resisting

⁵ <http://www.reaktproject.eu/>

mechanism comprises longitudinal and externally transverse reinforced concrete moment resisting frames (Figure 1a). The columns have variable dimensions along the height of the building starting from 0.45m to 0.70m at the lowest level (basement) and resulting to 0.35m by 0.35m at the upper floor. In the longitudinal direction the outer and inner columns are connected by beams with cross-section of 0.20m by 0.60m and 0.35m by 0.40m respectively. In the transverse direction on the other hand only the exterior columns are connected by beams with dimensions of 0.20m by 0.95m. The presence of beam to beam connections at all floor levels near the staircases and elevator shafts, constitute a complex structural system which is particularly evident in the middle floor where the RC beams are inverted. Reinforced concrete walls are present in both building units, surrounding partially the staircases and the lift shafts; they are not specially detailed for seismic performance. More specifically there are two walls in the transverse and one in the longitudinal direction of UNIT 1 and only one wall in the transverse direction of UNIT 2. The RC walls are 0.20m thick while their length is decreasing significantly along the structures height. Moreover a perimeter reinforced concrete wall with dimensions of 0.20m by 3.00m has been constructed at top of the building. The foundation system consists of simple footings of variable geometries without tie-beams combined partially with a raft foundation. Figure 1b represents a typical cross-section of the hospital with the foundation soil profile and the average shear wave velocities V_s estimated from down-hole tests (Raptakis et al., 1994). The soil consist of a stiff clay with average V_s of about 400-450 m/s, The rock basement (schist) is found at 30 to 35m depth having V_s velocities greater than 750 m/s. The foundation soil at the hospital building can be characterized as soil type B according to EC8 soil classification. Using the SYNER-G taxonomy (Pitilakis et al., 2014) for RC structures to describe the typology of the hospital building, it may be considered typical of high-rise infilled moment resisting frame buildings designed with low seismic code level. The Sosewin (Picozzi et al., 2011) permanent network operates in Ahepa hospital since May 2012. It comprises 13 triaxial accelerometers (MEMS ADXL203 chip) installed on the basement, the first and fourth floors and the roof, as shown in Figure 2. One more accelerometer is installed on the roof of a nearby building and used as bridge node for the data transmission to the two gateways installed outside of the Laboratory of Soil Mechanics, Foundations and Geotechnical Earthquake Engineering.

3 Data and Fourier analysis

Ambient noise measurements were performed on February 12th and 13th, 2013 using seismic stations (i.e. sensor's output proportional to ground velocity). During the first day of experiment, the two building units were instrumented with 39 stations. For each building, two instruments were deployed at each floor, the first on the external side and the second close to the structural joint. Due to restrictions in the logistics, the stations were deployed along the longitudinal corridors, located almost in the middle of the structure (Figures 2 and 3). Two additional stations were deployed at the corners on the roof of the two buildings and one stations outside the structure. The stations were equipped with short period L4C-3D Mark sensors (1Hz natural frequency, three components) connected to Earth Data Logger (EDL PR6-24) 24bit digitizers. The sampling rate was set to 500 samples per second and a gain 10 was used for the pre-amplifier. GPS antennas guaranteed the time synchronizations among the instruments. At four locations, a second station equipped with Güralp broadband seismometers (CMG-40T, 30s natural period) coupled to Reftek recorders (DAS-130) was also deployed for instrumental comparison purposes. In the second day, 51 stations were used (44 EDL and 7 Reftek), adding one station at certain floors. In this study, we analyze the short-period data acquired during the first day of measurements

(Table 1).

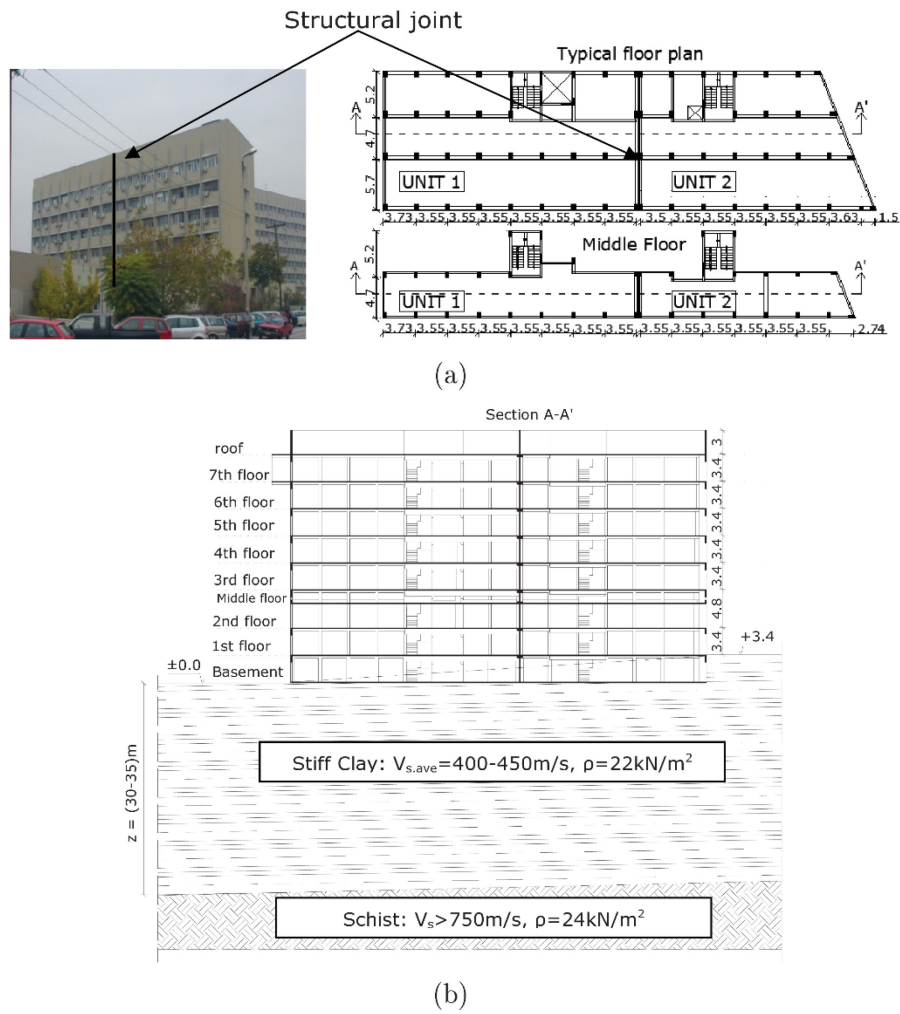


Figure 1. (a) Typical floor plan and middle floor with the structural joint and (b) typical soil profile in correspondence of AHEPA hospital building.

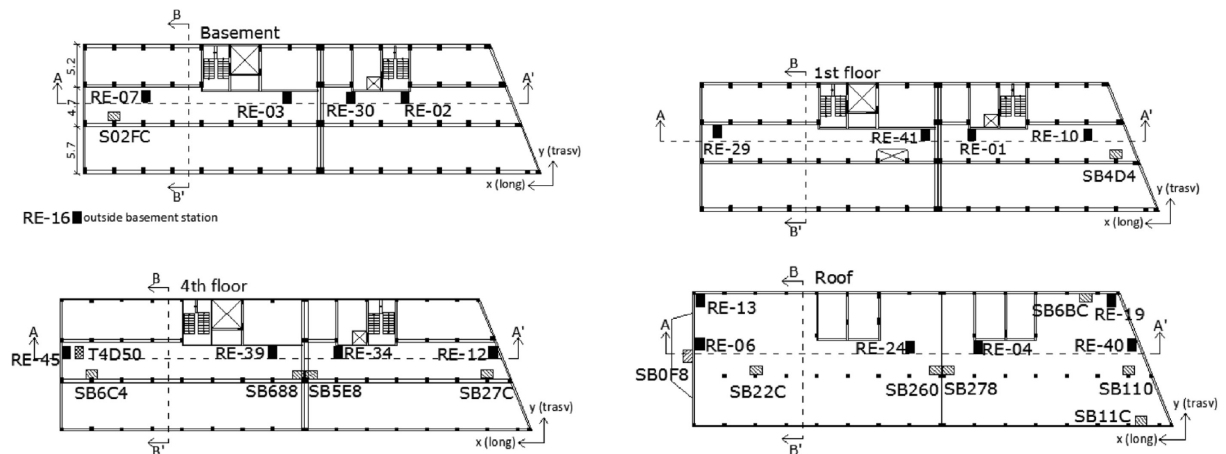


Figure 2. Floor plans of the basement, the first and fourth floor and the roof. The permanent strong motion (code SB or SC) and temporary seismometers (code RE or T4) are also shown.

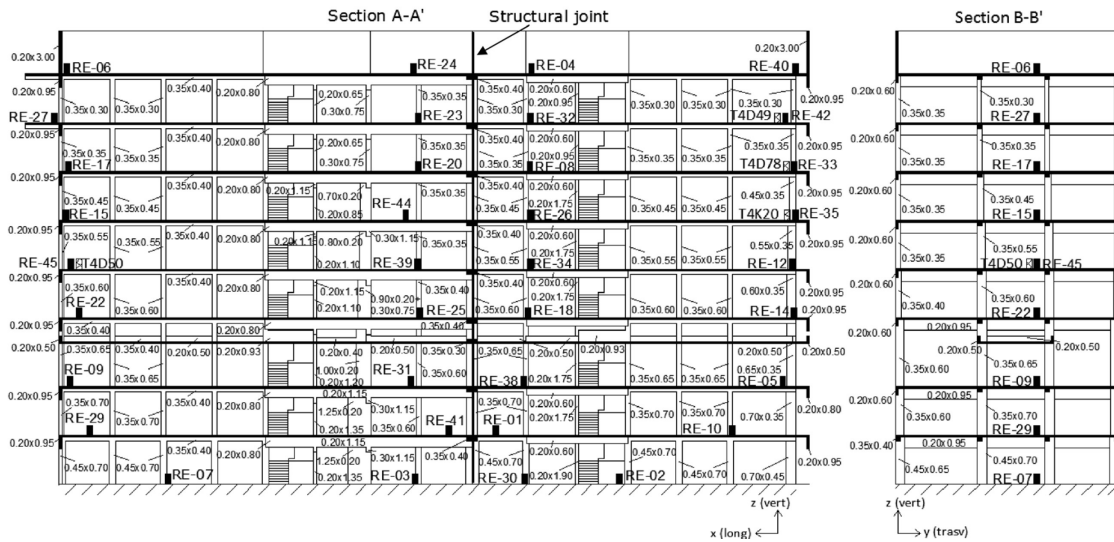


Figure 3. Sections A-A and B-B along the longitudinal and transverse direction of the hospital building with the temporary instrumentation.

Figure 4 shows the power spectral densities (PSD) versus time for the station installed outside the building and for two stations installed inside at the first floor and on the roof. The power spectra are computed considering running windows two minutes in length, overlapping by 50% and tapered at both ends. The power spectra recorded on the roof clearly indicate the main spectral features (i.e. resonance frequencies) of the coupled building-soil system, and their stability over the analyzed time window. Since the station outside was installed few meters from the structure, the main resonance frequencies of the building are still recognizable in the spectra observed at this station.

Table 1. Serial number and position of all the stations used in the first day ambient noise experiment.

Station position	Unit 1		Unit 2	
	Column 1	Column 2	Column 1	Column 2
Basement	RE-07	RE-03	RE-30	RE-02
1st floor	RE-29	RE-41	RE-01	RE-10
2nd floor	RE-09	RE-31	RE-38	RE-05
3rd floor	RE-22	RE-25	RE-18	RE-14
4th floor	RE-45, T4D50*	RE-39	RE-34	RE-12
5th floor	RE-15	RE-44	RE-26	RE-35, T4K20*
6th floor	RE-17	RE-20	RE-08	RE-33, T4D78*
7th floor	RE-27	RE-23	RE-32	RE-42, T4D49*
Roof	RE-06	RE-24	RE-04	RE-40

Note: * broad-band seismometers, not used in the present study

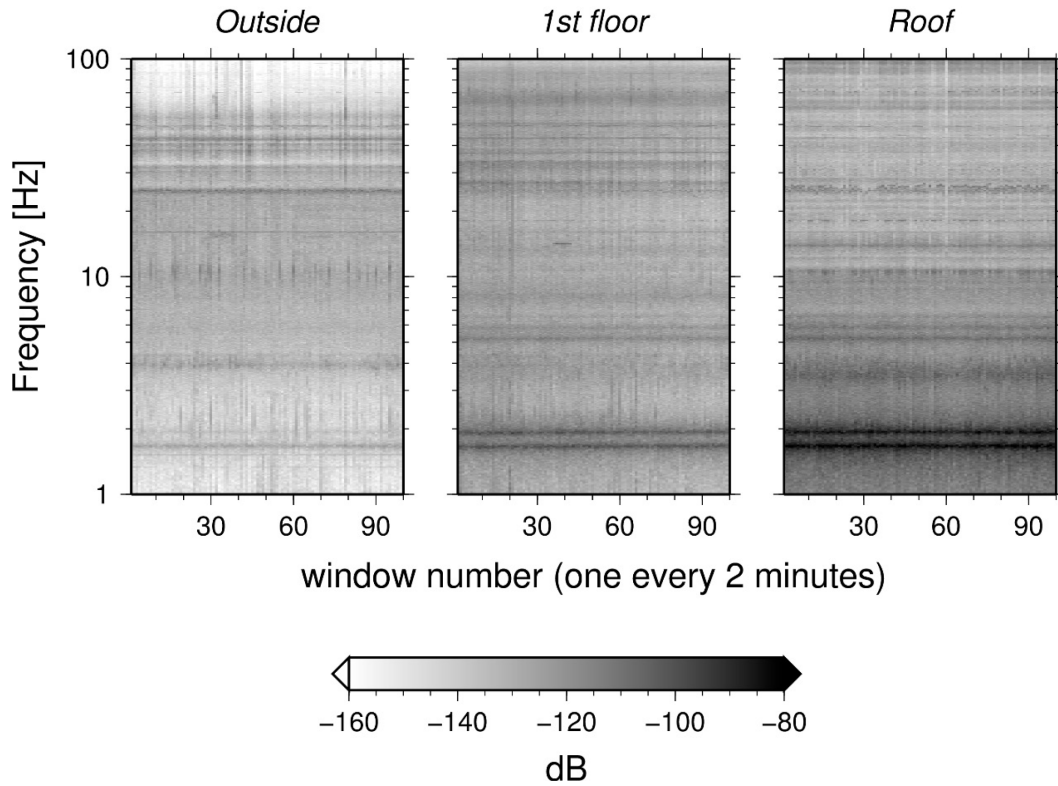


Figure 4. Longitudinal power spectra densities (PSD) computed for the stations installed outside (left panel), on the 1st floor (middle panel) and on the roof (top panel). The spectral values are expressed in decibel (dB) with respect to velocity ($\text{m/s}^2/\text{Hz}$).

The probability density functions (PDF) (e.g. McNamara and Buland, 2004; Marzorati and Bindi, 2006) computed for the power spectral values are shown in Figure 5. The PDF shows that, for frequencies above 1Hz, the level of noise during the measurements is close to the upper limit of Peterson noise model (Peterson, 1993), and well above the self-noise of the instrument (e.g. Strollo et al., 2008). The narrow spread around the mode values shown by the PDF evaluated for the roof recordings confirms the stability of the spectral features over the analyzed time window. The differences between the 95th and the 5th percentiles of the power spectra distribution ranges between 2 and 10 dB for the longitudinal direction on the roof (between 3 and 10 dB when the vertical component is considered) and between 5 and 11 dB for the station installed in the first floor (from 12 to 24 dB considering the vertical component). This confirms the presence of a more variable noise field inside the building and, in particular, in the first three floors where different entrances to the hospital and connection with adjacent buildings are present.

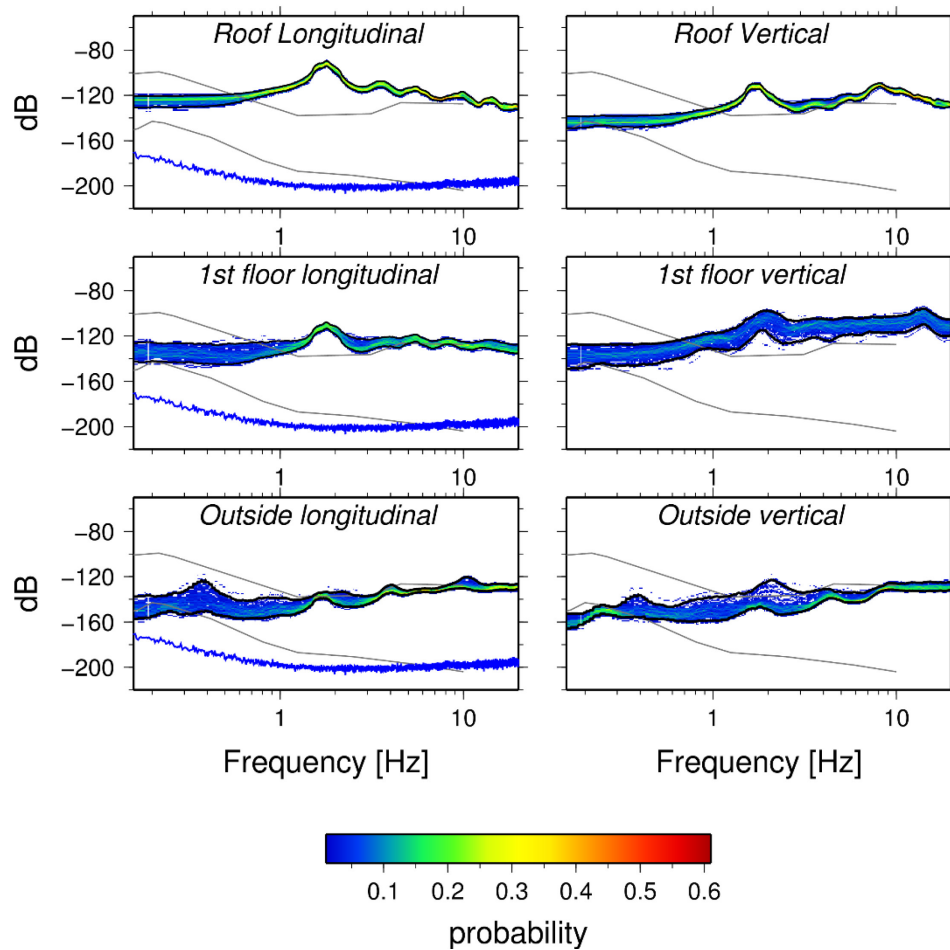


Figure 5. Probability Density Function (PDF) for the stations installed outside the building (bottom), on the first floor (middle) and on the roof (top). The longitudinal components are shown on the right, the vertical ones on the left. The power spectra are expressed in decibel (dB) with respect to velocity ($m/s^2/Hz$). The black curve identify the 5-th and 95-th percentiles of the distributions. The New High Noise Model and the New Low Noise Model of Peterson (1993) are shown as gray lines. The self-noise of the instrument (sensor and digitizer), shown by the blue curve in the longitudinal plots, was derived by coherency measurements (Holcomb, 1989).

Figure 6 exemplifies the longitudinal Fourier amplitude spectra (FAS) computed for Unit 1. The average spectra \pm one standard deviation are computed considering moving windows 1 minute long and overlapping by 50%. The spectra identify the main resonances of the system at about 1.65 and 1.91 Hz, as will be discussed in the section devoted to the modal analysis. The amplitude of the fundamental peak of resonance increases of about two order of magnitude when moving from the basement to the roof. Except for one station installed in the 6th floor of UNIT 1, which is not considered for further analysis, the FAS are stable over the time of measurements. The FAS for different components are summarized in Figure 7, considering stations installed on the roof, in the basement and outside the building. The peaks of amplification at different frequencies are related to the different modes of vibration, as detailed in the modal analysis presented in the next section.

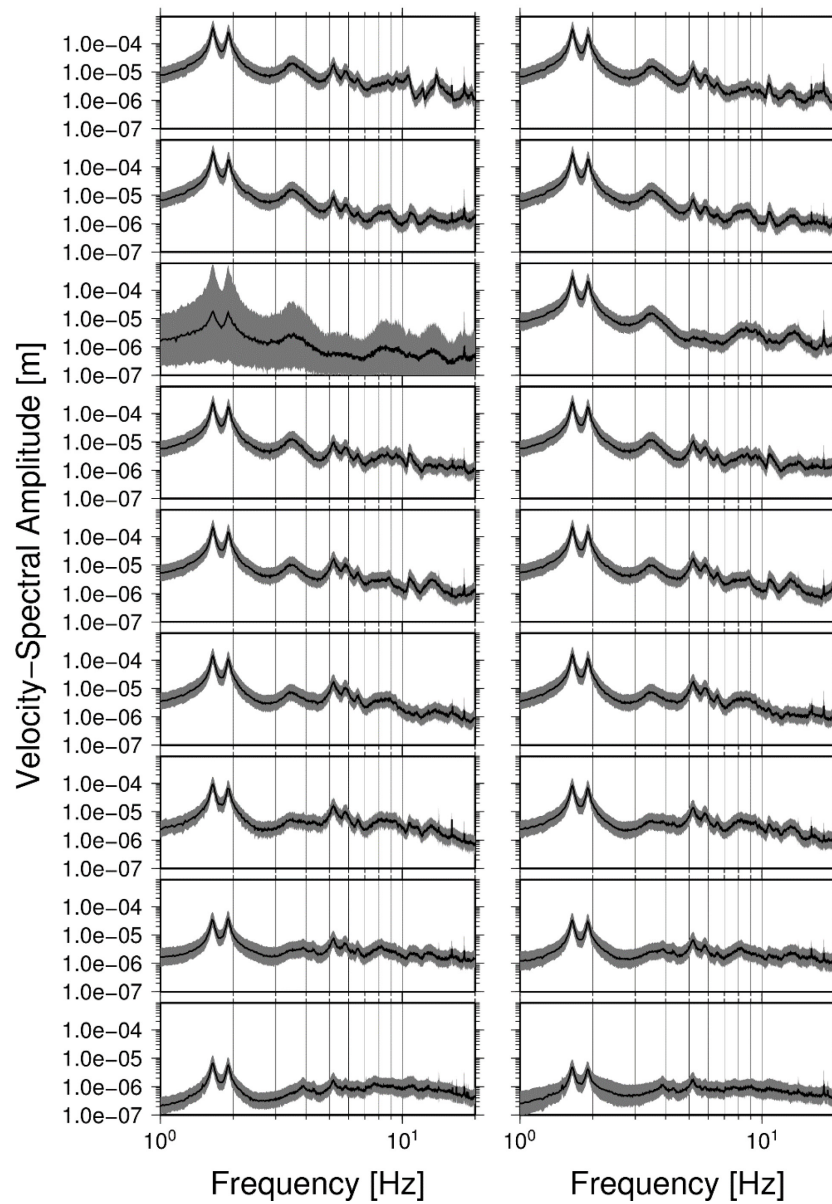


Figure 6. Fourier Amplitude Spectra (FAS) for the longitudinal component, considering the instruments installed along the external (left panels) and internal (right panels) vertical lines of Unit 1 (see Figure 3). The black line indicates the mean value, $\pm 1\sigma$ is shown in gray.

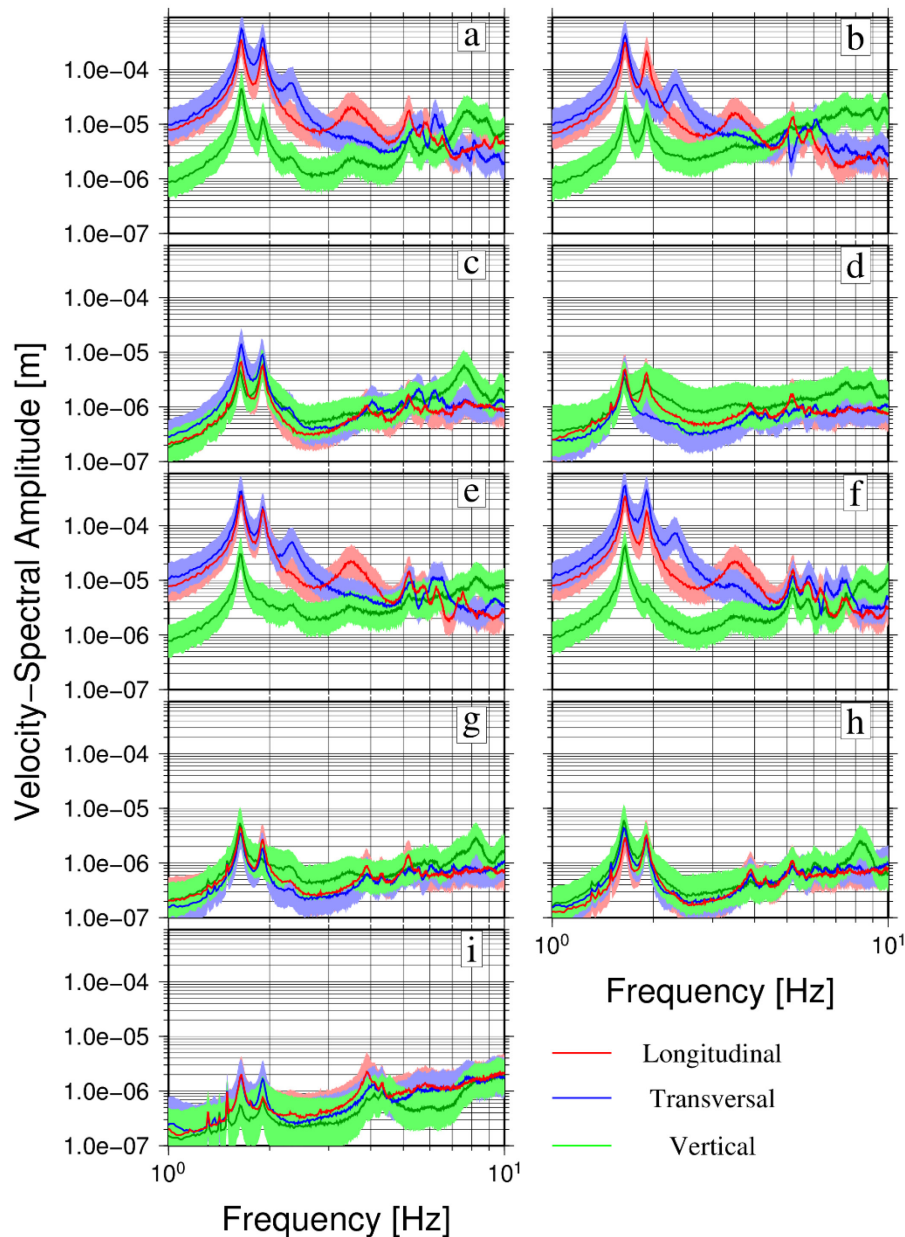


Figure 7. Fourier amplitude spectra (mean $\pm 1\sigma$) for the three components of motion computed for stations installed on the roof (a and b are the two columns in Unit 1; e and f in Unit 2) and in the basement (c and d in Unit 1; g and h in Unit 2). The spectra for the station installed outside AHEPA are shown in panel i.

4 System identification and Operational modal analysis.

In order to predict or modify the response of a structure, an accurate well-known mathematical model is required that represents the dynamics of the structure, the so-called modal model. The process of building a modal model of a physical system based on experimental data is called system identification (Ljung, 1999). The modal model expresses the behavior of a linear time-invariant system as a linear combination of contributions from the different resonance modes of the structure (Parloo, 2003). Based

on the knowledge of the systems experimental response (output data) to an excitation source (input data) a parametric modal model can be derived that is defined by a set of modal parameters (eigenfrequencies, mode shapes, damping ratios). There are several deterministic or stochastic techniques that have been developed over the past years that can be used to build the mathematical model of the dynamic structural systems in frequency or time domain based on measured data. A modal model of an artificially excited structure can be obtained based on Experimental Modal Analysis (EMA); however in case of real scale civil engineering structures applying an artificial excitation might be difficult from technical and economical point of view. Therefore, Operational Modal Analysis (OMA) is generally preferred to forced vibration measurements since the same modal parameters can be obtained from vibration data in operational rather than laboratory conditions by modeling the interaction between the structure and its environment (e.g. wind, traffic, etc.). Ambient vibration measurements are usually used to perform OMA and to identify the modal parameters of a structure. In contrast to Experimental Modal Analysis, the properties of ambient excitation in Operational or Output- Only Modal Analysis are difficult or impossible to be measured. Therefore stochastic identification techniques have been developed by the assumption that the response is a realization of a stochastic process with unknown white Gaussian noise as input characterized by a flat spectrum in the frequency range of interest. Based on this assumption the excitation input is considered to have the same energy level at all frequencies implying that all modes are excited equally (Van Overschee and De Moor, 1996; Peeters, 2000). There are different stochastic identification techniques to extract the modal parameters of a structural system, namely the parametric and non-parametric methods. In non-parametric methods the modal parameters are estimated directly by post-processing the measured data whereas in the parametric methods the dynamic characteristics are extracted based on a parametric model that is updated to fit the recorded data. To evaluate the dynamic characteristics of the hospital building, namely the natural frequencies and mode shapes, system identification and Operational Modal Analysis were performed using MACEC 3.2 software (Reynders et al., 2011) for the two adjacent building units separately (UNIT 1 and UNIT 2) as well as for the entire hospital building complex, analyzed as one taking into account the interaction of the two building units due to their connection with the structural joint (BUILDING). Operational modal analysis was initially conducted for the horizontal components of the measurements. The grid of the models was built so that the defined nodes correspond to nodes that have been actually measured. The sensors that were used for the identification process are illustrated in Figures 2 and 3.

Before identification a time window of 1800 s (30 minutes) was applied and the data were decimated with a factor 10. The data were filtered with a low-pass anti-aliasing filter with a cut-off frequency of 25 Hz and re-sampled at 50 Hz reducing thus the number of data from 900,000 to 90,000 points avoiding thus unnecessary computational burden in the modal analysis were the frequencies of interest are smaller than 25 Hz.

System identification and modal analysis of the structural models under study have been conducted using non-parametric identification techniques, namely the Peak Picking (PP) (Bendat and Piersol, 1993), and the Frequency Domain Decomposition (FDD) (Brincker et al., 2001) methods. The FDD method is considered to be an improved version of the Peak Picking method and consists of decomposing the systems cross power spectral density into its singular values. It is shown that taking the Singular Value Decomposition SVD of the spectral matrix, the latter is decomposed into a set of auto spectral density functions each corresponding to a single degree of freedom (SDOF) system (Brincker et al., 2001).

For the power spectra density estimation of the measured outputs collected from all channels, the correlogram method was applied. In the correlogram approach, the auto and cross-PSDs of one or two

quasi-stationary ergodic sequences is estimated as the Laplace transform of the auto or cross correlation functions respectively (Reynders, 2012). In the PP method the averaged normalized power spectral density (ANPSD) is computed and the well separated modes are estimated by picking the peaks in the ANPSD. In the FDD method, the singular values are obtained from the decomposition of the PSD matrix and the modal parameters are estimated by picking the peaks of the first singular value. The results of the modal analyses for the two adjacent buildings analyzed separately (UNIT 1 and UNIT 2) and as one single building (BUILDING) are presented in Figure 8. In Table 2, the eigenfrequencies computed with the two system identification methods are summarized. It is seen that the estimated frequency values for the five well separated modes are very close to each other (practically the same at the first three modes) for the two non-parametric methods applied as well as for the different system models identified.

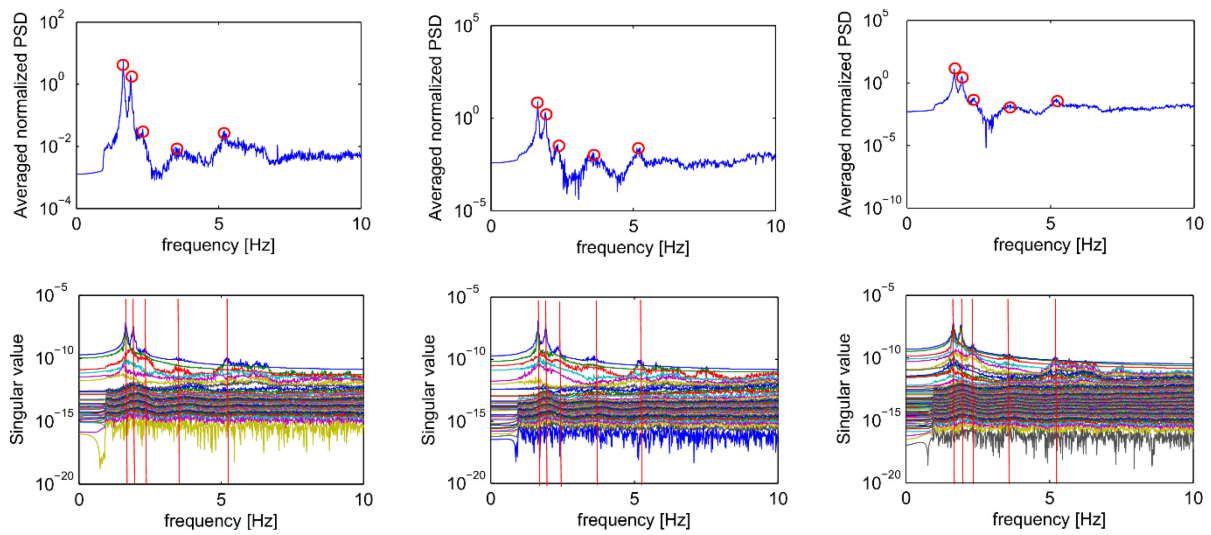


Figure 8. Modal identification using the Peak Picking (top) and the Frequency Domain Decomposition (bottom) applied to ambient noise measurements. The first five modes are indicated with red circles (top panels) and dashed lines (bottom panels).

Table 2: Eigenfrequencies of UNIT 1, UNIT 2 and BUILDING estimated using the nonparametric system identification techniques

Mode	Mode type	UNIT1		UNIT2		BUILDING	
		PP [Hz]	FDD [Hz]	PP [Hz]	FDD [Hz]	PP [Hz]	FDD [Hz]
1	Coupled translational	1.65	1.65	1.65	1.65	1.65	1.65
2	Coupled translational	1.91	1.9	1.91	1.91	1.91	1.91
3	Torsional	2.33	2.33	2.35	2.35	2.35	2.35
4	Coupled translational	3.5	3.5	3.58	3.58	3.54	3.58
5	Coupled translational	5.2	5.2	5.2	5.22	5.2	5.2

Similar orders and shapes of the modes are estimated for the different system models as illustrated in Figures 9, 10 and 11. This implies that the dynamic interaction of the two adjacent buildings due their connection with the structural joint is reflected on the measured outputs, and the dynamic characteristics of the complex hospital building is possible to be captured by monitoring and analyzing the two adjacent building units separately. Moreover the fact that frequencies and mode shapes are identical for both units may be attributed to their similar structural configuration. The building is exhibiting coupled sway and torsional modes in the frequency range of interest which are expected in case of geometric and structural irregularities or eccentricities between the center of mass and center of rigidity. The highly coupled obtained mode shapes confirm the complex vibrational characteristics of the building especially for the first two identified frequencies. Figure 12 represents indicatively for UNIT 1 the contribution of the transverse, longitudinal and torsional motion in the first two modes. It should be noted herein that a comparison with the modal identification results extracted using the SSI-Stochastic Subspace Identification method (Van Overschee and De Moor 1996) confirms the reliability of the identified frequencies and mode shapes with the nonparametric approaches presented in this paper (Karapetrou et al. 2014).

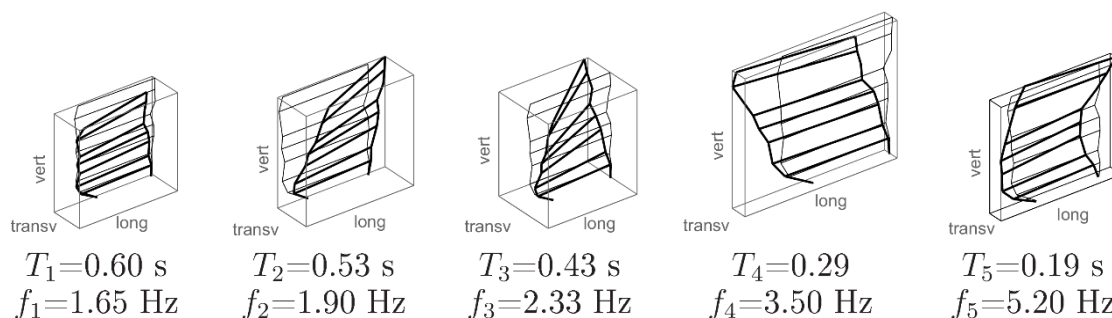


Figure 9. Mode shapes corresponding to the first five identified frequencies for UNIT 1.

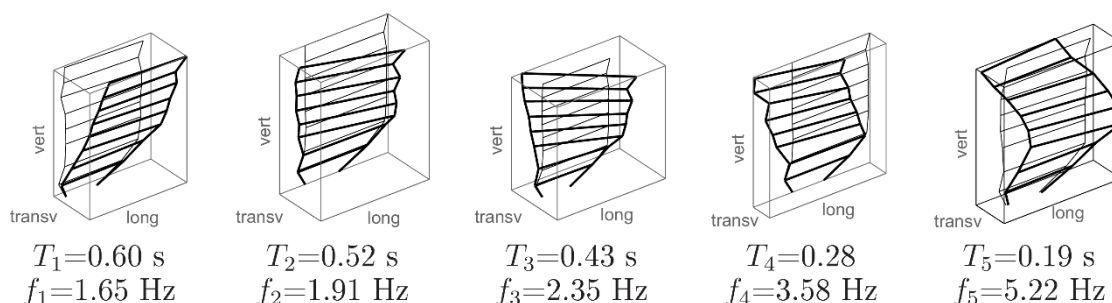


Figure 10. Mode shapes corresponding to the first five identified frequencies for UNIT 2.

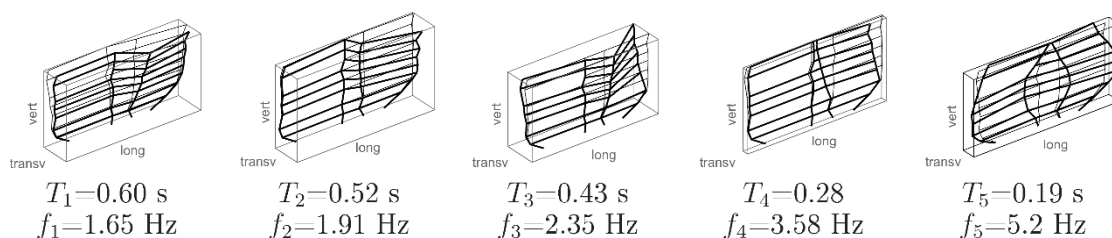


Figure 11. Mode shapes corresponding to the first five identified frequencies for BUILDING.

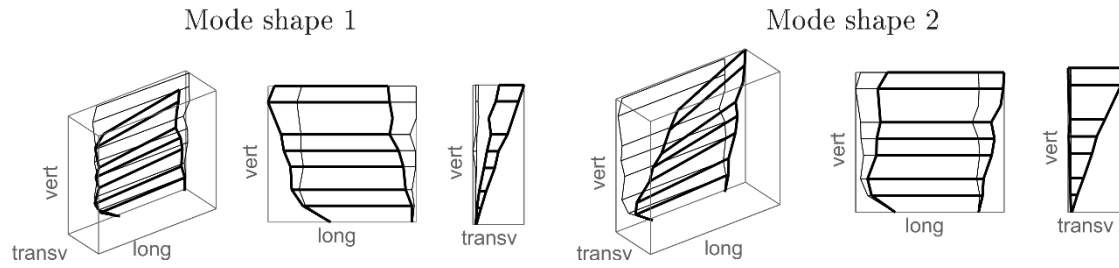


Figure 12. Contribution of the lateral components in the first two modes along the longitudinal and transverse direction for UNIT 1.

5 Interferometry

In this section, we determine the building impulse response function (IRF) by following a waveform approach based on seismic interferometry. Differently from the vibrational approach, that describes the soil-building system as a whole, deconvolution interferometry allows us to get an insight about the spatial distribution inside the building, using parameters, like the shear wave velocity, that are connected to the dynamic characteristics of the structure alone. Assuming a linear and time invariant system, the interferometric approach is based on deconvolving the signal $u_{ref}(t)$ recorded at a reference location from the signal $u(t)$ recorded at a generic location. In the Fourier domain, the deconvolution can be written as (e.g. Snieder and Şafak, 2006)

$$D(\omega) = \frac{\hat{u}(\omega)}{\hat{u}_{ref}(\omega)} \quad (1)$$

where the symbol $\hat{\cdot}$ indicates the Fourier transform and $\omega = 2\pi f$ is the angular frequency. Considering the ill-posed nature of the deconvolution, the spectral ratio has to be regularized. Among different possible regularization schemes (e.g. Bertero and Boccacci, 1998; Bindi et al., 2010), we apply the so-called water-level regularization (e.g. Wiggins and Clayton, 1976)

$$D(\omega) = F(\omega)\hat{u}(\omega) \quad (2)$$

$$F(\omega) = \frac{\hat{u}_{ref}^*(\omega)}{|\hat{u}_{ref}(\omega)|^2 + \varepsilon} \quad (3)$$

where ε is the regularization parameter which controls the degree of filtering applied to the spectral ratio to stabilize the retrieved Impulse Response Function $D(\omega)$. In this study, the values of ε are given as percentage (hereinafter referred to as α) of the average spectral power. The vertical propagation of the seismic waves in the building can be easily described if assuming a shear-beam model (Iwan, 1997). Following Snieder and Şafak (2006) the deconvolution of the motion recorded at a generic height z with respect to the motion recorded at the highest floor $z = H$ is given by

$$T(z, \omega) = \frac{1}{2} \left[e^{ik(z-H)} e^{-\gamma|k|(z-H)} + e^{ik(H-z)} e^{-\gamma|k|(H-z)} \right] \quad (4)$$

where k is the wavenumber $k = \omega/c$, c is the shear wave velocity of the building, and γ is the viscous

damping related to the quality factor Q by $\gamma = \frac{1}{2Q}$. $T(z, \omega)$ describes the response of the system when a virtual source is acting at the top of the building at $t = 0$. The first term in equation (4) describes an acausal (i.e. $t < 0$) up-going wave, while the second term describes the causal down-going wave. When the deconvolution is performed with respect to the motion at the base of the building, the impulse response function is given by (Snieder and Şafak, 2006)

$$B(z, \omega) = \frac{e^{ikz} e^{-\gamma|k|z} + e^{ik(2H-z)} e^{-\gamma|k|(2H-z)}}{1 + e^{2ikH} e^{-2\gamma|k|H}} \quad (5)$$

Expressing the denominator in term of geometric series, equation (5) can be rewritten as (Snieder and Şafak, 2006)

$$B(z, \omega) = \sum_{n=0}^{\infty} (-1)^n [e^{ik(z+2nH)} e^{-\gamma|k|(z+2nH)} + e^{ik(2(n+1)H-z)} e^{-\gamma|k|(2(n+1)H-z)}] \quad (6)$$

where the summation index n counts the number of bounces off the base. $B(z, \omega)$ is a causal function composed by an infinite sum of up-going and down-going waves. Both $B(z, \omega)$ and $T(z, \omega)$ are independent on the reflection coefficient at the base of the building, that is they are not depending on the coupling with soil. For a detailed discussion about how the deconvolution is changing the boundary conditions with respect to those for the original wave field, see (Snieder and Şafak, 2006).

Many studies applied equations (4) and (5) to extract the building response using earthquake data. When ambient vibrations are considered, the presence of multiple internal sources simultaneously exciting the building introduces a dependence of the deconvolved waveforms on the ground coupling, in particular for the attenuation (Nakata and Snieder, 2014). To obtain stable deconvolved waveforms, a stacking procedure is applied to the deconvolution computed for several time windows (Prieto et al., 2010; Nakata and Snieder, 2014). In this study, we analyze 1 hour of ambient vibration.

5.1 Deconvolution and parameters selection.

The scheme applied to compute the IRFs is exemplified in Figure 13, considering three sensors, installed in the basement, on the 4th floor, and on the roof (Figure 3). Panel (a) shows the moving windows running over the noise records, with a duration of about 32s, overlapping for 50% and cosine-tapered at both ends. The spectra computed for each window (panel b) are lowpass filtered and used to compute the regularized spectral ratio given by equation (4). The spectrum at the reference station (located on the roof in this example) is used to construct the filter $F(\omega)$ given by equation (3), shown in panel (c). The shape of the filter is determined by the spectrum at the reference station and the degree of filtering is controlled by the regularization parameter ε . The filter applied to the spectra computed at the different floors provide the impulse response function between each considered sensor and the reference one, as shown in Fig. 14 both in the frequency and time domains. The IRFs in the time domain are used to estimate the average shear wave velocity by measuring the time lag τ between the a-causal and causal pulses. In particular, the average velocity between the floor at height z and H (roof) is given by $v = D/\tau$ where $D = 2(H - z)$. The average velocity is estimated using a least-squares fit by considering the time lag measured at different floors. The amplitude ratio A_-/A_+ between the a-causal (A_-) and causal (A_+) pulses can be used to estimate the quality factor Q using $1/2 Q = \ln(A_-/A_+) / \omega_{\text{eff}} \tau$, where ω_{eff} is the effective bandwidth.

Both the regularization parameter and the passband of the filter applied to the original waveforms affect

the resolving power of the restored IRFs. To choose the regularization parameter, we analyzed the spectra of the IRF obtained at $z = H$, i.e. the motion recorded at the top deconvolved with itself, considering different values for α . As expected, we observed that an increase of α reduces the bandwidth of the IRF and we found that $\alpha=10^{-3}$ is a good compromise between stability and resolution for the inverse problem analyzed in this study.

Finally, to evaluate the impact of the selected filter on the average velocity estimation for a single station. We compared the estimated velocities obtained for different low-pass corner frequencies, from 10 to 50 Hz. Considering $\alpha=10^{-3}$, the difference of the velocity estimates for low-pass frequencies larger than 20 Hz is about 5 m/s. In the remainder of the paper, we show the results obtained filtering the data over the band [0.1-20] Hz.

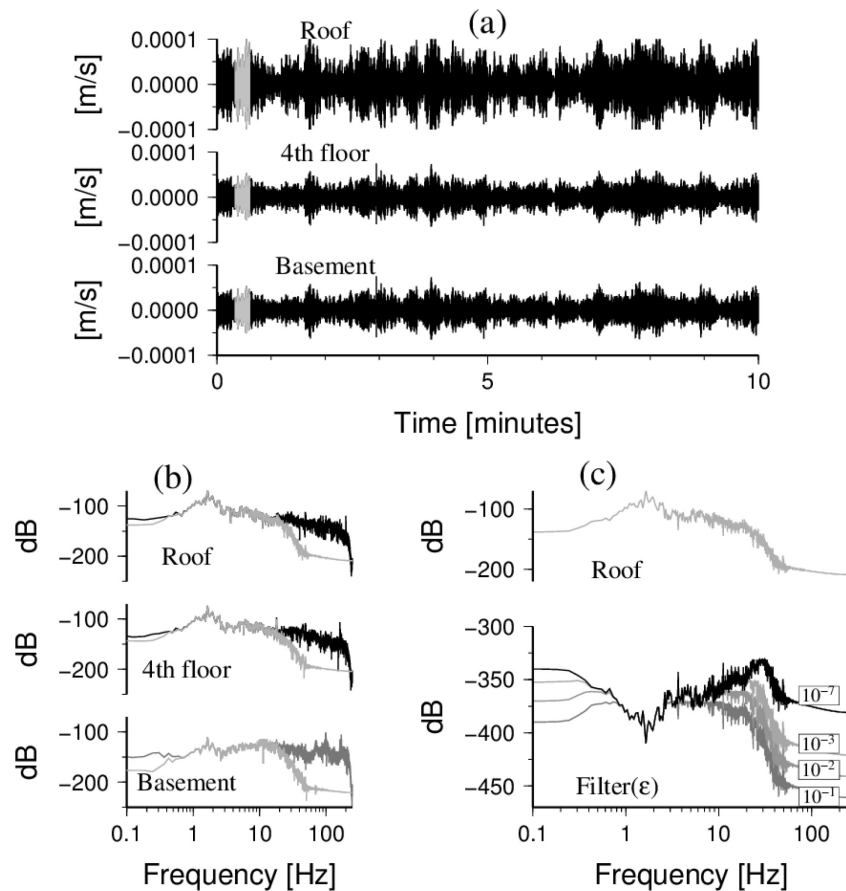


Figure 13. Sketch of the applied deconvolution scheme. (a): velocity recorded at three different locations inside the building; the signal in gray indicates a moving time window used to compute the Fourier spectrum. (b): Fourier amplitude spectra (black) computed for a given time window and filtered spectra (gray). (c): spectrum on roof and filter functions for different values of α (see equation (3)).

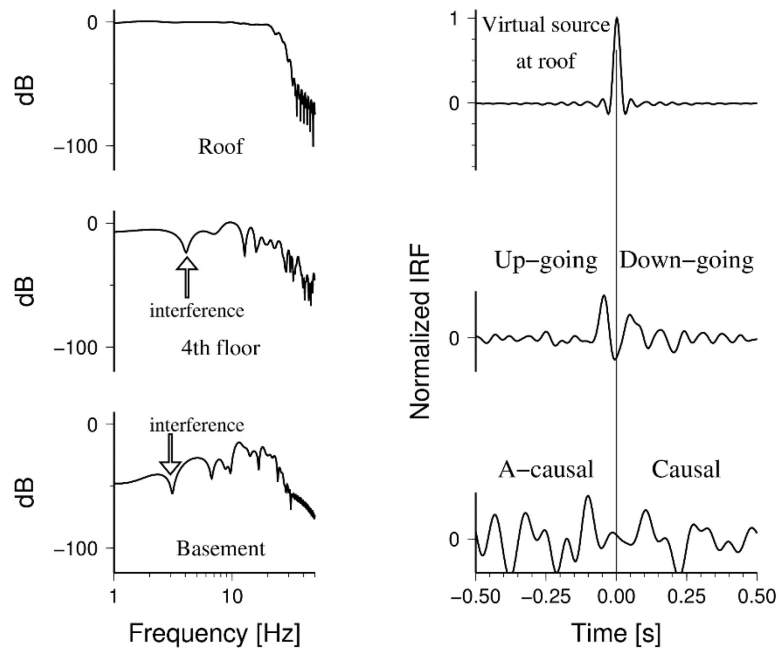


Figure 14. Example of deconvolution results (IRF), computed with respect to the motion on the roof for three different locations within the building. (left) IRFs in frequency domain; (right) IRFs in time domain.

5.2 Velocity and attenuation

Figure 15 shows the IRFs obtained for the three components of the motion of UNIT 2 using as reference the motion recorded at the roof (equation (4)). The compressional P-waves characterize the IRF along the vertical component. Although a larger frequency band of [0.1-50] Hz has been used for this component to better resolve the up-going and down-going pulses, the wavelength associated to the P-wave is still too long to measure reliable the time delay between the pulses. In the remainder of the paper, the results for the vertical component are not further discussed.

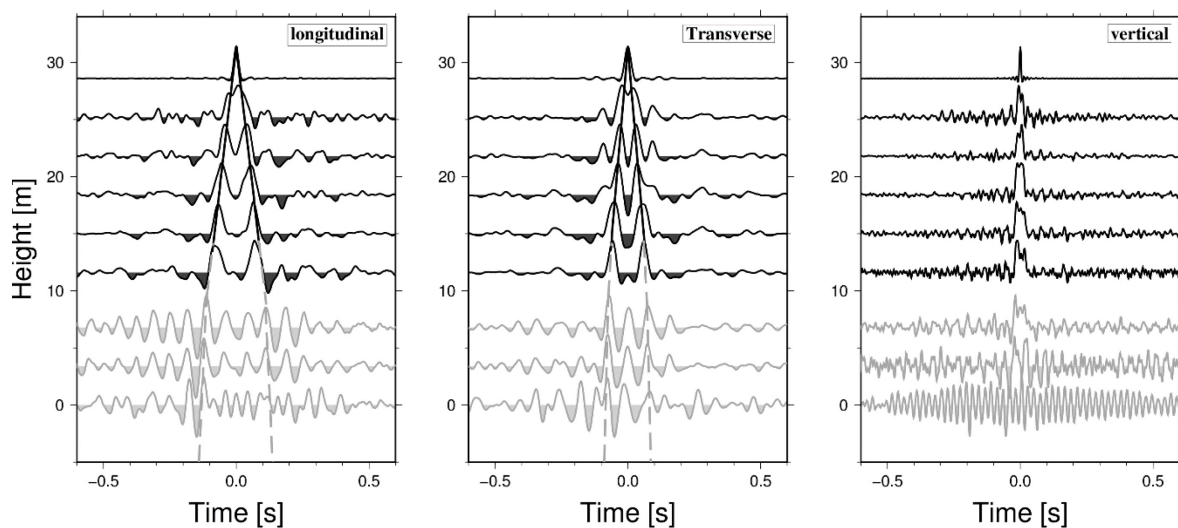


Figure 15. Deconvolution for UNIT 2 with respect to the motion on the roof, considering the three components. The black traces are characterized by the up-going and down-going waves, the gray traces show a more complex pattern. The black lines indicate the average velocities obtained by the interferometry. The dashed gray lines represent the velocities estimated by a comparison of empirical and theoretical IRFs.

The IRFs for the basement and for the first two floors (gray traces) show more complex patterns than the IRFs for the upper floors (black traces). The latter are mainly characterized by the up and down-going pulses. We ascribe the complex structure of the IRFs for the first three levels to the complex distribution of internal sources within these levels. In particular, the main hospital entrance is located at the second floor on the east side, while service entrances are located both at the basement and on the first floor. Due to structural changes, e.g. the increase of floor height on the second floor, internal reflection may also contribute to the complex structure of the IRFs, not only in the lower layers. Moreover, the first three levels are connected to adjacent buildings with structural joints in all four directions, with corridors connecting the different buildings. The short time of data acquisition (from one to few hours) does not mitigate the effect of these sources of noise and stacking over longer time periods are probably needed to enhance the IRFs.

The time lag between the propagation pulses at different floors is used to estimate the shear wave velocity. For each horizontal component, the estimates are performed separately for each of the four columns described in Figure 3, and the results are shown in Figure 16. Using a least squares fit either considering the columns separately or grouping all the results together, the slowness, which corresponds to the slope of the line, is determined. The values of the height are assumed to be error free and only an error for the lag time is assumed. Only the observation between the third and sixth floors are considered for performing the linear fit, since a significant interference between up-going and down-going waves can occur in the IRF for the seventh floor. The velocities are calculated as $v = 1/u$ and listed in Table 3. The given errors are standard deviations calculated from the standard deviations of the slownesses. The average velocities are estimated as $v_{\text{longitudinal}}=200$ m/s and $v_{\text{transverse}}=276$ m/s for the longitudinal and transverse direction, respectively. The velocities determined for the four columns separately, are similar to the average velocities. The building can be assumed as homogeneous in the horizontal directions.

The different average velocities for the transverse and longitudinal components are also visible in the IRFs in Figure 15. Although more uncertain due to the noisy IRFs, the delays estimated at the first three layers suggest higher shear velocities for both components in this part of the structure. The velocity for the first floors is estimated by matching the empirical IRFs and the theoretical ones, obtained considering a shear-beam model (e.g. Rahmani and Todorovska, 2013) and varying the model characteristics until the best fit is obtained. The code developed by Wang (1999) is considered for the determination of the vertical propagation of SH-waves in a layered medium. The soil profile described in Figure 1b is considered at the base of the building. The building is divided into three parts: one from the basement to the second floor, one from the second to the third floor and the third from the third floor to the roof. Since the third floor differs in height and structure from the other floors, it is considered as one layer. For the upper layer the velocities obtained by the least squares fit (Table 3) are used. The quality factor is fixed to $Q=60$ to reasonably reproduce the amplitudes of the IRFs, and density to $\rho=600$ kg/m³. It is worth noting that the simulation aims at estimating the shear wave velocities of the lowest layers by finding the best match between the arrival times of theoretical and empirical up-going and down-going pulses. An optimized modeling of the pulse shapes is beyond the scope of the present work. The obtained velocities for the three layers (Figure 17) are given in Table 4.

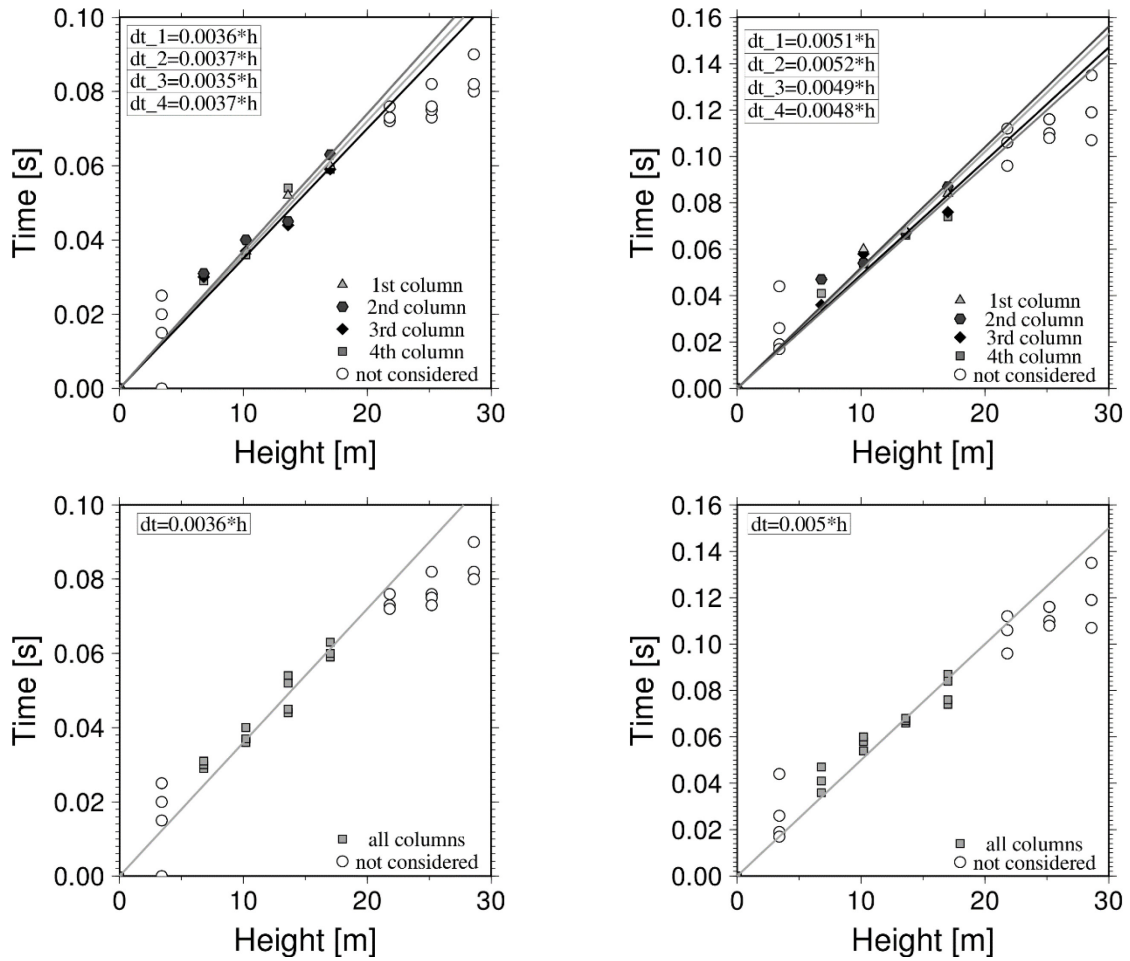


Figure 16. Travel times between the propagation pulses at different floors versus distance to the roof, considering the transverse (left) and longitudinal (right) components. In the uppermost panels, the slowness u is estimated using a least squares fit, considering the columns separately. Each line indicates the slowness of one column. In the lower panels, the slowness is determined grouping the results of all columns.

Table 3: Propagation shear wave velocities

	1st column	2nd column	3rd column	4th column	all columns
$v_{\text{transverse}}$ [m/s]	275 ± 7	271 ± 14	286 ± 14	271 ± 12	276 ± 6
$v_{\text{longitudinal}}$ [m/s]	195 ± 10	191 ± 11	205 ± 11	209 ± 13	200 ± 6

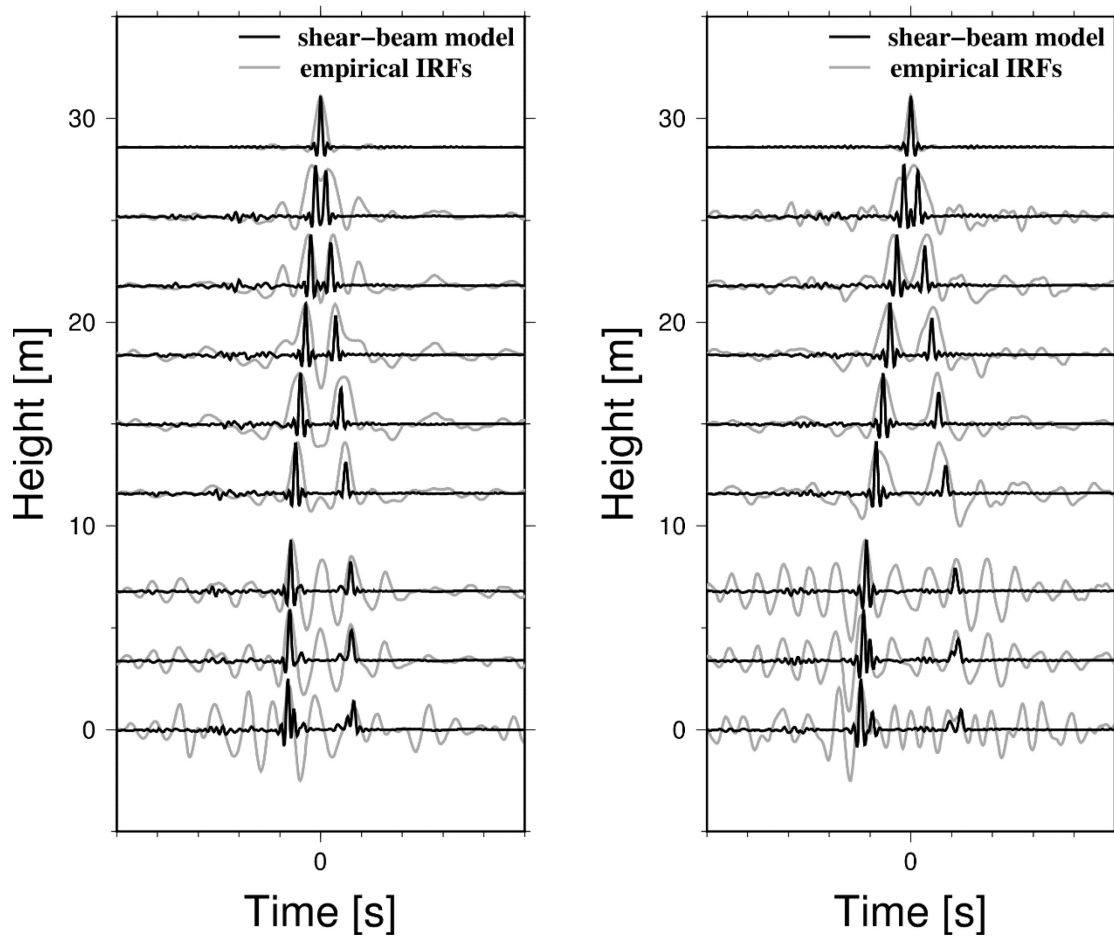


Figure 17. Comparison between empirical IRFs and those computed for the shear-beam model, considering the longitudinal (left) and the transverse (right) directions. For the uppermost floors (3rd floor-roof), the velocities estimated in Figure 16, and listed in Table 3, are used.

Table 4. Wave velocities obtained for the shear-beam model (see Figure 17).

	1st layer	2nd layer	3rd layer
$v_{\text{transverse}}$ [m/s]	1000	400	276
$v_{\text{longitudinal}}$ [m/s]	500	200	200

For all layers and hence, the whole building, the propagation velocity is higher in the longitudinal than in the transverse direction. The velocity decreases with the height of the building, since the stiffness decreases as well. The velocity changes between the second and the third floor for both components which can be explained by the changes in construction. Furthermore, the velocity decreases for the transverse direction between the 2nd and the 3rd layer, no change in velocity is observed for the longitudinal direction.

The seismic waves attenuate during the propagation inside the building due to intrinsic attenuation, scattering and radiation losses. We analyze the IRFs obtained through the deconvolution interferometry for evaluating the intrinsic attenuation, which quantifies the anelastic dissipation of the building's

motion and breaks the symmetry of the IRF for time reversal (e.g. Newton and Snieder, 2012).

Following Parolai et al. (2010), the transfer function between a generic floor inside AHEPA and the roof (see equation 4) is fit in the Fourier domain with the theoretical model (e.g. Şafak, 1997):

$$|T(z, \omega)| = \frac{\sqrt{1 + e^{\frac{4\pi f\tau}{Q_S}} + 2e^{\frac{2\pi f\tau}{Q_S}} \cos(4\pi f\tau)}}{2e^{\frac{\pi f\tau}{Q_S}}} \quad (7)$$

where the quality factor Q_S is related to the damping coefficient $\zeta = 1/2Q$. A grid search procedure is applied over the quality factor Q_S and the travel time τ , in order to minimize the root mean square error between the logarithm of the empirical and theoretical spectra. The model in equation (7) reproduces the trough in the spectrum generated by the negative interference (e.g., see Figure 13). The positions of the troughs are controlled by the travel time while the intrinsic attenuation controls the amplitude of the troughs and their attenuation with frequency. As already discussed in Parolai et al. (2010), the role played by Q_S in the cost function decreases with increasing Q_S . Therefore, by fitting the model of equation (7) to the empirical spectra, we obtain a reliable estimate for the minimum quality factor which allows us to reproduce the main spectral features.

Considering the complex patterns characterizing the transfer functions for the three lowest floors, model (7) is applied considering the motion recorded at the fourth floor for the transverse component and at the fifth floor for the longitudinal one. In the grid search, τ is allowed to assume values in the range $\pm 10\%$ with respect to the empirical values measured from the IRF, while the range of variability for Q_S is fixed to 1-100. It is worth noting that the quality factor is considered frequency independent and is not associated to a specific mode but describing the overall attenuation of the system over the frequency range used for the spectral fit (i.e. 1-15 Hz). The results are shown in Figure 18. The quality factors for the best fit models are $Q=54$ and $Q=25$ for the longitudinal and transverse components, respectively. The grid search results for different Q and τ values are shown in panel c. The position of the minimum misfit is marked by a white cross. The cross sections (panels d and e) confirm that the cost function has a steep gradient toward lower Q values and an almost flat variability toward higher Q . A visual inspection of the fit result (panel a and b) confirms that the fit is satisfactory for both the longitudinal and transverse directions.

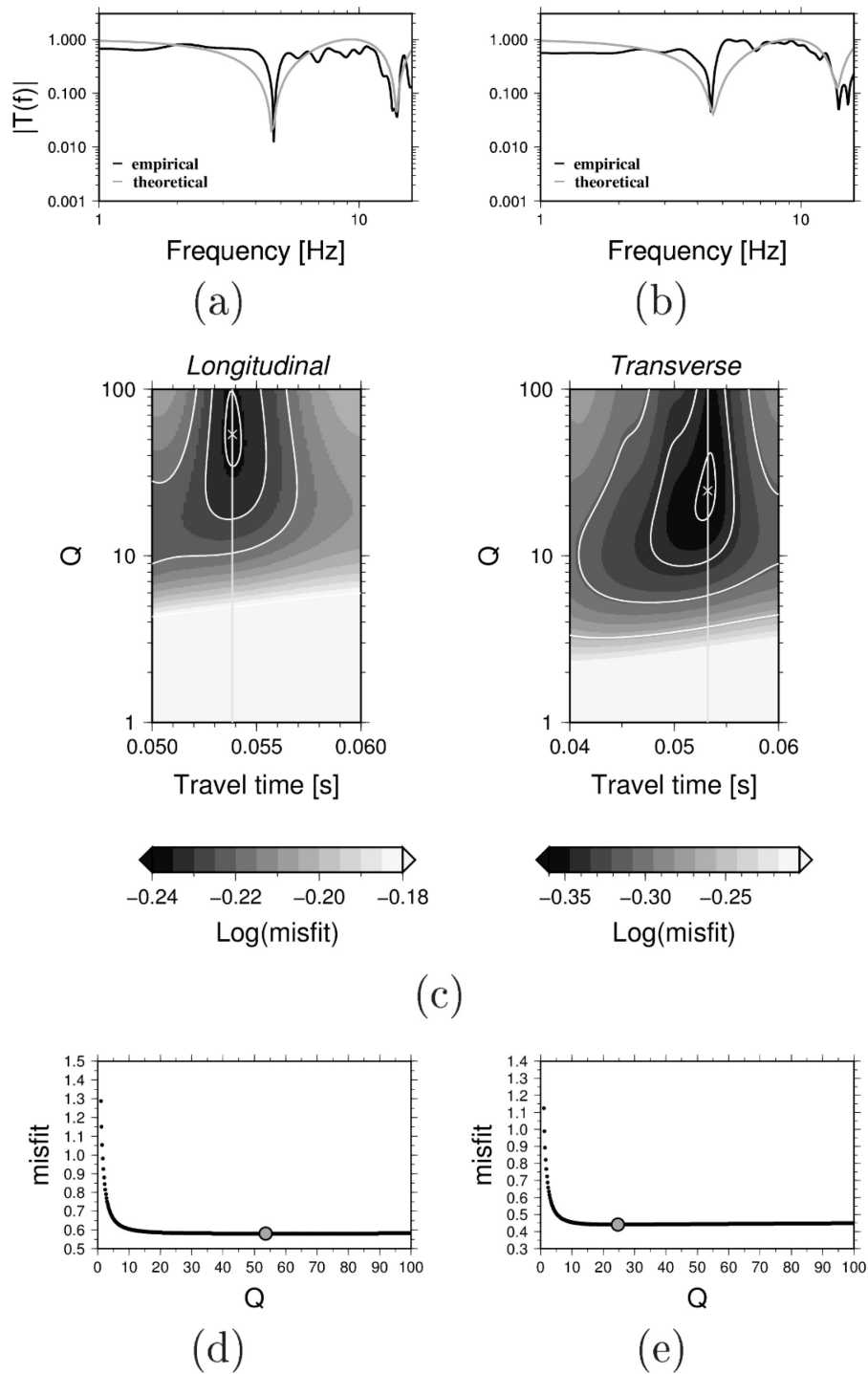


Figure 18. Results for Q estimation using ambient vibration for the longitudinal (left) and transverse (right) directions. (a) Comparison between the empirical (black) and the best fit model IRF spectra (gray); (b) grid search results for different travel time- Q values. The minimum misfit is indicated by a white cross. (c) Cross section along the Q values for the travel time of the minimum misfit function (white line in b). The minimum of Q is indicated by a gray point.

6 Discussion and Conclusions

In the present paper, the dynamic response of an eight-story RC building, belonging to the AHEPA general hospital complex in Thessaloniki (Greece), has been investigated and evaluated using ambient noise measurements. The special feature of the building is that it is composed of two adjacent tall building units that are connected with a structural joint. It was selected within the framework of European funded REAKT project as representative of high-rise infilled moment resisting frame buildings in Europe designed with low seismic code level; the aim is to implement a real-time permanent monitoring system to evaluate its risk for various earthquake scenarios and generate real-time risk estimates. Ambient vibration measurements were used for system identification and operational modal analysis to extract the natural frequencies and mode shapes for the two adjacent buildings first separately, and then for the entire building analyzed as one single structure taking into account the interaction of the two building units. The estimated modal parameters for five clearly identified modes were similar for the applied non-parametric identification methods (Peak Picking and Frequency Domain Decomposition methods) as well as for the different system models analyzed, implying that it is possible to capture the dynamic characteristics of the hospital building by monitoring and analyzing the two adjacent buildings separately. The identified modal characteristics indicate that the first two modes, corresponding to $f_1=1.65$ Hz and $f_2=1.91$ Hz respectively, are mainly translational along the transverse direction, although a significant coupling exists. The first two mode shapes are similar; however the contribution of the torsional motion is higher in the second mode. For the third ($f_3=2.35$ Hz), fourth ($f_4=3.58$ Hz) and fifth ($f_5=5.2$ Hz) frequencies, mode shapes are clearer and correspond to a torsional and two translational modes in the longitudinal direction, respectively. The modal characteristics will be used in a future stage of the research to calibrate the numerical model of the building and derive fragility curves that reflect the actual state and behavior of the building subjected to seismic loading.

The ambient vibration recordings were also used to perform interferometric analyses to investigate the shear wave propagation in the building and the intrinsic attenuation. The average velocities along the longitudinal and transverse directions are about (200 ± 6) m/s and (276 ± 6) m/s, respectively, while the quality factors estimated for the two components are 54 and 25, respectively. The availability of a couple of earthquakes recorded inside the building allows to compare the interferometric results from ambient vibration and earthquakes, as shown in Figures 19 and 20. The time lags between the a-causal and causal pulses observed at first and fourth floors are in good agreement with the ambient vibration results. Differently from the ambient vibration case, the deconvolution with earthquake data provides a reliable IRF also at the basement. The quality factor estimated for the analyzed earthquake is 40 and 28 along the longitudinal and transverse component (Figure 20), in good agreement with the noise results.

The distribution of the shear wave velocity estimated from interferometric analysis using both ambient noise and earthquake recordings indicates that the structure is stiffer at the base and along the transverse direction. The increased stiffness at the base building is expected due to the fact that the basement is partially embedded (in one side only, see Figure 1) and because the dimensions of the reinforced concrete elements (columns) are progressively decreasing along its height. However, the higher stiffness in the transverse (shorter) direction is not matching with the results of operational modal analysis. According to the modal analysis, the fundamental mode shape, although highly coupled, corresponds to a mode that is mainly translational along the transverse direction implying that in this direction the building is expected to be more flexible. Considering the complex vibration characteristics of the

building the differences may be due to a number of reasons, which undergo further investigation in order to reach conclusions. For example, considering the complex vibrational characteristics of the building, further investigations are needed to conciliate the waveform and vibrational outcomes. In order to further validate the results of system identification and operational modal analysis, a comparative study between non-parametric and parametric identification techniques is needed, including also estimation of damping ratios. Further analysis is also required taking into account the vertical component to interpret its high amplitude and investigate potential effects of rocking on the building. Since deconvolution interferometry with earthquake data provides building responses independent from soil-structure coupling, the data set of earthquakes recorded by the permanent network installed in the building can be exploited in future studies to evaluate the importance of the soil-structure interaction.

In order to enhance the reliability and robustness of the results, and to come up with final conclusions regarding the dynamic characteristics of the complex building, further investigation studies are currently underway using both ambient noise and earthquake recordings. The modal identification results will be used in the framework of REAKT to update and better constrain the initial finite element models of the hospital building units aiming to the vulnerability assessment of the building considering its actual state, taking into account potential structural degradation due to time (it is already 40 years old), possible structural damages, changes in geometry and mass distribution. It is concluded that ambient vibration measurement in combination with interferometry analysis of the wave propagation from the same ambient noise recording within the building skeleton can be used to yield more reliable models with respect to their real condition on the basis of real-time risk assessment and pre- or/and post-event fragility updating.

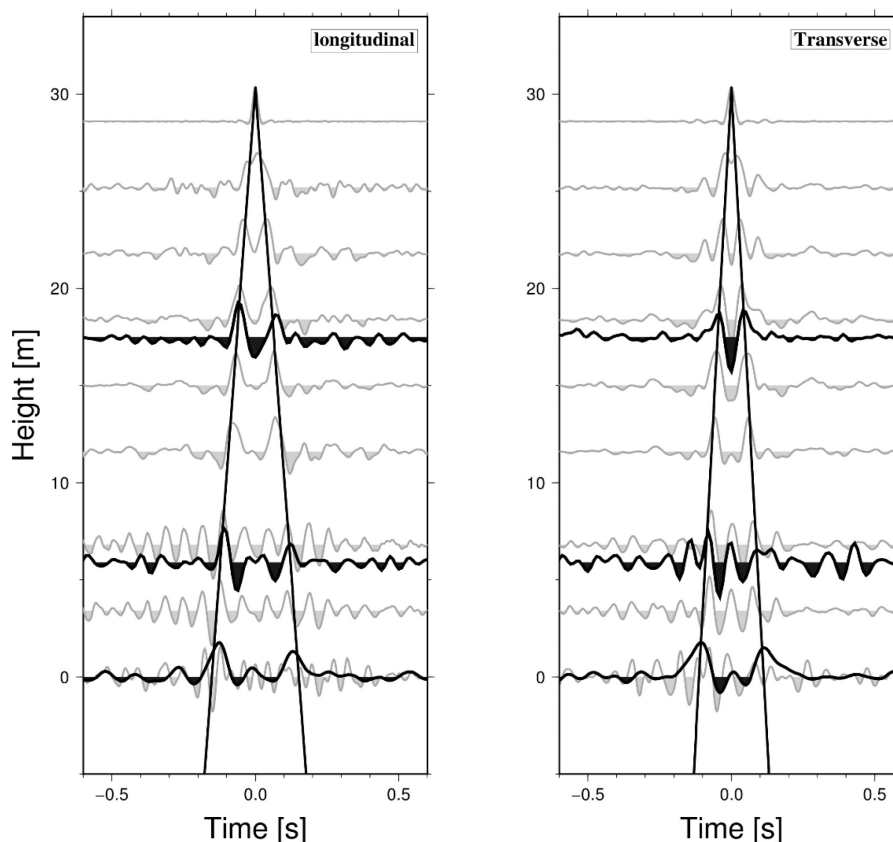


Figure 19. IRFs for noise (gray) and earthquakes (black) for the longitudinal (left) and the transverse component (right). Recordings of two different earthquakes (Volvi earthquake of 11 October 2013; Mw 4.2; distance 38 km and Cephalonia earthquake of 26 January 2014; Mw 6.1; distance 350 km) are used.

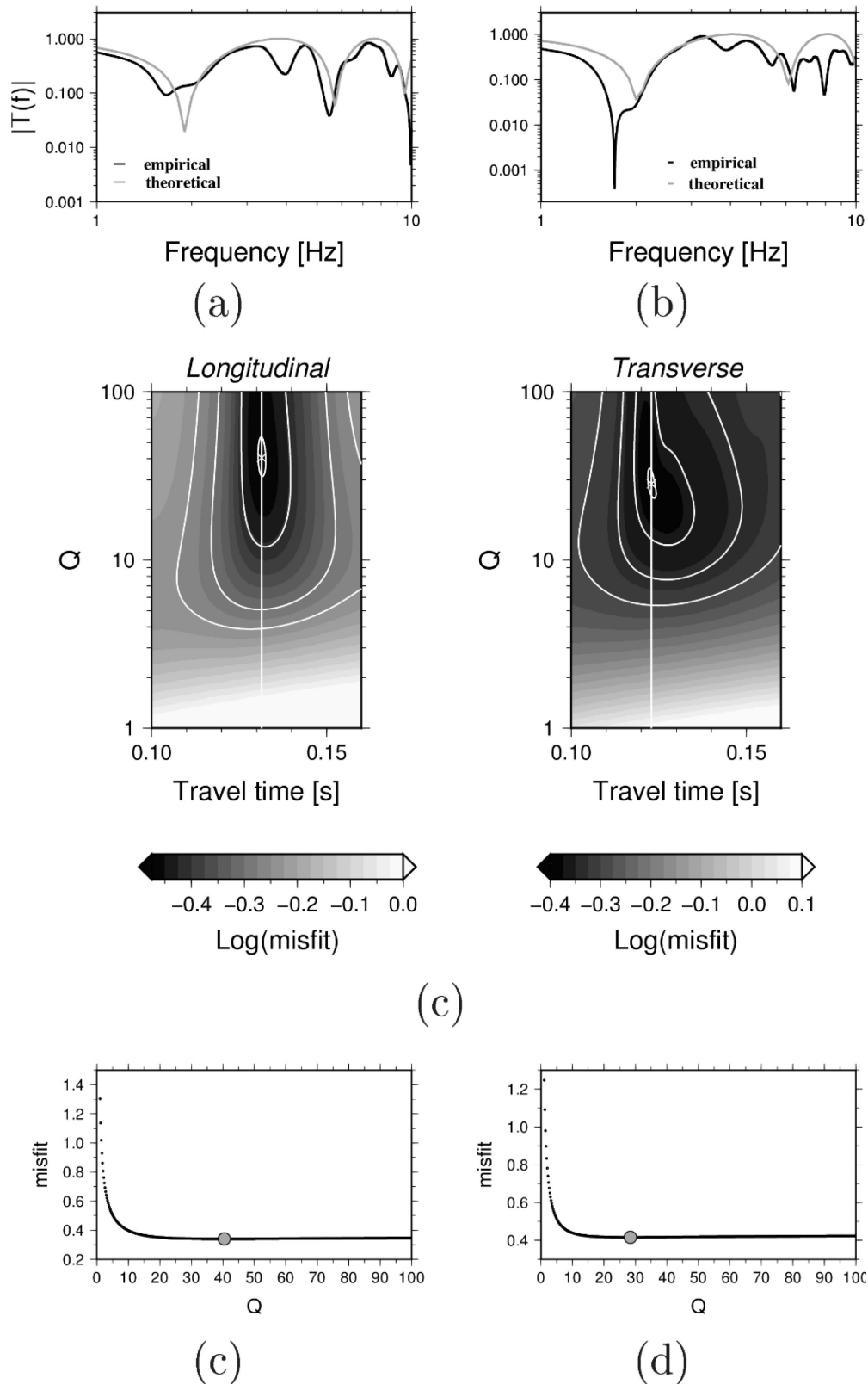


Figure 20. Results for Q estimation for the longitudinal (left) and transverse (right) directions, using a recording of the Cephalonia earthquake. (a) Comparison between the empirical (black) and the best fit model IRF spectra (gray); (b) grid search results for different travel time- Q values. The minimum misfit is indicated by a white cross. (c) Cross section along the Q values for the travel time of the minimum misfit function (white line in b). The minimum of Q is indicated by a gray point.

Acknowledgements

The ambient vibration survey in AHEPA was performed using the seismic instruments provided by the Geophysical Instrument Pool Potsdam (GIPP) and supported by the REAKT (Strategies and tools for Real Time EArthquake RiSk ReducTion) project. The staff of AHEPA hospital is acknowledged for their kind support during the experiment.

References

- Aki K (1957). Space and time spectra of stationary stochastic waves with special reference to microtremors. *Bulletin Earthquake Research Institute*; 35: 415-457.
- Assimaki D, Li W, Steidl JH, Tsuda K. (2008) Site amplification and attenuation via downhole array seismogram inversion: a comparative study of the 2003 Miyagi-Oki aftershock sequence. *Bulletin of the Seismological Society of America*; 98: 301330.
- Bendat JS, Piersol AG. (1993) Engineering Applications of Correlation and Spectral Analysis. *John Wiley & Sons*
- Bertero M, Boccacci P. (1998) Introduction to Inverse Problems in Imaging. *IOP Publishing Bristol*.
- Bindi D, Parolai S, Picozzi M, Ansal A. (2010) Seismic input motion determined from a surface-downhole pair of sensors: a constrained deconvolution approach. *Bulletin of the Seismological Society of America*; 100: 13751380.
- Brincker R, Zhang L, Andersen P. (2001) Modal identification of output only systems using frequency domain decomposition. *Smart Materials and Structures*; 10:441445.
- Brownjohn JMW (2003). Ambient vibration studies for system identification of tall buildings. *Earthquake Engineering Structural Dynamics*; 32: 71-95.
- Carder DS. (1936) Observed vibration of buildings. *Bulletin of the Seismological Society of America*; 26: 24577.
- Chopra AK. (1996) Modal analysis of linear dynamic systems: physical interpretation, *Journal of Structural Engineering*; 122: 517-527.
- Clearbout JF. (1968) Synthesis of a layered medium from its acoustic transmission response. *Geophysics*; 33: 264-269.
- Davison C. (1924) Fusakichi Omori and his work on earthquakes. *Bulletin of the Seismological Society of America*; 14:240255.
- Guéguen P, Michel C, Le Corre L. (2007) A Simplified Approach for Vulnerability Assessment in Moderate-to-low seismic hazard Regions: Application to Grenoble (France). *Bulletin of Earthquake Engineering*; 5:467490.
- Holcomb LG. (1989) A direct method for calculating instrument noise levels in side-by-side seismometer evaluations. *U.S. Geological Survey Open File Report*: 89-214
- Housner GW, Brady AG. (1963) Natural periods of vibration of buildings. *Journal of the Engineering Mechanics Division*; 89:3165.
- Ivanović SS, Trifunac MD, Todorovska MI. (2000) Ambient vibration tests of structures. A review. *Journal of Earthquake Technology*; 37: 165197.
- Iwan WD. (1997) Drift spectrum: measure of demand for earthquake ground motions. *Journal Structural Engineering*; 123: 367404.

- Jaishi B, Ren WX. (2005) Structural finite element model updating using ambient vibration test results. *Journal of Structural Engineering*; 131: 617-628
- Kanai K. (1965) Some new problems of seismic vibrations of a structure. *Proceedings of the 3rd World Conference on Earthquake Engineering*, Auckland and Wellington, New Zealand.
- Kohler MD, Heaton TH, Bradford SC. (2007) Propagating waves in the steel, moment-frame Factor building recorded during earth- quakes. *Bulletin of the Seismological Society of America*; 97: 13341345.
- Ljung L. (1999) System identification: Theory for the User. *Prentice Hall, Upper Saddle River, 2nd Edition*
- Lobkis OI, Weaver RL. (2001) On the emergence of the Greens function in the correlations of a diffuse field. *Journal of the Acoustical Society of America*; 110: 30113017.
- Marzorati S, Bindi D. (2006) Ambient noise levels in north central Italy. *Geochemistry Geophysics Geosystems*; 7: Q09010, doi 10.1029/2006GC001256.
- McNamara DE, Buland RP. (2004) Ambient noise levels in the continental United States. *Bulletin of the Seismological Society of America*; 94: 15171527.
- Mehta K, Snieder R, Grazier V. (2007) Downhole receiver function: a case study. *Bulletin of the Seismological Society of America*; 97: 13961403.
- Michel C, Guéguen P, Bard PY. (2008) Dynamic Parameters of Structures extracted from Ambient Vibration Measurements: An Aid for the Seismic Vulnerability Assessment of Existing Buildings in Moderate Seismic Hazard Regions. *Soil Dynamics and Earthquake Engineering*; 28:593604.
- Michel C, Gueguen P, Causse M. (2012) Seismic Vulnerability Assessment to Slight Damage based on Experimental Modal Parameters. *Earthquake Engineering and Structural Dynamics*; 41: 81-98.
- Nakata N, Snieder R, Kuroda S, Ito S, Aizawa T, Kunimi T. (2013) Monitoring a building using deconvolution interferometry, I: Earthquake-data analysis. *Bulletin of the Seismological Society of America*; 103:1662 1678
- Nakata N, Snieder R. (2014) Monitoring a building using deconvolution interferometry, II: Ambient vibration analysis. *Bulletin of the Seismological Society of America*; 104: 204-213.
- Newton C, Snieder R. (2012) Estimating intrinsic attenuation of a building using deconvolution interferometry and time reversal. *Bulletin of the Seismological Society of America*; 5; 2200-2208.
- Parloo E. (2003) Application of Frequency Domain System Identification Techniques in the Field of Operational Modal Analysis. *PhD Dissertation, VRIJE Universiteit, Brussel*
- Parolai S, Bindi D, Ansal A, Kurtulus A, Strollo A, Zschau J. (2010) Determination of shallow S-wave attenuation by down-hole waveform deconvolution: a case study in Istanbul (Turkey), *Geophysical Journal International*; 181: 1147-1158
- Peeters B, De Roeck G. (1999) Reference-based stochastic subspace identification for output-only modal analysis. *Mechanical Systems and Signal Processing*; 13: 855-878.
- Peeters B. (2000) System Identification and Damage Detection in Civil Engineering. *PhD thesis, Department of Civil Engineering, K.U.Leuven*

- Peterson J. (1993) Observations and modeling of background seismic noise, *U.S. Geological Survey Open File Report*: 93-322.
- Picozzi M, Parolai S, Mucciarelli M, Milkereit C, Bindi D, Ditommaso R, Vona M, Gallipoli MR, Zschau J. (2011) Interferometric Analysis of Strong Ground Motion for Structural Health Monitoring: The Example of the L'Aquila, Italy, Seismic Sequence of 2009. *Bulletin of the Seismological Society of America*; 101: 635651.
- Pitilakis KD, Karapetrou ST, Fotopoulou SD. (2014) Consideration of Aging and SSI effects on Seismic Vulnerability Assessment of RC Buildings. *Bulletin of Earthquake Engineering*; (article in press)
- Prieto GA, Lawrence JF, Chung AI, Kohler MD. (2010) Impulse response of civil structures from ambient noise analysis, *Bulletin of the Seismological Society of America*; 100; 23222328.
- Rahmani MT, Todorovska MI. (2013) 1D system identification of buildings from earthquake response by seismic interferometry with waveform inversion of impulse responses - method and application to Millikan Library. *Soil Dynamics and Earthquake Engineering*; 47: 157-174.
- Raptakis DG, Anastasiadis AJ, Pitilakis KD, Lontzetidis K. (1994) Shear wave velocities and damping of Greek natural soils, *Proceeding of the 10th Conference on Earthquake Engineering*; 1: 477-482.
- Reynders E, Schevenels M, De Roeck G. (2011) MACEC 3.2: A Matlab toolbox for experimental and operational modal analysis-User's manual. *Katholieke Universiteit, Leuven*
- Reynders E. (2012) System Identification Methods for (Operational) Modal Analysis: Review and Comparison. *Archives of Computational Methods in Engineering*; 19; 51-124
- Şafak E. (1997) Models and methods to characterize site amplification from a pair of records. *Earthquake Spectra*, EERI; 13: 97-129.
- Snieder R, Şafak E. (2006) Extracting the building response using interferometry: theory and applications to the Millikan Library in Pasadena, California. *Bulletin of the Seismological Society of America*; 96: 586598.
- Strollo A, Parolai S, Jäkel K.H., Marzorati S, Bindi D. (2008) Suitability of short-period sensors for retrieving reliable H/V peaks for frequencies less than 1 Hz. *Bulletin of the Seismological Society of America*; 98: 671681
- Teughels A. (2003) Inverse modeling of civil engineering structures based on operational modal data. *PhD thesis, Katholieke Universiteit of Leuven*.
- Todorovska MI. (2009) Soil-structure system identification of Millikan library northsouth response during four earthquakes (1970-2002): what caused the wandering of the observed system frequencies. *Bulletin of the Seismological Society of America*; 99: 626635
- Todorovska MI, Trifunac MD. (1990) A note on the propagation of earthquake waves in buildings with soft first floor. *Journal of Engineering Mechanics*; 116:892-900
- Trampert J, Cara M, Frogneux M. (1993) SH propagator matrix and Qs estimates from borehole- and surface-recorded earthquake data. *Geophysical Journal International*; 112: 290299.
- Trifunac MD. (1972) Comparisons between Ambient and Forced Vibration Experiments. *Earthquake Engineering and Structural Dynamics*; 1: 133-150.

Van Overschee P, De Moor B. (1996) Subspace Identification for Linear Systems: Theory-Implementation-Applications. *K.U.Leuven Academic Publishers*

Ventura C, Liam Finn W-D, Lord JF, Fujita N. (2003) Dynamic characteristics of a base isolated building from ambient vibration measurement and low level earthquake shaking. *Soil Dynamics Earthquake Engineering*; 23:31322.

Wapenaar K. (2004) Retrieving the elastodynamic Greens function of an arbitrary inhomogeneous medium by cross correlation. *Physical Review Letters*; 93; 254301

Wang R., (1999). A simple orthonormalization method for stable and efficient computation of Greens functions. *Bulletin of the Seismological Society of America*; 89: 733741.

Wiggins RW, Clayton RA. (1976) Source shape estimation and deconvolution of teleseismic bodywaves. *Geophysical Journal of the Royal Astronomical Society*; 47: 151-177

Appendix b): A real data and numerical simulations-based approach for estimating the dynamic characteristics of a tunnel formwork building: preliminary results

The final publication is available at Springer via <https://dx.doi.org/10.1007/s10518-017-0250-3>

Petrovic, B., Dikmen, S. U., Parolai, S. (2017a). A real data and numerical simulations-based approach for estimating the dynamic characteristics of a tunnel formwork building: preliminary results, *Bulletin of Earthquake Engineering*.

Abstract

Due to their expected high seismic resistance, a significant number of tunnel formwork buildings have been built over the past few decades, especially in regions of high seismic hazard. However, only few real data analyses have been reported and available so far. Different techniques, including real data analysis, numerical simulations, and their combination, are employed to investigate and compare their potentials for estimating different aspects of a tunnel formwork building. This study is based on data from a 16-story residential building in Istanbul, Turkey. The real data analysis of the building's dynamic characteristics is based on both the vibrational (spectral analysis) and waveform (deconvolution interferometry) approaches, which yield information on the soil-structure system and the fixed-base building. For this purpose, dense ambient vibration/generated source measurements and earthquake recordings of both temporary and permanent networks are used. Furthermore, Finite Element Analysis (FEA) of the building is carried out. The order of the first bending and torsional modes is reversed in the results of the numerical simulations compared to those from the real data. This can be attributed to the simplifications and assumptions made in the numerical simulations of tunnel formwork structures. It emphasizes the importance of analyzing real data for better constraining numerical simulations. Finally, the response of the building (synthetic seismograms) to a real data input is calculated using FEA. Deconvolved wave fields of synthetic and the real data are estimated. Despite the changed order of the modes, the deconvolved wave fields for both cases match very well.

1 Introduction

The excitation that a structure may experience during an earthquake is affected by the earthquake source, seismic wave travel path effects, local site effects, soil-structure interaction and the building's dynamic behavior. The investigation of all of these parameters is thus an important issue, with the focus of this study being the analysis of buildings' dynamic behavior.

The tunnel formwork technology is a construction technique which involves the casting of walls and slabs in a single cycle operation. Hence, tunnel formwork buildings are shear wall dominant structures. The technology has been in use in the building construction for over 50 years. Currently, the tunnel formwork technology is used not only in Turkey (since the late 1970s, over 1 million buildings have been built), but also in other parts of the world, such as Russia, North Africa, the Caucasus, Europe and the Middle East. Due to the monolithic form of the walls and the slabs, the buildings have a high seismic resistance. Their seismic performances have been observed during 3 major earthquakes in Turkey (M_w 7.4 Kocaeli, 1999; M_w 7.2 Duzce, 1999 and M_w 6.4 Bingöl, 2003). Neither collapsed nor damaged buildings of this construction type have been reported, only some minor non-structural damage has been observed (Yakut and Gulkan 2003). For this reason, this construction type is especially preferred in regions prone to high seismic hazard, and in social housing projects. Moreover, due to the achievable speed of construction, typically one story per day, or two, tunnel formwork buildings are widely used for rebuilding earthquake-devastated cities. However, although tunnel formwork is used extensively, almost no analysis using real data sets has been carried out until now and hence, the comprehension of the building's dynamic behavior is based on analytical studies.

Consequently, current seismic codes comprise relatively limited provisions and guidelines specific for their seismic design. This may be partly due to the limited number of studies made until now on this type of building using in-situ collected data. Different studies have been performed which aim at the derivation of new formulas for the estimation of their fundamental periods. Lee et al. (2000), for example, determined the fundamental periods of 50 different buildings with shear wall dominant systems in South Korea, both experimentally and analytically. They concluded that the periods calculated by the formulae specified by the 1988 Korean Building Code (KBC), the 1997 Uniform Building Code (UBC) and the 1995 Canadian Building Code failed to determine the fundamental period of these type of structures. However, their study was limited to the translational modes and did not cover the torsional modes. Furthermore, the soil conditions, as well as the foundation types, were not reported. Balkaya and Kalkan (2003) and later Balkaya et al. (2012) undertook analytical studies in an effort to determine an empirical equation for the estimation of the fundamental periods of these types of structures. They concluded that in most cases, the fundamental mode is the first torsional mode. Nevertheless, information on the reliability of results retrieved from analytical studies can be only obtained if results from real data sets and numerical simulations are compared.

Structural vibration monitoring offers the opportunity to better understand the dynamic behavior of built structures under seismic loading (e.g., Snieder and Safak 2006; Trifunac et al. 2008; Picozzi et al. 2009a; Celebi et al. 2016) and to monitor the evolution of damage (e.g., Poudel et al. 2007; Todorovska and Trifunac 2008a, b, c; Ditommaso et al. 2015). Consequently, vibration monitoring makes it possible to improve the performance and reliability of such structures. In this respect, both ambient seismic noise and active source vibration measurements enable the estimation of the dynamic characteristics of

structures (e.g., Ivanovic et al. 2000; Michel et al. 2008; Prieto et al. 2010; Nakata and Snieder 2014; Bindi et al. 2015). Short-time (from minutes up to hours) non-destructive vibration measurements of weak seismic signals provide the possibility to analyze and understand the seismic behavior of a large number of buildings with different structural typologies by installing dense instrument networks. Applying different techniques, including the vibrational (Chopra 1996) and wave approaches (Kanai 1965) to real data sets, makes it possible to obtain information about both the global (i.e., mode shapes and corresponding frequencies) and local dynamic properties of the building (i.e., wave propagation through the building), as well as about the soil-structure system and the fixed-base building (e.g., Trifunac et al 2008; Rahmani and Todorovska 2013). These techniques have been applied to investigate the dynamic characteristics of various buildings in the past (e.g., Clough and Penzien 1993; Snieder and Safak 2006; Picozzi et al. 2009a; Todorovska 2009; Bendat and Piersol 2010; Petrovic et al. 2015; Pitilakis et al. 2016).

The aim of this study is to investigate the dynamic behavior of a 16-story residential tunnel formwork building using different techniques, based on both real data analysis and numerical simulations, and their combination. The real data set composed of both earthquake recordings and ambient vibration/generated source measurements. The analysis of the building's dynamic characteristics based on the real data set is composed of both the vibrational (Fourier Amplitude Spectra, FAS) and the waveform (deconvolution interferometry) approaches. On the one hand, information on the fundamental frequencies and the mode shapes of the building soil-system (global properties) are obtained. On the other hand, studying the wave propagation in buildings by the wave approach gives insights into the local characteristics of the building. Moreover, from the wave propagation velocity through the building, information on the fixed-base frequencies is obtained (e.g., Trifunac et al. 2008). In addition to in-situ measurements, Finite Element Analysis (FEA) is performed. This makes it possible to carry out a comparison of the results obtained by real data analysis under weak loading and numerical simulations, and hence, to give an estimation of the reliability of the results obtained from the finite element analysis. Moreover, the response of the building (synthetic accelerograms) to real input (earthquake recording at the ground level) is calculated based on the model. Afterwards, the deconvolution approach is applied also to the synthetic seismograms in order to study the wave propagation. A comparison of the deconvolved wave field of real and synthetic data gives further information about the precision of the FEA produced results of the building.

2 Test site and description of the building

The investigated tunnel formwork building, so-called "B22", was constructed in the late 1980's as part of a major housing development (Fig. 1a). It is typical for the Ataköy district, where multiple buildings with the same design or with some slight variations have been built as part of the same development project. As a matter of fact, buildings with very similar design have been built at numerous places in Turkey. The B22 building is located on geologically soft sediments, in the western side of Istanbul. Picozzi et al. (2009b) performed a site characterization study using seismic noise and estimated the fundamental resonance frequency of the soil in the Ataköy area to lie between 0.5 and 1.0 Hz. Dikmen et al (2015), on a study using the recordings of the May 24, 2014 Northern Aegean Earthquake made at Ataköy, have demonstrated that the resonance frequency near the B22 site is around 1.0 Hz. This is

typically in the same range as the fundamental frequencies of 10-15 story buildings, similar to the analyzed one.



Figure 1. **a)** The B22 building and permanent SOSEWIN installation (green symbols) from the south (left) and west (right) directions. **b)** Experimental set up showing the thumper truck and the B22 building. **c)** Building floor plan with locations of the temporary sensors installation (4.5 Hz Geophone connected to CUBE digitizer) for each floor (blue triangles) and additional sensor's location on the roof (orange triangles). Moreover, the locations of the permanent SOSEWIN installations are shown (green triangles). **d)** Exemplary installation of a 4.5 Hz Geophone connected to a CUBE digitizer.

The building, including the basement, has a total height of 46.65 m (with a standard floor height of 2.81 m, except for 4.0 m at the basement) above the foundation to the roof, excluding the elevator machine room at the top. The building sits on a raft foundation approximately 1.20m thick with an approximately square footprint (23.10 m x 23.90 m, Fig. 1c). At each floor of the building four apartments of the same

size and floor plan are located, two at each side of the corridor that runs in the east-west direction (y-direction, Fig. 1c). Hence, the building is symmetrical in both x and y directions. The building is equipped with two elevators (one at each side of the corridor) and an interior reinforced concrete staircase. There also exists an exterior steel construction fire escape staircase. The interior concrete walls casted as part of the structure are 20 cm thick, except for the elevator shaft walls that are 15 cm thick. The floor slabs are 16 cm thick. Concrete precast panels are used to form the exterior walls (façade wall), filling the openings where the tunnel formwork was pulled out. These precast panels are hung on the sides of their neighboring walls, with the hangers forming a simple support.

3 Experimental set-ups and data set

Earthquake recordings from a permanent Self-organizing Seismic Early Warning Information Network (SOSEWIN; Fleming et al. 2009) installation, as well as dense ambient vibration/generated source measurements from a temporary dense network installed during a thumper truck experiment are used in the study.

3.1 The permanent installation – SOSEWIN

The building was initially instrumented with three SOSEWIN units installed at the basement, the 8th floor and the roof since summer 2013. The stations at the basement and on the roof were connected to a Güralp 5TC strong motion accelerometer. In September 2015, the B22 was equipped with additional SOSEWIN units, resulting in a network of 15 stations on seven floors⁶. In this case, four of the units are connected to a Güralp 5TC strong motion accelerometer (the SOSEWINs acting only as the digitizer in these cases), while the others are equipped with Micro-Electro Mechanical System (MEMS) sensors. The units are installed at two locations within the building, namely the building's center and the fire escape exit (Fig. 1c, green triangles). The sampling rate is set to 100 samples per second.

Five events with magnitudes ranging from M_w 3.7 to 4.8 with epicentral distances of 20 km to 100 km (Table 1, Fig. 2) were registered at least at the top and the bottom of the building since the establishment of the SOSEWIN network in 2013. Since the analyzed events have small magnitudes, the recordings of the MEMS sensors have rather poor quality. Hence, only the recordings of the SOSEWINs connected to the 5TC Güralp strong motion accelerometers are used in this study. An example of the recordings of event 2015-1 (Table 1) are shown in Fig. 3 on different floors (basement, 5th and 10th floor, roof) for the three components.

⁶ <https://lhotse21.gfz-potsdam.de/nagvis/frontend/nagvis-js/index.php?mod=Map&act=view&show=istanbul>

Table 1. List of earthquake events used in this study.

Event ID	Date	Time	Location	Depth (km)	Magnitude	PGA (mm/s^2)	Distance to epicenter
2013-1	27.11.2013	04:13:37	40.85N, 27.92E	9	4.8	11	80 km
2013-2	27.11.2013	04:21:35	40.85N, 27.91E	7	4.0	4	80 km
2014	05.02.2014	01:56:44	41.36N, 28.61E	12	3.7	37	45 km
2015-1	28.10.2015	16:20:03	40.80N, 27.72E	16	4.6	10	100 km
2015-2	16.11.2015	15:45:43	40.83N, 28.76E	8	4.3	77	20 km

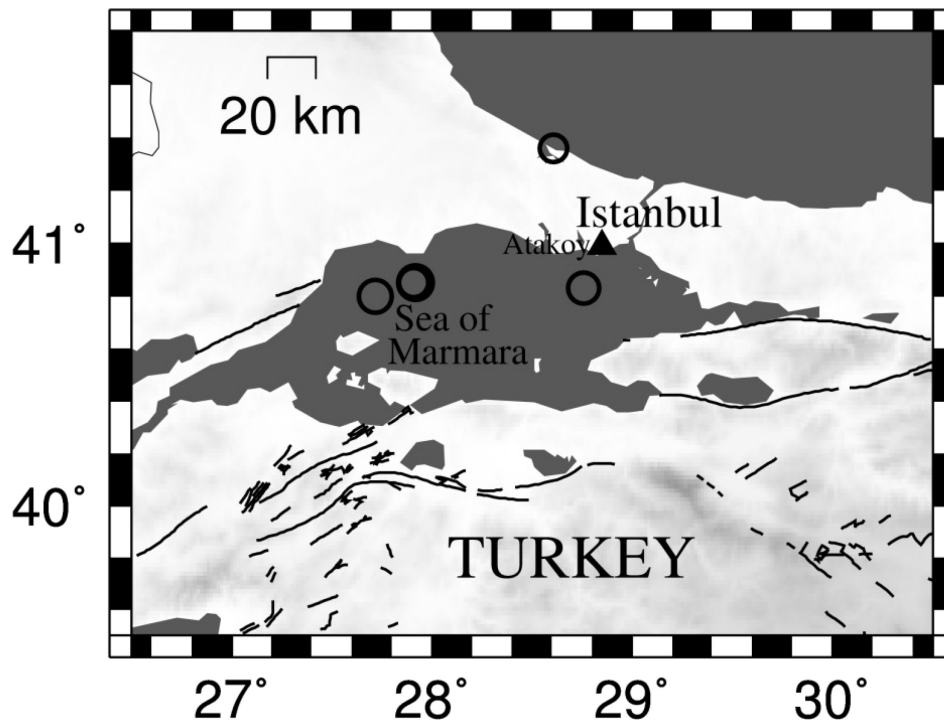


Figure 2. Locations of epicenters of the earthquakes (Table 1) used in this study.

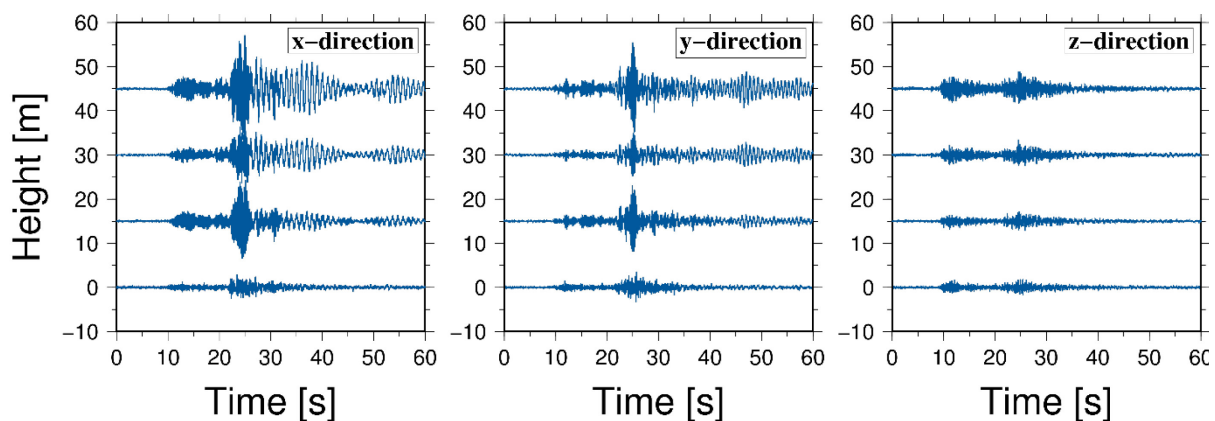


Figure 3. Recordings of event No. 2015-1 (Table 1) by the permanent installation in the building (left: x-direction, middle: y-direction, right: z-direction).

3.2 Temporary installation - The thumper truck experiment

The Kandilli Observatory and Earthquake Research Institute⁷ (KOERI) owns and operates a 27 kN thumper (seismic vibrator) truck. The truck can generate both P and S-wave motions with a frequency content of up to 225 Hz through its dynamic shaker unit (Fig. 1b). In September 2015, an experiment was performed in order to use the waves generated by the thumper truck to study soil-structure interaction effects and the seismic response of the B22 building. 36 units of 4.5 Hz geophones connected to CUBE⁸ digitizers (Fig. 1d) with a sampling rate of 400 samples per second were installed at two locations per floor (Fig. 1c, blue triangles) and at four additional locations on the roof (Fig. 1c, orange triangles). Since it was not possible to enter the apartments, no units were installed in the corners of the intermediate floors of the building. Therefore, the stations were installed in the floor hallway. However, four additional stations installed in the corners at the roof account for a robust identification of the torsional modes. Two different experimental set-ups were employed consisting of two different locations of the thumper truck: at the parking 40 m away from the building and at a location 10 m away from the side of the building, using different excitation frequencies from 1 Hz to 150 Hz.

The data set of the temporary installation consists of 8s vertical excitation phases of different frequencies (from 1 Hz to 150 Hz). Moreover, in total, several hours of ambient vibrations were recorded before, in between and after the two experimental set ups. Exemplarily, the vertical recordings at the basement, the 7th floor and the roof are shown in Figure 4.

⁷ http://www.koeri.boun.edu.tr/depmuh_index_eng.aspx

⁸ <https://www.gfz-potsdam.de/en/section/geophysical-deep-sounding/infrastructure/geophysical-instrument-pool-potsdam-gipp/instruments/seismic-pool/recorder-dss-cube/> The DSS CUBE recorders are stand-alone digital data recorders characterized by a small and light-weight design and extremely low power consumption.

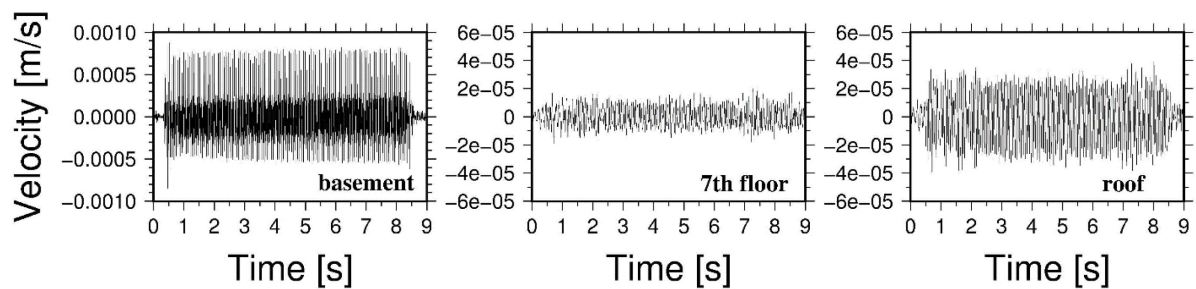


Figure 4. Vertical registrations during the thumper truck experiment at the basement, 7th floor and roof.

4 Analysis of the empirical data set

As already mentioned, both the vibrational and the waveform approaches are used to study the building's dynamic behavior. The vibrational approach aims at the identification of natural frequencies and normal modes of the soil-foundation-structure system and thus, provides the global properties of the building.

Furthermore, the waveform approach aims at the estimation of the properties of seismic wave propagation, and thus the fixed base frequencies, by using the deconvolution approach (e.g., Snieder and Safak 2006; Picozzi et al. 2009a; Todorovska 2009; Nakata et al. 2013; Bindi et al. 2015). By the application of the deconvolution approach (when a certain number of sensors is installed at different heights in the building) the local characteristics of the building, i.e., the wave propagation velocity between two sensors, and hence, the structural characteristics between these two points, are obtained. Therefore, the waveform approach can also be applied in the field of damage detection (Todorovska and Trifunac 2008 a,b,c; Pianese et al. 2018).

First, the results of the Fourier analysis obtained from the data set recorded by the dense temporary installation are presented. Then, the results obtained by the deconvolution approach applied to ambient vibration/generated source measurements from the temporary installation and earthquake recordings from the permanent installation are shown.

4.1 Frequency Amplitude Spectrum (FAS)

The investigation of the Fourier Amplitude Spectra calculated from three component recordings at different floors of a building makes it possible to perform a preliminary identification of the building's natural frequencies and the corresponding mode shapes (e.g., Clough and Penzien 1993; Bendat and Piersol 2010). The differentiation between coupled and torsional modes directly from the FAS curves is only possible if recordings from stations installed in the opposite corners of the building, in the best case on the building's roof, are available. In order to estimate the center of rigidity and thus to separate the translational and the rotational components, additional analysis is needed (e.g., Safak and Çelebi 1990a, Safak and Çelebi 1990b). Nevertheless, it is worth mentioning that real buildings rarely show pure translational or rotational modes, but a combination of both. In the following, we refer to torsional or translational modes, when the modes show mainly torsional or translational contribution.

The Fourier amplitude spectra are estimated for the two horizontal (x and y) and the vertical (z) directions using a moving window of about 120 seconds, overlapping by 50%, and cosine tapering at both ends. The average spectra for one hour of recordings including both excitations of different frequencies and ambient vibration is calculated. In Figure 5, the Fourier amplitude spectra (FAS) of the recordings of the temporary installation of all sensors installed in the same position (on the corridor) on different floors are shown from the 1st floor to the roof (from bottom to top) for two selected frequency ranges ($f=0.7-1.7$ Hz, $f=3.0-6.0$ Hz), to accommodate visible scales. The FAS in the x, y and z-directions are shown with red, blue and black lines, respectively. It is worth mentioning that the estimated frequencies and modes are related to the soil-foundation-structure system (e.g., Trifunac et al. 2008). In the first frequency range, namely the two first bending modes in the x and y-directions (see the floor plan in Fig. 1c) are identified at $f=1.01$ Hz and $f=1.35$ Hz, respectively. The amplitudes of the Fourier spectra increase with increasing floor level and reach a maximum at the building's roof. In the second frequency range, the two second bending modes are shown at $f=3.84$ Hz (x-direction) and $f=5.04$ Hz (y-direction). The amplitudes of the Fourier spectra first increase with the floor level until they reach a maximum at the 8th floor. Then, they decrease with higher floors until the zero point at the 13th floor is reached. The amplitude of the Fourier spectra increases again from the sensor installed at the 13th floor up to the one at the roof. Pinpointing the exact frequency values of the third bending modes is difficult since the peaks of these modes are not very well defined. For this reason, due to the large uncertainties involved, the results for the third bending modes are not shown here.

Analyzing the stations installed at the floor corridors, namely close to the building's axis of rotation normal to the x-y plane, it is possible to univocally identify the bending modes but not the torsional modes. For this reason, in order to identify the torsional modes, the recordings of two stations (903 and 809, locations shown in Fig.1, bottom, center) installed at opposite corners on the roof are analyzed. The Fourier Amplitude Spectra are calculated for the recordings at the two stations, as well as the sum and the difference (in the time domain) of the both recordings (Fig. 6, red, blue and black lines correspond to the x, y and z directions, respectively). This makes it possible to separate the bending modes (sum) from the torsional modes (difference). The applied approach is similar to the one proposed by Safak and Çelebi (1990a). In our case, the torsional modes are very close to and almost overlap the bending modes. Nevertheless, by calculating the FAS of the sum and difference, the torsional and translational modes can be separated univocally. Subsequently, the first two torsional modes are determined to have frequencies of $f=1.26$ Hz and $f=4.15$ Hz. The results for all identified modes are summarized in Table 2, first column. The center of rigidity C was estimated following the Safak and Çelebi (1990a) approach in the time domain and is shown in Figure 1c. Other methods in the frequency domain are also available to calculate the center of rigidity (e.g., Safak and Celebi, 1990b).

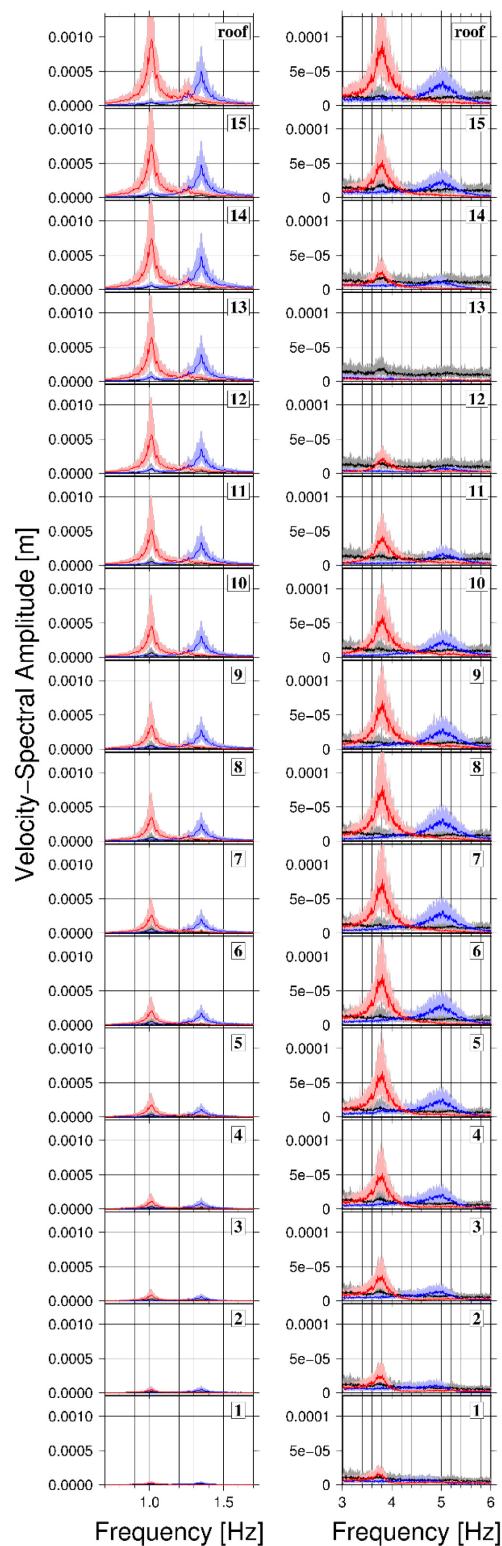


Figure 5. Fourier amplitude spectra (mean \pm 1 σ) for the temporary installation in B22 for two frequency ranges. Please note the different scales used for the x and y axes for the two frequency ranges. The spectra are plotted from the first floor (lowermost panel) to the roof (uppermost panel). Red, blue and black lines correspond to the x, y and z-components, respectively.

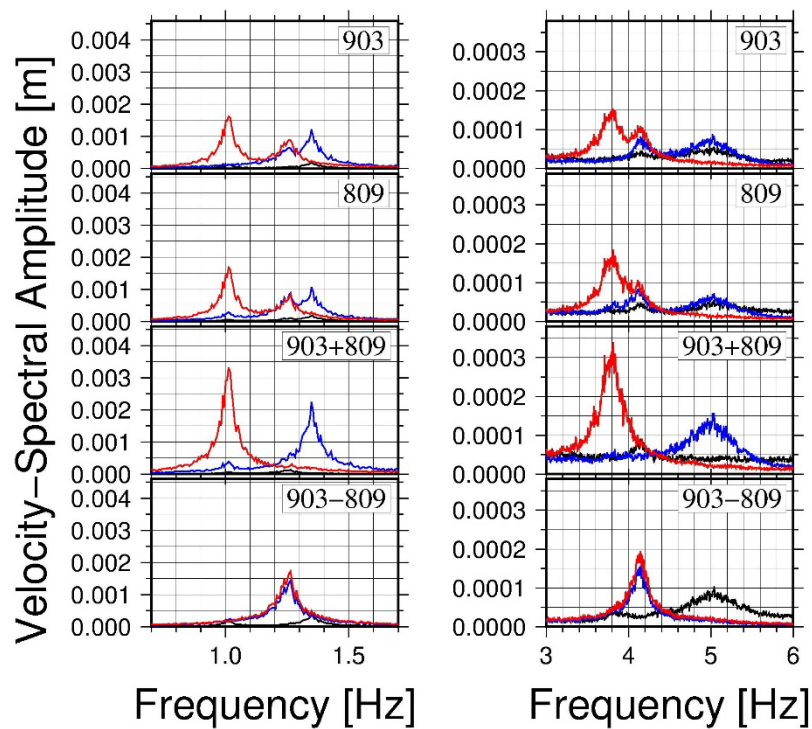


Figure 6. Fourier amplitude spectra (FAS) for the temporary installation in B22 for two different frequency ranges. The spectra are plotted for two stations installed in opposite corners of the roof (station 903 and 809, Fig. 1c), their sum and difference. Red, blue and black lines correspond to the x, y and z-components, respectively.

Table 2. Comparison of modes determined from the in-situ recordings and the analytical study.

Mode No.	Frequency f (Hz)				Mode type
	In-situ recordings		Analytical study		
	FAS	Transfer function	Fixed base case	Winkler springs case	
1	1.01	1.00	1.00	0.90	1 st bending in x-dir.
2	1.26		0.84	0.76	1 st torsional
3	1.35	1.37	1.60	1.43	1 st bending in y-dir.
4	3.84	3.85	3.92	3.76	2 nd bending in x-dir.
5	4.15	-	3.21	3.06	2 nd torsional
6	5.04	5.13	5.36	5.23	2 nd bending in y-dir.
7		8.13	8.12	7.93	3 rd bending in x-dir.
8	-		6.67	6.48	3 rd torsional
9	-		8.01	8.79	3 rd bending in y-dir.

4.2 Deconvolution interferometry

In this study, the deconvolved wave fields are calculated by applying the regularized Tikhonov deconvolution (Tikhonov and Arsenin 1977). The regularized deconvolution is defined as

$$D(\omega) = \frac{u(\omega)u_{ref}^*(\omega)}{|u_{ref}(\omega)|^2 + \varepsilon} \quad (1)$$

where $\omega = 2\pi f$ is the angular frequency and ε a regularization parameter, which controls the degree of filtering required to stabilize the deconvolution.

4.2.1 Temporary installation results

The deconvolution approach was applied to one hour of data, including vibrations generated by the thumper truck and ambient vibrations. The deconvolved wave fields are calculated for a moving window of about 120 seconds, overlapping by 50%, and cosine tapering at both ends and then averaged. Both the station at the roof (Fig. 7) and the one at the first floor (Fig. 8) are used as the reference. The results are shown for both horizontal (x and y) and the vertical (z) directions for the deconvolved wave field with reference on the roof and for the x and y- directions for the deconvolved wave field with the reference at the first floor. Considering the deconvolved wave field with the reference at the top of the building (Fig. 7), the up and downward propagating waves can be identified in the acausal and causal part (orange lines), respectively. For both horizontal directions, but especially for the y-direction, there are two close peaks propagating as up and downward going waves, while only for the z-direction there is one clear peak for the up and downward propagating waves. If the wave propagation through a simple homogeneous layer is considered, the deconvolved wave field (with the reference station on the roof) would be dominated by one upward propagating peak in the acausal and one downward propagating peak in the causal part. The more sophisticated nature of the deconvolved wave field of the investigated building indicates a more complex structure, suggesting either a non-homogeneous material distribution or the influence of different modes (e.g., torsional modes) on the deconvolved wave field. Moreover, peaks with inverted polarity (Fig. 7, green lines) propagate with the same shear wave velocity close to the up and down-going waves, related to the second mode as will be discussed later.

Considering the deconvolved wave field with respect to the bottom (i.e. first floor), the up and downward going waves are obtained, propagating from the bottom to the roof in the acausal and causal parts, reflected at the roof and propagating down again to the bottom of the building (Fig. 8, top, magenta lines). Moreover, the oscillation of the building with the frequencies of the first and second bending modes ($f_{x_1}=1.02$ Hz, $f_{y_1}=1.37$ Hz, green lines, $f_{x_2}=3.85$ Hz, $f_{y_2}=5$ Hz, red lines) is clearly visible for both directions. In order to better visualize the oscillation of the building with the first and second modes, the first mode is marked in the acausal, the second in the causal part. The oscillation with the first mode can be identified best for the higher floors (maximum FAS for the highest floors), and with the second mode around the 7th floor (maximum FAS). Especially for the y-direction, the oscillation with the second mode is better visible in the causal part. Please note that there is a polarity change between the 12th floor and the roof (Fig. 8, bottom, marked with orange circles) which is due to the zero-crossing of the second bending mode at that height (see above) and hence, results in an inverted polarity.

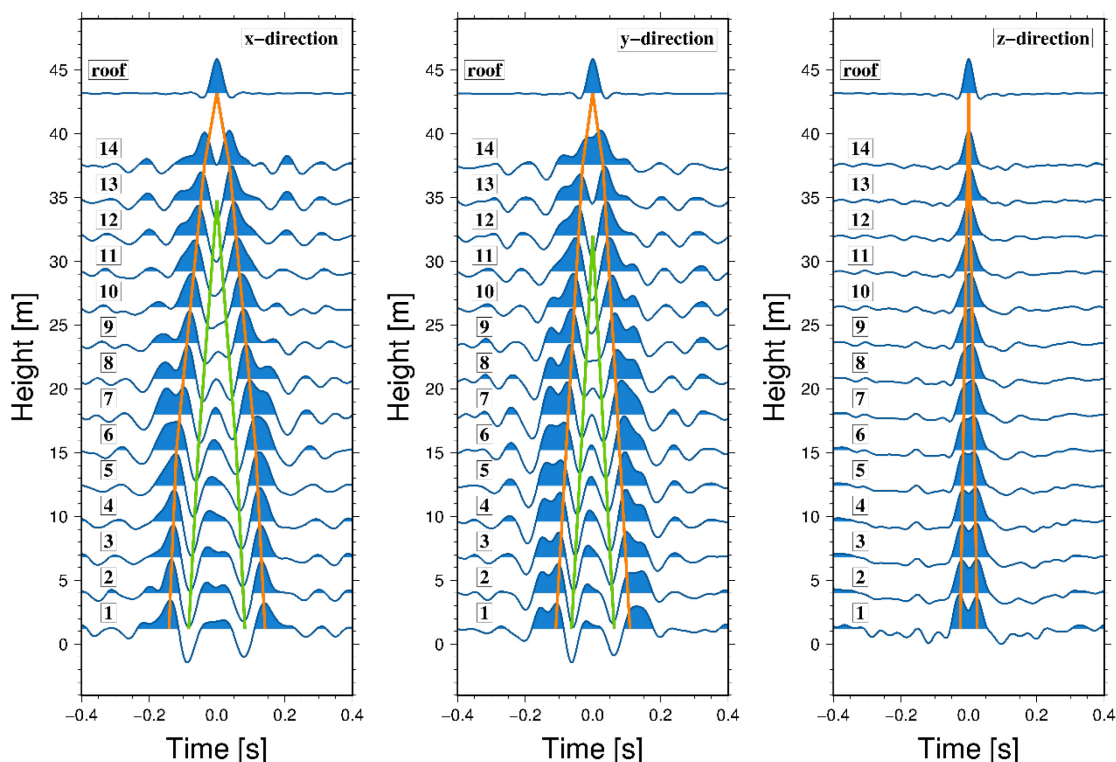


Figure 7. Deconvolved wave fields using the station at the roof as the reference (left: x-direction, middle: y-direction, right: z-direction). Orange lines mark the up and downward propagating waves, green lines the up and downward propagating waves with changed polarity (due to the second mode), but the same propagation velocity.

The time lag between up and down-going waves is estimated from the peaks in the deconvolved wave field, and hence, the velocity profile of the building is obtained (Snieder and Safak 2006). It is worth mentioning that the time-lag between the up-going and down-going waves would give only the approximate values for velocities, when the damping is very high (Futterman 1962). It is assumed that this is not the case for the B22 building. Changes in the velocity along the structure provide insights about the spatial variations in the properties of the structure, e.g., due to different materials used. Moreover, when considering the temporal variations in the dynamic properties of a building over a long time or before, during and after a strong earthquake, changes in the mechanical characteristics might be either due the influence of atmospheric conditions (e.g., temperature, wind etc.) on the building's behavior (e.g., Clinton et al. 2006; Todorovska and Al 2006; Herak and Herak 2010; Mikael et al. 2013, Pitilakis et al. 2016) or due to structural damage (e.g., Todorovska and Trifunac 2008 a, b, c).

The estimation of the velocity will be shown for the deconvolved wave fields using the station at the bottom as reference, since the peak picking is more precise for this case. Due to the two close peaks of up and downward propagating waves in the deconvolved wave field when using the recording at the top as reference, for some floors the peaks overlap and thus, influence the peak picking precision. The height of the sensors (with respect to the sensor at the reference location) is shown versus the estimated time lags for the x-direction in Figure 9. It is visible that the slowness and hence the velocity is not constant, but changes with the height of the building. In this respect, the analyzed building can be divided into 3 velocity layers with $v_1=450$ m/s from the 1st to the 5th floor, $v_2=330$ m/s from the 5th to the 14th floor, and $v_3=160$ m/s from the 14th floor to the roof. These layers are likely connected to

variations in the use of materials, i.e., the thickness of the RC walls used for the construction of the building. Thus, regarding the first velocity layer, it should be noted that the height of the basement of the building is 4.00 m as compared to 2.81 of other floors. Moreover, the outer walls of the basement are cast in place reinforced concrete, making it much more rigid compared to other floors having precast concrete infill walls, thus resulting in a higher shear wave velocity. It is also important to note that the basement is embedded about 3.0 m in soil.

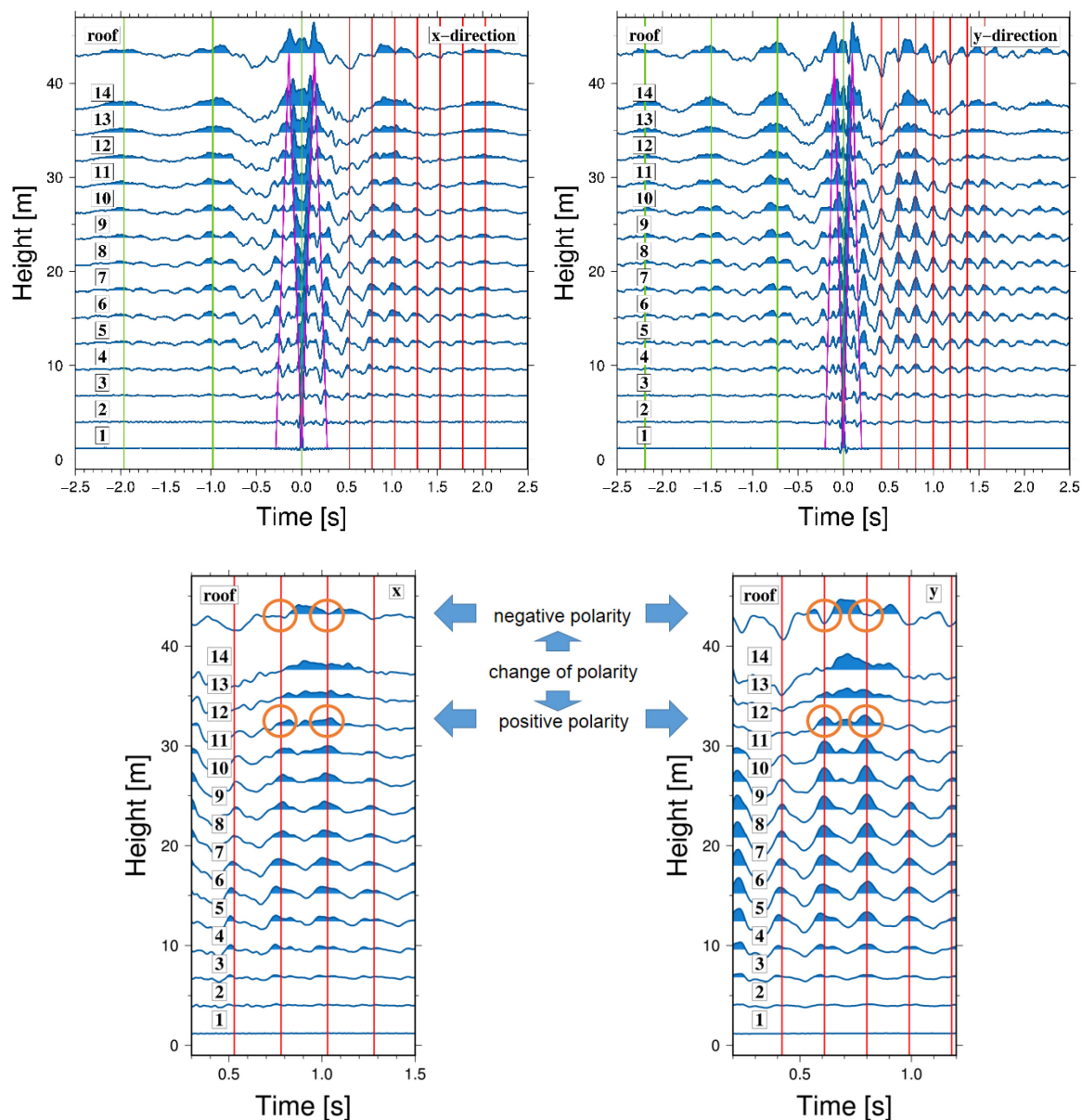


Figure 8. Top: Deconvolved wave fields using the station at the first floor as the reference (left: x-direction, right: y-direction). Magenta lines show up and downward propagating waves, green lines the oscillation of the building with the first and red lines the oscillation with the second modes. Bottom: Zoom-in on the deconvolved wave fields (top), showing the change of polarity.

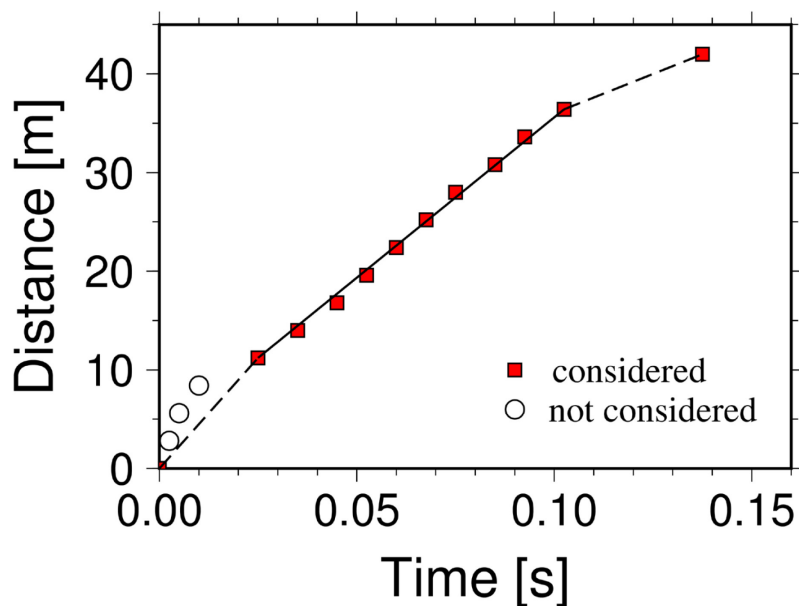


Figure 9. Travel times between pulses of up and down-going waves at different floors versus the distance of the considered sensor to the sensor at the bottom. The slope of the curve corresponds to the average shear wave velocity for the different layers.

4.2.2. Permanent installation results

The analysis of earthquake recordings is necessary in order to retrieve further insights into the building's behavior. Studies based on weak motion make it possible at least to identify the dynamic parameters for small lateral loads when the behavior of the structure is linear. In this study, five earthquake recordings (Table 1) are analyzed by the deconvolution approach using both the registration at the top and the ones at the bottom of the building as reference. The results of the deconvolution approach for the x-direction with the recording at the roof as reference are shown for the five earthquakes separately (left) and after stacking of the results of all five earthquakes (right) in Figure 10. It is worth mentioning that for three of the five earthquakes, the recordings are available only at the top and bottom of the building since they occurred before the new installation of the SOSEWINs in September 2015. When considering the deconvolved wave fields of the different earthquakes (Fig. 10, left), almost no variation of the position of the upward and downward propagating pulses between the events can be observed. This is due to the fact that the analyzed events are only small events that did not cause any damage and the behavior remained linear. Thus, no changes in the dynamic characteristics of the building occurred.

Clear upward and downward propagating peaks (Fig. 10, orange lines) are identified in the deconvolved wave fields. The velocity structure is estimated as three layers between the sensors with the average velocities of: ground level-5th floor: $v_1=470$ m/s, 5th floor-10th floor: $v_2=300$ m/s and 10th floor-roof: $v_3=220$ m/s. This is consistent with the results obtained from the ambient vibration/generated source measurements when considering the same layers as here, defined by the locations of the permanently installed sensors.

Please note also the peaks with inverted polarity in the deconvolved wave fields between the basement and the 10th floor (Fig. 10, green lines) next to the up and downward propagating waves. These peaks

are due to the inverted polarity of the motion around the 13th floor due to the excitation of the second mode. It can be clearly seen also in the deconvolved wave fields of the generated source / ambient vibration (Fig. 7, green lines). When considering the S-transform (Stockwell et al. 1996), a time frequency distribution of the registration at the top of the building for event 2015-1 (Table 1, Fig. 2), shown in Figure 11, it can be observed that at the beginning of the shaking (approximately up to 15 s and 20 s for the x and y-directions, respectively) the 2nd mode is more dominant than the 1st one.

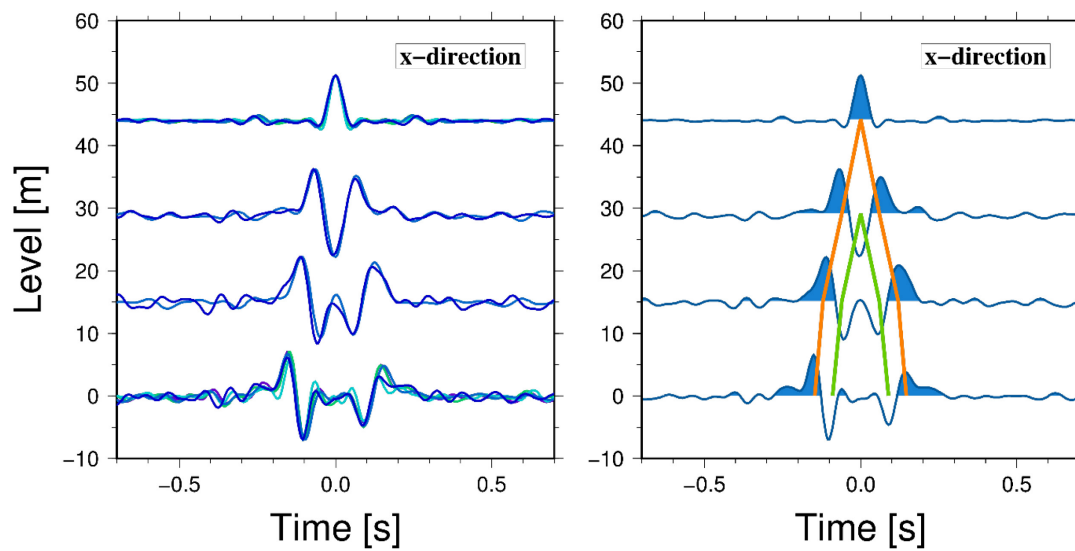


Figure 10. Deconvolved wave fields (x-direction) using the station at the roof of the building as the reference. Left: the results for the five earthquakes separately, right: after stacking the results of the five earthquakes (left). Orange lines mark the up and downward propagating waves, green lines the up and downward propagating waves with changed polarity (due to the second mode), but the same propagation velocity.

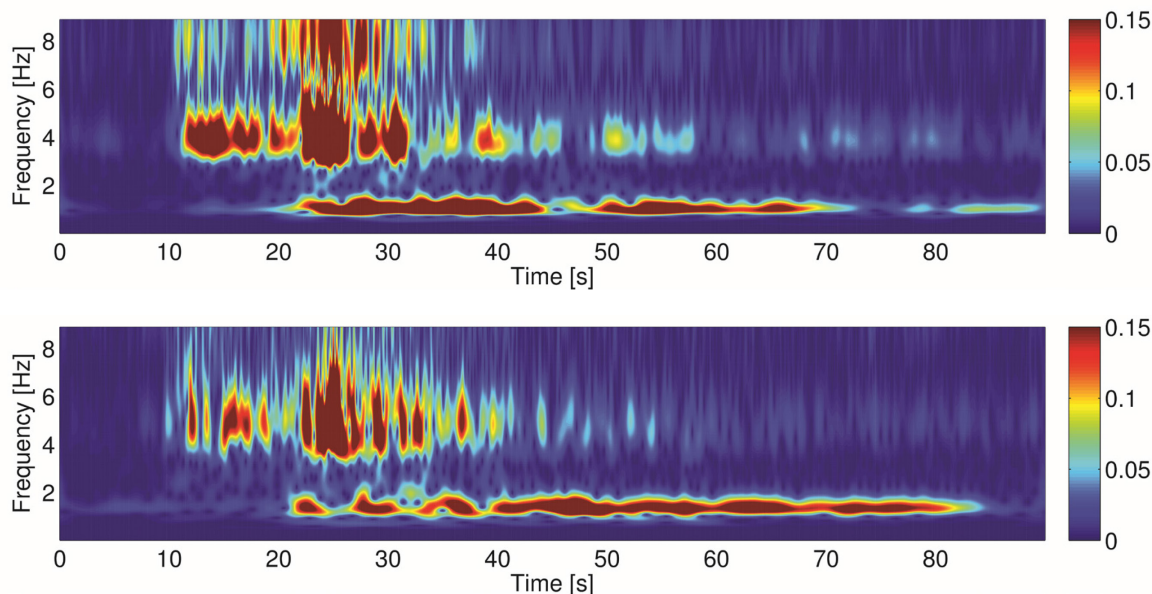


Figure 11. Time-Frequency representation (S-Transform) of the registrations at the roof of event 2015-1 for the x (top) and y (bottom) directions.

5 Numerical simulations – Finite Element Analysis (FEA)

The building was modeled using SAP2000, Ver. 18 (2016), for modal analysis. Both the walls and the slabs were modeled using thick shell elements. The slabs of each chamber, namely the area bordered by 2 or more walls, were split generally into 6x6 grids of shell elements. On the other hand, the walls, i.e., the vertical elements, were split into four elements over the floor height. Thus, the element sizes both in the vertical and horizontal planes are approximately 0.70x0.70 m (Fig. 12a).

Concrete strength was obtained from the design documentation as 18MPa. The elastic and shear moduli were calculated accordingly. The dead and live loads were estimated in accordance with the guidelines of Turkish Standard TS498 (TSI 1997) as well as the design documentation of the building. In this respect 2.0kN/m² is used as the live load.

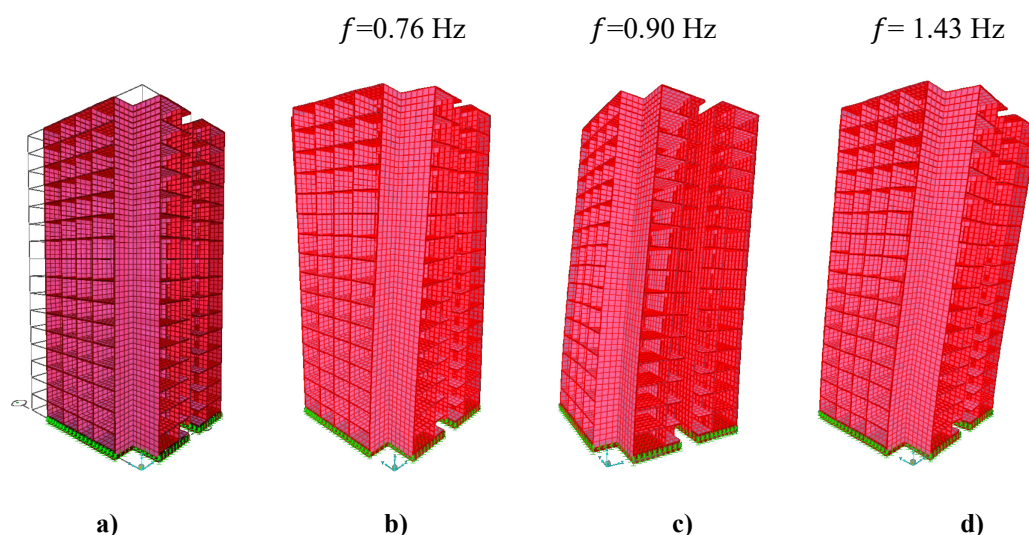


Figure 12. SAP2000 model results. **a)** Undeformed shape, **b)** 1st torsional mode, **c)** 1st bending mode in the x-direction and **d)** 1st bending mode in the y-direction).

Finite element analysis was carried out in order to estimate the dynamic behavior of the structure, through the assessment of the mode shapes and the corresponding frequencies.

The modal frequencies were calculated considering two different base conditions. In the first case, the base nodes are assumed to be fixed, whereas in the second case, Winkler springs were placed in the vertical (z) direction per ASCE/SEI 41-13 to consider soil structure interaction (ASCE 2013). The stiffness values of the springs are calculated assuming an average V_s of 450 m/s and soil density of 18 kN/m³.

The modal frequencies obtained and their corresponding mass modal participation (mmp) ratios are presented in Table 3. As can be seen, in both translational directions, the first two modes have a total mass modal participation ratio of over 85% and when the third mode is included, the total mass modal

participation ratio exceeds 90%. The un-deformed shape and the 1st modes, namely in the x and y directions and the torsional around the z axis are shown in Figure 12.

Table 3. Fundamental frequencies determined by the Finite Element Analysis.

Mode No.	Fixed case					with Winkler springs				
	Period (s)	Frequency (Hz)	mmp ratio			Period (s)	Frequency (Hz)	mmp ratio		
			x-dir	y-dir	Tor.			x-dir	y-dir	Tor.
1	1.18	0.84	0%	0%	68%	1.31	0.76	0%	0%	71%
2	1.00	1.00	67%	0%	0%	1.11	0.90	70%	0%	0%
3	0.62	1.60	0%	69%	0%	0.70	1.43	0%	70%	0%
4	0.31	3.21	0%	0%	17%	0.33	3.06	0%	0%	16%
5	0.26	3.92	18%	0%	0%	0.27	3.76	18%	0%	0%
6	0.19	5.36	0%	17%	0%	0.19	5.23	0%	17%	0%
7	0.15	6.67	0%	0%	6%	0.15	6.48	0%	0%	5%
8	0.12	8.01	0%	1%	0%	0.13	7.93	5%	0%	0%
9	0.12	8.12	6%	0%	0%	0.11	8.79	0%	2%	0%
10	0.11	8.92	0%	2%	0%	0.10	9.95	0%	0%	2%
11	0.10	10.10	0%	0%	2%	0.09	11.72	1%	0%	0%
12	0.08	11.94	2%	0%	0%	0.08	11.77	1%	0%	0%
13	0.08	12.08	0%	3%	0%	0.08	11.89	0%	3%	0%

6 Comparison of results obtained from finite element and empirical data analyses

The modes and corresponding frequencies obtained from the FEA are compared to those from the vibrational approach applied to real data. Furthermore, modal time history analysis was carried out to calculate the building's response using the selected earthquake time histories and to calculate the synthetic accelerograms. The synthetic accelerograms are used, like the real ones, to compare the analytical and empirical data results and to gain information on the reliability of the numerical model. Finally, an attempt is made to calculate the fixed-base frequency of the building.

6.1 Mode shapes and fundamental frequencies from FEA and real data analysis

When the results of both the finite element analysis (i.e., with and without Winkler springs) and field measurements (Table 2) are compared, there are two points to be discussed. The first one is the appearance of the 1st torsional mode as the first mode in the analytical study, whereas the first torsional mode is determined as the second mode from the field measurements. This outcome can basically be due to two factors. First, the torsional mode is oftentimes the first mode for the shear wall dominant type structures, as in this case, due to their high lateral rigidity and the symmetry in plan in both horizontal directions. This outcome, namely the torsional mode being the first, was also reported in the studies by Balkaya and Kalkan (2003) and Balkaya et al. (2012). The second important factor concerns neglecting the stiffness of the exterior infill walls in the model, which contribute to the torsional rigidity of the structure. In order to test this hypothesis, several other models with very thin infill walls were tested, and it was observed that the frequency of the torsional mode shifts upwards without any significant change in the frequencies of the translational modes. It is concluded that the nonstructural infill walls, namely the outside façade walls, cause the shift in the frequency of the torsional mode in the finite element analysis.

The second point to discuss is the difference between the analytically determined frequencies and those measured. In the first FE model, the soil-structure interaction was ignored while it was included to some extent in the second model through the Winkler springs. The analysis of the second case, as would be expected, produced lower frequencies. Yet, in both cases, although a perfect match with the measured frequencies was not achieved, the results obtained are reasonably close. Hence, for additional studies using the FE model, the second case, namely the one with Winkler springs, was selected.

6.2 Wave propagation through modelled and real building

In order to understand the results obtained from empirical data better and to evaluate the reliability of the model, modal time history analysis of the FE model was performed to calculate the building's response, namely the synthetic seismograms, by using the recordings registered at the ground level. Afterwards, the deconvolved wave fields are calculated using the sensor at the roof (Fig. 13) and the one at the 1st floor as reference (Fig. 14). Figure 13 shows the comparison of the deconvolved wave fields of the real data (blue lines), and the results of the synthetic seismograms obtained from the model (gray lines), for the x (left) and y (right) directions. For the x-direction, the high level of similarity of the results obtained from real and synthetic data is clearly visible, with the deconvolved wave fields being almost identical. The average propagation velocities ($v_{xreal}=300$ m/s, $v_{xsynth_with_springs}=290$ m/s) are proportional to the fundamental frequencies of the fixed-base system. There is a slight discrepancy between the times of the up and downward propagating pulses for the y-direction, since for this direction there is some difference between the fundamental frequencies obtained from real data ($f_{y1real}=1.35$ Hz) and the model ($f_{y1model}=1.43$ Hz). Moreover, the deconvolved wave field of the synthetic seismograms (y-direction) is dominated by two close up and downward propagating peaks in the acausal and causal parts, respectively. The deconvolved wave field of the y-direction calculated from ambient noise / generated sources is also dominated by these two peaks (Fig. 7), different from the deconvolved wave field obtained after stacking the results of 5 events, where one up and one downward propagating peak is observed.

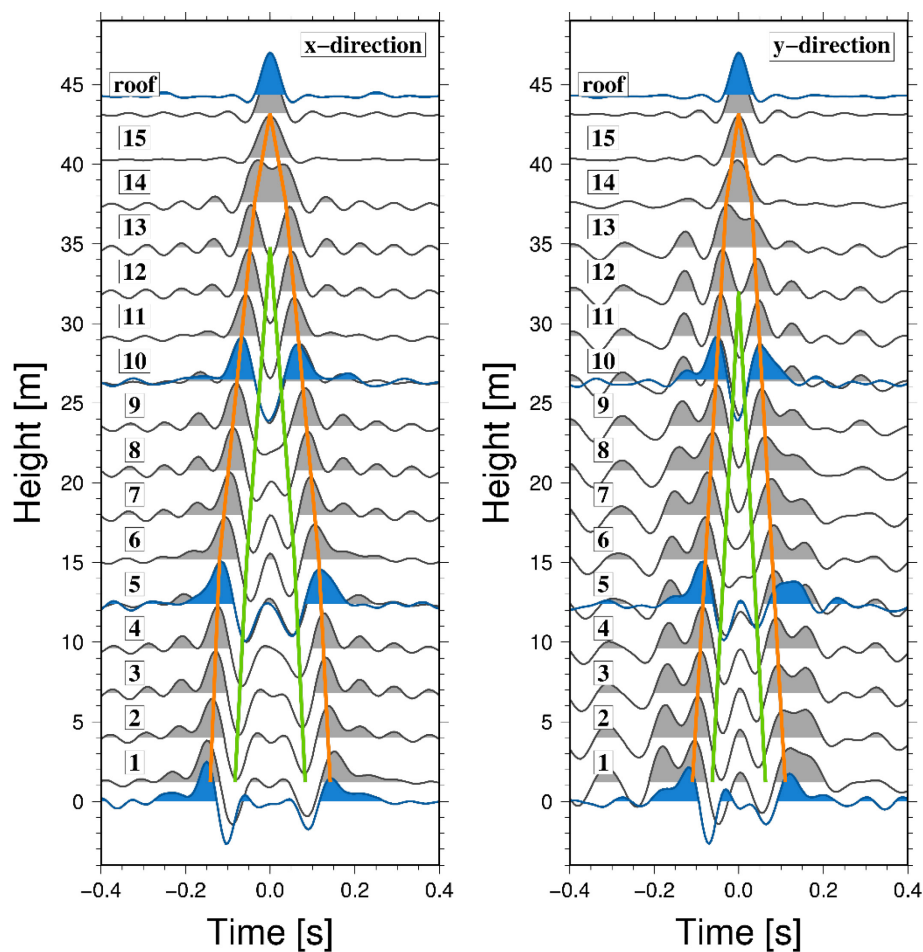


Figure 13. Comparison of the deconvolved wave fields (using the registration at the roof as the reference) of synthetic seismograms (gray) and the real data results after stacking (blue) for the x (left) and y (right) directions. Orange lines mark the up and downward propagating waves, green lines the up and downward propagating waves with changed polarity (due to the second mode), but with same propagation velocity.

Figure 14 shows the deconvolved wave field (with respect to the ground level) of the real data (left, in blue) and the synthetic seismograms (right, in gray) for the x (top) and y (bottom) directions for event 2015-1 (Table 1). Not only are the up and downward propagating pulses (magenta lines) that are directly connected to the fixed-base frequencies of the building (wave velocity is linear function of fixed-base frequencies) clearly visible, but also the oscillation of the system with the first and second mode (system frequencies) for both the real and synthetic data (first mode shown with green lines, second mode with red lines). Please note that for clearer visualization, the first and second modes are marked for two different time periods of the deconvolved wave field. For the y-direction, the deconvolved wave fields are almost identical for the real and synthetic data, including wave propagation through the building and the oscillation of the building with first and second modes. Interestingly, this is not the case for the x-direction for which the synthetic results show clearly the oscillation of the B22 with the first and second modes while for the real case, although the second mode is excited much more, the oscillation with the first mode is almost not visible.

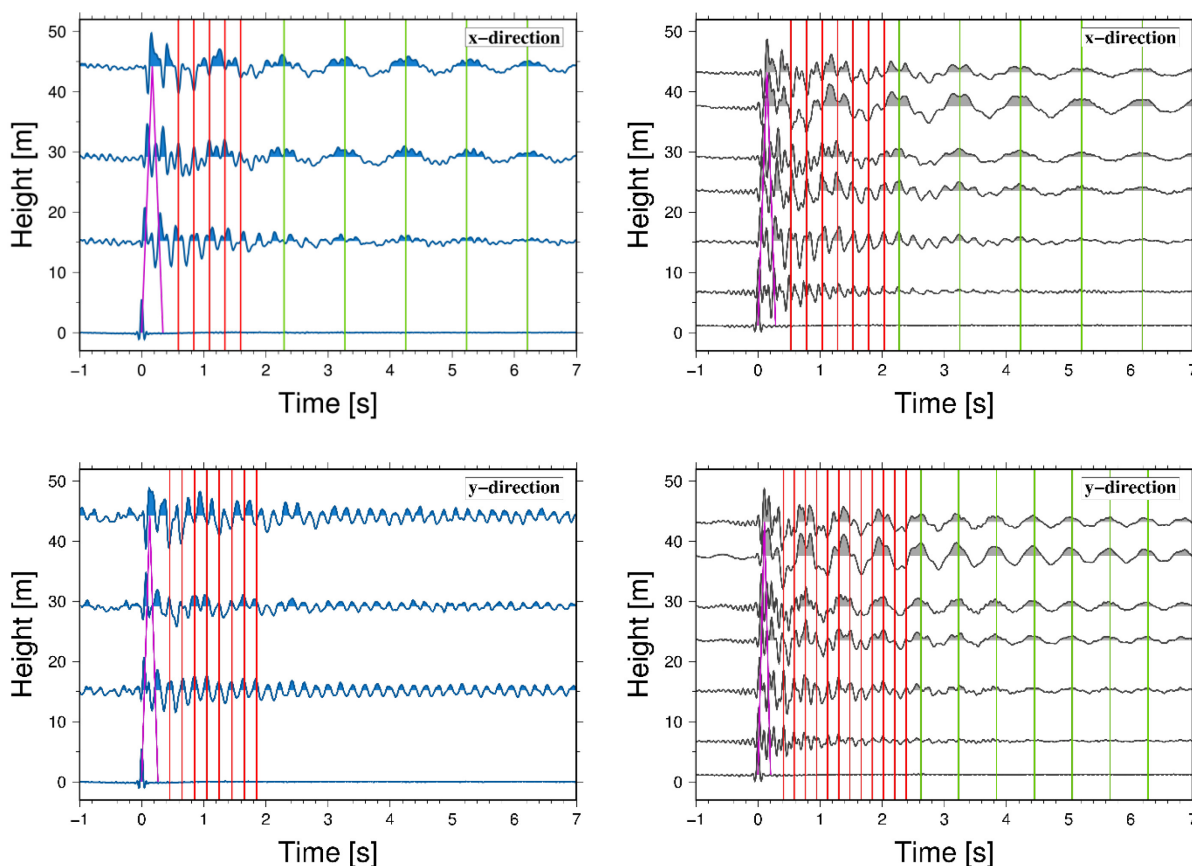


Figure 14. Comparison of the deconvolved wave fields (using the registration at the first floor as the reference) of synthetic seismograms (gray) and the real data results after stacking (blue) for the x (left) and y (right) directions. Magenta lines show up and downward propagating waves, green lines the oscillation of the building with the first and red lines the oscillation with the second modes.

7 Fixed-base frequency of the building

There are conflicting views about the calculation of the fixed base frequencies from the roof-to-ground transfer function. Following the Safak (1995) approach the dominant frequencies of the transfer function roof-to-ground correspond to the fixed-base frequencies of the building. Other studies have shown that the dominant frequencies of the transfer function roof-to-ground, does not correspond to the fixed-base frequencies (e.g. Paolucci 1993, Stewart and Fenves 1998, Muria-Vila et al. 2001, Rahmani and Todorovska 2013). In these studies, buildings with a high rocking contribution are considered. For the B22 building, the dominant frequencies estimated from the roof-to-ground transfer function (Figure 15, red lines: x component, blue lines: blue components, Table 2) are very similar to the system frequencies obtained from FAS. Since the fixed base frequencies obtained simply calculating the transfer function roof-to-ground may be misleading, also other approaches to calculate the fixed-base frequencies are considered.

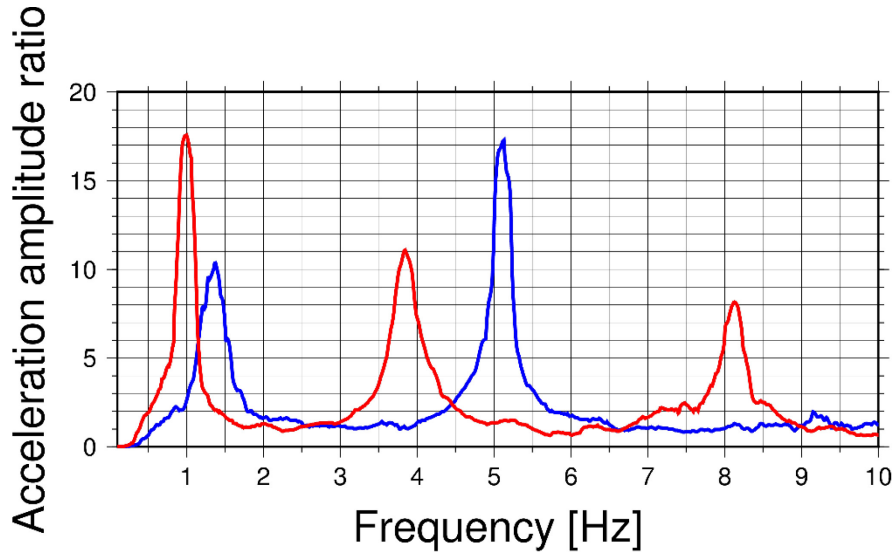


Figure 15. Transfer function roof-to-ground. Red and blue lines correspond to x and y-components, respectively.

For a building behaving as a shear beam, the fixed-base frequencies can be estimated by

$$f_{\text{shear_fixed-base}} = \frac{v}{4H} \quad (2)$$

with v being the propagation velocity estimated by the deconvolution approach and H the total height of the building (Trifunac et al. 2008). The shear beam approximation can be assumed for buildings with a frequency sequence of $(f_1, f_2 = 3f_1, f_3 = 5f_1, \dots)$. If the frequency sequence is close to $(f_1, f_2 = (3/1.2)^2 f_1, f_3 = (5/1.2)^2 f_1, \dots)$, the building behaves as a bending beam (Michel et al. 2006). Most buildings cannot be associated with one of ideal beam approximations, since bending and shear elements are often combined within one building. For this reason, the sequence of frequencies for a real building is usually between the sequences of these two models (Michel et al. 2006). Nevertheless, eq. (2) has found a wide application when estimating the fixed-base frequencies from the deconvolution approach, applied often also to buildings that cannot be described as a pure shear beam.

The fixed-base fundamental frequency of a building that behaves as a bending beam can be estimated as

$$f_{\text{bending_fixed-base}} = \frac{vb^{3/2}}{4H^2} \quad (3)$$

where b is the dimension of the building of the axis perpendicular to the bending direction. The values obtained by equations (2) and (3) can be combined as follows,

$$\frac{1}{f_{\text{building_fixed-base}}^2} = \frac{1}{f_{\text{shear_fixed-base}}^2} + \frac{1}{f_{\text{bending_fixed-base}}^2}. \quad (4)$$

Equations (2) and (3) yield 1.62 Hz and 3.91 Hz for pure shear and bending beams respectively. However, when combined using equation (4), the resulting value is 1.49 Hz for the lowest mode.

Hence, the B22 building is one of the buildings where bending and shear beam elements are combined. If the x-direction is considered, the ratio between f_2 and f_1 is estimated as 3.8, and similarly, 3.73 for the y-direction.

8 Discussion and conclusions

Tunnel formwork buildings are assumed to have a good seismic performance and hence, have found a wide application in regions prone to high seismic hazard. Until now, only a few studies on the dynamic characteristics of this type of buildings have been performed based on real data sets, most of the available studies are analytical. In this study, the dynamic behavior of a 16 story tunnel formwork building is studied using different techniques including both real data analysis and numerical simulations, as well as a combination of them.

For the real data analyses, a data set consisting of both ambient vibration / generated sources (dense network consisting of 36 stations) and earthquake recordings (permanent installation, due to small events, only 4 stations used in this study) is used. Ambient vibration / generated source measurements recorded by the dense network have been used to estimate the modes of the building-soil structure. The first mode at a frequency of $f_1=1.01$ Hz is estimated as the 1st bending mode in the x-direction, followed by the 1st torsional mode at $f_2=1.26$ Hz and the 1st bending mode in y-direction at $f_3=1.35$ Hz. This is different from the studies performed by Balkaya and Kalkan (2003) and Balkaya et al. (2012), who performed analytical studies with the aim of determining an empirical equation for the estimation of the fundamental frequencies of tunnel formwork buildings, the fundamental mode is not identified as the first torsional one. As it was observed from the FEA was performed in our study, the nonstructural infill walls, namely the outside façade walls, cause the inversion of the first two modes. Usually, when buildings are modelled, these elements are not taken into account. Once again, it is shown how important it is to perform a comparison of the results obtained by a Finite Element Analysis with results from empirical data to find a model which describes the dynamic behavior of a building in a satisfactory way.

The deconvolution approach was applied to ambient vibration / generated source recordings, to earthquake recordings of the permanent network and to synthetic seismograms obtained as the building's response to an earthquake registration at the ground level of the building using the FEA. For all three cases, when using either the recordings at the top of the building or at the bottom, the influence of the second mode is also clearly visible in the deconvolved wave field. When considering the deconvolved wave fields using the recording at the top of the building as reference, a second peak with inverted polarity and the same shear wave propagation velocity is observed close to the up and downward propagating pulses in the acausal and causal parts (Fig. 7 and Fig. 13, green lines). Moreover, both the up and downward propagating pulses in the deconvolved wave fields of the ambient vibration / generated source recordings and of the synthetic seismograms are characterized especially for the y-direction by two close peaks (with the same polarity). This fact is probably due to the torsional mode with a frequency very close to the one of the first bending mode in the x-direction.

For the deconvolved wave fields using the station at the bottom as reference, not only from the up and downward propagating waves (e.g., Fig.8, top, magenta lines), but also the oscillation of the building

with the first (Fig. 8, top, green lines) and second (Fig. 8, red lines) modes is clearly visible. For the second mode, the polarity of the peaks changes between the 12th floor and the roof (Fig. 8, bottom).

Although the order of the first two modes (1st bending mode in x-direction and 1st torsional mode) is inverted for the FEA used in our study (nonstructural infill panels not modelled), when considering the deconvolved wave fields (especially using the recording at the top of the building as reference), the results of the empirical and synthetic data are almost identical for the x-direction. There are some discrepancies between the results of the real and synthetic data when considering the y-direction, first due to the difference between the fundamental frequency for this direction for real data and model, and second due to the appearance of a second up and downward propagating peak. These second peaks are observed also for the data set of ambient vibration / generated source measurements.

Moreover, the fixed-base frequency is estimated from the propagation velocity obtained from the deconvolution approach. Usually, a building does not behave as a pure shear or bending beam, but as a combination of both. Nevertheless, in the literature, it is often noted that in order to estimate the fixed-base frequency, the simple shear beam model is used. For the B22 building, bending and shear elements have a contribution to the building's behavior, and to correctly reconstruct the fixed-base frequencies, both contributions have to be taken into account.

Furthermore, identifying fundamental frequencies as well as understanding the wave propagation in the B22 building is also an important issue since the building (equipped with a permanent network) together with the nearby downhole installation (e.g., Parolai et al. 2009, 2010, 2012) makes it possible to study the interactions between a building and the soil, as proposed by Petrovic and Parolai (2016). The interpretation of results obtained from the joint analysis of the building-downhole data sets (Petrovic et al. 2017) are simplified if first the building's dynamic behavior, including especially the wave propagation through the building, is understood.

In this study, a dense data set of ambient vibration, generated source and earthquake measurements was used to analyze the dynamic characteristics of the B22 building. Depending on the aim of a study already few instruments recording ambient vibration may be sufficient, as for example to estimate the fundamental frequencies of a building. Nevertheless, it has to be kept in mind, that the number of sensors which are installed, will always limit the information that can be retrieved from the recorded data, as for example when variations in the propagation velocity through the building are considered.

Acknowledgments

The authors wish to acknowledge Erdal Safak and an anonymous reviewer for their helpful suggestions to improve the manuscript. The authors would like to thank Tobias Boxberger and Stefan Mikulla for the installation of the Self-Organizing Seismic Early Warning Information Network (SOSEWIN) in the B22 in Istanbul. Furthermore, the authors thank Messrs. Ahmet Korkmaz and Nafiz Kafadar of KOERI for their efforts in keeping up the permanent installation at the B22 Building. The thumper truck was operated by Mr. Oktay Cirag of KOERI and the technical team of BIAS Mühendislik, producer of the thumper truck. The ambient vibration / generated source measurements in B22 were performed using the seismic instruments provided by the Geophysical Instrument Pool Potsdam (GIPP) and supported with POF expedition money of the GFZ. This research was moreover supported by the Plate Boundary Observatory Turkey of the GFZ, and the European MARSite project. Kevin Fleming kindly revised our English.

References

- Aki K (1957) Space and time spectra of stationary stochastic waves, with special reference to microtremors. *Bulletin of the Earthquake Research Institute* 35:415-436
- ASCE, American Society of Civil Engineers (2013) ASCE standard ASCE/SEI 41-13: Seismic Evaluation and Retrofit of Existing Buildings. *American Society of Civil Engineers*, Reston, VA, USA
- Balkaya C, Kalkan E (2003) Estimation of fundamental periods of shear-wall dominant building structures. *Earthquake Eng Struct Dyn* 32:985-998
- Balkaya C, Yuksel SB, Derinoz O (2012) Soil-structure interaction effects on the fundamental periods of the shear-wall dominant buildings. *Structural Design of Tall Buildings* 21:416-430
- Bendat JS, Piersol AG (2010) Random Data: Analysis and Measurement Procedures. *John Wiley & Sons 4th Ed*
- Bindi D, Petrovic B, Karapetrou S, Manakou M, Boxberger T, Raptakis D, Pitilakis KD, Parolai S (2015) Seismic response of an 8-story RC-building from ambient vibration analysis. *Bull Earthq Eng* 13:2095-2120
- Brincker R, Zhang L, Andersen P (2001) Modal identification from Ambient Responses using Frequency Domain Decomposition. *Smart Mater Struct* 10:441-445
- Celebi M, Ulusoy HS, Nakata N (2016) Responses of a tall building in Los Angeles, California as inferred from local and distant earthquakes. *Earthquake Spectra* 32:1821-1843
- Clinton JF, Bradford SC, Heaton TH, Favela J (2006) The observed wander of the natural frequencies in a structure. *Bull Seismol Soc Am* 96:237-257
- Clough RW, Penzien J (1993) Dynamics of Structures. *Mc Graw-Hill, New York*
- Chopra AK (1996) Modal analysis of linear dynamic systems: physical interpretation. *J Struct Eng* 122:517-527
- Dikmen SU, Edincliler A, Pinar A. (2015) Northern Aegean Earthquake (Mw=6.9): observations at three seismic downhole arrays in Istanbul. *Soil Dyn Earthq Eng* 77:321-36.
- Ditommaso R, Ponzo FC, Auletta G (2015) Damage detection on framed structures: modal curvature evaluation using Stockwell Transform under seismic excitation. *Earthq Eng & Eng Vib* 14:265-274
- Fleming K, Picozzi M, Milkereit C, Kühnlenz F, Lichtblau B, Fischer J, Zulfikar C, Özel O, SAFER and EDIM working groups (2009) The Self-organizing Seismic Early Warning Information Network (SOSEWIN). *Seismological Research Letters* 80:755-771
- Futterman WI (1962) Dispersive Body Waves. *Journal of Geophysical Research* 67, 13: 5279-5291
- Gabor D (1946) Theory of communications. *J Inst Electr Eng* 93:429-457
- Herak M, Herak D (2010) Continuous monitoring of dynamic parameters of the DGFSM building (Zagreb, Croatia). *Bull Earthq Eng* 8:657-669

- Ivanovic SS, Trifunac MD, Todorovska MI (2000) Ambient vibration tests of structures – a review. *ISSET Journal of Earthquake Technology* 37:165-197
- Kanai K (1965) Some new problems of seismic vibrations of a structure. In: *Proceedings of the 3rd world conference on earthquake engineering, Auckland and Wellington, New Zealand*
- Lee L, Chang K, Chun Y (2000) Experimental formula for the fundamental period of RC buildings with shear-wall dominant systems. *Structural Design of Tall Buildings* 9:295-307
- Mehta K, Snieder R, Grazier V (2007a) Extraction of near-surface properties for a lossy layered medium using the propagator matrix. *Geophys J Int* 169:271–280
- Mehta K, Snieder R, Grazier V (2007b) Downhole receiver function: A case study. *Bull Seismol Soc Am* 97:1396–1403
- Michel, C., S. Hans, P. Gueguen and C. Boutin (2006) In situ experiment and modelling of RC- structure using ambient vibration and Timoshenko beam, *First European Conference on Earthquake Engineering and Seismology, Geneva, Switzerland, 3-8 September 2006*, paper no. 1246.
- Michel C, Gueguen P, Bard PY (2008) Dynamic parameters of structures extracted from ambient vibration measurements: An aid for the seismic vulnerability assessment of existing buildings in moderate seismic hazard regions. *Soil Dynamics and Earthquake Engineering* 28:593-604
- Mikael A, Gueguen P, Bard PY, Roux P, Langlais M (2013) The analysis of long-term frequency and damping wandering in buildings using random decrement technique. *Bull Seismol Soc Am* 103:236-246
- Murià-Vila D, Rodriguez G, Zapata A, Toro AM (2001) Seismic response of a twice-retrofitted building, *ISSET Journal of Earthquake Technology* 38:67-92
- Nakata N, Snieder R, Kuroda S, Ito S, Aizawa T, Kunimi T (2013) Monitoring a building using deconvolution interferometry. I: Earth- quake-data analysis. *Bull Seismol Soc Am* 103:1662-1678
- Nakata N, Snieder R (2014) Monitoring a building using deconvolution interferometry, II: ambient vibration analysis. *Bull Seismol Soc Am* 104:204-213
- Oth A, Parolai S, Bindi D (2011) Spectral analysis of K-NET and KiK-net data in Japan, Part I: Database compilation and peculiarities. *Bull Seismol Soc Am* 101:652–666
- Paolucci R (1993) Soil-structure interaction effects on an instrumented building in Mexico City, *European Earthquake Engineering*, VII (3): 895-908
- Parolai S, Ansal A, Kurtulus A, Strollo A, Wang R, Zschau J (2009) The Ataköy vertical array (Turkey): Insights into seismic wave propagation in the shallow-most crustal layers by waveform. *Geophys J Int* 178:1649–1662
- Parolai S, Bindi D, Ansal A, Kurtulus A, Strollo A, Zschau J (2010) Determination of shallow S-wave attenuation by down-hole waveform deconvolution: A case study in Istanbul (Turkey). *Geophys J Int* 181:1147–1158
- Parolai S, Bindi D, Ullah S, Orunbaev S, Usupaev S, Moldobekov B, Echtler H (2013) The Bishkek vertical array (BIVA): Acquiring strong motion data in Kyrgyzstan and first results. *J Seismol* 17:707–719

Parolai S, Wang R, Bindi D (2012) Inversion of borehole weak motion records observed in Istanbul (Turkey). *Geophys J Int* 188:535–548

Petrovic B, Parolai S (2016) Joint deconvolution of building and downhole strong-motion recordings: evidence for the seismic wave field being radiated back into the shallow geological layers. *Bull Seismol Soc Am* 106:1720-1732

Petrovic B, Bindi D, Pilz M, Serio M, Orunbaev S, Niyazov J, Hakimov F, Yasunov P, Begaliev UT, Parolai S (2015) Building monitoring in Bishkek and Dushanbe by the use of ambient vibration analysis. *Annals of Geophysics* 58:1-13

Petrovic B, Dikmen SU, Parolai S, Safak E (2016) Studying the soil-structure interaction by joint deconvolution: The Ataköy (Istanbul, Turkey) vertical array. ACE2016 – 12th International Congress on Advances in Civil Engineering, Istanbul, Turkey

Petrovic B, Parolai S, Pianese G, Dikmen SU, Moldobekov B, Orunbaev S, Paolucci R (2017). Joint deconvolution of building and downhole seismic recordings: An application to three test cases. *Bulletin of Earthquake Engineering*, DOI :10.1007/s10518-017-0215-6

Pianese G, Petrovic B, Parolai S and Paolucci R (2018). Non-linear seismic response estimation of buildings by a combined Stockwell Transform and deconvolution interferometry approach. *Bulletin of Earthquake Engineering*, DOI: 10.1007/s10518-018-0307-y

Picozzi M, Parolai S, Mucciarelli M, Milkereit C, Bindi D, Ditommaso R, Vona M, Gallipoli MR, Zschau J (2009a) Interferometric analysis of strong ground motion for structural health monitoring: The example of the L'Aquila, Italy, seismic sequence of 2009. *Bull Seismol Soc Am* 101:635–651

Picozzi M, Strollo A, Parolai S, Cakti E, Ozel O, Karabulut S, Zschau J, Erdik M (2009b) Site characterization by seismic noise in Istanbul, Turkey. *Soil Dynamics and Earthquake Engineering* 29: 469-482

Pitilakis K, Karapetrou S, Bindi D, Manakou M, Petrovic B, Roumelioti Z, Boxberger T, Parolai S (2016) Structural monitoring and earthquake early warning systems for the AHEPA hospital in Thessaloniki. *Bull Earthq Eng* 14:2543-2563

Poudel UP, Fu G, Ye J (2007) Wavelet transformation of mode shape difference function for structural damage location identification. *Earthquake Engineering and Structural Dynamics* 36:1089-1107

Prieto GA, Lawrence JF, Chung AI and Kohler MD (2010) Impulse response of civil structures from ambient noise analysis. *Bull Seismol Soc Am* 100:2322-2328

Rahamani M, Todorovska MI (2013) 1D system identification of buildings from earthquake response by seismic interferometry with waveform inversion of impulse responses—method and application to Millikan Library. *Soil Dyn Earthq Eng* 47:157–174

Raub C, Bohnhoff M, Petrovic B, Parolai S, Malin P, Yanik K, Kartal RF, Kilic T (2016) Seismic-wave propagation in shallow layers at the GONAF-Tuzla site, Istanbul, Turkey. *Bull Seismol Soc Am* 106:912-927

SAP2000, Ver.18 (2016), Computers and Structures Inc., Walnut Creek, CA

- Safak E (1995) Detection and identification of soil-structure interaction in buildings from vibration recordings. *Journal of Structural Engineering*, ASCE 121, 5:899-906
- Safak E, Çelebi M (1990a) New techniques in record analyses: Torsional vibrations, Proceedings of the *Fourth U. S. National Conference on Earthquake Engineering, May 20-24, 1990, Palm Springs, California*, 2: 411-420.
- Safak E, Çelebi M (1990b) Method to estimate center of rigidity of a building using vibration recordings. *Journal of Structural Engineering*, ASCE 116, 1:85-97
- Snieder R, Şafak E (2006) Extracting the building response using seismic interferometry: Theory and application to the Millikan library in Pasadena, California. *Bull Seism Soc Am* 96:586-598
- Stewart J and Fenves G L (1998) System identification for evaluating soil–structure interaction effects in buildings from strong motion recordings. *Earthquake Engng. Struct. Dyn.* 27:869-885
- Stockwell RG, Mansinha L, Lowe RP (1996) Localization of the Complex Spectrum: The S Transform. *IEEE Trans Signal Process* 44:998–1001
- Tikhonov AN, Arsenin VY (1977) Solution of ill-posed problems. *Washington: Wiston/Wiley*.
- Todorovska MI (2009) Seismic Interferometry of a Soil-Structure Interaction Model with Coupled Horizontal and Rocking Response. *Bull Seismol Soc Am* 99:733-741
- Todorovska MI, Al RY (2006) Effects of rainfall on soil-structure system frequency: example based on poroelasticity and a comparison with full-scale measurements. *Soil Dyn Earthq Eng* 26:708-717
- Todorovska MI, Trifunac MD (2008a) Earthquake damage detection in the imperial country services building III: Analysis of wave travel times via impulse response functions. *Soil Dynamics and Earthquake Engineering* 28:387-404
- Todorovska MI, Trifunac MD (2008b) Earthquake damage detection in structures and early warning. *The 14th World Conference on Earthquake Engineering, October 12-17, 2008, Peking, China*
- Todorovska MI, Trifunac MD (2008c) Impulse response analysis of the Van Nuys 7-story hotel during 11 earthquakes and earthquake damage detection. *Structural Control and Health Monitoring* 15:90-116
- Trifunac MD, Todorovska MI, Manic MI, Bulajic BD (2008) Variability of the fixed-base and soil-structure system frequencies of a building — the case of Borik-2 building. *Struct Control Health Monit* 17:120-151
- TSI, Turkish Standards Institute (1997). TS498 – Design loads for buildings
- Yakut A, Gulkan P (2003) HOUSING REPORT Tunnel form building, *World Housing Encyclopedia*, www.world-housing.net/WHEReports/wh100104.pdf, accessed on August, 2016

Appendix c): Seismic-wave propagation in shallow layers at the GONAF-Tuzla site, Istanbul, Turkey

The final publication is available at SSA via <https://dx.doi.org/10.1785/0120150216>

Raub, C., M. Bohnhoff, B. Petrovic, S. Parolai, P. Malin, K. Yanik, R. F. Kartal, and T. Kilic (2016). Seismic-wave propagation in shallow layers at the GONAF-Tuzla site, Istanbul, Turkey, *Bull. Seismol. Soc. Am.*, 106, no. 3, 912-927.

Abstract

Using the first dataset available from the downhole Geophysical Observatory of the North Anatolian Fault, we investigated near-surface seismic wave propagation on the Tuzla Peninsula, Istanbul, Turkey. We selected a dataset of 26 seismograms recorded at Tuzla at sensor depths of 0, 71, 144, 215, and 288 m. To determine near-surface velocities and attenuation structures, the waveforms from all sensors were pairwise deconvolved and stacked. This produced low-noise empirical Green's functions for each borehole depth interval. From the Green's functions, we identified reflections from the free surface and a low-velocity layer between ~ 90 and ~ 140 m depth. The presence of a low-velocity zone was also confirmed by a sonic log run in the borehole. This structure, plus high near-surface P- and S-wave velocities of $\sim 3600 - 4100$ m/s and ~ 1800 m/s, lead to complex interference effects between up-going and down-going waves. As a result, the determination of quality factors (Q) with standard spectral ratio techniques was not possible. Instead, we forward modeled the Green's functions in the time domain to determine effective Q values and to refine our velocity estimates. The effective Q_P values for the depth intervals of 0–71 m, 0–144 m, 0–215 m and 0–288 m were found to be 19, 35, 39 and 42, respectively. For the S-waves, we obtained an effective Q_S of 20 in the depth interval of 0–288 m. Considering the assumptions made in our modeling approach, it is evident that these effective quality factors are biased by impedance contrasts between our observation points. Our results show that, even after correcting for a free-surface factor of 2, the motion at the surface was found to be 1.7 times greater than that at 71 m depth. Our efforts also illustrate some of the difficulties of dealing with site effects in a strongly heterogeneous subsurface.

Introduction

For numerous scientific applications such as earthquake source parameter studies (e.g. Hauksson et al., 1987; Abercrombie and Leary, 1993) it is important to quantify how near-surface geological structures influence the waveforms and amplitudes of seismic waves. Shallow subsurface geological features affect the seismic wave field through, amplification due to near surface low-impedance layers, resonance effects caused by strong impedance contrasts, and high frequency attenuation due to scattering, and intrinsic attenuation. Studies of these effects are usually based on a two-geographical-location comparison method. A common practice is to compare recordings from the site of interest to those from a close-by reference station, preferably one installed on outcropping bedrock or in a deep borehole – the optimum being a vertical array of seismometers from the surface down to competent rock (Steidl et al., 1996). In the latter circumstance, with a sufficient number of sensors the mechanical properties of the soil can be measured directly for different depth intervals.

Such an arrangement exists at the Tuzla Peninsula site of the Geophysical Observatory of the North Anatolian Fault (GONAF), southeastern Istanbul, Turkey (Fig. 1). The GONAF-Tuzla array includes five levels of borehole seismometers extending down to ~300 m depth (Fig. 2). It was the first of seven GONAF vertical arrays to be installed around the eastern Marmara Sea (Prevedel et al., 2015). The seismic data collected at Tuzla provide a base for a better understanding of wave propagation in the shallow geological layers around this site, and improve source parameter and ground motion estimates that are necessary for preparing hazard scenarios locally and in the immediate surrounding area of Istanbul, with its 15 million inhabitants.

We focus here on the 1 kHz sampling-rate seismograms of 26 nearby microearthquakes recorded at Tuzla. Our study is an initial investigation of this site's amplification, attenuation (quality factor Q), seismic velocity and shallow wave propagation effects. Spectral ratio techniques are widely used to determine near-surface amplification and the quality factor (e.g. Malin et al., 1988; Safak, 1997; Assimaki et al., 2008). However, as discussed later in the text, the high seismic velocities and heterogeneities at the Tuzla site lead to strong interference effects between up- and down-going waves, the latter ones being reflected at the surface and at reflectors between the borehole seismometers. These interference effects cause complicated spectra, which makes a stable determination of Q based on spectral ratios difficult (Trampert et al., 1993; Bethmann et al., 2012). As a result, our application of them failed to give meaningful results.

Accordingly, we chose to apply an alternative approach based on deconvolution interferometry which makes use of the complete wave field and takes advantage of the surface reflected wave, instead of regarding it as a troublesome source of interference. The method also enables us to determine the velocity structure between the borehole seismometers and to evaluate amplification and shallow wave propagation effects.

Deconvolution interferometry is used to estimate the impulse response between two receivers (e.g. Vasconcelos and Snieder, 2008a). It is applied, for example, for imaging purposes (Vasconcelos and Snieder, 2008b), retrieving building response to ground shaking (Snieder and Şafak, 2006; Bindi et al., 2015) and for determining near-surface velocities (van Vossen et al., 2004; Parolai et al., 2009; Nakata and Snieder, 2012). Deconvolution interferometry has also found applications in estimating site specific Q values. Parolai et al. (2010) determined site related Q values by fitting the amplitude spectrum of the

deconvolved wave field using analytical models, and Parolai et al. (2012) derived Q by performing a full inversion of the spectrum.

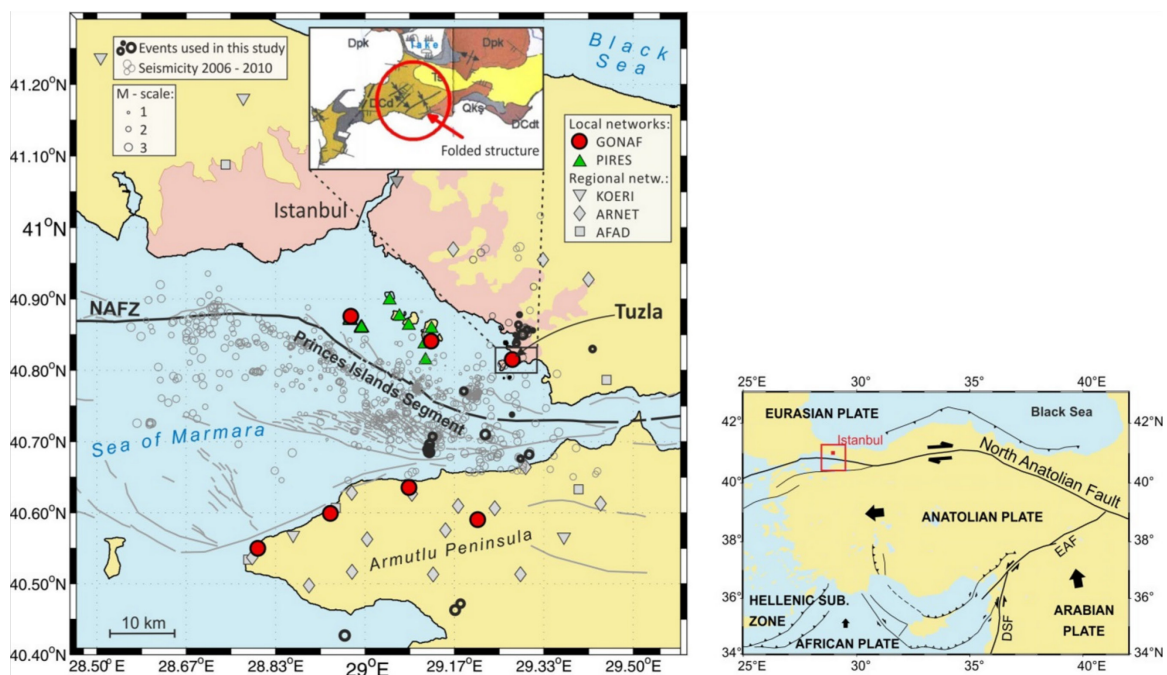


Figure 1. Right) Location map of the Anatolian region with the main tectonic features forming the North Anatolian Fault. The red box marks the study area (enlarged left). Bold black arrows indicate the direction of the plate motion with respect to stable Eurasia. Left) Map of the eastern Marmara Sea showing the local microseismic activity (light gray circles, after Bohnhoff et al., 2013) obtained from the island-based PIREs network and selected regional seismometer stations during 2006 – 2010. The GONAF wells with vertical seismometer arrays are indicated by bold filled circles. Black open circles are the earthquakes used in this study. Fault locations are from Armijo et al. (2005). The bold black line marks the Princess Islands segment and adjacent portions as the main branch of the NAFZ below the eastern Sea of Marmara. The inset shows the geological map of the vicinity of the Tuzla area as the location of the GONAF borehole array (Apart, 2012 rpt., pers. comm.).

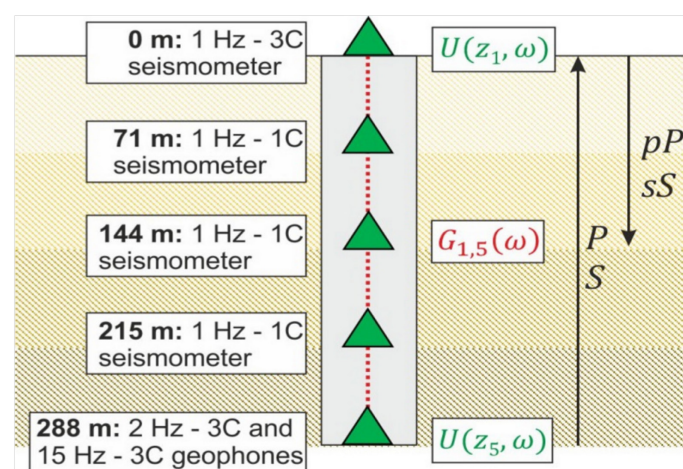


Figure 2. Sketch of the GONAF-Tuzla vertical borehole array and experiment geometry. Instruments are indicated with triangles and the direct P- and S-waves (P, S) and their corresponding surface reflections (pP, sS) are sketched with arrows. Details of the instrumentation are described in Prevedel et al. (2015).

Time domain approaches for the estimation of Q are less common. For example Snieder and Safak (2006) determined Q_S in a building by fitting the slopes of the logarithm of envelopes of deconvolved seismograms. Trampert et al. (1993) estimated Q_S between a 500 m deep borehole geophone and a surface seismometer by a time domain SH-propagator inversion. The theory of the propagator inversion technique was extended by Mehta et al. (2007) for the P-SV case for attenuating media. However, their paper did not provide an application of it to actually determine Q values.

In our data analysis we pairwise deconvolve the downhole recordings of the 26 events with their surface recordings. The deconvolution was also checked in the reverse sense, using the deepest sensor as reference. Instead of performing an inversion as proposed by Trampert et al. (1993), or analyzing the deconvolved wave field in the frequency domain as proposed by Parolai et al. (2010, 2012), we forward model the deconvolved seismograms in the time domain. With a grid search we found the seismic velocities for P- and S-waves V_P , V_S and quality factors Q_P and Q_S that best fit the data in a least squares sense.

For the estimation of effective velocities and quality factors we assumed a single homogeneous layer above each borehole sensor. With the further assumption that the P- and S-wave parameters can be determined independently the modeling procedure could be reduced to a simple 2-D grid search. Given that the interferometric results and logging data reveal the presence of a low velocity layer, these strong heterogeneities bias our Q estimates. The resulting Q values need to be regarded as apparent values that are mixtures of intrinsic and scattered attenuation and impedance effects.

Tectonic setting and the GONAF project

The North Anatolian Fault Zone (NAFZ) is a right-lateral strike-slip transform fault. It spans ~1300 km from eastern Anatolia to the northern Aegean Sea (e.g. Barka, 1992). It forms the plate boundary between the Anatolian plate in the south and the Eurasian plate in the north and slips at a rate of 20 – 30 mm/a (McClusky et al., 2000). This kinematic framework is driven by the northward pushing Arabian plate in the east and the southward pulling rollback of the Hellenic subduction zone in the west (Flerit et al., 2004; Bohnhoff et al., 2005) (Fig. 1, right, bottom).

In the last century ~900 km of the NAFZ has ruptured in a series of $M > 6.7$ earthquakes that started in 1939 near Erzincan in eastern Anatolia. This series then systematically propagated westward towards the Istanbul-Marmara area (Stein et al., 1997). The most recent events occurred near Izmit and Düzce in 1999, which suffered M_w 7.4 and 7.1 earthquakes respectively (Tibi et al., 2001; Barka et al., 2002).

The only NAFZ segment that has not experienced a major earthquake since 1766 lies to the west of the Izmit rupture and below the Sea of Marmara. It is considered to be in the final stage of its seismic cycle, with a 35 – 70 % probability for a $M > 7$ earthquake to occur by 2034 (HubertFerrari et al., 2000; Parsons, 2004). The eastern part of this ‘Marmara seismic gap’ is located within 20 km of Istanbul’s historic city center. Due to this regional seismic hazard and its associated risks, numerous local and regional seismic monitoring projects are being conducted along the seismic gap. One focus of these studies is the eastern part of the Marmara region offshore Istanbul.

For example, Bohnhoff et al. (2013) studied microearthquakes recorded by a near-fault seismic network on the Princes Islands – the PIREs network (Bulut et al., 2009, 2011). Based on a four-year hypocenter

catalogue, these authors identified a ≥ 30 km long aseismic fault patch extending down to 10 km depth south of the Princes Islands. They concluded that this sub-segment might be locked and thus represents a potential nucleation point for an impending Marmara earthquake. This view is also supported by GPS data (Ergintav et al., 2014).

The recently implemented GONAF borehole observatory is part of an intensified monitoring effort in the eastern Marmara region. It includes seven vertical arrays of seismometers in ~ 300 m deep boreholes. Five of these are on-land and two are on-island sites surrounding the eastern Sea of Marmara (Fig. 1). These stations are unique in that they make use of the only possible long term on-land and near-fault sites surrounding the seismicity gap. Their borehole designs enables monitoring under low-noise conditions even in this highly populated area. This results in that the GONAF network has lowered the magnitude of completeness in the study area by two magnitude units with respect to the present regional networks, allowing the detection of nearly 2 orders of magnitude more seismic events (Prevedel et al., 2015).

In this study, we use recordings from the first GONAF borehole, completed in January 2013 on the Tuzla peninsula southeast of Istanbul (Fig. 1). The GONAF-Tuzla array consists of a three component (3C) Mark Products L4 seismometer with a natural frequency of 1 Hz at the surface, three L4 vertical component (1C) seismometers at ~ 75 m depth-spacing and a bottom sonde with two 3C Geospace geophones of 2 Hz and 15 Hz natural frequency, both in the same housing at 288 m depth (Fig. 2). More detailed information about the borehole construction and instrumentation is given in Prevedel et al. (2015). In the current study we use data from May 2013. Up to mid May 2013 the sampling rate was 2000 Hz. It was reduced to 1000 Hz thereafter.

Local geology at Tuzla

The Tuzla peninsula was selected for a GONAF site due to its short distance to the Princes Islands seismic gap and a prominent seismicity cluster. It also has the advantage of being in some distance from the central-city-induced seismic noise. It is, however, still within a densely populated area that includes industrial infrastructure. The ground water level is shallow in this area at ~ 10 m depth. Drilling at this site was conducted in late 2012, during which cutting samples were taken every meter.

From the cuttings, it appears that the 288 m deep Tuzla borehole was drilled into a single limestone formation (Esen Arpat, 2012 rpt., pers. comm.). The cuttings have the lithological characteristics of the Tuzla Limestone, a member of the Denizli Köyü formation of late Devonian age. The thickness of the Tuzla Limestone at neighboring Marmara coastal sites is estimated to be ~ 60 m (Özgül, 2012). However, northeast-southwest trending tight folds have been mapped in the eastern Istanbul area (inset, Fig. 1, left), which makes it difficult to obtain a reliable thickness (Özgül, 2012). There is no information available on the inclination of the beddings, but it is possible that the substantial difference between the 288 m thickness obtained from the Tuzla cuttings and the 60 m estimated from outcrops can be explained by a steeply dipping limb of folded limestone beds. This is illustrated in a simplified sketch in Fig. 3a. Due to the lack of geological cross sections from the Tuzla area, the sketches in Fig. 3 are speculative, but are shown here to guide our interpretation of Tuzla data.

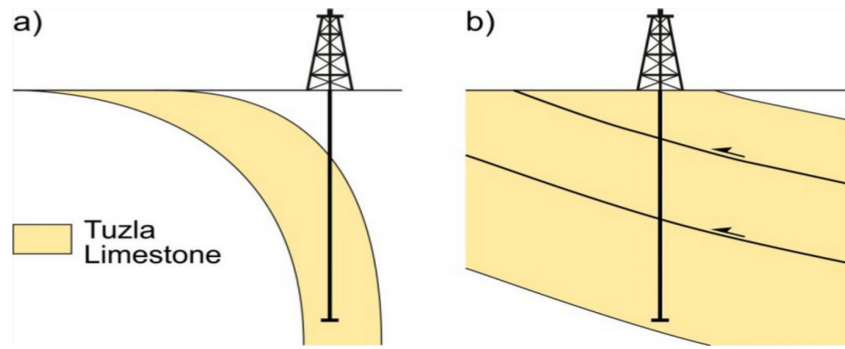


Figure 3. Sketch to illustrate two possible models derived for the observed 288 m deep Tuzla Limestone formation. a) The borehole was drilled into a steeply dipping limb of folded limestone beds. b) The borehole was drilled into a repeating sequence of the Tuzla Limestone caused by thrust faulting.

Additional information on the local structure comes from well-logging measurements down to a depth of 258 m (Jochem Kueck, GFZ rpt., pers. comm.). The P- and S-wave velocity profiles from the sonic log are displayed in Fig. 4. The sampling of these logs is 10 cm, which is substantially finer than the spatial resolution to be obtained from microearthquake waveform data, suggesting these data need to be averaged. Silva and Stovas (2009) have quantified to what extent different well-log averaging methods preserve lower-frequency seismic properties and how they are suitable for velocity model building. Following their results we generated our velocity model from the sonic log using Equation (1) for calculating interval velocities:

$$V_i = \left[\left(\sum_{n=1}^N V(n) \right) / \left(\sum_{n=1}^N V(n)^{-1} \right) \right]^{-1/2}, \quad (1)$$

where N is the number of sonic log velocity samples $V(n)$ within a given layer. We chose our layer boundaries to be at the sensor depths, at 71 m, 144 m and 215 m. The derived velocity model is presented in Fig. 4 and listed in Table 2.

Spectra of well log sequences usually follow a power-law scaling of $k^{-\alpha}$ with spatial frequency k and $\alpha \approx 1$. This rule is irrespective of rock type or observation scale (e.g. Shiomi et al., 1997; Leary and Al-Kindy, 2002). The α value of the Tuzla P-wave log is 1.01, a typical value for fractured rock, whereas the value for the S-wave log is 0.28. This suggests that while the V_P log is a valid measure of the local P-wave velocity, the V_S log appears to be unreliable, perhaps due to some aspect of the logging procedure or well conditions.

The P-wave sonic log shows a complex seismic velocity structure. Most significantly, near surface P-wave velocities of ~ 3600 m/s lie above a velocity inversion to less than ~ 3400 m/s at ~ 90 m depth. This ~ 50 m thick interval is followed by an increasing trend to ~ 4100 m/s at the bottom of the well log at 258 m.

This P-wave sonic log seems somewhat at odds with the uniform lithological character of the well cuttings. However, some features of the other types of well logs also indicate a more heterogeneous layering (see Fig. S1 in the Supplementary material). We observe relatively low resistivity values for the interval of ~ 85 m to ~ 105 m, and irregularities in the whole diameter caliper log at ~ 90 m to ~ 140 m depth. While these irregularities are not enough to account for the observed low velocities, they do add to their uncertainties. The resistivity and caliper logs might be interpreted as an indication for a

weak zone, perhaps of thrust faulting origin. Thus, another possible explanation for the unexpected thickness of the limestone layer could be repetition of the sequence as a result of thrust faulting associated with the local folding (Esen Arpat, pers. comm.) (Fig. 3b).

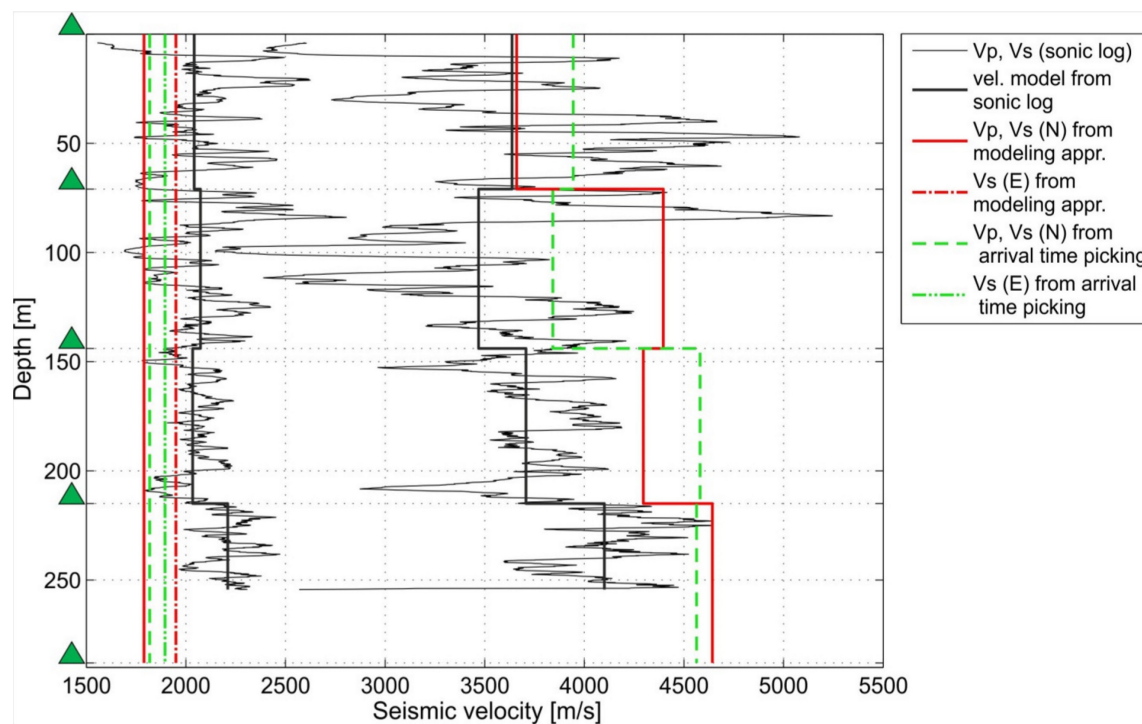


Figure 4. Sonic log velocities (black thin line) and P and S-wave velocity model derived from the sonic log (black bold line) are presented together with the velocity models obtained from the modeling approach and from arrival time picking in the deconvolved seismograms. For the Swave velocity different results are obtained from the E and N components, thus both values are shown. Triangles on the left indicate the positions of the borehole geophones along the well (see Fig. 2).

Dataset

We used both GONAF-Tuzla (vertical array) and PIRES (island-based surface stations) waveform recordings to compile a local hypocenter catalog to study near-surface wave propagation effects. For earthquake detection we applied a short-term average / long-term average trigger to the vertical component signals from all of these stations. A seismic event was declared when three or more verticals triggered within a time window of 5 s.

We also took into account events that were too weak to be detected on the surface PIRES stations, but detected with the GONAF-Tuzla borehole array. In the May 2013 time period considered here, 188 events were detected by the combined network. Of these, 153 could be located using the HYPOCENTER computer code (Lienert et al., 1986) and the optimized 1-D velocity model for the eastern Marmara region of Bulut et al. (2007).

For this study we selected events with signal-to-noise ratios > 4 at the GONAF-Tuzla sensor at 215 m depth. The ratio was calculated by dividing the root-mean-square amplitude of the first 0.3 s of the P-wave train by that of a 10 s noise window before the P-wave arrival. A total of 26 events with duration magnitudes from 0.6 to 2.9 and hypocentral distances from 7 to 51 km from the GONAF-Tuzla array fit this criterion (black open circles in Fig. 1 and list of earthquakes in Tab. 1). The seismograms from all the 1 and 2 Hz sensors for these events were used to analyze the wave propagation effected in the shallowest layers.

Fig. 5 shows an unfiltered, but instrument corrected, waveform example from the GONAF-Tuzla array for event number 18 in Table 1. The up-going direct P- and S-waves and their corresponding down-going surface reflections (pP and sS) can be clearly seen in these seismograms. As expected, the attenuation of the waves as they travel to the surface and then down again significantly reduces their amplitudes. At the surface station one also sees reverberations following the direct P-wave. As we will discuss, these secondary arrivals are observed for many events and appear to be due to the shallow subsurface structure.

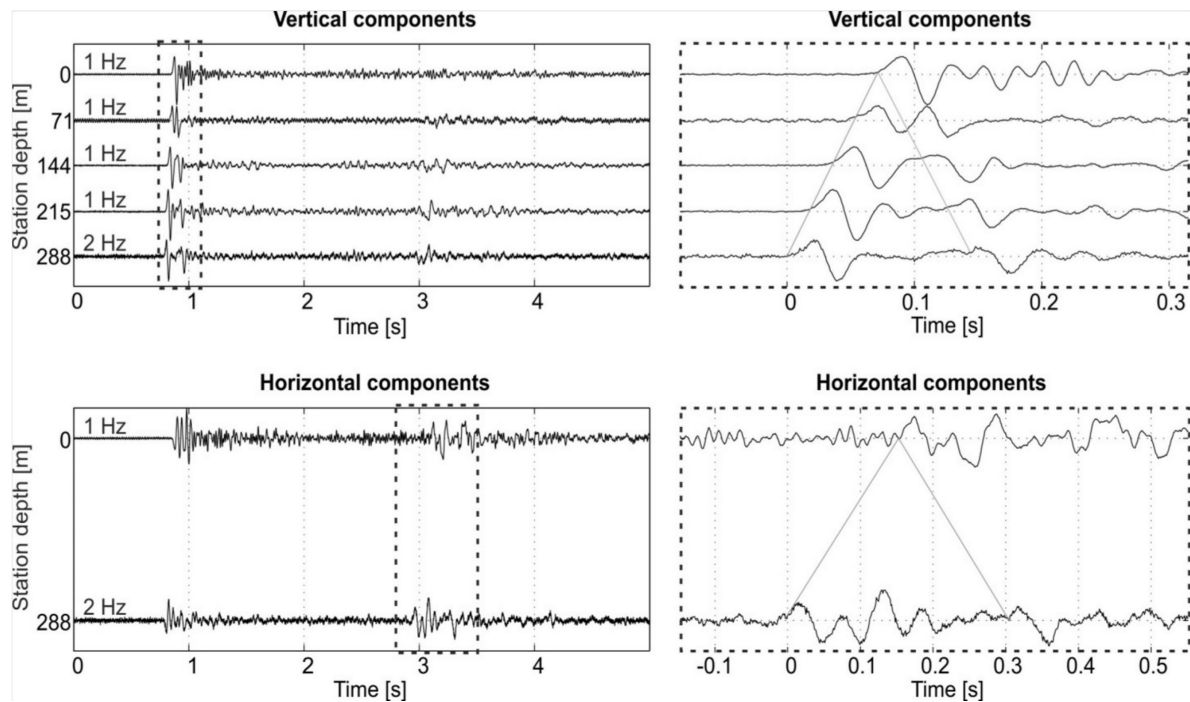


Figure 5. Waveform example from vertical and north-south horizontal components of the GONAF-Tuzla array. The respective sensor depth is plotted at the y-axis and each trace is normalized to its maximum. The instrument response has been corrected for and the seismograms are otherwise unfiltered. Note that only the surface station and the very deepest sensor have horizontal components. Left hand side figures show complete waveforms of event 18 (Table 1) and the right side figures present close up windows of the same event containing only the P-wave (top) and S-wave (bottom), respectively. The direct up-going P- and S-waves and their corresponding down-going surface reflections are marked with gray lines.

Table 1. Source Parameters of the 26 Earthquakes Used for Shallow Wave-Propagation Study

Event	Date, Time (UTC)	Longitude	Latitude	Depth [km]	Magnitude [M _D]	Hypocentral distance [km]
1	2013/5/1 17:43:50.8	29.1680	40.4630	8.2	2.7	41.0
2	2013/5/1 22:43:46.5	29.3020	40.8570	7.8	1.8	9.4
3	2013/5/1 23:13:51.9	29.2940	40.8500	7.3	2.6	8.4
4	2013/05/03 00:36:10.2	29.184	40.771	8.5	2.0	12.4
5	2013/05/03 12:17:23.1	29.282	40.842	7.2	1.1	7.8
6	2013/05/03 09:45:10.7	29.424	40.83	0.4	1.7	12.7
7	2013/05/05 20:34:24.0	29.313	40.856	5.0		7.5
8	2013/05/07 09:41:39.8	29.286	40.864	4.6	1.7	7.2
9	2013/05/09 04:53:4.5	29.12	40.685	8.6	2.7	21.3
10	2013/05/09 05:37:9.4	29.126	40.707	11.0	2.2	20.5
11	2013/05/09 06:05:48.5	29.117	40.689	11.6	2.5	22.5
12	2013/05/10 01:59:14.9	29.119	40.691	9.9	1.9	21.5
13	2013/05/10 08:24:42.1	29.119	40.691	9.1	2.4	21.1
14	2013/05/10 23:57:18.9	29.12	40.686	8.7	2.4	21.2
15	2013/05/11 09:52:7.8	29.28	40.85	6.0	0.9	7.2
16	2013/05/12 04:32:39.4	29.118	40.685	7.8	2.4	21.1
17	2013/05/12 23:16:13.6	29.29	40.676	7.2	1.7	17.1
18	2013/05/12 23:43:35.1	29.306	40.682	9.0	2.4	17.5
19	2013/05/14 14:26:49.5	29.288	40.878	0.6	1.2	7.1
20	2013/05/18 20:02:27.1	29.286	40.857	5.6	0.6	7.3
21	2013/05/19 19:42:21.3	29.178	40.472	7.7	2.3	39.8

22	2013/05/19 22:16:41.0	29.12	40.696	11.4	2.5	21.8
23	2013/05/21 10:05:23.3	28.962	40.427	0.0	2.9	50.6
24	2013/05/24 20:24:40.9	29.274	40.738	8.0		11.7
25	2013/05/26 00:11:45.8	29.224	40.71	9.1	2.6	15.4
26	2013/05/30 07:49:52.7	29.282	40.838	7.9	1.9	8.3

Method

One aim of the GONAF effort is to determine the P- and S-wave velocity and attenuation structure for each borehole site. A common method used to find the quality factor Q is the spectral ratio technique (e.g. Gibbs et al., 1994; Parolai et al., 2007; Ge et al., 2009). It typically begins by computing the ratio of the Fourier spectra of isolated P and S waves between the surface and downhole seismograms, after taking into account instrument responses and other gain factors not related to attenuation. At the Tuzla site the travel time differences between P and pP and S and sS at the 288 m deep sensor are only ~ 0.13 s and ~ 0.32 s, respectively. These separations are relatively short compared to other studies (e.g. Blakeslee and Malin, 1991; Bethmann *et al.*, 2012). This limits the bandwidth over which the spectral ratios can be fit with a constant Q model, $Q = \pi \delta t m^{-1}$, m being the slope of the ratio and $\pi \delta t$ the travel time difference between the recording levels (Aki and Richards, 2002). These and other interference effects result in meaningless Q values.

In order to make use of the complete wave field, including the signals from down-going waves, we chose instead to apply a seismic interferometry approach to determine the characteristics of the Tuzla site. This approach also allows us to determine the velocity structure between the borehole sensors. Several algorithms exist for interferometry, but here we focus on the deconvolution technique (e.g. Trampert et al., 1993; Vossen et al., 2004; Mehta et al., 2007; Parolai et al., 2009; Nakata and Snieder, 2012).

We first applied instrument response corrections to each seismogram and assumed near-vertical incidence at the bottom sensor, and that all sensors in the borehole are subject to the same source and path effects (from the source to the deepest sensor). The deconvolution of the earthquake signal at sensor at depth z_1 with that at depth z_2 yields the plane wave Green's function $G_{1,2}$ for propagation from z_2 to z_1 . This can be written in frequency domain as

$$G_{1,2}(\omega) = \frac{U(z_1, \omega)}{U(z_2, \omega)}, \quad (2)$$

where ω is the angular frequency and $U(\omega)$ is the Fourier spectrum of the seismogram. The fraction in Equation (2) also can be turned around to yield the Green's function for propagation from z_1 to z_2 .

Since the signals are band-limited, contaminated by background noise, and contain site related notches in their spectra, the spectral division in Eq. (2) is inherently unstable. To prevent this instability a

regularized deconvolution is typically used. We tested two different regularizations. The first is used for example by Mehta et al. (2007), Parolai et al. (2009) and Nakata and Snieder (2012), and the second is the method of Helmberger and Wiggins (1971) and Dey-Sarkar and Wiggins (1976). The first turned out to be more stable for our data, and is given by:

$$G_{1,2}(\omega) \approx W(\omega) \frac{U(z_1, \omega)}{U(z_2, \omega)}, \quad (3)$$

where

$$W(\omega) = \frac{|U(z_2, \omega)|^2}{|U(z_2, \omega)|^2 + \varepsilon} \quad (4)$$

is the filter, hence

$$G_{1,2}(\omega) \approx \frac{U(z_1, \omega)U(z_2, \omega)^*}{|U(z_2, \omega)|^2 + \varepsilon}. \quad (5)$$

The regularization parameter ε refers to a constant added to the denominator to prevent numerical instabilities in Eq. (2) (e.g. Parolai et al., 2009). It is chosen as a percentage of the average spectral power of (ω) at the station selected as reference. Tests have shown that an ε of 3 % seems to be the appropriate value for our data.

Data Processing

In order to use the horizontal components of the surface and downhole sensors it is necessary to rotate the downhole horizontal components into N and E directions so that their orientation equals the orientation of the surface horizontal components. How the rotation angle is determined is explained in detail in Appendix A.

After orienting the downhole horizontal components the seismograms of all channels were then rotated into radial and transverse directions and corrected for instrument response and DC offset. As in previous deconvolution studies (Mehta et al., 2007; Parolai et al., 2009), our results were insensitive to the data window selection. Accordingly, we chose to use windows containing the complete signal of the event. This data window was tapered to avoid spectral leakage.

The deconvolution was performed by applying Eq. (5). The bandwidth of the deconvolution was set to 0.1 to 40 Hz, as all 26 events have energy at least up to ~ 40 Hz (see spectra in Fig. S2 – S14 in the Supplementary material). The lower limit of the bandpass turned out to be helpful in removing very-low-frequency noise, but its influence on the deconvolution result was only minor. Thus, a low corner frequency of 0.1 Hz was chosen to include as many octaves of bandwidth as possible. As the last step all the deconvolved spectra are inverse Fourier transformed into time domain and then stacked to improve the signal-to-noise ratio. The stacking requires the assumption of nearly vertical incidence, meaning equal moveouts along the borehole for all events. We checked these times in the deconvolved seismograms and found only minor travel time differences of < 0.01 s. Fig. 6 shows the surface-to-144 m vertical component deconvolution results for each event and their stacking result.

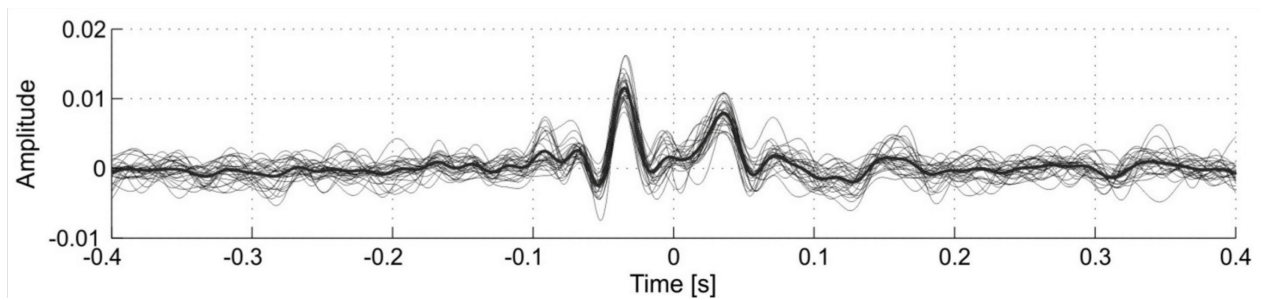


Figure 6. Seismograms from the sensor at 144 m depth after deconvolution from the surface signal. Thin traces show the results from each of the 26 events. The bold trace is the stacked deconvolved seismogram.

Deconvolution results and discussion

Fig. 7a and b display the deconvolved seismograms with the surface and 288 m sensor used as reference. When the signal at the surface is used as reference the up-going waves are mapped onto times before their surface arrival. Thus the up- and down-going waves are symmetric around the surface arrival time, which is taken to be the zero reference. When the 288 m sensor is used as reference, all the signals appear after its arrival time. In Fig. 7a each trace is normalized to its maximum to show the relatively small down-going signal amplitudes at the deepest sensor. To allow for amplitude comparisons between different depth levels, each trace in Fig. 7b is normalized to the maximum of the entire array.

Fig. 7b shows clearly how the amplitude of the up-going wave decreases while propagating from 288 m to 71 m depth. However, in the upper tens of meters between the sensor at 71 m depth and the surface the amplitude increases. After correcting for the free surface amplitude factor of 2 the surface sensor still records a 1.7 times stronger signal than the sensor at 71 m. This factor of 2 is only correct for vertically incident and SH waves. For P- and SV-waves it varies with incidence angle and can be even below 1 (Shearer and Orcutt, 1987). The amplitude increase in the upper few tens of meters indicates that in these shallow depths at the Tuzla site amplification due to impedance contrasts influences the waveforms more strongly than the effects of attenuation. If these impedance effects are not taken into account, it is only possible to determine an apparent attenuation, as will be discussed later.

The average seismic velocities between sensors can be calculated from the travel time differences between them in the deconvolved records (Table 2 and Fig. 4). Since only the surface sensor and the sensors at 288 m depth have horizontal components, an average S-wave velocity could be determined only between them.

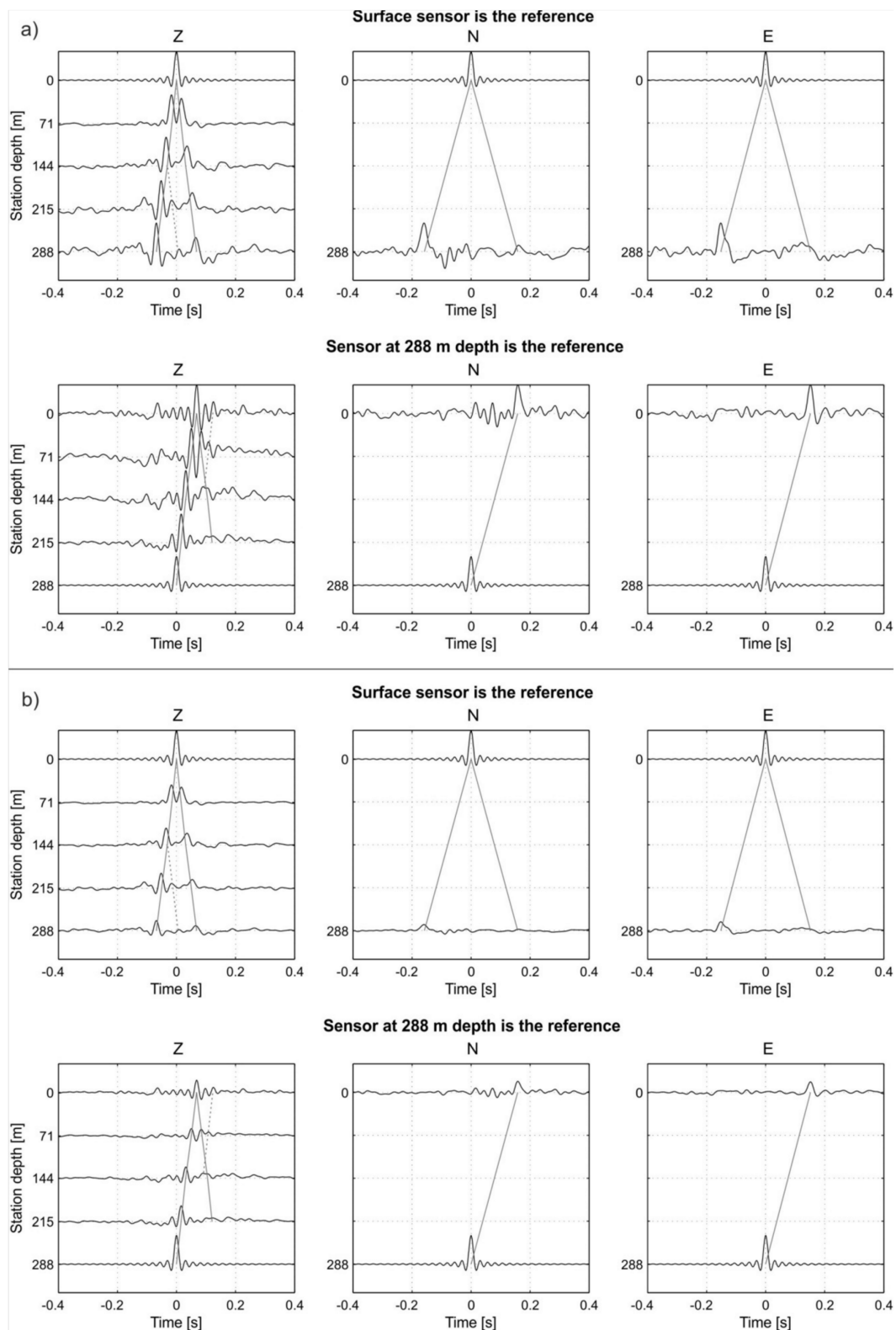


Figure 7. Stacked deconvolved seismograms from vertical and horizontal components. Once the surface sensor is used as reference sensor (top) and the other time the sensor at 288 m depth is used as reference (bottom). Gray solid lines mark the travel times of the direct up- and down-going waves and dashed gray lines indicate reflected phases. a) Each trace is normalized to its maximum. b) Each trace is normalized to the maximum of the entire array.

Table 2. Seismic interval velocities between the sensors of the GONAF-Tuzla array derived from sonic logs and arrival time picking.

Depth [m]	Sonic log		Arrival time picking	
	V_P [m/s]	V_S [m/s]	V_P [m/s]	V_S [m/s] (N/E)
0 – 71	3637	2042	3944 ± 46	$1818 \pm 3 / 1895 \pm 3$
71 – 144	3469	2073	3842 ± 40	
144 – 215	3707	2034	4581 ± 63	
215 – 288	4100	2210	4563 ± 13	

Velocities are derived from sonic-log measurements using Eq. (1) and from arrival time picking of the direct P- and S-waves in the deconvolved seismograms with the downhole sensor at 288 m depth used as reference (7a and b, bottom, left).

The arrival time picking of the direct up-going P-wave shows that a strong change in P-wave velocity exist somewhere between 71 m and 215 m depth (Fig. 7a and b, bottom left). Further, two reflected P-waves can be seen in the deconvolved seismograms. These are marked with gray dashed lines in Fig. 7. The up-going reflected wave, seen on the bottom left in Fig. 7a and b, and the down-going reflected wave, seen on the top left in Fig. 7a and b appear to originate from an interface between the sensors at 71 and 144 m. Such a horizon could correspond to the low velocity zone evident in the sonic log velocity profile between ~ 90 and ~ 140 m depth (Fig. 4). Reassuringly, the polarities of the reflected waves agree with the presence of a low-velocity layer. The reverberations after the direct P-wave arrival at the surface sensor seen in the unfiltered seismograms (Fig. 5) could be created by multiple reflections from this layer.

The arrival time picking of the S-wave suggests that the S-wave velocity appears to be 4 % slower on the N component than at the E component. This could be an indication of shear-wave splitting – a difference in S-wave velocity as a function of azimuth – rather than an artefact of the method. The eastern Sea of Marmara is known to show this type of anisotropy as reported by Hurd and Bohnhoff (2012) and Eken et al. (2013). The S-anisotropy in the depth range of ~ 3 to ~ 10 km was estimated to be $\sim 1 - 3$ %. Moreover, Eken et al. (2013) also found the fast polarization direction north of the Princes Islands segment to be parallel to the main NAFZ strand, and along maximum horizontal stress direction, $S_{Hmax} \sim N125^\circ E$ (Kiratzi, 2002; Bohnhoff et al., 2006). These observations could account for the splitting direction seen at Tuzla. A further indication for having a true shear-wave splitting observation in our data is that following Nakata and Snieder (2012) deconvolution interferometry can be used for shear wave splitting analysis, which however, would be beyond the scope of this study.

Forward modelling

We modeled the deconvolved seismograms from the Tuzla site with the layered, frequency wavenumber propagator method of Wang (1999). The source for these time-domain synthetic seismograms was placed 1 km directly below the receiver points. The aim was to obtain a first order estimate of the apparent P- and S-wave Q values and to refine the velocities of the layers between the sensors.

Because of the uncertainties introduced by the unconstrained structures evident at the Tuzla site, we chose to reduce the layering above each sensor to a single, homogeneous, effective unit. This approach allowed us to use a grid search method for the best fit model. It resulted in four different effective P-

wave velocity and attenuation models, covering the depth ranges 0 – 71, 0 – 144, 0 – 215, and 0 – 288 m. The effective S-wave velocity and quality factor was determined for a homogeneous layer between the horizontal components at 0 – 288 m. These effective parameters are indicated here by an over-bar, as in $\overline{V_P}$ versus V_P for the interval velocities, and $\overline{Q_P}$ for the effective quality factors. We discuss later how these values relate to ones that might have been obtained for the individual intervals.

After the computation of synthetic seismograms the same processing steps as for the observed waveform data were applied and then the results compared to the observations. In our grid search, we sought to find for the minimum misfit between the observed amplitudes and arrival times of the up- and down-going waves (A_u^o, A_d^o and t_u^o, t_d^o) and their corresponding synthetic values (A_u^s, A_d^s and t_u^s, t_d^s) as given by

$$m(V, Q) = \sqrt{(A_u^o - A_u^s)^2 + (A_d^o - A_d^s)^2 + (t_u^o - t_u^s)^2 + (t_d^o - t_d^s)^2}. \quad (6)$$

To reduce computation time this 4-D grid search (V_P, Q_P, V_S and Q_S) was separated into two 2-D searches, with the P- and S-wave parameters being determined independently. Q_S and V_S for SH waves are inherently independent of Q_P and V_P . For the P-SV case, the S-parameters are held fix while determining V_P and Q_P and similarly for Q_S and V_S . Also, under the assumption of frequency constant Q_P, V_P could be determined independently from the other parameters, since it depends only on the arrival times of the P-wave. Only Q_P has a dependency on both, P- and Swave velocity, because it is determined from the amplitude of the P-wave recording which in turn depends on the impedance contrast that is controlling the amount of energy reflected and refracted as P-wave and converted S-wave. Under the assumption of vertical incidence, these conversions are reliable. Nevertheless, even if this assumption is broken, if the S-wave velocity is fixed to a value close to the true value the error in Q_P introduced by this simplification will be small, as we will show. For the P- and S-wave parameters we searched a range of velocities from 3000 – 4600 m/s and 1600 – 2100 m/s, and quality factors from 1 – 100 and 1 – 50, respectively.

The misfit functions are presented in Fig. 8, with their minima marked by a white dot. For all three components we observe that in the misfit functions the apparent Q values are well constrained, whereas the velocities appear less well constrained. Nonetheless, clear minima can be observed for the horizontal components, but less so for the vertical components. To better constrain the velocity, tests have shown that the terms in Eq. (6) containing the arrival times should be weighted more heavily than the amplitude terms. This however, reduces the capability for resolving Q . Since we already have good velocity information from sonic log data and arrival time picking in the deconvolved seismograms, we decided against a velocity weighted misfit function to obtain better constrained Q values. On the E component the velocity and Q are less constrained compared to the N component. This is because the down-going wave is poorly resolved on the E component due to interference with two peaks that precede its arrival (Fig. 7a, top right).

The best fit model effective velocities and quality factors are summed in Table 3. We observe increasing Q_P with increasing depth and (288 m) $\approx 2Q_S$ (288 m), which is in good correspondence with theory. Overall, the average P-wave velocities obtained from the modeling approach are very similar to the P-wave root-mean-square velocities derived from the arrival time picking. Going from the uppermost homogeneous layer to the deepest these are 3944 m/s, 3892 m/s, 4106 m/s, and 4217 m/s. The effective P-wave velocities obtained from the modeling approach can be transferred to interval velocities using the Dix Equation (Dix, 1955) (see Table 3). These values are in contrast to the velocities derived from

arrival time picking and the P-wave sonic log: the forward modeling places a more modes low velocity layer at a deeper depth.

Figure 9 presents the model seismograms computed with the parameters listed in Table 3 in comparison to the observed deconvolved seismograms. The modeled up- and down-going S- and P-waves on the N and Z components fit better than on the E component. This can be explained by the weak down-going S-wave on the E component which is interfered with two preceding signals.

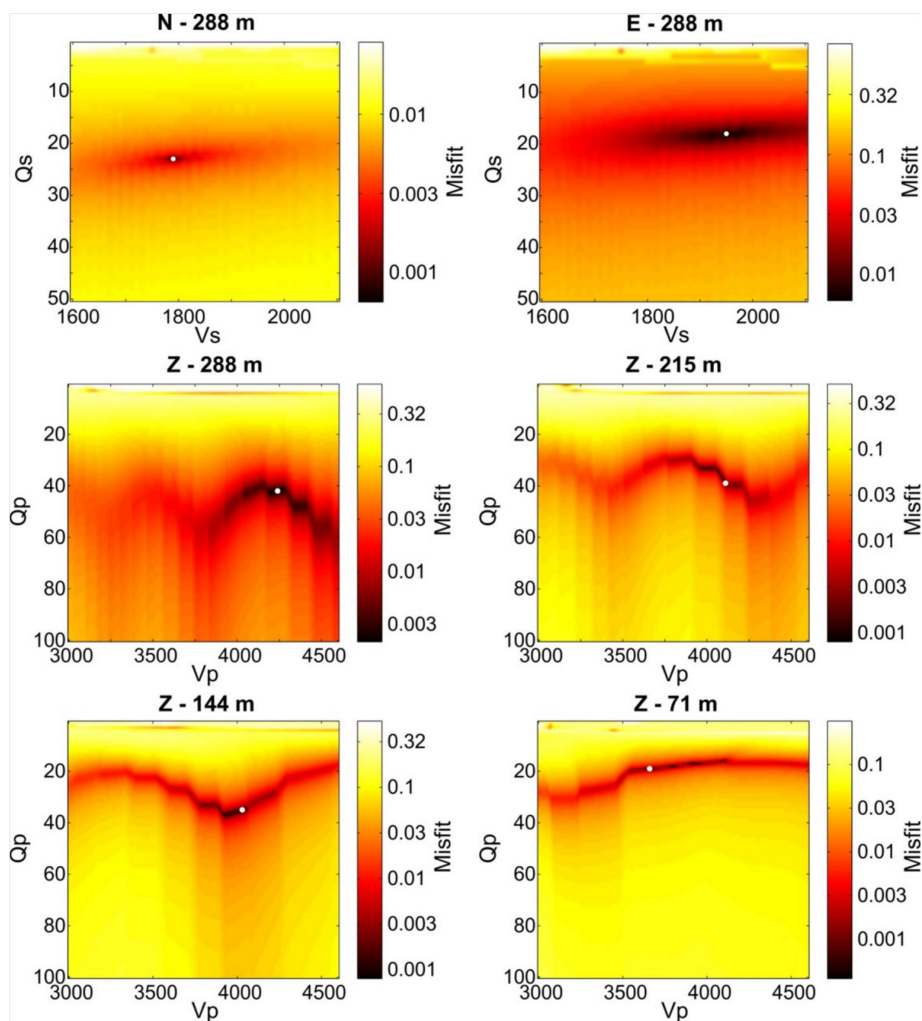


Figure 8. Misfit functions of all three components for the sensor at 288 m depth and of all verticals. The horizontal components N and E were used for the determination of V_S and Q_S and the vertical Z components for the determination of V_P and Q_P . The white dot marks the minimum of each misfit function.

Table 3. Effective seismic velocities and apparent quality factors obtained from the forward modeling approach.

Depth [m]	$\overline{V_P}$ [m/s]	$\overline{Q_P}$	$\overline{V_S}$ [m/s] (N / E)	$\overline{Q_S}$ (N / E)	Depth [m]	V_P [m/s]	Q_P
0 – 71	3660	19			0 – 71	3660	19
0 – 144	4030	35			71 – 144	4396	160
0 – 215	4110	39			144 – 215	4296	54
0 – 288	4240	42	1790 / 1950	23 / 18	215 – 288	4643	56

The parameters marked with over-bars are the effective velocities and apparent quality factors corresponding to a homogenous layer between the surface and the sensor. S-wave parameters could be determined for the depth range 0 – 288 m only and they were derived independently on the N and E components. The parameters written without bar correspond to a specific depth interval.

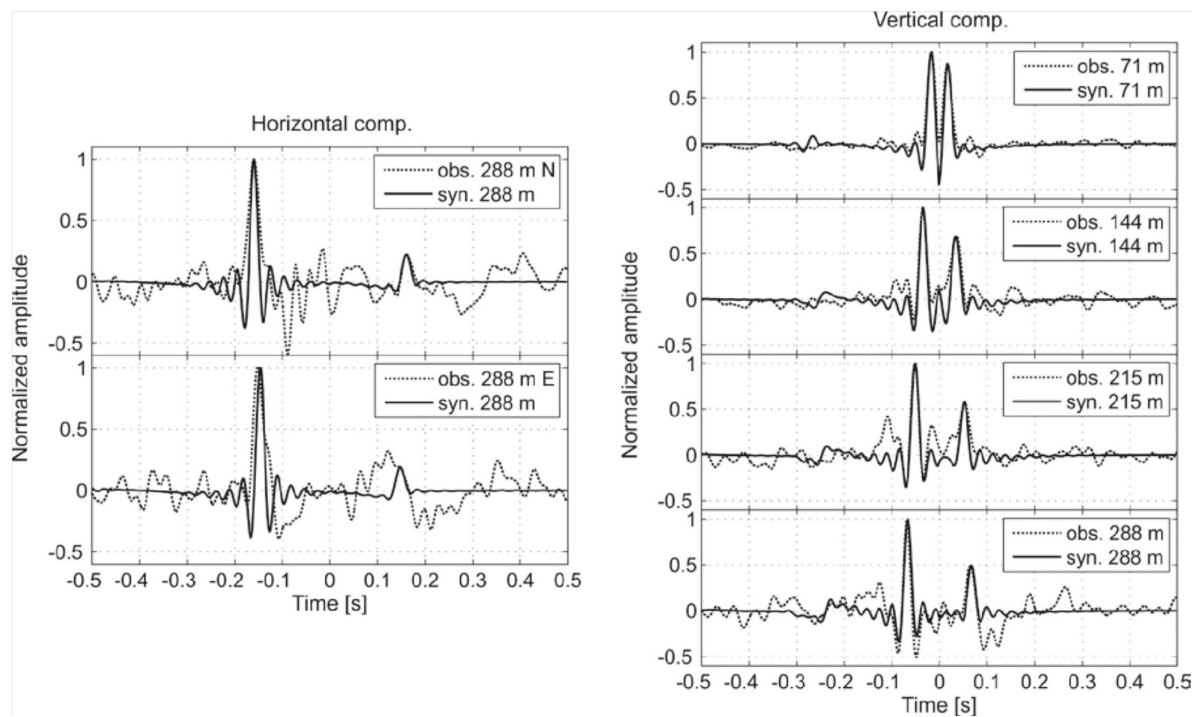


Figure 9. Comparison of waveforms of the observed and synthetic deconvolved seismograms. The solid traces show the deconvolved synthetic seismograms for the best fit (parameters are listed in Table 3). The observed deconvolved seismograms are plotted with a dotted line.

Error analysis

From Figures 8 and 9 it can be concluded that our simple forward modeling approach gives well constrained velocities and apparent quality factors. However, the simplifications of (1) a homogeneous layer and (2) deriving P- and S-wave parameter independent from each other can introduce significant errors. To evaluate these we computed synthetic seismograms for several models. These include one-layer models, two-layer models (with both, a faster layer over a slower layer and vice versa), and four-layer models based on the velocities derived from the modeling approach and arrival time picking, and the sonic logs. To define S-wave velocities for the shallower layers in the four-layer models a V_P/V_S

ratio of $2.27 (\bar{V}_P(288 \text{ m})/\bar{V}_S(288 \text{ m}))$ was assumed. The modeling approach results and the ones from arrival time picking give this same V_P/V_S ratio. For Q values for each layer of the four-layer models we use Equation (2) in Tonn (1991) for the calculation of interval Q_P values from the effective values obtained from the modeling approach. The interval Q_P values are 19, 160, 54 and 56 from the shallowest to the deepest layer. The interval Q_S values are set to $Q_P/2$.

We apply to the synthetic data the same forward modeling approach as used for the recorded waveform data. While performing the grid search for V_S and Q_S , the P-wave velocity was fixed to 4200 m/s (V_P). This is close to the root-mean-square velocity of a homogeneous layer above the sensor at 288 m, as determined from arrival time picking in the deconvolved seismograms. During the grid search over V_P and Q_P the S-wave velocity was fixed to 1850 m/s (V_S). This is in between the two S-wave velocities derived from arrival time picking: 1818 m/s and 1895 m/s on the N and E components, respectively. During the error analysis we evaluate how the error depends on the difference between the fixed velocity (V_{mod}) and the real one (V_{real}). We call the difference between these velocities ΔV .

The error estimates from the one-layer models and the four-layer models are summarized in Table 4. As expected the simple one-layer models yield very small errors for V_S and also Q_S . Furthermore, we did not observe a dependency of the S-wave parameters on ΔV , which is also as expected, as they are determined from the SH component which does not contain P-wave energy. The four-layer models also show small errors in V_S , but the errors in Q_S increased noticeably due to the unconstrained impedance contrasts between the sensor levels.

Table 4. Estimated errors of the modeling approach.

Depth [m]	One-layer models				Four-layer models			
	Err. \bar{V}_S [%]	Err. \bar{Q}_S [%]	Err. \bar{V}_P [%]	Err. \bar{Q}_P [%]	Err. \bar{V}_S [%]	Err. \bar{Q}_S [%]	Err. \bar{V}_P [%]	Err. \bar{Q}_P [%]
71	0.9	6.5	4.4	+100-(-27)	3.3	20.3	5.5	+35-(-27)
144	0.4	1	1.4	+51-(-6)	0.7	8.8	1.2	+81-(+3)
215	0.3	0.6	0.6	+34-(-9)	0.5	7.9	0.7	+65-(+7)
288	0.25	0.1	0.7	+13-(-8)	0.5	5.1	0.7	+43-(+7)

Summary of error analysis: The errors presented here are the average errors obtained from several one-layer models and four-layer models. The error bounds given for Q_P correspond to a range of $\Delta V = -10\% - (+10\%)$ (see explanation in the text). Positive values indicate an overestimation of Q_P and negative values an underestimation.

The errors in V_P for the one-layer and four-layer models are similar to the errors of V_S . It also appears that V_P is insensitive to changes in ΔV . In contrast, it is more difficult to evaluate the error in Q_P due to its strong dependency on ΔV . The range of errors in Q_P given in Table 4 are based on the assumption that $V_{S,real}$ differs from $V_{S,mod}$ not more than $\pm 10\%$. The first table value corresponds to -10% ($V_{S,real} > V_{S,mod}$) and the second to $+10\%$ ($V_{S,real} < V_{S,mod}$). A negative error implies that Q_P is underestimated and positive values correspond to overestimation. We observe that the modeling approach has a tendency to overestimate the Pwave quality factor. Keeping in mind that $V_{S,mod}$ has been chosen based

on the S-wave velocity measured on the deepest sensor, $V_{S, \text{real}}$ at the shallower sensors is probably smaller than $V_{S, \text{mod}}$. Hence the expected error in Q_P corresponds to $\Delta V = +10\%$ rather than the value given for -10% . Considering that $V_{S, \text{mod}}$ is close to the S-wave velocity determined from arrival time picking at 288 m depth, the range of $\pm 10\%$ is probably too large for the deep sensors. For the shallower sensors this range could be realistic.

In summary, it appears that the simplification of a homogeneous layer over each sensor has only a minor effect on V_S and V_P , while the errors in the P- and S-wave quality factor increase with increasing model complexity. The simplification of determining V_S and Q_S independent from V_P and Q_P only effects the accuracy of Q_P .

The errors of the velocities and Q depend also on the stability of the deconvolution result of the observed data. To evaluate this we performed a Jackknife test. To do this test, we successively removed two different earthquakes from the 26 events. For each subset the stacked deconvolved seismograms were computed and the amplitudes and arrival times of the up- and down-going waves determined. They were then forward modeled by minimizing Eq. (6) to determine the velocities and quality factors. These results are presented in Fig. 10 in form of histograms which show the distributions of V and Q . Since Q depends on the logarithm of the amplitude ratio between up- and down-going waves we observe a lognormal distribution of Q (Fig. 10, left). Hence, for Q , the logarithmic mean and standard deviation was calculated. In contrast to that there is no specific distribution observable for V . (Fig. 10, right). We calculate for V the mean and standard deviation of a normal distributed dataset. The values of the mean and standard deviation of Q and V are given in the legends in Fig. 10. These calculations show that the deconvolution results are mostly stable. However, for the sensor at 71 m depth we observe a larger standard deviation of V_P of $\sim 4\%$ and for the sensor at 288 m depth Q_P has a large standard deviation of $\sim 27\%$. The errors of the velocities derived from arrival time picking in the deconvolved seismograms are determined with the same Jackknife test. These are around 1% (see Table 2).

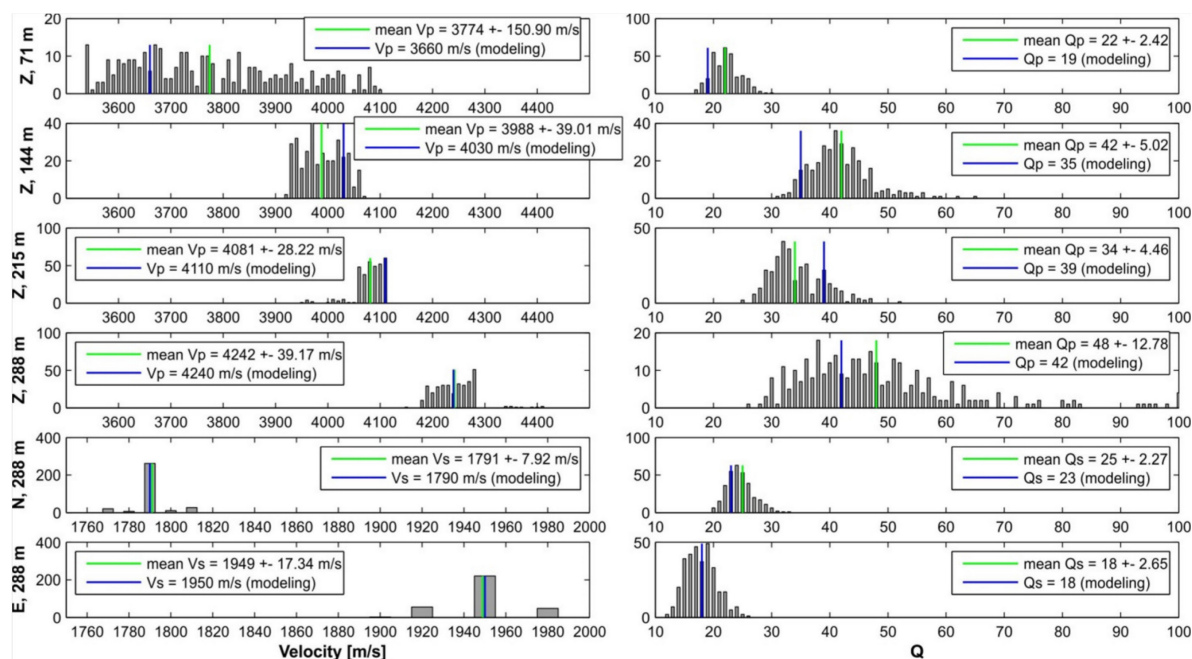


Figure 10. Results of Jackknife test. The histograms present the distribution of results obtained from each subset. Left and right figures present the results for P- and S-wave velocity and quality factors, respectively. The mean and standard deviation and results of the modeling approach are marked with lines and given in the legend.

Discussion

With deconvolution interferometry we analyzed near-surface wave propagation effects, such as amplification and attenuation and determined the velocity structure below the Tuzla site in southeastern Istanbul. From arrival time picking in the deconvolved seismograms and from forward modeling the Green's functions we derived two different velocity models down to 288 m depth. The first model sees a low-velocity zone between the sensors at 71 and 144 m and the second one between the sensors at 144 and 215 m depth (Fig. 4). Since logging measurements confirm a low-velocity zone between ~90 to ~140 m the first velocity model seems to be more reliable. Despite these differences both models have similar root-mean-square velocities. This reflects the common problem of uniqueness, i.e. several models can describe the same observation. In our modeling approach we focused on fitting the amplitudes and travel times of the direct up-going wave and its surface reflection. If we also would have taken into account the arrival times of the phases that are reflected from the low-velocity layer (gray dotted lines in Fig. 7a and b) we might have been able to better constrain the low-velocity zone at the right depth. However, this was not possible, since we performed a simple grid search for a homogeneous layer above each sensor. We recommend for future modeling studies to choose more complex techniques, e.g., a full wave field inversion, to be able to better capture the heterogeneities in the subsurface. Further, additional information from logging would be invaluable.

Both of our P-wave velocity models derived from interferometry overestimate the P-wave sonic log velocities by ~10 – 20 % even though the estimated errors for the velocities are only ~1 to 5 %. One possible reason for an overestimation is the assumption of vertical incidence of the incoming wave field. If this assumption is not fulfilled, apparent higher velocities will be determined. Another reason for the difference in velocities could be related to the higher frequencies used in sonic log measurements that sample only a few decimeters around the borehole. Thus, the seismic waves sample a larger volume of the rock formations including potential lateral variations. A comparison of our S-wave velocity model with the sonic log Swave velocity model is not reasonable, since the latter is likely to be erroneous, as discussed in section 'Geology at Tuzla'.

The forward modeling approach allowed us to determine apparent P- and S-wave quality factors. The apparent Q_P values for the depth ranges 0 – 71 m, 0 – 144 m, 0 – 215 m and 0 – 288 m increase with depth and we find $Q_P \approx 2Q_S$, in accordance with theory. Nevertheless our Q estimates have to be interpreted with caution. They are biased due to the fact that we did not account for impedance changes during the modeling, since we assumed in the model a single homogeneous layer above each sensor. Thus our apparent Q values contain both, intrinsic and scattered attenuation, and impedance effects. The latter means, if waves travel from higher to smaller impedance layers, as in our case between the sensors at 288 to 71 m, the decreasing impedance causes amplification due to energy conservation, with energy being proportional to ρVA^2 (ρ density, V velocity and A amplitude). This impedance amplification could lead to apparent higher Q values. On the other hand, increasing impedances, as in our case from the lowvelocity zone to the layer above, would lead to apparent lower Q values. Despite this bias, which causes large errors especially in Q_P , our apparent quality factors are similar to the ones found in other studies in the Marmara Sea region. E.g., Parolai et al. (2010) estimated Q_S values of 30, 46, and 99 for the depth ranges 0 – 50 m, 0 – 70 m, and 0 – 140 m in Ataköy (western Istanbul). They also used the recordings of a vertical borehole array and fitted the borehole-to-surface spectral ratios with a theoretical transfer function to derive Q_S . Using the ratio between S-wave and coda-wave amplitudes, Gündüz *et al.* (1998) determined a frequency dependent average Swave attenuation of $Q_S(f)$

$= (50 \pm 1.7)f^{1.09 \pm 0.05}$ for the crust below the Sea of Marmara, which is higher than our Q_S since they sample larger depths down to the base of the crust.

Conclusions

We studied the first-order wave propagation effects at the GONAF-Tuzla vertical array in southeastern Istanbul, Turkey. Using a seismic interferometry technique based on deconvolution and a simple forward modeling approach we obtained estimates of near-surface apparent quality factors and seismic velocities for P- and S-waves.

The near-surface seismic velocities at the Tuzla site are high compared to other Istanbul sites and other borehole sites around the world with comparable depth. We found P-wave velocities of more than 3600 m/s and S-wave velocities of ~ 1800 m/s in a 300 m deep borehole. An additional uniqueness comes from a strong impedance change somewhere between 71 and 215 m depth, which is probably related to a velocity inversion observed by sonic logs between ~ 90 and ~ 140 m depth. These impedance steps introduce reverberations in the recordings of the surface sensor and the high velocities lead to strong interference of up- and down-going waves on the downhole sensors.

Due to the given complicated structure and the resulting impedance contrasts it was not possible to derive attenuation parameters with standard techniques such as spectral ratios. Instead we proposed a forward modeling approach and found that the apparent Q_P increase with depth, with values of 19, 35, 39, and 42 for the depth ranges 0 – 71 m, 0 – 144 m, 0 – 215 m, and 0 – 288 m. For the apparent Q_S we observe a value of ~ 20 for the depth range 0 – 288 m. These attenuation estimates are interpreted to be biased by the strong heterogeneities observed at the Tuzla site.

If borehole seismometers are installed within a relatively simple almost homogeneous subsurface our forward modeling approach based on a 2-D grid search would be sufficient to derive reliable quality factors. However, in the presence of a complex geological setting, such as at the Tuzla site, it is recommendable to use more comprehensive modeling techniques that invert for Q and impedance contrasts simultaneously and also take the incidence angle into account.

Our results are derived from a carefully selected set of local microseismic events, with a bandwidth between 0.1 to 40 Hz. They were obtained from the first available data from the recently implemented GONAF observatory and are encouraging signs of this networks utility. They reveal not only the complex near-surface factors that need to be considered in ground motion studies of the Tuzla site, but also open the door for more sophisticated analysis and modeling research.

Data and resources

Seismograms used in this study were collected by instruments of the GONAF-Tuzla vertical array as part of the Geophysical Observatory at the North Anatolian Fault (GONAF) borehole network jointly operated by the Helmholtz-Centre Potsdam GFZ German Centre for Geosciences and the Disaster and Emergency Management Presidency AFAD, Ankara, Turkey. Waveform recordings are proprietary and will be released with a retention period of three years. Data will be made available through the GEOFON webpage hosted at GFZ Potsdam and through AFAD Ankara. Borehole logs were provided from the ICDP-OSG (Operational Support Group) and are freely available. All data processing and generation of figures was done using the MATLAB software, version R2012a.

Acknowledgements

The GONAF project is funded by the Helmholtz-Centre Potsdam GFZ German Centre for Geosciences, the Disaster and Emergency Management Presidency AFAD, Ankara, Turkey, the International Continental Drilling Program ICDP, and the Helmholtz Association, Germany. We acknowledge funding within the Helmholtz Young Investigators Group ‘From Microseismicity to Large Earthquakes’ and from the German Research Foundation (DFG) within the project Bo1877/7. The GONAF instrumentation was assembled by the technical staff of IESE. We thank Georg Dresen and Murat Nurlu for their strong and invaluable support in the GONAF project. Fatih Bulut was on-site party chief and managed to improve local recording conditions at the Tuzla site together with Recai Kartal which is highly appreciated. We thank the ICDP-OSG (Operational Support Group), in particular Jochem Kueck for conducting the logging measurements and Bütün Geothermal Ltd for performing the drilling of the Tuzla well. We also would like to thank Esen Arpat from the Technical University of Istanbul for the Tuzla boreholecutting analysis and his valuable contribution to understanding the geology at Tuzla.

References

- Abercrombie, R., and P. Leary (1993). Source parameters of small earthquakes recorded at 2.5 km depth, Cajon Pass, southern California: Implications for earthquake scaling, *Geophys. Res. Lett.*, 20, 1511–1514.
- Aki, K. and P. G. Richards (2002). *Quantitative Seismology: Theory and Methods*, W. H. Freeman and Company, New York.
- Armijo, R., N. Pondard, B. Meyer, G. Uçarkus, B. M. de Lépinay, J. Malavieille, S. Dominguez, M.-A. Gustcher, S. Schmidt, C. Beck, N. Çagatay, Z. Çakir, C. Imren, K. Eris, B. Natalin, S. Özalaybey, L. Tolun, I. Lefèvre, L. Seeber, L. Gasperini, C. Rangin, O. Emre and K. Sarikavak (2005). Submarine fault scarps in the Sea of Marmara pull-apart (North Anatolian Fault): Implications for seismic hazard in Istanbul, *Geochem. Geophys.* 6, Q06009.
- Assimaki, D., W. Li, J. H. Steidl, and K. Tsuda (2008). Site amplification and attenuation via downhole array seismogram inversion: A comparative study of the 2003 Miyagi-Oki aftershock sequence, *Bull. Seismol. Soc. Am.*, 98, 301-330.
- Barka, A. A. (1992). The North Anatolian fault zone, *Ann. Tetonicae*, 6, 164 - 195.
- Barka, A., H. S. Akyüz, E. Altunel, G. Sunal, Z. Çakir, A. Dikbas, B. Yerli, R. Armijo, B. Meyer, J. B. de Chabalier, T. Rockwell, J. R. Dolan, R. Hartleb, T. Dawson, S. Christofferson, A. Tucker, T. Fumal, R. Langridge, H. Stenner, W. Lettis, J. Bachhuber and W. Page (2002). The Surface Rupture and Slip Distribution of the 17 August 1999 İzmit Earthquake (M 7.4), North Anatolian Fault, *Bull. Seism. Soc. Am.*, 92, 43-60.
- Bethmann, F., N. Deichmann and P. M. Mai (2012). Seismic wave attenuation from borehole and surface records in the top 2.5 km beneath the city of Basel, Switzerland, *Geophys. J. Int.* 190, 1257-1270.
- Blakeslee, S. and P. Malin (1991). High-frequency site effects at two Parkfield downhole and surface stations, *Bull. Seism. Soc. Am.* 81, 332-345.
- Bohnhoff, M., H.-P. Harjes and T. Meier (2005). Deformation and stress regimes in the Hellenic subduction zone from focal Mechanisms, *J. Seismol.* 9, 341-366.
- Bohnhoff, M., H. Grosser, G. Dresen (2006). Strain partitioning and stress rotation at the North Anatolian fault zone from aftershock focal mechanisms of the 1999 İzmit Mw= 7.4 earthquake, *Geophys. J. Int.* 166, 373-385.
- Bohnhoff, M., F. Bulut, G. Dresen, P. E. Malin, T. Eken and M. Aktar (2013). An earthquake gap south of Istanbul, *Nat. Commun.* 4.
- Bulut, F., M. Bohnhoff, M. Aktar and G. Dresen (2007). Characterization of aftershock-fault plane orientations of the 1999 İzmit (Turkey) earthquake using high-resolution aftershock locations, *Geophys. Res. Lett.* 34, L20306.
- Bulut, F., M. Bohnhoff, W. L. Ellsworth, M. Aktar and G. Dresen (2009). Microseismicity at the North Anatolian Fault in the Sea of Marmara offshore Istanbul, NW Turkey, *J. Geophys. Res.* 114, B09302.

- Bulut, F., W. L. Ellsworth, M. Bohnhoff, M. Aktar and G. Dresen (2011). Spatiotemporal Earthquake Clusters along the North Anatolian Fault Zone Offshore İstanbul, *Bull. Seism. Soc. Am.* 101, 1759-1768.
- Dey-Sarkar, S. K. and R. A. Wiggins (1976). Source deconvolution of teleseismic P wave arrivals between 14° and 40°, *J. Geophys. Res.* 81, 3633-3641.
- Dix, C. H. (1955). Seismic velocities from surface measurements, *Geophysics*, 20, 68-86.
- Eken, T., M. Bohnhoff, F. Bulut, B. Can and M. Aktar (2013). Crustal Anisotropy in the Eastern Sea of Marmara Region in Northwestern Turkey, *Bull. Seism. Soc. Am.* 103, 911-924.
- Ergintav, S., R. E. Reilinger, R. Çakmak, M. Floyd, Z. Cakir, U. Doğan, R. W. King, S. McClusky and H. Özener (2014). Istanbul's earthquake hot spots: Geodetic constraints on strain accumulation along faults in the Marmara seismic gap, *Geophys. Res. Lett.* 41, 5783-5788.
- Flerit, F., R. Armijo, G. King and B. Meyer (2004). The mechanical interaction between the propagating North Anatolian Fault and the back-arc extension in the Aegean, *Earth Planet. Sci. Lett.* 224, 347-362.
- Ge, J., J. Pujol, S. Pezeshk and S. Stovall (2009). Determination of Shallow Shear-Wave Attenuation in the Mississippi Embayment Using Vertical Seismic Profiling Data, *Bull. Seism. Soc. Am.* 99, 1636-1649.
- Gibbs, J. F., D. M. Boore, W. B. Joyner, T. E. Fumal (1994). The attenuation of seismic shear waves in quaternary alluvium in Santa Clara Valley, California, *Bull. Seism. Soc. Am.* 84, 76-90.
- Gündüz, H., K.-Ö. Ayşe, B.-G. Aysun and T. Niyazi (1998). S-wave attenuation in the Marmara Region, northwestern Turkey, *Geophys. Res. Lett.* 25, 2733-2736.
- Hauksson, E., T.-L. Teng, and T. L. Henyey (1987). Results from a 1500 m deep, three-level downhole seismometer array: Site response, low Q values, and fmax, *Bull. Seism. Soc. Am.* 77, 1883-1904.
- Helmberger, D. and R. A. Wiggins (1971). Upper mantle structure of midwestern United States, *J. Geophys. Res.* 76, 3229-3245.
- Hubert-Ferrari, A., A. Barka, E. Jacques, S. S. Nalbant, B. Meyer, R. Armijo, P. Tapponnier and G. C. P. King (2000). Seismic hazard in the Marmara Sea region following the 17 August 1999 Izmit earthquake, *Nature*, 404, 269-273.
- Hurd, O. and M. Bohnhoff (2012). Stress and Structural-Induced Shear-Wave Anisotropy Along the 1999 Izmit Rupture, Northwest Turkey, *Bull. Seismol. Soc. Am.*, 102(5), 2177-2188.
- Kiratzi, A. A. (2002). Stress tensor inversions along the westernmost North Anatolian Fault Zone and its continuation into the North Aegean Sea, *Geophys. J. Int.* 151, 360-376.
- Leary, P. C. and F. Al-Kindy 2002. Power-law scaling of spatially correlated porosity and log (permeability) sequences from north-central North Sea Brae oilfield well core, *Geophys. J. Int.* 148, 426-442.
- Lienert, B. R., E. Berg and L. N. Frazer (1986). HYPOCENTER: An earthquake location method using centered, scaled, and adaptively damped least squares, *Bull. Seism. Soc. Am.* 76, 771-783.
- McClusky, S., S. Balassanian, A. Barka, C. Demir, S. Ergintav, I. Georgiev, O. Gurkan, M. Hamburger, K. Hurst, H. Kahle, K. Kastens, G. Kekelidze, R. King, V. Kotzev, O. Lenk, S. Mahmoud, A. Mishin, M. Nadariya, A. Ouzounis, D. Paradissis, Y. Peter, M. Prilepin, R.

- Özgül, N. (2012). Stratigraphy and Some Structural Features of the İstanbul Palaeozoic, *Turkish J Earth Sci*, 21, 817–866.
- Reilinger, I. Sanli, H. Seeger, A. Tealeb, M. N. Toksöz and G. Veis (2000). Global Positioning System constraints on plate kinematics and dynamics in the eastern Mediterranean and Caucasus, *J. Geophys. Res.* 105, 5695-5719.
- Mehta, K., R. Snieder and V. Graizer (2007). Extraction of near-surface properties for a lossy layered medium using the propagator matrix, *Geophys. J. Int.* 169, 271-280.
- Nakata, N. and R. Snieder (2012). Estimating near-surface shear wave velocities in Japan by applying seismic interferometry to KiK-net data, *J. Geophys. Res.* 117, B01308.
- Parolai, S., M. Mucciarelli, M. R. Gallipoli, S. M. Richwalski and A. Strollo (2007). Comparison of Empirical and Numerical Site Responses at the Tito Test Site, Southern Italy, *Bull. Seism. Soc. Am.* 97, 1413-1431.
- Parolai, S., A. Ansal, A. Kurtulus, A. Strollo, R. Wang and J. Zschau (2009). The Ataköy vertical array (Turkey): insights into seismic wave propagation in the shallow-most crustal layers by waveform deconvolution, *Geophys. J. Int.* 178, 1649-1662.
- Parolai, S., D. Bindi, A. Ansal, A. Kurtulus, A. Strollo and J. Zschau (2010). Determination of shallow S-wave attenuation by down-hole waveform deconvolution: a case study in Istanbul (Turkey), *Geophys. J. Int.* 181, 1147-1158.
- Parsons, T. (2004). Recalculated probability of $M \geq 7$ earthquakes beneath the Sea of Marmara, Turkey, *J. Geophys. Res.* 109.
- Prevedel, B., F. Bulut, M. Bohnhoff, C. Raub, R. Kartal, F. Alver, P. Malin, 2015. Downhole geophysical observatories: best installation practices and a case history from Turkey, *Int. J. Earth. Sci. (Geol. Rundsch.)*, 1-11.
- Şafak, E. (1997). Models and methods to characterize site amplification from a pair of records, *Earthq. Spectra*, 13, 97-129.
- Snieder, R. and E. Şafak (2006). Extracting the Building Response Using Seismic Interferometry: Theory and Application to the Millikan Library in Pasadena, California, *Bull. Seism. Soc. Am.*, 96, 586-598.
- Shearer, P. M. and J. A. Orcutt (1987). Surface and near-surface effects on seismic waves— theory and borehole seismometer results, *Bull. Seism. Soc. Am.* 77, 1168-1196.
- Shiomi, K., H. Sato and M. Ohtake (1997). Broad-band power-law spectra of well-log data in Japan, *Geophys. J. Int.* 130, 57-64.
- Silva, M. B. C. and A. Stovas (2009). Comparison of averaging methods for velocity model building from well logs, *J. Geophys. Eng.* 6, 172.
- Steidl, J. H., A. G. Tumarkin and R. J. Archuleta (1996). What is a reference site?, *Bull. Seism. Soc. Am.*, 86, 1733-1748.
- Stein, R. S., A. A. Barka, and J. H. Dieterich (1997). Progressive failure on the North Anatolian fault since 1939 by earthquake stress triggering, *Geophys. J. Int.* 128, 594-604.

Tibi, R., G. Bock, Y. Xia, M. Baumbach, H. Grosser, C. Milkereit, S. Karakisa, S. Zünbül, R. Kind and J. Zschau (2001). Rupture processes of the 1999 August 17 Izmit and November 12 Düzce (Turkey) earthquakes, *Geophys. J. Int.* 144, F1-F7.

Tonn, R. (1991). The determination of the seismic quality factor Q from VSP data: a comparison of different computational methods, *Geophys. Prospect.*, 39, 1-27.

Trampert, J., M. Cara and M. Frogneux (1993). SH Propagator Matrix and Qs Estimates From Borehole- and Surface-Recorded Earthquake Data, *Geophys. J. Int.* 112, 290-299.

Vasconcelos, I. and R. Snieder (2008a). Interferometry by deconvolution: Part 1 — Theory for acoustic waves and numerical examples, *Geophysics*, 73, S115-S128.

Vasconcelos, I. and R. Snieder (2008b). Interferometry by deconvolution: Part 2 — Theory for elastic waves and application to drill-bit seismic imaging, *Geophysics*, 73, S129-S141.

Vossen, R. v., J. Trampert and A. Curtis (2004). Propagator and wave-equation inversion for near-receiver material properties, *Geophys. J. Int.* 157, 796-812.

Wang, R. (1999). A simple orthonormalization method for stable and efficient computation of Green's functions, *Bull. Seism. Soc. Am.* 89, 733-741.

Appendix A: Orientation of downhole horizontal components

During the deployment of the downhole three-component geophones the vertical component of the instruments follow the direction of the well path, which deviates from verticality by less than 2° (Prevedel et al., 2015), whereas the orientation of the horizontal components cannot be controlled due to rotation of the instruments around their vertical axis while they are lowered into the hole. Therefore, before comparing the horizontal components of the surface and downhole sensors with each other the downhole horizontal components need to be rotated into the same direction as the orientation of the surface components, i.e. into N and E directions.

The rotation angle is determined by calculating cross-correlations between the horizontal components of the surface sensor with rotated horizontal components of the downhole sensor. Thereby the downhole sensor is clockwise rotated in 1° steps. The angle that yields the largest cross-correlation coefficient is regarded as the angle of deviation from N and E.

To avoid a false angle determination due to scattered high-frequency waves we low-pass filtered the data below the first trough in the downhole spectra of the P- and S-waves at ~ 3 Hz. Thus for this analysis we had to select a second dataset of well recorded regional and teleseismic events that have a sufficiently strong content of low-frequency energy. Eleven events with hypocentral distances between 114 km and 1614 km and magnitudes of 4.7 – 6.4 were selected from KOERI catalog. Due to their lack of high-frequency energy these eleven events are not part of the dataset used in the shallow wave propagation study.

For the cross-correlation analysis we selected the whole signal (P- and S-waves) and used instrument corrected recordings. The cross-correlation functions for all eleven events are presented in Fig. A1. They are very coherent, thus present a stable result. Averaging the maximum cross-correlation coefficients yields the angle of deviation from N and E of $313^\circ \pm 15^\circ$. Thus, as first processing step of the shallow wave propagation study, the downhole horizontal components of the sensor at 288 m depth are clockwise rotated by 313° .

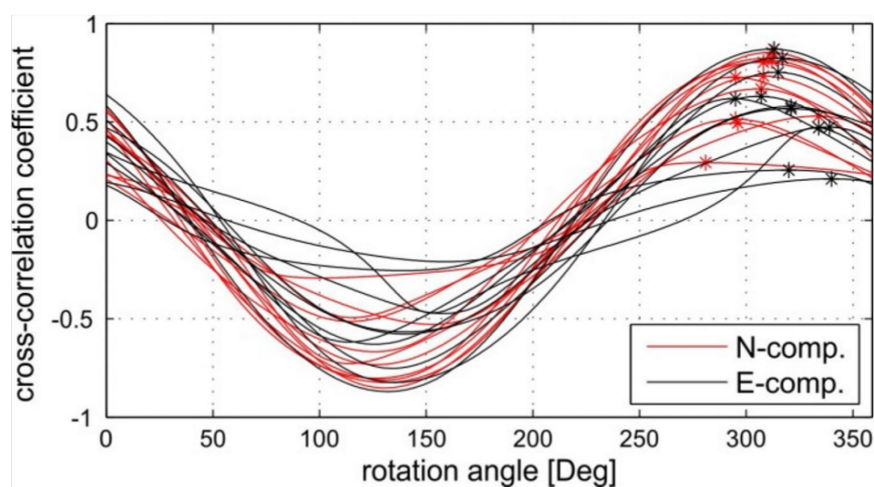


Figure A1. Cross-correlation functions of the 2 Hz geophone at 288 m depth from all eleven events that were selected for the orientation of the downhole horizontal components. The maximum cross-correlation coefficient is marked by a star.

Appendix d): Joint deconvolution of building and downhole strong-motion recordings: evidence for the seismic wave field being radiated back into the shallow geological layers

The final publication is available at SSA via <https://dx.doi.org/10.1785/0120150326>

Petrovic, B., and S. Parolai (2016). Joint deconvolution of building and downhole strong-motion recordings: evidence for the seismic wave field being radiated back into the shallow geological layers, *Bull. Seismol. Soc. Am.*, 106, no. 4, 1720-1732.

Abstract

In this study the strong motion recordings collected by a vertical array of borehole sensors and a network of accelerometers installed in a nearby building (distance between borehole and building ~ 10 m) are innovatively jointly analyzed through wave field deconvolution analysis. The analysis shows complicated patterns in the deconvolved wave field of the borehole sensors that are interpreted by taking advantage of synthetic seismograms generated considering vertically propagating plane waves in the soil and building. By using a constrained deconvolution approach, we show that it is possible to separate the different components of the wave field and, in particular, to retrieve the input ground motion and the wave field radiated back by the building at different levels in the borehole, without a priori information about the attenuation structure (and velocity) of the building and soil. This therefore allows the energy radiated back by the structure to different depth to be estimated, which in the case of the bottom of the borehole (at -145 m) is of the order of 10% of the energy of the input wave field in the frequency band 1-10 Hz.

Introduction

In recent years, great attention has been paid to the seismic wave field that is radiated back by a building in the free field, therefore modifying the amplitude of ground shaking during earthquakes (e.g., Bard et al., 1996). Recent studies have focused on the multiple interactions between soil layers and civil engineering structures, the so-called site-city interaction, by means of 2D and 3D numerical simulations of ground motion (e.g., Kahm et al., 2006, Semblat et al., 2002), concluding that the influence of site-city interaction can be significant. Empirical studies (e.g., Chavez-Garcia and Cardenas-Soto, 2002; Ditommaso et al., 2010) have provided evidence of both soil-structure interaction and of the influence of a single vibrating building on the free-field ground motion. Since Snieder and Safak (2006), several studies (e.g., Picozzi et al., 2009, Newton and Snieder, 2012, Rahmani and Todorovska, 2013, Nakata et al., 2013, 2015, Nakata and Snieder, 2014, Cheng et al. 2015) have focused their attention on the study of wave propagation in buildings by using deconvolution interferometry. When coupled with standard engineering approaches such as modal analysis using Frequency Domain Decomposition (Brincker et al., 2001) or Fourier spectral analysis of earthquake, active and/or passive source measurements, this approach allows the separation of the building's dynamic behavior from that arising from the soil-structure interaction. Deconvolution interferometry has also been extensively applied to borehole strong motion data (e.g., Mehta et al., 2007a, 2007b, Parolai et al., 2009, 2010, Oth et al., 2011) in order to gain information about wave propagation in the shallow geological layers. However, a full picture of the wave field propagation from the subsurface through the structure and back to it and an identification and quantification of the wave field radiated back from a structure to the soil can only be obtained if simultaneous recordings from boreholes and instrumented buildings located nearby are available and jointly analyzed.

In 2011, the GFZ installed a vertical array of six strong motion sensors in a 150 m deep borehole in the city of Bishkek, Kyrgyzstan (Parolai et al., 2013) within the framework of cooperation with the Central Asia Institute for Applied Geosciences (CAIAG). The borehole is located in the courtyard of CAIAG and the nearby building of the institute is instrumented with seven SOSEWIN sensors (Self-Organizing Seismic Early Warning Information Network, Fleming et al., 2009) located at different floors. The building is a three story reinforced masonry structure with a rectangular footprint. This 3D real-time sensors network has recorded four local earthquakes with magnitudes ranging between 4.8 and 5.4, which are particularly suitable for a comprehensive analysis of wave radiation by means of deconvolution interferometry.

In this study, the simultaneous recordings of earthquake data by the vertical array and building sensors are jointly analyzed by deconvolution interferometry in order to estimate the Green's functions related to the wave propagation in the borehole, through the building and back. In this way, an overall picture of the wave propagation is obtained and the wave field that is radiated back from a structure to the soil at different depths is investigated and isolated. In order to interpret the deconvolution interferometry results, numerical simulations of ground motions are carried out, considering the building structure to be described as a simple shear beam (Iwan, 1997). The synthetic seismograms calculated are then deconvolved in the same way as the real data. The results are compared with those obtained from the real data and discussed. Finally, and innovatively, in order to estimate the proportion of the seismic wave field that is radiated back by the structure into the shallow geological layers, 1) the real input ground motion (after down-going waves reflected at the surface, at discontinuities between different soil layers and at the top of the building are removed) at the bottom seismometer and at 10 m depth is estimated and 2) the ground motion relevant only to the down-going waves radiated back by the building

is extracted from the recorded seismograms using an approach similar to the constrained deconvolution proposed by Bindi et al. (2010).

Array Description

A 150 m deep borehole was drilled in the courtyard of CAIAG in Bishkek (Figure 1). The borehole is equipped with a 3-components accelerometer at the surface, and a chain of five 3-component borehole accelerometers at depths of 10, 25, 45, 85 and 145 m. The sensors are connected to two 24 bit digitizers. The output is set to ± 2 g and the sampling rate is 500 samples per second (sps). The orientation of the sensor components with respect to the cardinal points was obtained by low pass filtering the seismograms at 1 Hz (that is, below the frequency affected by down going waves, following Parolai et al., 2013) and rotating the recordings of each sensor with respect to the recordings at the surface by steps of 1° . For each rotation angle, the cross-correlations are calculated and the recorded components are rotated in the direction leading to the maximal cross-correlation. Finally, the borehole sensors are oriented along the main building axes. The borehole, cased along its entire length, crossed several quaternary layers (Parolai et al., 2010 and references therein). In particular, the uppermost 80 m are dominated by alternating layers of coarse gravel-shingle, and sandy layers with varying thicknesses (Figure 1) while below 80 m depth, only one thick gravel-shingle layer is present until the final depth. The ground water table was encountered at a depth of 55 m. Using the deconvolution interferometry of only one event recorded by a few borehole instruments, Parolai et al. (2013) estimated that the S-wave velocity in the shallowest 15 m is 500 m/s, increasing to 700 m/s by a depth of 43 m, at which it increases to 820 m/s until 75 m. Between 75 m depth and the bottom of the borehole, a S-wave velocity of 1590 m/s was estimated. These values are also in fair agreement with the S-wave velocity estimated by Rayleigh wave dispersion curve inversion (Parolai et al., 2010). The quality factor for S-waves, Q_s , was estimated to be around 5 for the shallowest 15 m, and around 50 for the remaining investigated depth.

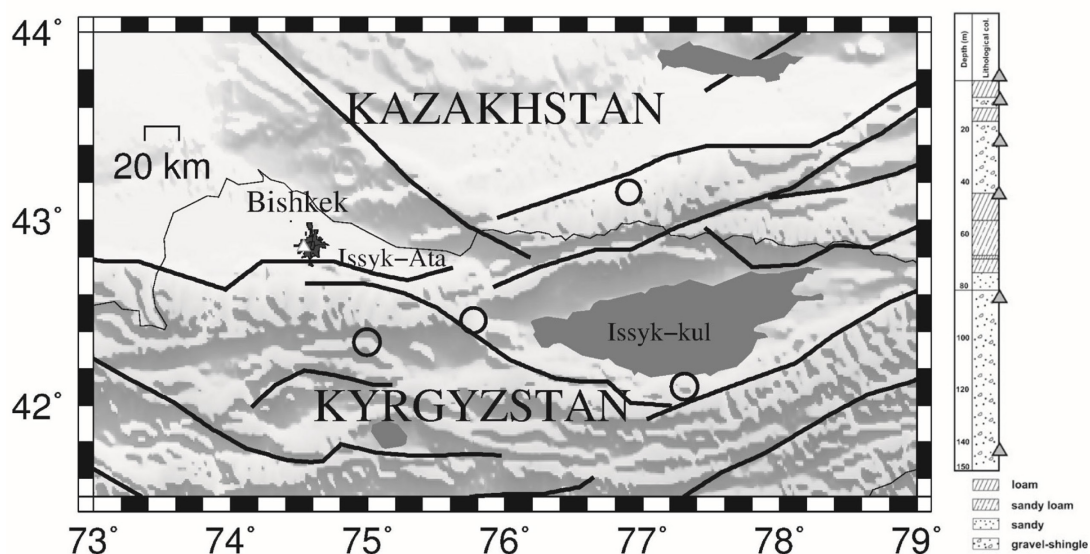


Figure 1. Locations of the epicenters (circles) of earthquakes used in this study and listed in Table 1 (left) and the Bishkek vertical array stratigraphic column (right). The triangles on the stratigraphic column mark the depths of the borehole instruments. The black lines show the known faults in this area.

Appendix d): Joint deconvolution of building and downhole strong-motion recordings: evidence for the seismic wave field being radiated back into the shallow geological layers

The CAIAG building (Figure 2) is a three story reinforced masonry structure with a rectangular shape, 37.81 m long and 16.3 m wide and was built in 1975. The walls are made of fired clay solid bricks and the lateral resistance is provided by the walls themselves. The floor is made of concrete and the floor system type can be described as a pre-cast concrete floor with reinforce concrete topping. The roof is pitched and hipped and made of wood covered by metal or asbestos. Six SOSEWIN units (Fleming et al., 2009; Bindi et al., 2015) are installed at the two edges of the three floors of the building, with one unit installed under the roof. These units are equipped with a MEMS sensor with a sampling rate of 100 sps. A detailed description of these units is provided by Fleming et al. (2009). The data are stored locally and transmitted in real-time via the internet to CAIAG and the GFZ.

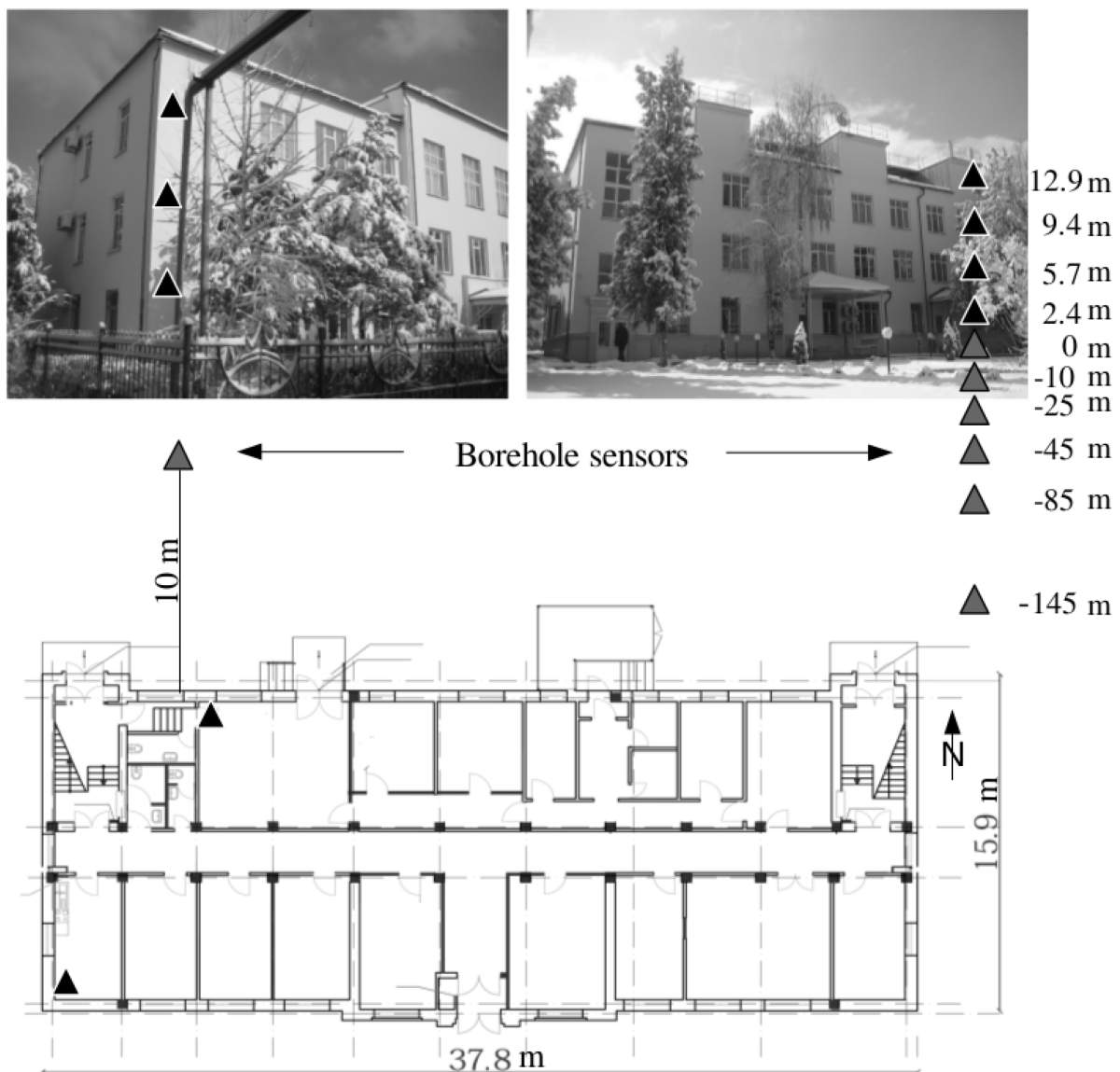


Figure 2. SOSEWIN installations in the CAIAG building (black triangles) and borehole sensors (gray triangles). Top left-hand panel: view from south, top right-hand panel: view from north, bottom panel: footprint.

Methodology

The deconvolution of ground motion recorded at a depth z_1 with that at depth z_2 can be written in the frequency domain as:

$$S(\omega) = \frac{u(z_1, \omega)}{u(z_2, \omega)} \quad (1)$$

where $u(z_1, \omega)$ and $u(z_2, \omega)$ are the Fourier transforms of the motions recorded at depths z_1 and z_2 , respectively. However, the deconvolution operation is applied to data corrupted by noise and, therefore, this problem is ill-conditioned, since small errors in the data could lead to solutions that are unacceptable from a physical point of view.

To avoid this instability, a regularized Tikhonov deconvolution $S_\varepsilon(\omega)$ is used (Tikhonov and Arsenin, 1977; Bertero and Boccacci, 1998; Mehta et al., 2007a; 2007b, Parolai et al., 2009):

$$S_\varepsilon(\omega) = W_\varepsilon(\omega) \frac{u(z_1, \omega)}{u(z_2, \omega)} \quad (2)$$

where $u(z_1, \omega)$ and $u(z_2, \omega)$ denote the Fourier spectra of the deconvolved wave field and

$$W_\varepsilon(\omega) = \frac{|u(z_2, \omega)|^2}{|u(z_2, \omega)|^2 + \varepsilon} \quad (3)$$

is the filter. ε is the regularization parameter and refers to a constant added to the denominator to prevent the numerical instability of equation (1).

Consistent with the results of Mehta et al. (2007a, 2007b) and Parolai et al. (2009) who showed the independence of the deconvolution results of the signal window used, but their dependence on the analyzed component of ground acceleration, no window selection was carried out. In this way, the results obtained by deconvolving the horizontal component of ground motion are expected to be related mainly to the S-wave propagation function.

Data

In this study, the recordings of four earthquakes with magnitudes ranging between 4.8 and 5.4 (Figure 1 and Table 1) that occurred in Kyrgyzstan between 2013 and 2015 are analyzed. Due to small ground motion of the analyzed earthquakes, linear behavior can be assumed.

Figure 3 shows as an example the north-south (NS) component of recordings of event ID 4 (Table 1), corresponding to the transverse direction of the building. The modification of ground motion at different depths is obvious, as well as the larger level of shaking observable at the top of the building (please note in the figure the different scales used for plotting the borehole and building data). The Fourier spectra amplitudes of the recordings also show the frequency dependence of the ground motion variability at different depths and a clear resonant peak (likely corresponding to the first mode of the structure at around 5 Hz). Note that due to the different quality of the instruments used, the signal to

noise ratio is higher in the borehole recordings. The data collected in the building have been re-interpolated to 500 sps in order to harmonize them with those collected by the borehole array, before calculating the Fourier transform.

Table 1. List of events used in this study.

ID	Origin time (UTC)	Magnitude	Latitude (°)	Longitude (°)	Depth (km)
1	11/23/2013 09:42:08	5.1	42.46	75.77	10
2	11/14/2014 01:24:20	5.4	42.10	77.31	45
3	01/22/2015 15:52:29	5.3	42.34	77.99	0
4	03/15/2015 14:01:02	4.8	43.15	76.90	10

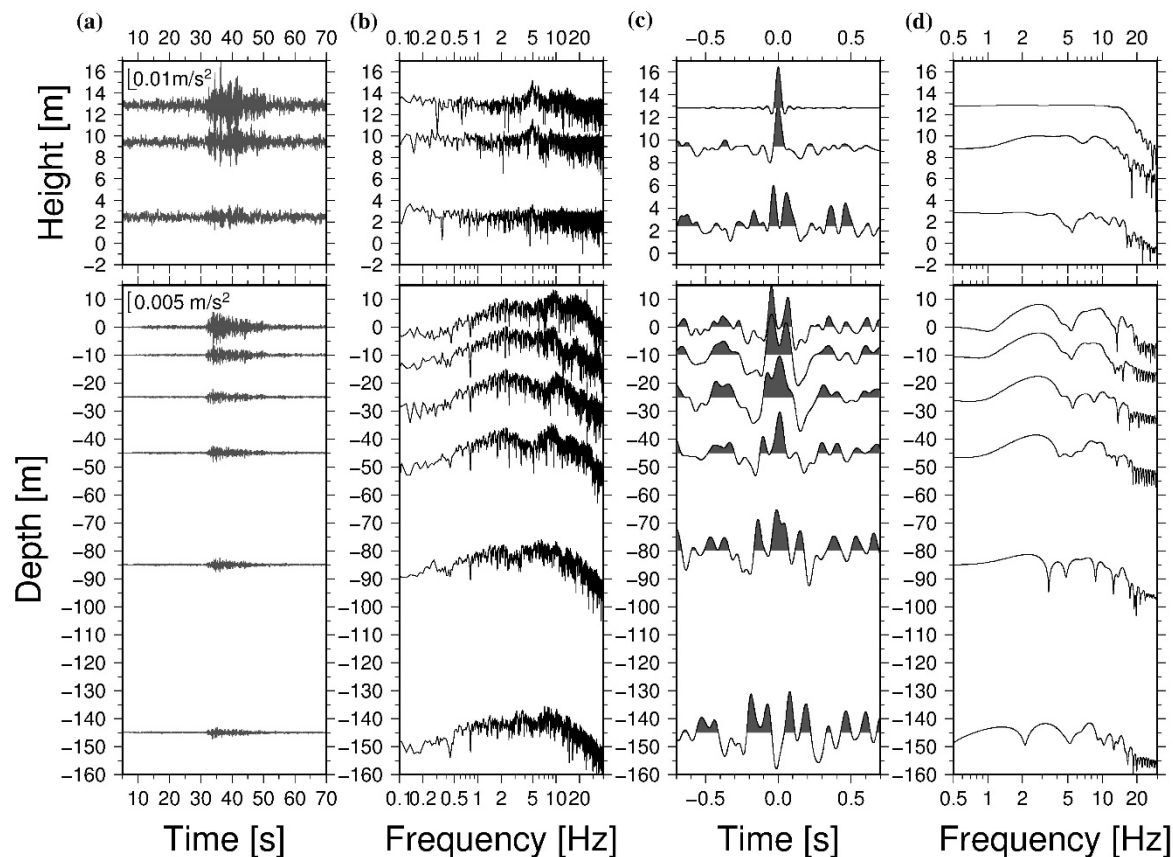


Figure 3. (a) North-south component (corresponding to the transverse direction of the building) recordings of the borehole accelerometers (from -145m to 0m) and the SOSEWIN sensors (2m to 13m) of the M=4.8 event that occurred on the 03/15/15 (ID4, Table 1). Please note the two different scales used for the plots, differing in a factor of 2, (b) Fourier amplitude spectra of the recordings, (c) deconvolved wave field using the recording at the top of the building as reference, and (d) the spectra of the deconvolved wave fields

Results

1) Joint deconvolution

The existence of peaks in the acausal and causal part of the deconvolved wave fields that can be related to up and downward propagating waves is obvious from Figure 3. The spectra of the deconvolved wave fields show spectral troughs at frequencies affected by the downward going waves which can be directly related to the travel times of the S-waves in the building-soil structure and therefore to their velocities in each layer. Interestingly, the trough at 0 m depth occurs at nearly 5 Hz (consistent with the resonant peak of the building, which is likely to correspond to the first translational (and dominant) mode of the structure) while the first spectral trough in the deepest sensor (145 m) occurs at around 2 Hz. Note that the spectrum of the deconvolved wave field at the reference station (station at the roof) is flat until 15 Hz, where it starts to decrease, therefore indicating where the influence of the filter $W_\epsilon(\omega)$ is strongest.

Figure 4 shows the deconvolved wave field obtained for the transverse direction of ground motion for all the events listed in Table 1 (left) and the results obtained after stacking (right). In the acausal part of the deconvolved wave field results for the downhole seismometer, a clear upward propagating pulse can be identified (first black line). When the pulse reaches the Earth's surface, a part of the energy is reflected back into the soil, as clearly visible from the downward-going wave pulse that can be followed until the deepest sensor (black dash-dot line). The remaining part of the wave field is transmitted into the building and propagates until its top (first black line), where it is reflected back (black dashed line). We will show later that two peaks belonging to different pulses overlie each other (see also Appendix). As matter of fact, the same black dashed line marks two different pulses. When reaching the Earth's surface again, the waves are transmitted into the ground (with a pulse that is then visible until the deepest sensor) and, although less clearly visible, reflected back (due to the impedance contrast between the "slow" building and the "fast" soil material) with a change of polarity in the building. The velocity inside the building can be estimated from the arrival times of the pulses at different floors, and is found to be around 300 m/s.

Note that different from the cases of wave propagation in nearly homogeneous materials, for example, in Parolai et al. (2009), the acausal part of the signal is not dominated by a single peak but by a couple of them (indicated by the black lines from -145 m to 0 m depth) moving in parallel along the time axes.

In order to better understand the wave propagation within the soil-building structure, numerical simulations were carried out using the Wang (1999) approach (and used in the forward propagation part of the inversion code employed by Parolai et al., 2012; Parolai et al., 2013). The building structure was simulated by considering a shear beam approximation and therefore by adding a layer with a S-wave velocity of 300 m/s, a density of $\rho=400 \text{ kg/m}^3$, appropriated for this kind of reinforced masonry structure, and a Q_s of 10 (equivalent to a 5% damping), at the top of the soil structure. Although simple, it has been shown that this model is able to capture the main features observed in real data (far- source) analyses. The S-wave and Q_s velocity profiles used, were taken from the best ones calculated by Parolai et al. (2013). Figure 5 shows the propagation of S-waves with nearly vertical incidence between the deepest borehole sensor and the top of the building.

Consistent with Parolai et al. (2013), part of the energy of the upward-going S-wave, when reaching the 75 m depth discontinuity between the loam and the gravel-shingle, is reflected back. The energy transmitted through the discontinuity is propagated towards the surface where the first downward-going wave is generated. The transmitted energy inside the building propagates as an upward-going wave and reaches the top of the structure where a second downward-going wave is generated. When reaching the

Earth's surface, the downward-going wave is both reflected back to the top of the structure (with a change of polarity) and transmitted down through the Earth.

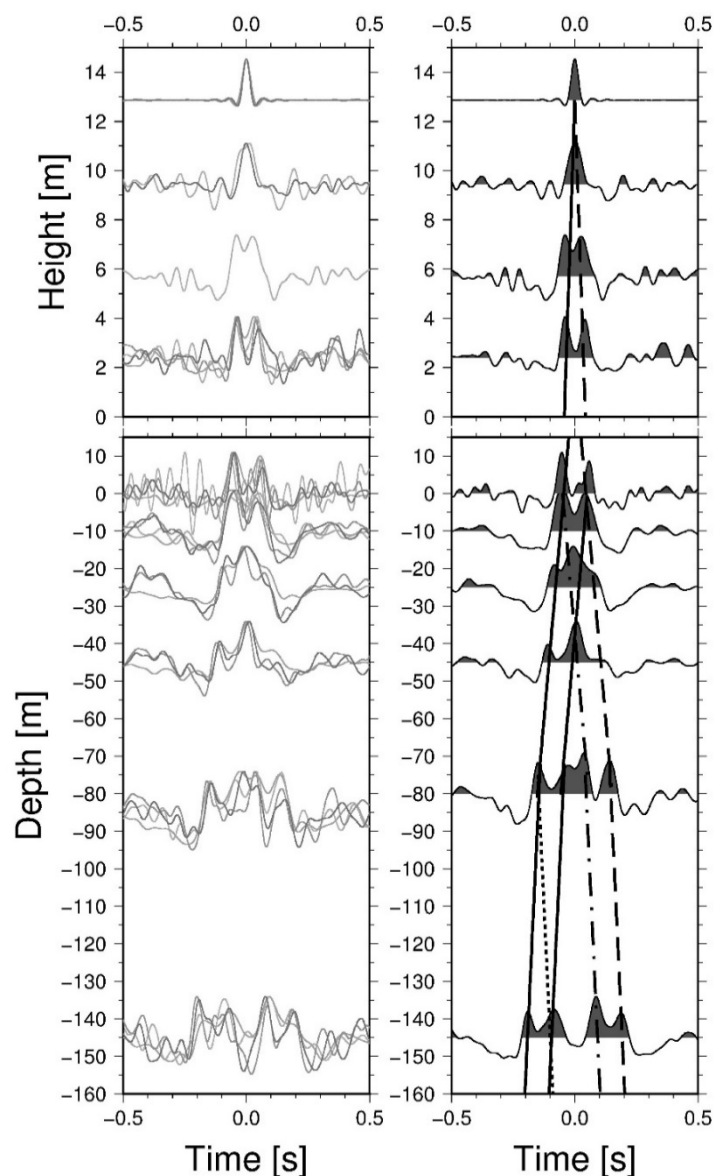


Figure 4. Left-hand panel: deconvolved wave fields obtained for the north-south component (transverse direction of the building) of ground motion arising from the four considered events (Table 1) using the recordings from the top of the building as the reference. There is only one line at 6 m, since the sensor at the 2nd floor had some problems and hence, registered only one of the four analyzed earthquakes. Right-hand panel: the results obtained after stacking the results shown in the left-hand panel. The upward going waves (black lines), the downward going waves reflected at the interface at 75 m depth (black dotted line), at the Earth's surface (black dash-dot line) and at the top of the building (dashed line) are also shown.

Figure 6 shows the deconvolved wave field results obtained by using the synthetic seismograms (gray) and the observed data (black). The high level of similarity between the two results is clearly visible, although, probably due to the usage of a narrower frequency bandwidth for the analysis of the observed

data ($f=1-10$ Hz) due to the signal to noise ratio, the real data shows a worse separation of the single peaks. In any case, although the velocity of propagation of the S-waves in the deepest part of the adopted model for the synthetic seismogram seems to be slightly too low (note the slight mismatch in the observed and calculated downward-going peaks), the favorable comparison between the observed and synthetic deconvolved wave fields allows us to assign univocally each of the observed peaks to a particular up and downward-going phase and to update the velocity model.

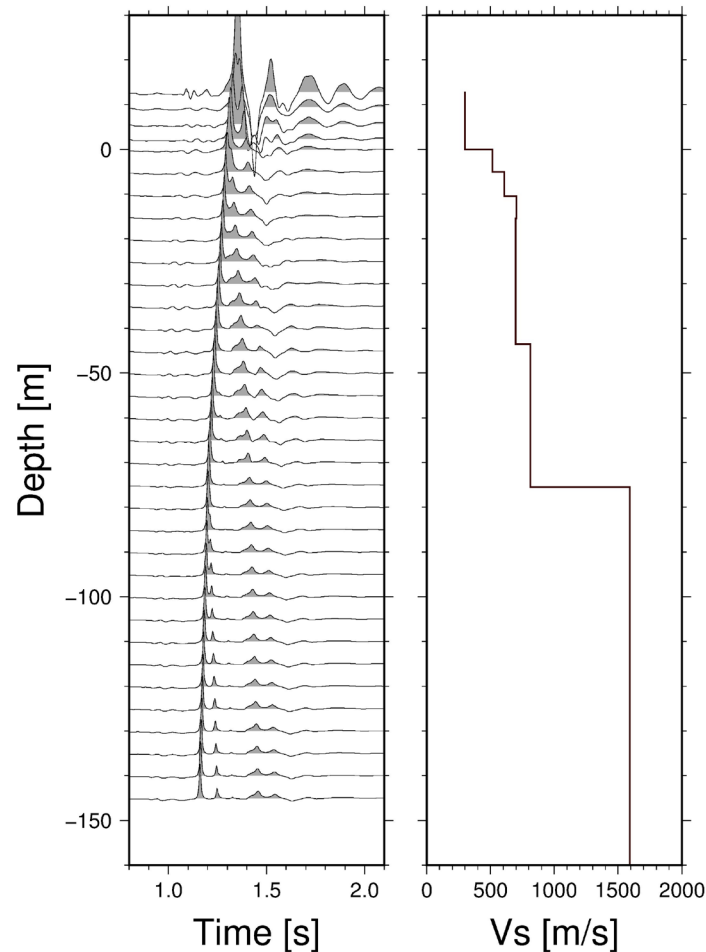


Figure 5. Left-hand panel: Synthetic seismograms showing the propagation of S-waves with nearly vertical incidence between the deepest borehole sensor and the sensor at the top of the building. Right-hand panel: v_s structure used for the simulation (velocity model v_s for the soil from Parolai et al., 2013, v_s for building layer estimated by the use of the interferometric approach).

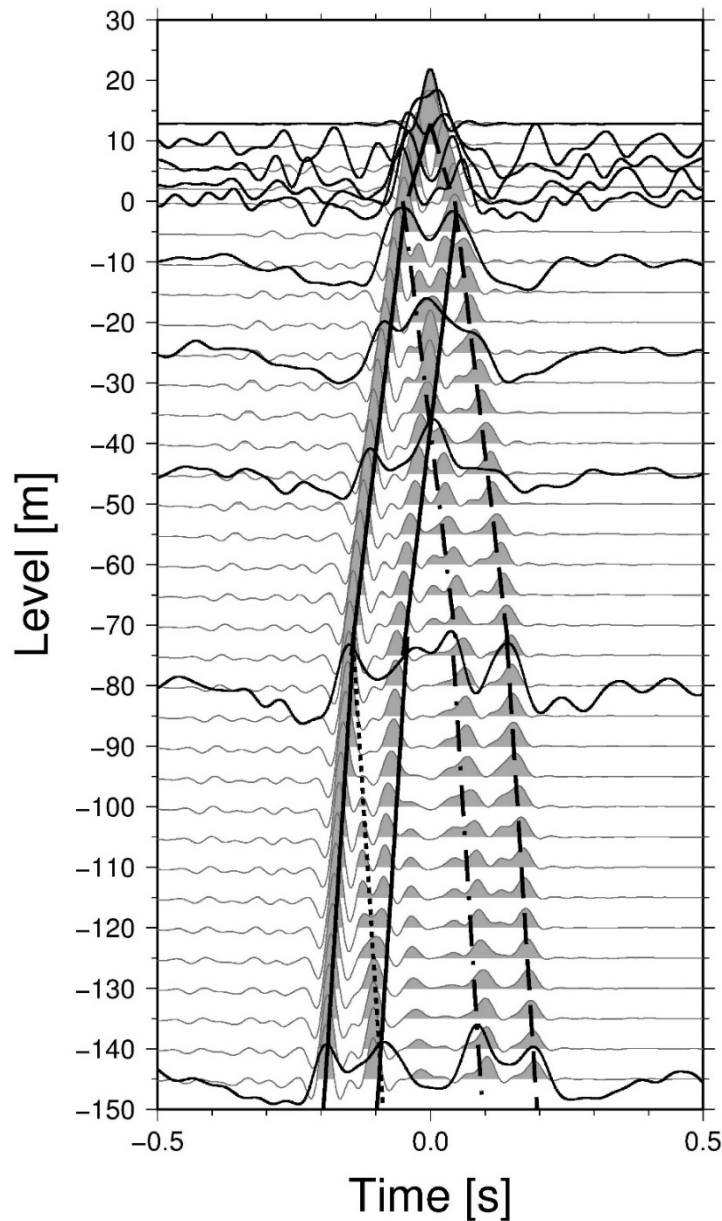


Figure 6. Deconvolved wave field obtained by the use of synthetic seismograms (gray) and the observed data after stacking the results of all events (black). The upward propagating waves (black lines), the downward going waves reflected at the interface at 75 m depth (black dotted line), at the Earth's surface (black dash-dot line) and at the top of the building (dashed line) are also shown.

2) Estimation of the wave field radiated back to the soil

The first step in this section involves the more detailed interpretation of the peaks obtained from the deconvolution of the observed signals by the use of the analytical transfer functions derived for 2 and 3-layers building-soil-structure (see the Appendix for their derivation). When considering the soil layer (and the sensors) above 75 m depth (2-layers-model), the double peak dominating the acausal part of the signal (black lines) can be explained by considering the first one to be related to the upward-going propagation of the wave field (Eq. (A4), a) while the second (Eq. (A4), c) is necessary, when back

projecting the recordings at the roof to the borehole. In fact, since the recordings at the roof are affected by multi reflections within the building, the effect of these multiple reflections (not existing in the acausal part of the signal) must be removed. Hence, for reconstruction of the real input ground motion, both acausal peaks (black lines, Eq. (A4), a and c) have to be taken into account. The first peak in the causal part of the deconvolved wave field (black dash-dot line, Eq. (A4), b) is related to the downward-going wave reflected from the surface, while the second one (black dashed line, Eq. (A4), d) is associated with the downward propagation of the wave field captured within the building (which acts as a soft, i.e., low velocity, layer). This peak (black dashed line, Eq. (A4), d) overlaps with the peak arising from the part of the energy missing in the rooftop recording (the reference) due to the reflection at the Earth's surface (Eq. (A4), e), which should be accounted for to correctly reconstruct the borehole recordings when projecting back the recordings on the top. In order to reconstruct correctly the downward going wave field amplitude, we have to separate the contribution of the two different waves to the retrieved wave field through the consideration of their relative importance directly from the terms $0.5(1 - r)$ (Eq. (A4), d) and $r^2/[2(1 + r)]$ (Eq. (A4), e) in the Appendix.

When considering the soil layer (and the sensors) below the 75 m discontinuity moreover, the downward-going wave reflected at the 75 m deep discontinuity is shown by a dotted black line (Fig. 6). In the case of the synthetic data, the downward propagating wave can be easily tracked since seismograms were calculated every 5 m. Since in the borehole installation there are only sensors at 85 m and 145 m depth, and by chance due to the propagation velocities, the second peak in the acausal part (second black line) interferes with the down-going wave reflected at 75 m depth (dotted black line), these two peaks cannot be separated.

In our case, considering the identified main discontinuity at 75 m depth, the underground structure can be approximated by a layer (from 0m to 75m) over a half-space with different characteristics. We obtain for the transfer function for the 3-layers-model, consisting of a building layer, a soil layer from 0 m to 75 m and the half-space, (deviation shown in the Appendix) two peaks, one arising from the part of the energy missing in the top roof recording due to the reflection at the discontinuity at 75m depth (Eq. (A9), j), and the other arising from the part of energy missing in the top roof recording due to reflection at the Earth's surface (Eq. (A9), i) that are overlying the peak of interest belonging to the downward going wave field radiated back from the building (Eq. (A9), k, Fig. 6, black dashed line). In order to retrieve correctly the amplitude of the wave field of interest (i.e., the wave field propagated back into the Earth after propagating through the building), a factor taking into account the relative importance of the contributions of the three waves has to be calculated. Considering also the building, the whole Earth plus building structure can be described by a three layer model with velocities $v_{\text{building}} = v_b = 300$ m/s, $v_{\text{soil}_1} = v_{s_1} = 870$ m/s and $v_{\text{soil}_2} = v_{s_2} = 1400$ m/s estimated by the results of deconvolution interferometry. The density of the building layer is computed to be $\rho_b = 400$ kg/m³, and of the two soil layers, $\rho_{s_1} = 1800$ kg/m³ and $\rho_{s_2} = 2100$ kg/m³. Considering these parameters and the terms $r_1^2 r_2 / [2(1 + r_1)(1 + r_2)]$ (Eq. (A9), i), $[r_2^2(1 - r_1)] / [2(1 + r_2)]$ (Eq. (A9), j) and $0.5(1 - r_1)(1 - r_2)$ (Eq. (A9), k) in the Appendix, it is estimated that 24% of the wave field that can be retrieved in the third layer will be due to the wave field radiated back from the structure.

In order to quantify in the seismic recordings the part of the wave field radiated back from the building to the soil, the real input (i.e., only the incoming waves from the event itself, without the down-going waves reflected at interfaces of the soil layers, the Earth's surface or the top of the building) at the deepest borehole sensor must be isolated first. Then, the portion of the wave field describing the propagation from the building to the ground needs to be identified by the part of the deconvolved wave field associated with the downward propagating waves from the building (Fig 6, black dashed lines).

Both, the real input and wave field radiated back from the building to the soil is estimated with an approach similar to that proposed by Bindi et al. (2010), that is, a constrained regularized scheme (projected Landweber method), is applied (Bertero et al., 1997; Bertero and Boccacci, 1998). For the most appropriate reconstruction of the wave field radiated back from the building to the soil (in terms of absolute amplitude), as indicated in the previous paragraph, the contribution to the retrieved wave field should be estimated by considering the main impedance contrasts in the whole building-subsoil-structure.

In Bindi et al. (2010), the first peak in the acausal part of the deconvolved wave field alone is associated with the real input ground motion and can be used to reconstruct the input wave field by convolution with the recordings at the surface. In our case, differently from Bindi et al. (2010), as shown in the previous section, the recordings on the top of the building are affected by multiple reflections, and both acausal peaks have to be used to retrieve correctly the real input ground motion. Moreover, as presented already in Parolai et al. (2013), a part of the energy of the upward-going S-wave is reflected back at the 75 m deep discontinuity between the loam and the gravel-shingle. The peak of this downward propagating wave reflected at 75 m depth (Fig. 6, back dotted line) overlaps with the second acausal peak (Fig. 6, second black continuous line) at 145 m depth. Therefore, the free-surface recordings obtained for a station outside of the building structure (sensor at 0 m of the borehole installation) were used as the reference for the interferometric approach (analog as in Bindi et al., 2010), i.e., only the borehole sensors are used to retrieve the real input ground motion. The acausal part of the stacked deconvolved borehole wave field is hence easily extracted and used to reconstruct the input ground motion in the borehole.

Figure 7, left-hand panels, show, as an example, the recorded ground motion at the free surface and at 145 m depth, as well as the retrieved real input ground motion at 145 m depth for event ID 4 (Table 1). The corresponding Fourier spectra are shown in the right-hand panels. A clear modification of the recorded spectra at 145 m is visible. In particular, at around 2 Hz, the spectral trough, related to the downward-going waves, disappears.

In order to obtain the ground motion arising from the wave field radiated back by the building structure into the soil at each depth, the deconvolution interferometry is performed using the recordings at the top of the building as reference. The downward going wave field is reconstructed by the convolution of the recordings at the top of the building and the second peak in the causal part of the deconvolved wave field using the Bindi et al. (2010) approach. In this case, the solution was constrained to be defined in a time interval $t=0.16-0.3$ s for the recordings at 145 m depth and $t=0.01-0.2$ s for the recordings at 10m depth. As mentioned before, the amplitude of the wave field has to be further corrected to consider the appropriate amplitude of the used Green's function.

Figure 8, left-hand panels, show as an example the recorded ground motion at the top of the building, as well as the retrieved wave field radiated back from the building at 10 m and 145 m depth for the case of event ID 4 in Table 1. The corresponding Fourier spectra are shown in the right-hand panels. Clearly the energy radiated back from the building is concentrated around 5 Hz, and is likely to correspond to the first bending (and dominant) mode in the transverse direction of the structure.

Figure 9 shows the input ground motion spectra and the spectra of the downward-going waves radiated back from the building to the soil at 10 m and 145 m depths for the four analyzed events. In all cases, independent of the spectral shape of the input, a large spectral peak in the downward-going wave field recording is observed. The amplitude of this peak is clearly diminishing with increasing depth, and is smaller than that observed at the top of the building (see for comparison Figure 8 for event ID4).

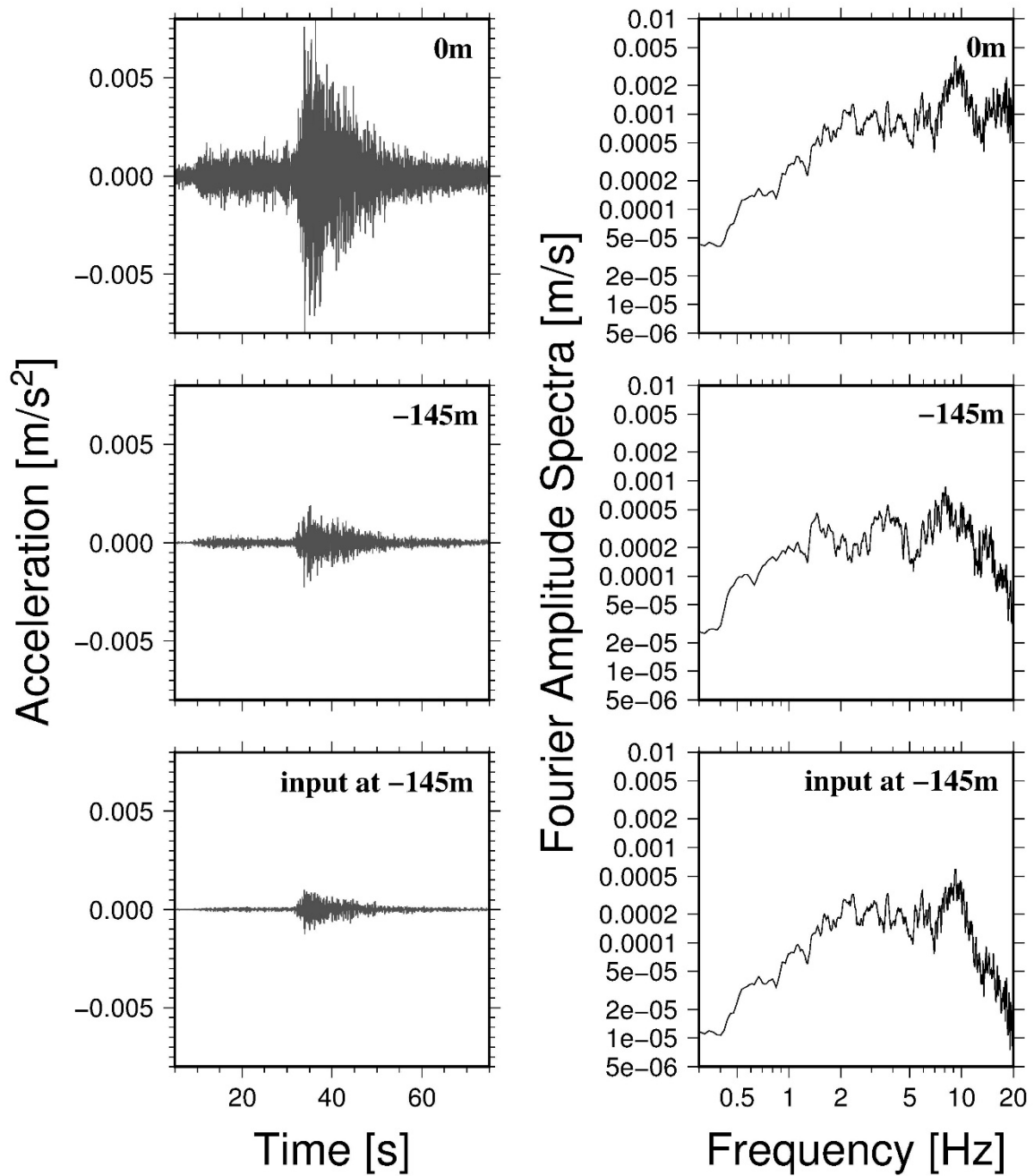


Figure 7. Left-hand panels: Ground motion recorded at the free surface (top), at 145 m depth (middle) and the reconstructed input motion at 145 m depth (bottom) for event 4 (Table 1). Right-hand panels: Corresponding Fourier spectra of ground motion recorded at the surface (top), 145 m depth (middle) and of retrieved input motion (bottom).

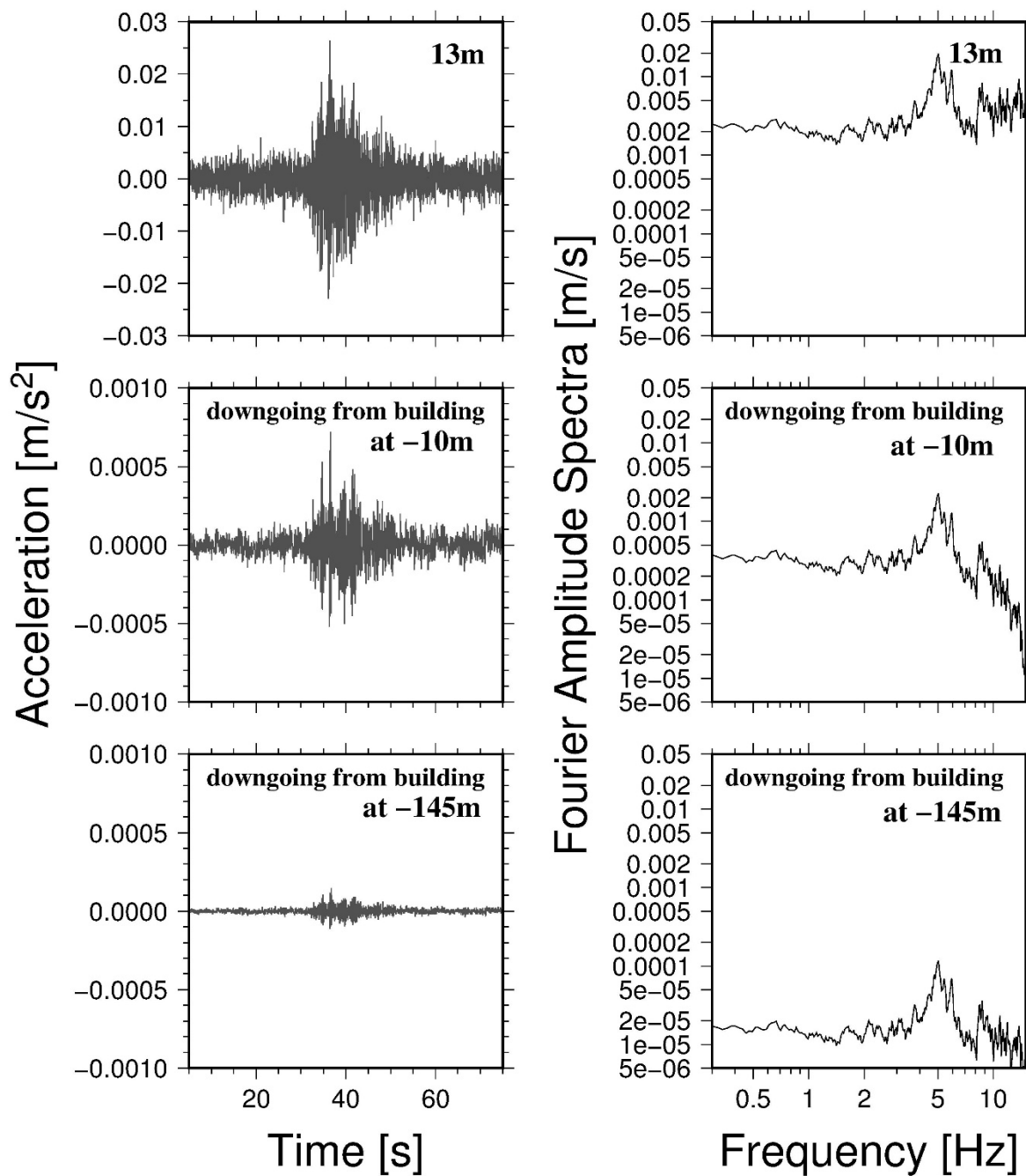


Figure 8. Left-hand panels: Ground motion recorded at the roof of the building (top), and the retrieved wave field radiated back from the building at 10 m depth (middle) and at 145 m depth (bottom) for event 4 (Table 1). Right-hand panels: Corresponding Fourier spectra of ground motion recorded at the roof (top), and of the retrieved wave field radiated back from the building at 10 m depth (middle) and 145 m depth (bottom).

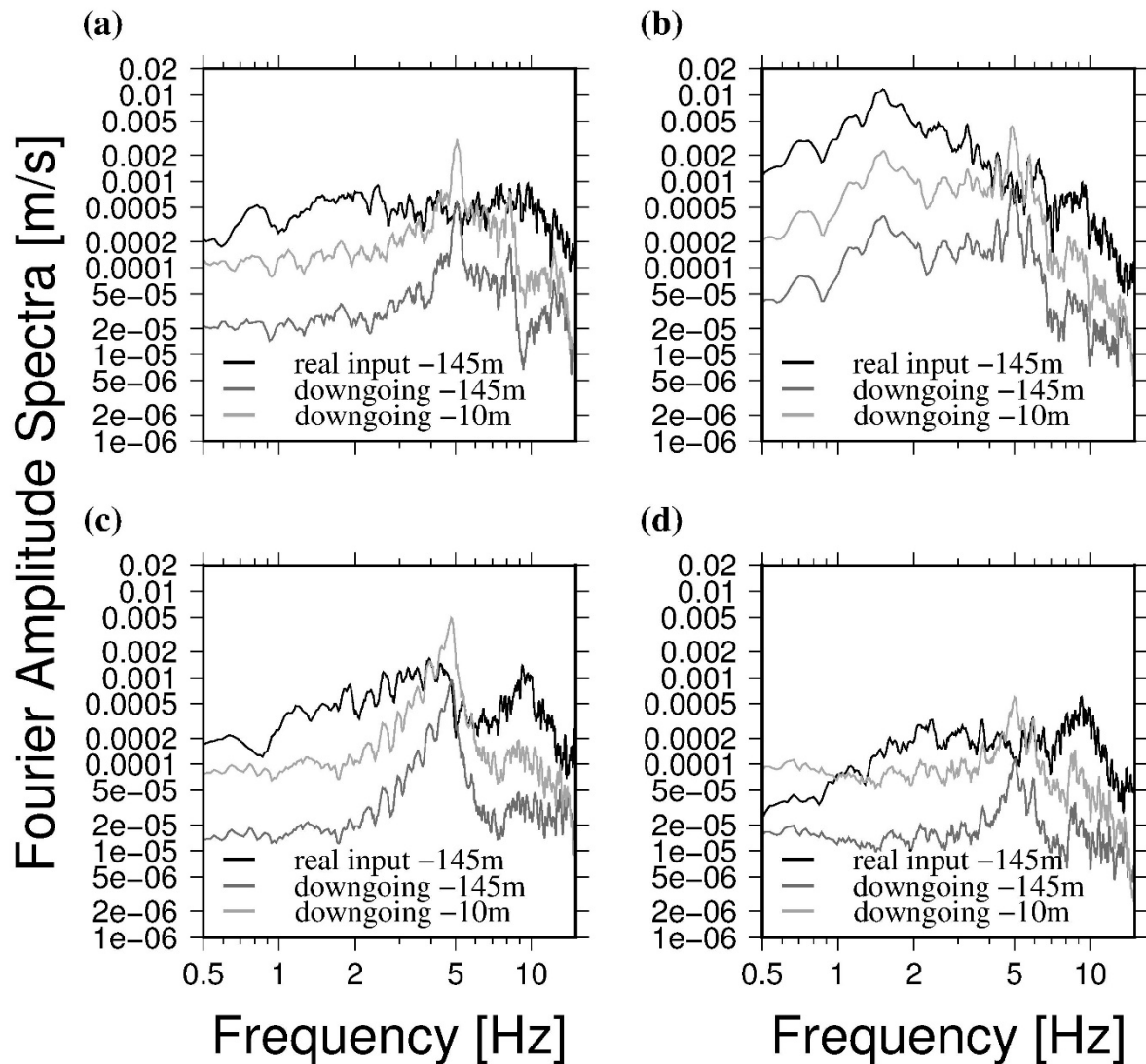


Figure 9. Input spectrum at -145 m (black), spectrum of down-going waves radiated back from the building at -10 m (light gray) and at -145 m (dark gray) for the four events. a) $M=5.1$ event (11/23/13), b) $M=5.4$ event (11/14/14), c) $M=5.3$ event (01/22/15) and d) $M=4.8$ event (03/15/15).

Discussion and conclusions

In this study, we present the results of an innovative deconvolution wave field analysis of simultaneous borehole and building recordings. Our results show that it is possible to separate the different components of seismic motion and to quantify them. For example, after having integrated the velocity spectra of Figure 9 over the frequency band 1-10 Hz (the same used for the deconvolution), the spectral energy was calculated. The results show that in this case, the energy radiated back by the structure at -145 m corresponds in average to nearly 10% of the energy contained in the real input ground motion within the selected frequency band. When considering the recordings at 10 m depth the effect of the wave field radiated back by the building is larger, leading in average to a 40%-50% energy ratio in the selected frequency band.

The potential of the method proposed by Bindi et al. (2010) to reconstruct different components of the wave field (in the linear regime) even for complicated underground velocity structures and without a

priori knowledge of the velocity and independent knowledge of the quality factor Q of the subsurface was shown. Only information about the velocity (which can incidentally be estimated directly by the interferometric approach) and density (mainly of importance for the building structure, but that can be easily estimated) are needed.

These results, although preliminary, highlight, consistent with results of numerical simulations (Bard et al., 1996, Semblat et al., 2004) that the amount of energy radiated back from a structure to the Earth is not negligible and interactions between nearby buildings are possible. The example considered here is typical for a structure with lower wave velocity than the soil. Analysis of different situations, where the building structure shows a velocity similar to or lower than the shallow geology layers, are necessary and underway. Furthermore, in this study, only far-source recordings are considered and in the future, when available, the analysis of near-source recordings will be necessary to better understand soil-structure interactions during strong ground shaking. In addition, studying the nonlinear behavior of both building and ground by the analysis of strong motion recordings might be also an interesting issue for the future. Finally, it is worth mentioning that the influence of the torsional mode of the building onto the deconvolved wave field is not well studied as yet, further analyses are needed to understand its influence in detail.

The potential to better understand city-soil interactions, possibly through multiple borehole-building network installations, is obvious and is perhaps one of the main challenges of the engineering seismology community for the future.

Data and Resources

The seismograms used in this study were collected by downhole accelerometers (located at different levels within a 150 m deep borehole in the vicinity of the main building of the Central Asia Institute for Applied Geosciences (CAIAG) in Bishkek) and SOSEWIN sensors (located at different floors in the CAIAG building⁹, last accessed 05/11/16). These instruments were installed by GFZ in cooperation with CAIAG and the data cannot be released to the public.

Acknowledgments

The authors wish to acknowledge Nori Nakata and Norman Sleep for their helpful suggestions to improve the manuscript. We would like to thank A. Strollo, S. Orunbaev and B. Moldobekov from the CAIAG who helped with the organization of the BIVA array planning and installation. Tobias Boxberger, Marco Pilz and Dino Bindi installed the SOSEWIN acceleration network in the CAIAG institute. We are grateful to Dino Bindi for the helpful discussions and suggestions to improve our work. Kevin Fleming kindly revised our English. The figures were drawn using GMT (Wessel and Smith 1991).

⁹ <https://lhotse21.gfz-potsdam.de/nagvis/frontend/nagvis-js/index.php?mod=Map&act=view&show=bishkek>

References

- Bard, P.-Y., P. Gueguen and A. Wirgin (1996). A note on the seismic Wave field radiated from large building structures into soft soils, *11th World Conference on Earthquake Engineering*
- Bertero, M. and P. Boccacci (1998). Introduction to inverse problems in imaging. Bristol: IOP Publishing.
- Bertero, M, D. Bindi, P. Boccacci, M. Cattaneo, C. Eva and V. Lanza (1997). Application of the projected Landweber method to the estimation of the source time function in seismology, *Inverse Problems*, 13, 465-486.
- Bindi, D., S. Parolai, M. Picozzi and A. Ansal (2010). Seismic input motion determined from a surface-downhole pair of sensors: a constrained deconvolution approach. *Bull. Seism. Soc. Am.*, 100, no. 3, 1375-1380.
- Bindi, D., T. Boxberger, S. Orunbaev, M. Pilz, J. Stankiewicz, M. Pittore, I. Iervolino, E. Ellguth, S. Parolai (2015). On-site early-warning system for Bishkek (Kyrgyzstan), *Annals of Geophysics*, 58, no 1, S0112, doi:10.4401/ag-6664.
- Brincker R., L. Zhang, P. Andersen (2001). Modal identification of output only systems using frequency domain decomposition. *Smart Mater. Struct.*, 10, 441-445.
- Chavez-Garcia, F.J. and M. Cardenas-Soto (2002). The contribution of the built environment to the free-field ground motion in Mexico City, *Soil Dyn. Earthq. Eng.*, 22, 773–780.
- Cheng, M. H., M. D. Kohler and T. H. Heaton (2015). Prediction of wave propagation in buildings using data from a single seismometer, *Bull. Seism. Soc. Am.*, 105, no. 1, 107-119.
- Ditommaso, R., S. Parolai, M. Mucciarelli, S. Eggert, M. Sobiesiak, and J. Zschau (2009). Monitoring the response and the back-radiated energy of a building subjected to ambient vibration and impulsive action: The Falkenhof Tower (Potsdam, Germany), *Bull. Earthquake Eng.*, 8, no. 3, 705–722.
- Fleming, K., M. Picozzi, C. Milkereit, F. Kühnlenz, B. Lichtblau, J. Fischer, C. Zulfikar, O. Özel., SAFER and EDIM working groups (2009). The Self-organizing Seismic Early Warning Information Network (SOSEWIN), *Seismological Research Letters*, 80, no. 5, 755-771.
- Iwan, W. D. (1997). Drift spectrum: measure of demand for earthquake ground motions, *J. Struct. Eng.*, 123, 367-404.
- Kham, M., J.-F. Semblat, P.-Y. Bard and P. Dangla (2006). Seismic site-city interaction: main governing phenomena through simplified numerical models, *Bull. Seism. Soc. Am.*, 96, no.5, 1934-1951.
- Mehta, K., R. Snieder, and V. Grazier (2007a). Extraction of near-surface properties for a lossy layered medium using the propagator matrix, *Geophys. J. Int.*, 169, 2171-280.
- Mehta, K., R. Snieder and V. Grazier (2007b). Downhole receiver function: a case study, *Bull. Seism. Soc. Am.*, 97, 1396-1403.
- Nakata, N. and R. Snieder (2014). Monitoring a building using deconvolution interferometry. II: Ambient-vibration-analysis, *Bull. Seism. Soc. Am.*, 104, no. 1, 204-213.

- Nakata, N., W. Tanaka, and Y. Oda (2015). Damage detection of a building caused by the 2011 Tohoku-Oki earthquake with seismic interferometry, *Bull. Seism. Soc. Am.*, 105, no. 5, 2411-2419.
- Nakata, N., R. Snieder, S. Kuroda, S. Ito, T. Aizawa, and T. Kunimi (2013). Monitoring a building using deconvolution interferometry. I: Earthquake-data analysis, *Bull. Seism. Soc. Am.*, 103, no. 3, 1662-1678.
- Newton, C. and R. Snieder (2012). Estimating Intrinsic Attenuation of a Building Using Deconvolution Interferometry and Time Reversal, *Bull. Seism. Soc. Am.*, 102, no. 5, 2200-2208.
- Oth, A., S. Parolai, D. Bindi (2011). Spectral analysis of K-NET and KiK-net data in Japan, Part I: Database compilation and peculiarities, *Bull. Seism. Soc. Am.*, 101, no. 2, 652-666.
- Parolai, S., A. Ansal, A. Kurtulus, A. Strollo, R., Wang and J. Zschau (2009). The Ataköy vertical array (Turkey): insights into seismic wave propagation in the shallow-most crustal layers by waveform, *Geophys. J. Int.*, 178, 1649-1662
- Parolai, S., D. Bindi, A. Ansal, A. Kurtulus, A. Strollo and J. Zschau (2010). Determination of shallow S-wave attenuation by down-hole waveform deconvolution: a case study in Istanbul (Turkey), *Geophys. J. Int.*, 181, no. 2, 1147-1158.
- Parolai, S. D. Bindi, S. Ullah, S. Orunbaev, S. Usupaev, B. Moldobekov, H. Echtler (2013). The Bishkek vertical array (BIVA): acquiring strong motion data in Kyrgyzstan and first results, *Journal of Seismology*, 17, no 2, 707-719.
- Parolai, S., R. Wang and D. Bindi (2012). Inversion of borehole weak motion records observed in Istanbul (Turkey), *Geophys. J. Int.*, 188, no 2, 535-548.
- Picozzi, M., S. Parolai, M. Mucciarelli, C. Milkereit, D. Bindi, R. Ditommaso, M. Vona, M. R. Gallipoli and J. Zschau (2009). Interferometric Analysis of Strong Ground Motion for Structural Health Monitoring: The Example of the L'Aquila, Italy, Seismic Sequence of 2009, *Bull. Seism. Soc. Am.*, 101, no. 2, 635-651.
- Rahmani, M. and M. I. Todorovska (2013). 1D system identification of buildings during earthquakes by seismic interferometry with waveform inversion of impulse responses – method and application to Millikan library, *Soil Dyn. Earthq. Eng.*, 47, 157–174.
- Safak, E. (1997). Models and methods to characterize site amplification from a pair of records, *Earthquake Spectra*, 13, 97-129.
- Semblat, J.F., M. Kham, P.Y. Bard and P. Gueguen (2004). Could “site-city interaction” modify site effects in urban areas? *13th World Conference on Earthquake Engineering Vancouver*, B.C., Canada
- Semblat, J.F., M. Kham, P. Gueguen, P.Y. Bard and A.M. Duval (2002). Site-city interaction through modifications of site effects, *7th Conference of Earthquake Engineering*, 2002, Bosten, United States
- Snieder, R. and E. Şafak (2006). Extracting the building response using seismic interferometry: Theory and application to the Millikan library in Pasadena, California, *Bull. Seism. Soc. Am.*, 96, 586-598.
- Tikhonov, A.N. and V.Y. Arsenin (1977). Solution of ill-posed problems. Washington: Wiston/Wiley.
- Wang R (1999). A simple orthonormalization method for stable and efficient computation of Greens functions. *Bull Seismol Soc Am*, 89, 733-741.

Appendix

Transfer function for Two-Layer Model

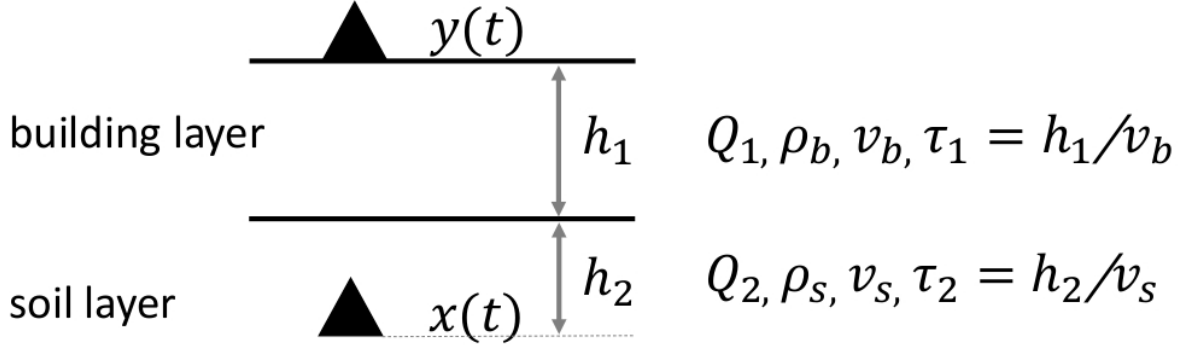


Figure A1. The two layer model, consisting of the building layer overlying the soil layer (a half-space), with recordings $y(t)$ at the top of the building and recordings $x(t)$ in the soil layer.

We are considering a building assumed to be described by the shear beam model and hence modeled as a layer over a soil layer as schematically shown in Figure A1. We are interested in calculating the transfer function $x(\omega)/y(\omega)$ from the Fourier transforms of $x(t)$ and $y(t)$. The reflection coefficient r for the up-going waves is defined as

$$r = \frac{\rho_s v_s - \rho_b v_b}{\rho_s v_s + \rho_b v_b} = \frac{1 - c}{1 + c} \quad (\text{A1})$$

with ρ_s and ρ_b being the density of the soil and building layer, respectively. v_s and v_b are the shear wave velocities in the soil and building layer.

The Fourier transform $x(\omega)$ of $x(t)$ at the soil station can be written as

$$x(\omega) = x_0(\omega) + r x_0(\omega) e^{-i4\pi f \frac{\tau_2}{Q_2}} + 0.5 y(\omega) (1 - r) e^{-i4\pi f \left(\frac{\tau_1}{Q_1} + \frac{\tau_2}{Q_2} \right)}. \quad (\text{A2})$$

$x_0(\omega)$ is the Fourier transform of the incident wave, τ_1 and τ_2 are the travel times for wave propagation from the top of the building to the impedance contrast (building-soil discontinuity), and Q_1 and Q_2 are the quality factors of the building and soil layer, respectively.

The Fourier transform of the recording at the top of the building $y(\omega)$ is given after some mathematical steps as

$$y(\omega) = \frac{2(1 + r)x_0(\omega) e^{-i2\pi f \left(\frac{\tau_1}{Q_1} + \frac{\tau_2}{Q_2} \right)}}{1 + r e^{-i4\pi f \frac{\tau_1}{Q_1}}}. \quad (\text{A3})$$

The transfer function $x(\omega)/y(\omega)$ is finally obtained, analogous to Safak (1997), as

$$\frac{x(\omega)}{y(\omega)} = \frac{1}{2(1+r)} e^{-i2\pi f \left(-\frac{\tau_1}{Q_1} - \frac{\tau_2}{Q_2} \right)} + \frac{r}{2(1+r)} e^{-i2\pi f \left(\frac{\tau_1}{Q_1} - \frac{\tau_2}{Q_2} \right)} + \frac{r}{2(1+r)} e^{-i2\pi f \left(\frac{\tau_2}{Q_2} - \frac{\tau_1}{Q_1} \right)} + 0.5(1-r) e^{-i2\pi f \left(\frac{\tau_1}{Q_1} + \frac{\tau_2}{Q_2} \right)} + \frac{r^2}{2(1+r)} e^{-i2\pi f \left(\frac{\tau_1}{Q_1} + \frac{\tau_2}{Q_2} \right)} \quad (A4)$$

Transfer function for Three-Layer Model

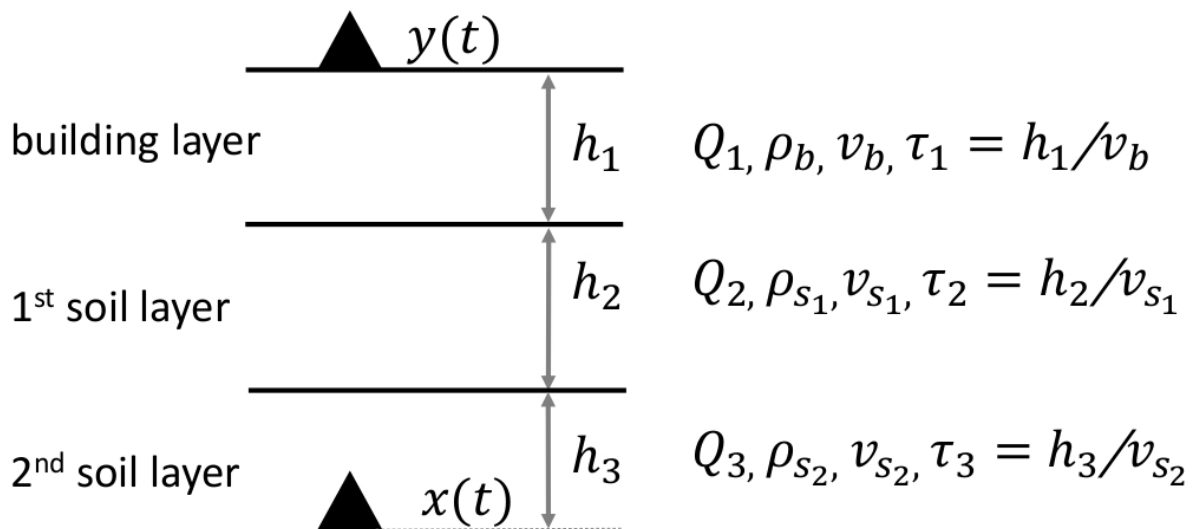


Figure A2. As in Figure A1 but for the three layer model made up of the building layer over two soil layers (where the first soil layer is from 0 m to -75 m and the second soil layer is a half-space) for simplifying the building-subsurface structure in Bishkek.

The layer structure, with the first layer representing the building, is shown in Fig. A2. The reflection coefficients r_1 and r_2 at the two impedance contrast for the up-going waves are defined as

$$r_1 = \frac{\rho_{s_2} v_{s_2} - \rho_{s_1} v_{s_1}}{\rho_{s_2} v_{s_2} + \rho_{s_1} v_{s_1}} \quad (A5)$$

$$r_2 = \frac{\rho_{s_1} v_{s_1} - \rho_b v_b}{\rho_{s_1} v_{s_1} + \rho_b v_b} \quad (A6)$$

with

ρ_{s_1} - density of first soil layer

ρ_{s_2} - density of second soil layer

ρ_b - density of building layer

v_{s_1} - velocity in first soil layer

v_{s_2} - velocity in second soil layer

v_b - velocity in building layer

The Fourier transform of $x(t)$ (of a sensor installed in the second soil layer) is given as

$$x(\omega) = x_0(\omega) + r_1 x_0(\omega) e^{-i4\pi f \frac{\tau_3}{Q_3}} + \frac{(1+r_1)x_0(\omega) e^{-i2\pi f (\frac{\tau_2+\tau_3}{Q_2+Q_3})}}{1+r_1 e^{-i4\pi f \frac{\tau_2}{Q_2}}} r_2 (1-r_1) e^{-i2\pi f (\frac{\tau_1+\tau_2}{Q_1+Q_2})} \quad (A7)$$

$$+ 0.5y(\omega)(1-r_1)(1-r_2) e^{-i2\pi f (\frac{\tau_1+\tau_2+\tau_3}{Q_1+Q_2+Q_3})}$$

with

τ_1 - time of wave propagation from top to bottom of the building

τ_2 - time of wave propagation from top to bottom of first soil layer

τ_3 - time of wave propagation from discontinuity to sensor at a certain depth in the second soil layer

Q_1 - quality factor of building layer

Q_2 - quality factor of first soil layer

Q_3 - quality factor of second soil layer

The Fourier transform of the recording at the top of the building, $y(t)$ can be obtained after some mathematical steps by

$$y(\omega) = \frac{2(1+r_2)(1+r_1)x_0(\omega) e^{-i2\pi f (\frac{\tau_1+\tau_2+\tau_3}{Q_1+Q_2+Q_3})}}{\left(1+r_1 e^{-i4\pi f \frac{\tau_2}{Q_2}}\right) \left(1+r_2 e^{-i4\pi f \frac{\tau_1}{Q_1}}\right)} \quad (A8)$$

Finally, the transfer function $\frac{x(\omega)}{y(\omega)}$ can be obtained by

$$\begin{aligned} \frac{x(\omega)}{y(\omega)} = & \frac{1}{2(1+r_1)(1+r_2)} e^{-i2\pi f (-\frac{\tau_1}{Q_1} - \frac{\tau_2}{Q_2} - \frac{\tau_3}{Q_3})} + \frac{r_1}{2(1+r_1)(1+r_2)} e^{-i2\pi f (-\frac{\tau_1}{Q_1} + \frac{\tau_2}{Q_2} - \frac{\tau_3}{Q_3})} \quad (A9) \\ & + \frac{r_2}{2(1+r_1)(1+r_2)} e^{-i2\pi f (\frac{\tau_1}{Q_1} - \frac{\tau_2}{Q_2} - \frac{\tau_3}{Q_3})} + \frac{r_1 r_2}{2(1+r_1)(1+r_2)} e^{-i2\pi f (\frac{\tau_1}{Q_1} + \frac{\tau_2}{Q_2} - \frac{\tau_3}{Q_3})} \\ & + \frac{r_1}{2(1+r_1)(1+r_2)} e^{-i2\pi f (-\frac{\tau_1}{Q_1} - \frac{\tau_2}{Q_2} + \frac{\tau_3}{Q_3})} + \frac{r_1^2}{2(1+r_1)(1+r_2)} e^{-i2\pi f (-\frac{\tau_1}{Q_1} + \frac{\tau_2}{Q_2} + \frac{\tau_3}{Q_3})} \\ & + \frac{r_1 r_2}{2(1+r_1)(1+r_2)} e^{-i2\pi f (\frac{\tau_1}{Q_1} - \frac{\tau_2}{Q_2} + \frac{\tau_3}{Q_3})} + \frac{r_2(1-r_1)}{2(1+r_2)} e^{-i2\pi f (-\frac{\tau_1}{Q_1} + \frac{\tau_2}{Q_2} + \frac{\tau_3}{Q_3})} \\ & + \frac{r_1^2 r_2}{2(1+r_1)(1+r_2)} e^{-i2\pi f (\frac{\tau_1}{Q_1} + \frac{\tau_2}{Q_2} + \frac{\tau_3}{Q_3})} + \frac{r_2^2(1-r_1)}{2(1+r_2)} e^{-i2\pi f (\frac{\tau_1}{Q_1} + \frac{\tau_2}{Q_2} + \frac{\tau_3}{Q_3})} \\ & + 0.5(1-r_2)(1-r_1) e^{-i2\pi f (\frac{\tau_1}{Q_1} + \frac{\tau_2}{Q_2} + \frac{\tau_3}{Q_3})} \end{aligned}$$

Appendix e): Joint deconvolution of building and downhole seismic recordings: An application to three test cases

The final publication is available at Springer via <https://dx.doi.org/10.1007/s10518-017-0215-6>

Petrovic, B., Parolai, S., Pianese, G., Dikmen, S. U., Moldobekov, B., Orunbaev, S., Paolucci, R. (2017b). Joint deconvolution of building and downhole seismic recordings: An application to three test cases, *Bulletin of Earthquake Engineering*.

Abstract

In this study, the joint deconvolution is applied to recordings of three test cases located in the cities of Bishkek, Kyrgyzstan, Istanbul, Turkey, and Mexico City, Mexico. Each test case consists of a building equipped with sensors and a nearby borehole installation in order to investigate different cases of coupling (impedance contrasts) between the building and the soil by analyzing the wave propagation through the building-soil-layers, and hence resolving the soil-structure-interactions. The three installations considering different dynamic characteristics of buildings and soil, and thus, different building-soil couplings, are investigated. The seismic input (i.e., the part of the wave field containing only the up-going waves after removing all down-going waves) and the part of the wave field that is associated with the waves radiated back from the building are separated by using the constrained deconvolution. The energy being radiated back from the building to the soil has been estimated for the three test cases. The values obtained show that even at great depths (and therefore distances), the amount of wave field radiated back by the building to the ground is significant (e.g., for the Bishkek case, at 145 m depth, 10-15% of the estimated real input energy is expected to be emitted back from the building; for Istanbul at 50 m depth, the value is also 10-15% of the estimated real input energy while for Mexico City at 45 m depth, it is 25-65% of the estimated real input energy). Such results confirm the active role of buildings in shaping the wave field.

1 Introduction

Studying the dynamic characteristics of civil engineering structures and the soil, and how earthquake-induced shakings influences each other, known as the dynamic soil-structure interaction (SSI), has been a subject of interest within the engineering and seismological communities (e.g., Wirgin and Bard 1996; Bard et al. 1996) since several decades. When the interaction is not limited to individual buildings and the underlying soil, but extended to the seismic interaction of an entire city with the soft soil layers during seismic events, it is called site-city interaction (SCI, e.g., Gueguen et al. 2002, Kham et al. 2006).

In the past, while SSI effects on buildings' dynamic behavior have been studied extensively, the modification of the seismic wave field in superficial soil layers induced by the vibration of surface structures have until now received only limited attention. Nevertheless, it is well known that SSI and SCI in densely urbanized areas may cause non-negligible modifications to ground motions compared with those recorded in the free-field.

The influence of surface structures on seismic wave propagation and the waves generated by structural vibrations in response to seismic ground motions recorded even at large distances in urban areas have been observed by experimental studies for several decades. Jennings (1970) performed one of the first studies in which waves generated by the forced vibration of the Millikan Library were registered at up to 10 km distance. It was followed by a study on the effects of high-rise buildings in Los Angeles excited by shock waves induced by the re-entry of the Columbia space shuttle into atmosphere by Kanamori et al. (1991). Gueguen et al. (2000) analyzed in the Volvi experiment the wave field radiated by a reduced-scale vibrating structure in the Volvi EuroSeisTEst site. Considering two close-by structures, Kitada et al. (1999) analyzed experimentally how structure-soil-structure interactions change the dynamic response of the structures themselves. Chavez-Garcia and Cardenas-Soto (2002) studied the influence of neighboring structures on free-field ground motion by using the H/V spectral ratio. Chazelas et al. (2001) investigated the interaction between structures through the soil by a reduced scale centrifuge experiment.

Primarily, 2D and 3D numerical studies have been performed to analyze the effects of the presence of many high-rise buildings on free-field ground motion and hence, the SSI effects in urban areas, e.g., Wirgin and Bard (1996) and Bard et al. (1996). Moreover, several 2D and 3D numerical simulations of ground motions have been carried out in order to investigate the SCI (e.g., Gueguen et al. 2002; Semblat et al. 2002, 2004, 2008; Kham et al. 2006). Different numerical studies have suggested both increases and decreases in ground motion due to buildings located at the Earth's surface. For example, Gueguen et al. (2002) carried out numerical simulations to analyze the contribution of the Roma Norte district of Mexico City to total seismic ground motion. They stated that modifications to the seismic wave field (compared to the free-field case) due to surface structures that behave as secondary seismic sources and local interactions between structures through the soil might be significant in urban areas and defined these effects of a city to the soil as SCI. Kham et al. (2006) analyzed the multiple interactions between soil layers and built structures in dense urban areas, and hence, the influence of the city on the ground motion using simplified 2D boundary elements models. Pioneering examples of more advanced numerical approaches, where a comprehensive 3D modeling of both soils and built structures in an urban environment is considered, were recently illustrated by Mazzieri et al. (2013) and Isbilibiroglu et al. (2015).

Moreover, several authors have attempted to give a semi-analytical description of the SCI effects. Gueguen et al. (2000) tried to describe the effects of a city by adding the single contribution of each building represented by a single oscillator. Boutin et al. (2004) described the multiple interactions of buildings through homogenization methods.

Studies combining both experimental tests and numerical simulations have been carried out. Bard et al. (2008) observed structure-soil-structure effects by centrifuge tests and numerical simulations. Ditommaso et al. (2009) analyzed the influence of a single vibrating building on the free-field ground motion, while Gueguen and Colombi (2016) investigated the clustering effects of structures on their response.

The deconvolution approach (Kanai 1965), following Snieder and Safak (2006) has found a wide application for studying wave propagation in buildings (e.g., Picozzi et al. 2009; Newton and Snieder 2012; Rahmani and Todorovska 2013; Nakata and Snieder 2014; Cheng et al. 2015; Petrovic et al., 2017) using both ambient vibration measurements and earthquake recordings. Moreover, when applied to downhole strong-motion data, information about the wave propagation in shallow geological layers is obtained (e.g., Mehta et al. 2007a, b; Parolai et al. 2009, 2013; Oth et al. 2011; Raub et al. 2016).

Recent studies have shown the importance of the interactions between objects located at the surface (trees or buildings) in the modification of the seismic wave field. Colombi et al. (2016) performed experimental studies and finite element simulations to better understand the interaction between trees and the soil. Petrovic and Parolai (2016) proposed a method to study the wave propagation in building-soil layers by joint deconvolution and to estimate the wave field being radiated back from a building to the soil.

In this study, we investigated three different cases of coupling (impedance contrast) between the building and the soil by analyzing the wave propagation through building-soil-layers, and thus the soil-structure interaction effects. The objective of this study was to determine the energy radiated back to the subsoil from a building under seismic excitation. For this purpose, the joint deconvolution (Petrovic and Parolai, 2016) is applied to earthquake recordings of three installations composed of a borehole and a nearby building equipped with sensors (in the cities of Bishkek, Kyrgyzstan, Istanbul, Turkey, and Mexico City, Mexico). The three test cases involve different soil conditions and building construction types. The ratio between the shear wave velocities of building and soil vary from test site to test site (Bishkek: $v_{\text{soil}} > v_{\text{building}}$, Istanbul: $v_{\text{soil}} \approx v_{\text{building}}$ and Mexico City $v_{\text{soil}} \approx /< v_{\text{building}}$), leading to different impedance contrasts. The shear wave velocity profiles of the soil were provided by previous studies (Parolai et al. 2012, 2013, Meli et al. 1998), while the shear wave velocity through the building was estimated by the application of the deconvolution approach. Although we are considering different ratios between buildings and soil, the impedance of the building is always lower than the impedance of the soil, leading to an impedance contrast below 1 for all considered test cases (Bishkek: $c \approx 0.1$, Istanbul: $c \approx 0.2 - 0.3$, Mexico City: $c \approx 0.3 - 0.6$). This is due to the fact that the effective density of buildings is always several times smaller than the density of the soil. The seismic input (i.e., the part of the wave field containing only the up-going waves after removing all down-going waves) and the wave field that is associated with the wave field radiated back from the building to the soil is reconstructed using the constrained deconvolution approach. Finally, the energy being radiated back from the buildings to different soil depths is estimated. The influence of different impedance contrasts on the wave field radiated back from the building to the soil is also investigated.

2 Methodology

A two stage approach proposed by Petrovic and Parolai (2016) is used to determine the energy radiated back by the building to subsoil. In the first stage, the joint deconvolution of recordings from the building and downhole sensors is carried out. Then in the second stage, the energy radiated back from the building to the shallow geological layers is estimated. In the following, the main steps of the procedure (Figure 1) are briefly summarized.

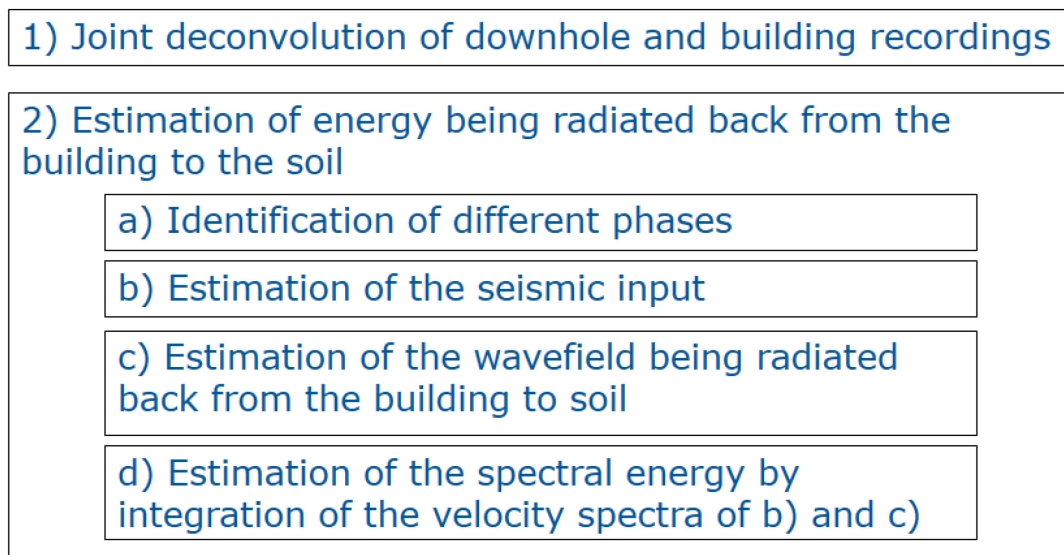


Figure 1. The general scheme of the methodology followed in this work.

1) Joint deconvolution of building and downhole recordings

The joint deconvolution is an upgrade of the deconvolution approach that has found wide application in the past when applied separately to recordings from buildings or downhole, making it possible to study the wave propagation either through the building or the shallow geological layers, respectively. In our case, the recordings of sensors installed in a building and a borehole are analyzed jointly.

The ground motion recordings at a generic location (within the building or the borehole) are deconvolved by the recording at a reference station (usually either the top or the bottom sensor of a building- downhole-installation) as follows

$$S(\omega) = \frac{u(z_1, \omega)}{u(z_2, \omega)} \quad (1)$$

with $u(z_1, \omega)$ and $u(z_2, \omega)$ being the Fourier transforms of the recordings at depths z_1 and z_2 , respectively. Since this problem is ill-conditioned, to avoid the potential instabilities in the inversion, a regularized Tikhonov deconvolution $S_\varepsilon(\omega)$, defined as

$$S_{\varepsilon}(\omega) = W_{\varepsilon}(\omega) \frac{u(z_1, \omega)}{u(z_2, \omega)}, \quad (2)$$

is used (Tikhonov and Arsenin 1977, Bertero and Boccacci 1998). $u(z_1, \omega)$ and $u(z_2, \omega)$ are the Fourier transforms of the recordings at depths z_1 and z_2 and the filter $W_{\varepsilon}(\omega)$ is given as

$$W_{\varepsilon}(\omega) = \frac{|u(z_2, \omega)|^2}{|u(z_2, \omega)|^2 + \varepsilon}. \quad (3)$$

where ε is the regularization parameter that is defined as a percentage of the average spectral power. It is a positive constant added to the denominator to prevent the numerical instability of $S(\omega)$. For $\varepsilon=0$, equation (2) is equal to equation (1).

In this study, the horizontal components of ground motion are considered, which are expected to be mainly related to the S-wave propagation (e.g., Mehta et al. 2007a, 2007b, Parolai et al. 2009). Before the application of the joint deconvolution, the data are first cosine-tapered at both ends and then, band-pass Butterworth filtered (Bishkek: 1-10Hz, Istanbul: 0.1-15Hz, Mexico City: 0.1-5Hz). The sensor at the top of the building is used as the reference station for the joint deconvolution. The regularization parameter was set to $\varepsilon=10$ % of the average spectral power for Bishkek and $\varepsilon=5$ % of the average spectral power for Istanbul and Mexico City after trial and error tests (e.g., Bindi et al 2015).

2) Estimation of the energy being radiated back from the building to the soil

The method for the estimation of the energy being radiated back from the building to the soil consists of four steps.

- a) Identification of the peaks in the deconvolved wave field related to the different phases (upward propagating waves, downward propagating waves reflected at the Earth's surface, at impedance contrasts and at the top of the building, etc.).
- b) Reconstruction of the seismic input at a certain depth related only to the upward propagating waves and hence, by removing all downward propagating waves (reflected at the building's roof, the Earth's surface and the impedance contrasts) using an approach similar to the one proposed by Bindi et al. (2010), based on a constrained regularized scheme (projected Landweber method).

The seismic input is obtained by convolving the peaks related to the upward propagating waves in the deconvolved wave field (using the recordings of the surface downhole sensor as reference) and the recordings at 0 m.

- c) Separation of the part of the wave field that is associated with the waves being radiated back from the building to the soil down to different depths using the same approach as the one used to reconstruct the seismic input (b). Differently from (b), however, the recordings by the roof sensor are used as the reference.

In order to reconstruct the wave field of interest, the peak in the deconvolved wave field, which is associated with the down-going waves being radiated back from the building to the soil, is convolved with the recordings made at the top of the building. Please note that different phases might arrive at the same time and hence overlap (Petrovic and Parolai, 2016). For this reason, the relative importance of the contributions of the different phases arriving at the same time has to be taken into account. This is

obtained by calculating the analytical transfer functions. Only information on the velocities (obtained from the deconvolution approach) and the densities (mainly of importance for the building's structure, can easily be estimated) is required. No information on the quality factor Q , which may be complicated to estimate, is needed.

d) Estimation of spectral energy radiated back from the building to the soil. The spectral energy of the seismic input (b) and the downward propagating waves (c) is obtained by the integration of the velocity spectra of (b) and (c) over a defined frequency band (the same as the one used for the joint deconvolution). The spectral energy of the waves being radiated back from the building to the soil is given relative to the energy of the seismic input and thus, obtained as the ratio of the spectral energies of (c) to (b).

3 Description of the test sites

In this study, three test cases (Bishkek, Kyrgyzstan; Istanbul, Turkey; and Mexico City, Mexico; Figures 2-5) with different soil and building characteristics are investigated. If no information is already available on the shear wave velocity profiles of the building and/or the soil, the shear wave velocity can be determined from the deconvolved wave fields. In this study, the shear wave velocity profiles of the soil are provided by previous studies and have been confirmed by the deconvolution approach, while for the buildings these are estimated by the deconvolution approach. After the deconvolution, the deconvolved wave fields are obtained by applying the inverse Fourier Transform. Then, the time lags between the upward and downward propagating waves in the deconvolved wave fields and the height differences between the floors where the sensors are installed, are considered. The shear wave velocity is then calculated using a least squares fit.

In Bishkek, the test case is a 3-story reinforced-concrete masonry building with a lower shear wave velocity (~ 300 m/s) than the underlying soil (~ 600 m/s). In Istanbul, the shear wave velocity in the uppermost layer (~ 300 m/s) is similar to that through the investigated 16 story tunnel formwork building (distance to downhole installation ~ 50 m). In Mexico City, a 14 story RC building constructed on low velocity clay soil has a similar/higher shear wave propagation velocity (70 m/s-140 m/s) to/than the subsurface (~ 70 m/s). Nevertheless, it is worth mentioning that the higher density contrast (compared to the velocity contrast) of the buildings and the soil has a major influence on the impedance contrast and hence, on the proportion of the wave field being radiated back from the building to the soil. Additional details of each site are given below.

3.1 Bishkek, Kyrgyzstan

A 150 m deep borehole was drilled in 2010 in Bishkek (Kyrgyzstan) in the courtyard of Central Asia Institute for Applied Geosciences (CAIAG, Fig. 2) and equipped with borehole sensors at 0, 10, 25, 45, 85 and 145 m depth (Parolai et al. 2013; Petrovic and Parolai 2016). Figure 2 shows the S-wave velocity (v_s) structure and the stratigraphy at this site, including the results of the best fitting S-wave velocity models obtained after the inversion of the spectra of the deconvolved wave field (Parolai et al. 2013). Above 80 m depth the soil is composed of alternating layers of coarse gravel shingle and sandy layers

of different thicknesses, while from 80 m to 150 m depth there is a thick gravel-shingle layer. For further information on this borehole installation, see Parolai et al. (2013).

The building of the CAIAG institute (distance to borehole installation ~ 10 m) has been equipped with seven SOSEWIN (Self-Organizing Seismic Early Warning information Network, Fleming et al., 2009) units since 2012, with six at two edges of the three floors and one under the roof (Fig. 2, Fig. 5a). The CAIAG building is a three story reinforced masonry structure built in 1975. The footprint (Fig. 5a) of the building is rectangular (37.8 m x 16.3 m), the walls are constructed of fired clay solid bricks, concrete floors and roof of timber frame with metal cover (Petrovic and Parolai 2016).

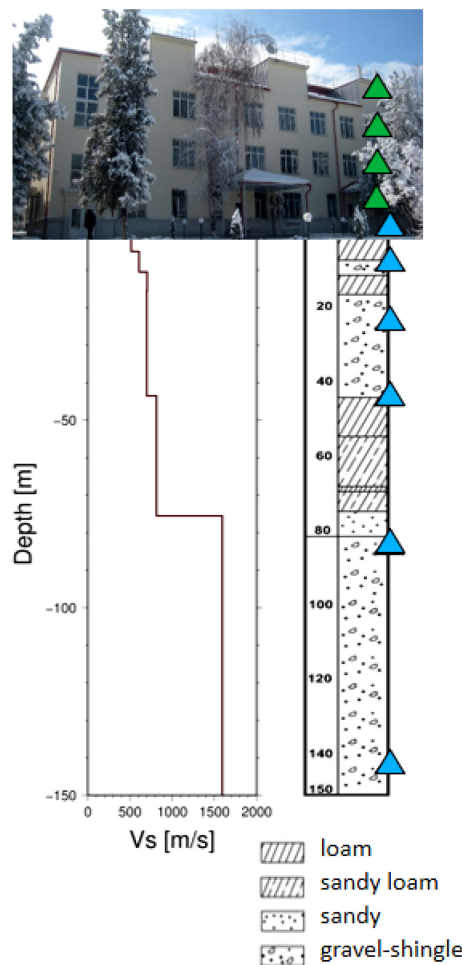


Figure 2. Installations in CAIAG (green squares) and the adjacent borehole (blue triangles) of the Bishkek test site, showing an image of the CAIAG building (top), the shear wave velocity profile obtained from inverting of the spectra of the deconvolved wave field and the stratigraphy (from Parolai et al. 2013).

3.2 Istanbul, Turkey

In December 2005, in the district of Ataköy, Istanbul (Turkey), four boreholes of 25 m, 50 m, 70 m and 140 m (Fig. 3) were drilled and equipped with 3 shallow boreholes accelerometers (at 25 m, 50 m and 70 m) and a deep borehole accelerometer (at 140 m depth). In addition, a sensor at 0 m was installed (Parolai et al. 2009, 2010, 2012; Bindi et al. 2010). The sensor at 70 m had experienced some

malfunctions during the analyzed time period and hence, its recordings could not be used. Figure 3 shows the S-wave velocity structure and the stratigraphy at the test site. The shear wave velocity profiles have been obtained by inversion of the spectra of the deconvolved wave fields for three events, with a best-fitting v_s model gained from each event, as shown in Figure 3 (Parolai et al. 2012). In this part of the city, alluvial deposits (unconsolidated sediments composed of gravel, sand, silt and clay) overlie the Bakirköy and Güngören formations over Palaeozoic bedrock (Sorensen et al. 2006). A detailed description of the borehole installation is given in Parolai et al. (2009).

A 16 story (including one basement story) tunnel formwork building (B22), located ~50 m from the borehole, has been equipped by a SOSEWIN network consisting of 15 stations (four of them connected to 5TC Güralp strong motion accelerometers) installed near to the building's center and the fire escape staircase (Fig. 5b) at different floors since September 2015. The first SOSEWIN installation, consisting of only three SOSEWIN stations placed at the basement, the 8th floor and the roof, was realized in the summer of 2013. The building was constructed in the early 1990s, and has a total height of about 45 m and an approximately square footprint with dimensions of 23.1 m x 23.9 m (Fig 5b). The building is symmetrical in both perpendicular directions in plan view, with four apartments of the same size located at each floor. The exterior walls with windows were constructed using precast panels. The interior walls and the remaining exterior walls, i.e., those without windows are made of reinforced concrete and are 15 cm and 20 cm thick. For further information on the building's structure and the dynamic characteristics of the building, see Petrovic et al. (2017).

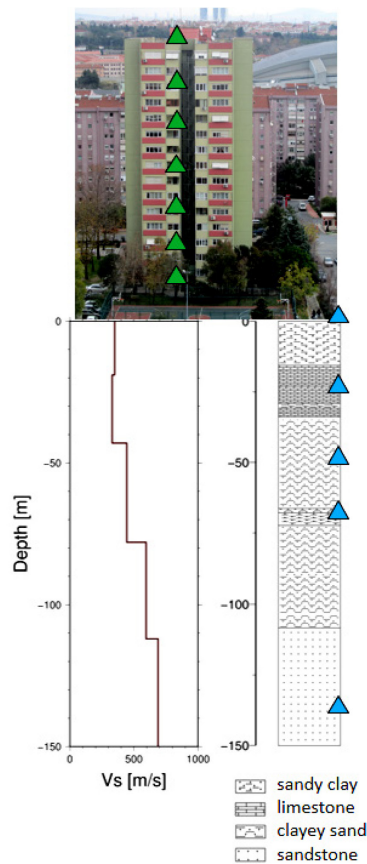


Figure 3. Installations in building B22 (green squares) and the borehole (blue triangles) of the Ataköy, Istanbul test site, showing a photo of the building, the shear wave velocity profile obtained from the inversion of the spectra of the deconvolved wave field and the stratigraphy (from Parolai et al. 2012).

3.3 Mexico City, Mexico

The Jalapa building in Mexico City, Mexico, constructed in 1981, is a 14 story reinforced concrete building (Fig 4, 5c), located in the central area of the city. The building was instrumented with 11 tridirectional solid state digital accelerographs (Terra Technology DCA-33R) at different locations on 4 floors (basement, 6th and 11th floor, roof, Fig. 4) from 1992 to 2004. The first three stories of the Jalapa building are used as parking, the others as offices. The building is 39.5 m high with a rectangular footprint (19.4 m x 40 m from the basement to the 3rd floor, and 19.4 m x 32.45 m from the 3rd floor to the roof, Fig 5c). The original structural system is of a waffle flat-plate on rectangular columns, with a small core of concrete shear walls around the shafts for the staircases and elevator, and masonry infill walls in external frames in a longitudinal direction and around the staircases.

The borehole installation consisted of two accelerographs (same instrument type as those installed in the building) at 20 and 45 m depth underneath the basement of the building. Beneath a superficial crust (5 m thick), soft clay deposits (down to 29.5 m depth) overlie a 3 m thick intermediate firm layer. A lower clay layer (from 32.5 m to 38.5 m depth) is followed by deep firm deposits. The shear wave velocity profile obtained from SCT tests (Meli et al. 1998) is shown in Figure 4.

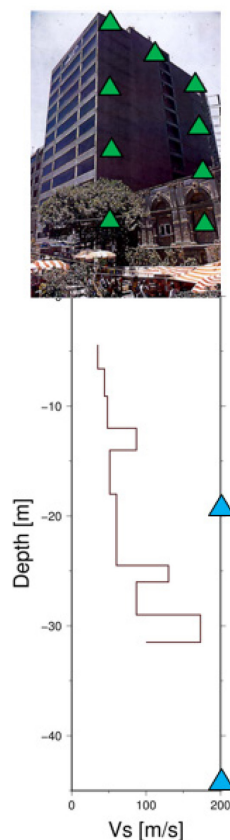


Figure 4. Installations in the Jalapa building (green triangles) and the borehole (blue triangles) of the Mexico City test site, showing an image of the Jalapa building and the shear wave velocity profile obtained from SCT tests (modified after Meli et al. 1998).

The Jalapa building is one of the few well-instrumented buildings in Mexico that have suffered structural and non-structural damage, and it has been retrofitted twice during its lifetime (Murià-Vila et al. 2001). Thus, it is of great interest for the earthquake engineering community, with the dynamic behavior of the building being studied in detail, e.g., by Meli et al. (1998) and Murià-Vila et al. (2001). Moreover, due to its location on a very soft clay soil, soil-structure interaction effects have also been observed (e.g., Paolucci 1993; Faccioli et al. 1996; Cardenas et al. 2000 and Murià-Vila et al. 2004). A first attempt to analyze the strong motion recorded by the borehole and building installation jointly was made by Cardenas-Soto (2007). Pianese et al. (2018) presented a new methodology for the detection of non-linear response of instrumented buildings during an earthquake by combining Stockwell Transforms (Stockwell 1996) and the deconvolution approach and applying this to the Jalapa building.

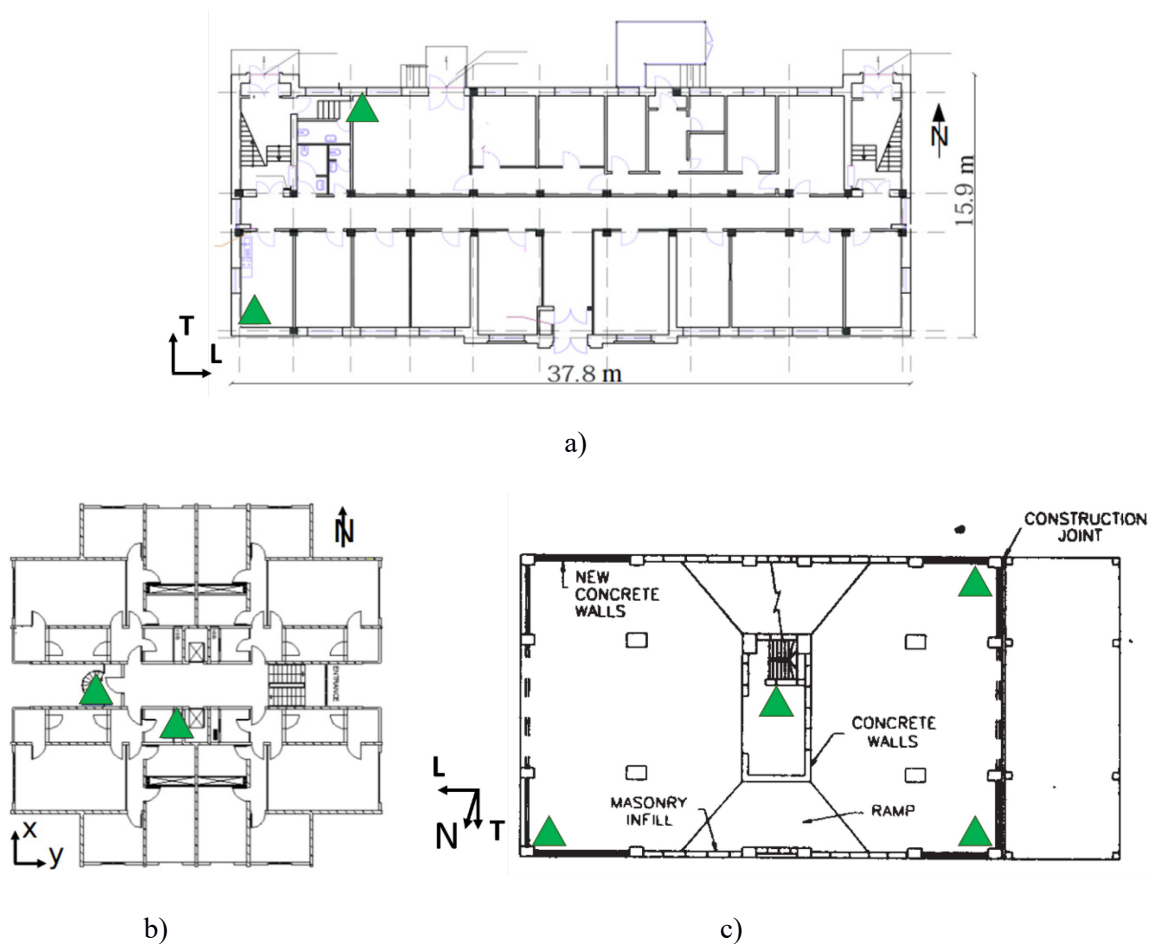


Figure 5. Footprints of the three investigated buildings (a: CAIAIG insitute, Bishkek, Kyrgyzstan, b: B22 building, Istanbul, Turkey, c: Jalapa building, Mexico City, Mexico). The location (green triangles) and orientation of the sensors is also shown.

4 Data set

4.1 Bishkek, Kyrgyzstan

The data set used in this study for the Bishkek test case is composed of four earthquake recordings (Table 1, Figure 6a) with magnitudes ranging from M 4.8 to 5.2 that occurred between November 2013 and March 2015 in Kyrgyzstan or Kazakhstan.

Table 1. List of events used in this study for the test site in Bishkek, Kyrgyzstan.

Event ID	Date	Time (UTC)	Location	Depth (km)	Magnitude M_w	Distance to epicenter (km)
BI-2013	23.11.2013	09:42:08	42.46N, 75.77E	10	4.9	110
BI-2014	14.11.2014	01:24:20	42.10N, 77.31E	45	5.2	350
BI-2015-1	22.01.2015	15:52:29	42.34N, 77.99E	0	4.9	280
BI_2015-2	15.03.2015	14:01:02	43.15N, 76.90E	10	4.8	190

The horizontal components of the borehole sensors are rotated in order to be orientated along the main building axes. The data of the SOSEWIN units is resampled by interpolation (originally 100 samples per second) in order to obtain the same sampling rate as the data from the downhole sensors (500 samples per second) to improve the resolution of the deconvolution results in the time domain (e.g., Céspedes et al. 1995; Tamim and Ghani 2010).

4.2 Istanbul, Turkey

The analyzed data set (Table 2, Fig. 6b) consists of six earthquake recordings with magnitudes between M_w 3.7-4.8 (with epicentral distances from 20 km to 165 km) that occurred between November 2013 and December 2015, four of which were in the Marmara Sea region. Earthquakes that were registered at least at the sensor at the building's roof and at the 140 m deep downhole sensor are considered. It is worth mentioning that three of the six events (Table 2, event 1-3) took place before the new dense SOSEWIN installation and hence, for these events only the recordings at the top and the bottom of the building are available. Moreover, since only small events and the corresponding weak motions are used for this study, and due to the lower quality of the MEMS sensors used by the SOSEWIN units, only recordings of 5TC Güralp strong motion accelerometers connected to the SOSEWINs are used.

Table 2. List of events used in this study for the test site in Istanbul, Turkey.

Event ID	Date	Time (UTC)	Location	Depth (km)	Magnitude M_w	Distance to epicenter (km)
IS-2013-1	27.11.2013	04:13:37	40.85N, 27.92E	9	4.8	80
IS-2013-2	27.11.2013	04:21:35	40.85N, 27.91E	7	4.0	80
IS-2014	05.02.2014	01:56:44	41.36N, 28.61E	12	3.7	45
IS-2015-1	28.10.2015	16:20:03	40.80N, 27.72E	16	4.6	100
IS-2015-2	16.11.2015	15:45:43	40.83N, 28.76E	8	4.3	20
IS-2015-3	15.12.2015	01:13:39	42.34N, 29.71E	30	4.1	165

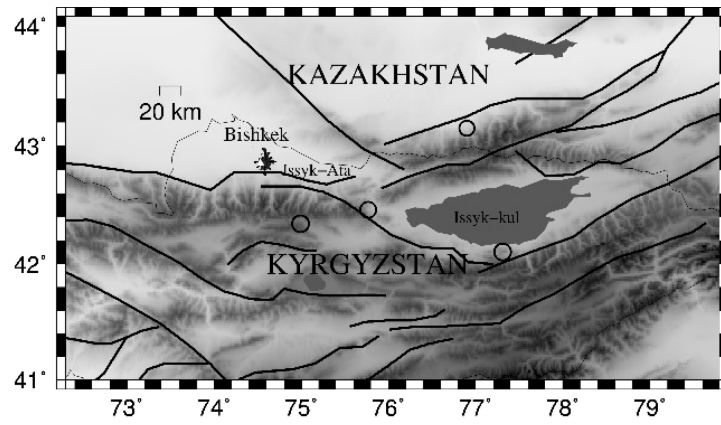
The data from the sensors installed in the borehole are rotated in such a manner that the two horizontal components are oriented along the main building axes. The data from the SOSEWIN sensors is resampled (original sampling rate 100 samples per second) in order to have the same sampling rate same as of the borehole sensors (200 samples per second).

4.3 Mexico City, Mexico

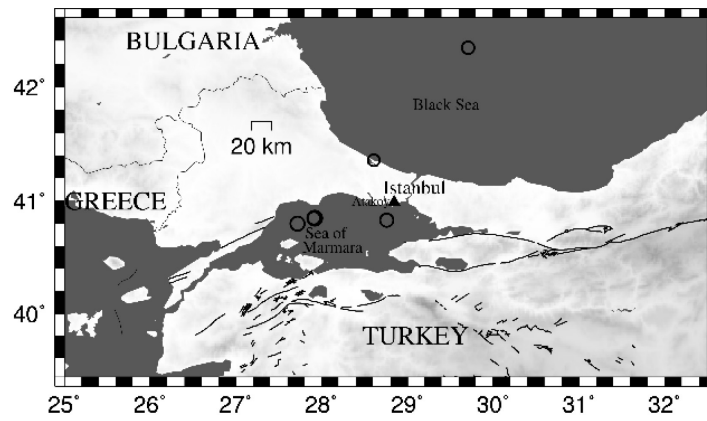
During the installation period, several seismic events were recorded in the Jalapa building. In our study, we focus on those events that did not cause any damage to the building, and hence the building's behavior can be approximated as being linear for the considered events (Meli et al. 1998; Murià-Vila et al. 2001). The characteristics of the 6 analyzed events with magnitudes M_w 6.0-7.2 and epicentral distances of approximately 300-400 km (Fig. 6c) are given in Table 3. Apart from the two other test cases where the buildings were not damaged until now and hence, the dynamical characteristics of the buildings can be assumed to be constant over time, for the Jalapa building, the dynamic properties have been altered due to structural damage and retrofitting.

Table 3. List of events used in this study for the test site in Mexico City, Mexico.

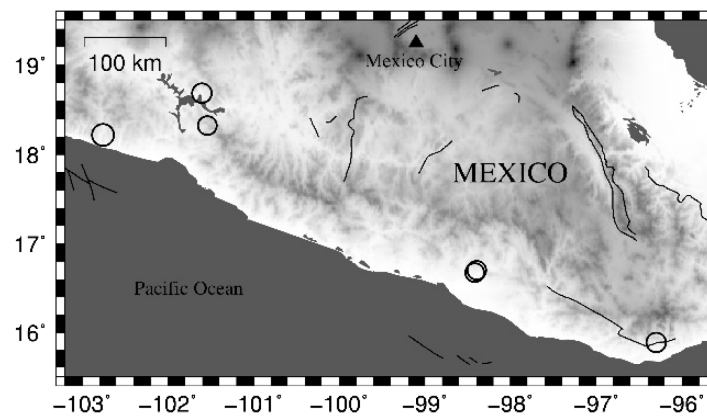
Event ID	Date	Time (UTC)	Location	Depth (km)	Magnitude M_w	Distance to epicenter (km)
MC-1993-1	15.05.1993	03:09:38	16.67N, 98.42W	19.7	6.0	318
MC-1993-2	15.05.1993	03:12:32	16.70N, 98.40W	20.8	6.1	315
			damage + retrofitting			
MC-1997-1	11.01.1997	20:28:26	18.22N, 102.0W	33	7.2	330
MC-1997-2	22.05.1997	07:50:53	18.68N, 101.6W	70	6.5	270
MC-1998	03.02.1998	03:02:00	16.67N, 96.42W	33	6.3	515
			damage			
MC-1999-2	21.06.1999	17:43:04	18.32N, 101.54W	68.7	6.2	285



a)



b)



c)

Figure 6. Locations of the epicenters (circles) of the earthquakes used in this study for a) Bishkek (events listed in Table 1), b) Istanbul (Table 2), and c) Mexico City (Table 3).

5 Results - Joint deconvolution and estimation of the energy being radiated back from the building to the soil

5.1 Joint deconvolution

The recordings for one horizontal component (Bishkek: transverse component, Istanbul: x-direction, Mexico City: transverse direction, see Fig. 5) of each building-downhole installation and the corresponding Fourier amplitude spectra (FAS) are shown exemplarily for one event for each test site in Figures 7-9 (Fig. 7: Bishkek, event BI-2015-2, M_w 4.8, Table 1; Fig. 8: Istanbul, event IS-2015-1, M_w 4.6, Table 2; Fig. 9: Mexico City, event MC-1993-2, M_w 6.1, Table 3).

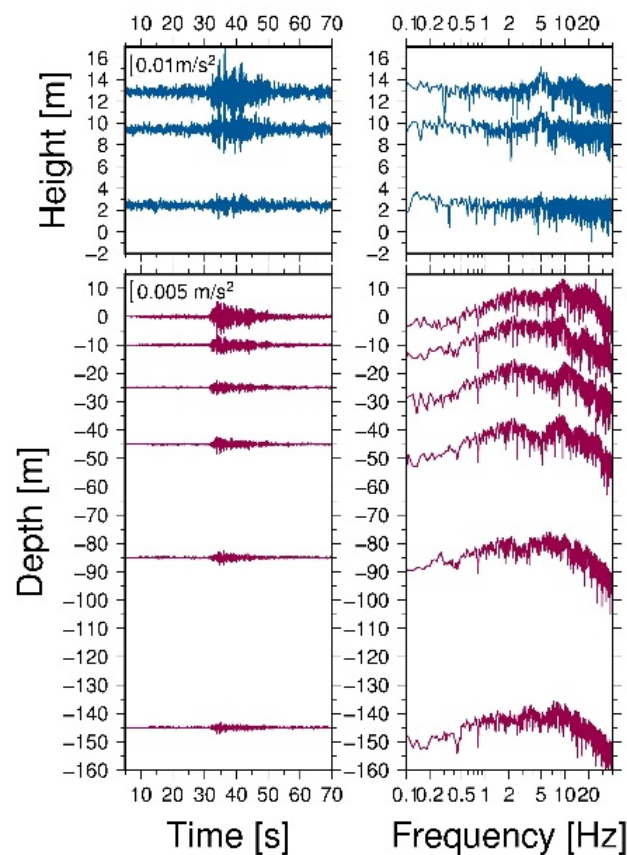


Figure 7. Recordings of transverse component (blue lines: building sensors, magenta lines: downhole sensors) and the corresponding Fourier Spectra for the Bishkek vertical array, event BI-2015-2, Table 1.

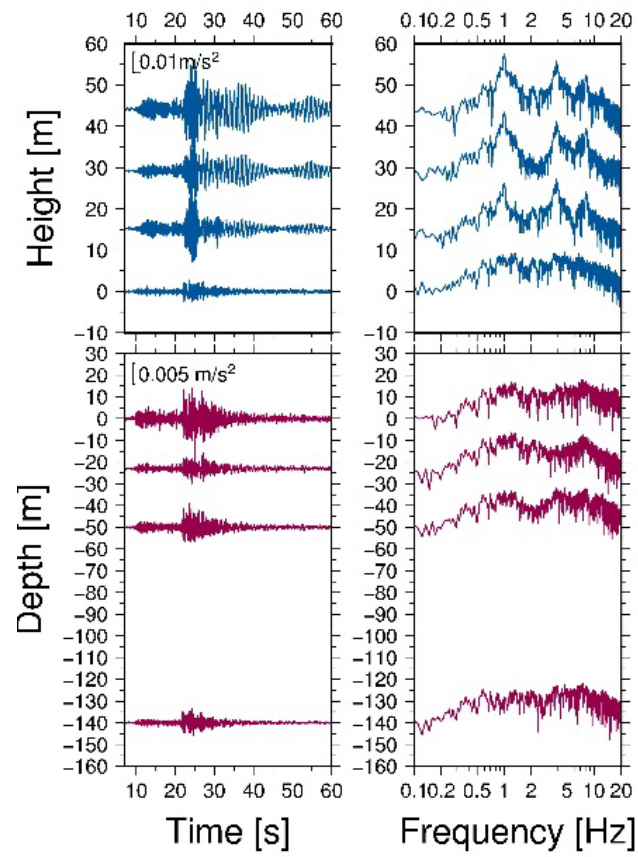


Figure 8. Same as Figure 7 but for the Istanbul vertical array, x-component, event IS-2015-1, Table 2.

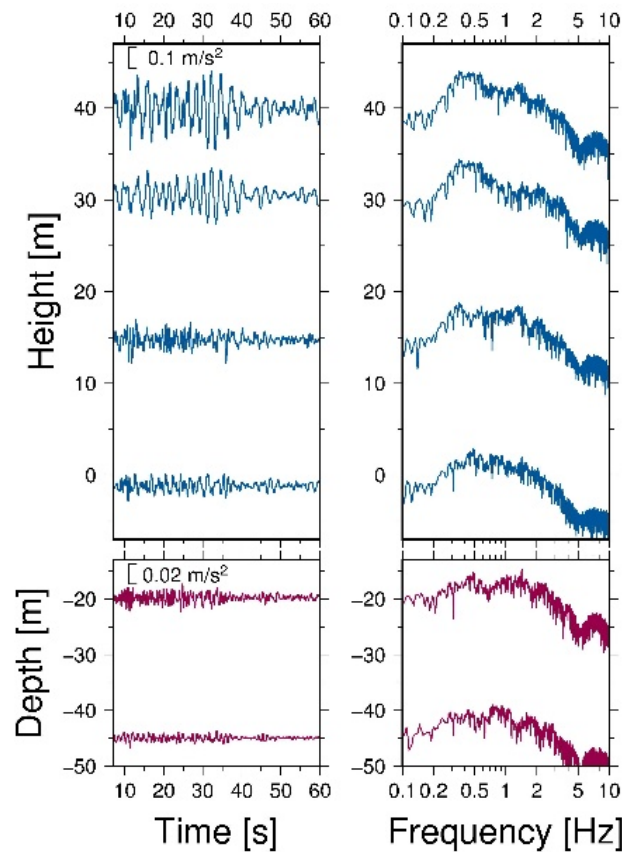


Figure 9. Same as Figure 7 but for the Mexico City vertical array, transverse component, event MC-1993-2, Table 3.

For all three test cases, the variation in the ground motion with depth/height and the higher level of shaking in the buildings is observed. When considering the recordings of the sensors installed in the buildings (especially the higher floors and the roof) for the Istanbul and Mexico City installations, the shaking of the building is univocal. The Fourier spectra show clearly the different frequency ranges where most of the energy is concentrated for the building and the downhole sensors for the test cases in Bishkek and Istanbul. The Fourier amplitude spectra of the Mexico City installation show only a small variation in the frequency content with depth due to similar fundamental frequencies (i.e., building: $f_{T1}=0.44$ Hz, soil: $f_{soil}=0.5$ Hz) and the frequency content of building and the soil (e.g., Meli et al. 1998). Moreover, the frequency band for the Mexico City case containing most of the energy is much narrower than for the other two test cases, with a frequency range only up to 3 Hz. For Mexico City, most of the energy is located between 0.2 and 2 Hz since the thick layers of extremely soft clay act as a band pass filter and greatly amplify the seismic waves coming from deeper firm strata. This results in an almost monochromatic ground motion of long duration and low frequencies (Murià-Vila 2001). For the Bishkek test case, a clear resonant peak is estimated at $f=5$ Hz in the Fourier spectra of the recording at the roof's station, most likely due to the 1st bending mode in this direction at $f=5$ Hz (Petrovic and Parolai 2016). For the installation in Istanbul, the Fourier spectra of the building sensors, especially for the higher floors and the roof, are not dominated by only one resonant peak, but by three ($f_1=1$ Hz, $f_2=3.84$ Hz and $f_3=7.5$ Hz), corresponding to the first three bending modes in this direction. Interestingly, for the B22 building, the higher modes (especially the second one) also make a high

contribution to the building's dynamic behavior and are clearly visible in the deconvolved wave field, as was shown and discussed in Petrovic et al. (2017). For the Jalapa building, a peak at around 0.4 Hz (corresponding to the first bending mode in the transverse direction) can be assumed in the FAS of the registrations at the higher floors (roof and 11th floor).

In Figures 10-12 (Fig. 10: BI-2015-2, Table 1; Fig. 11: IS-2015-1, Table 2 and Fig. 12: MC-1993-2, Table 3), the deconvolved wave fields using the recordings at the top of the buildings as reference and the corresponding spectra are shown for the same three events as in Figures 7-9 for the three test cases (blue lines: building sensors, magenta lines: downhole sensors). For all three test cases, the up and downward propagating waves can be identified through the building-soil layers in the acausal and causal parts, respectively. When comparing the deconvolved wave fields for the three test cases, it is noticed that the deconvolved wave field of the Istanbul test site is dominated by more peaks, resulting in a more complex deconvolved wave field compared to the other two cases. Moreover, for the Mexico City test case, due to the narrow range of the frequencies for the building and soil, the peaks of the deconvolved wave field are wider. The transfer functions in the frequency domain show troughs associated with up and downward propagating waves for all three test cases. For the Istanbul test site, the transfer function of the downhole sensors and the building sensor at 0 m show troughs at the frequencies of the first two bending modes of the B22 building.

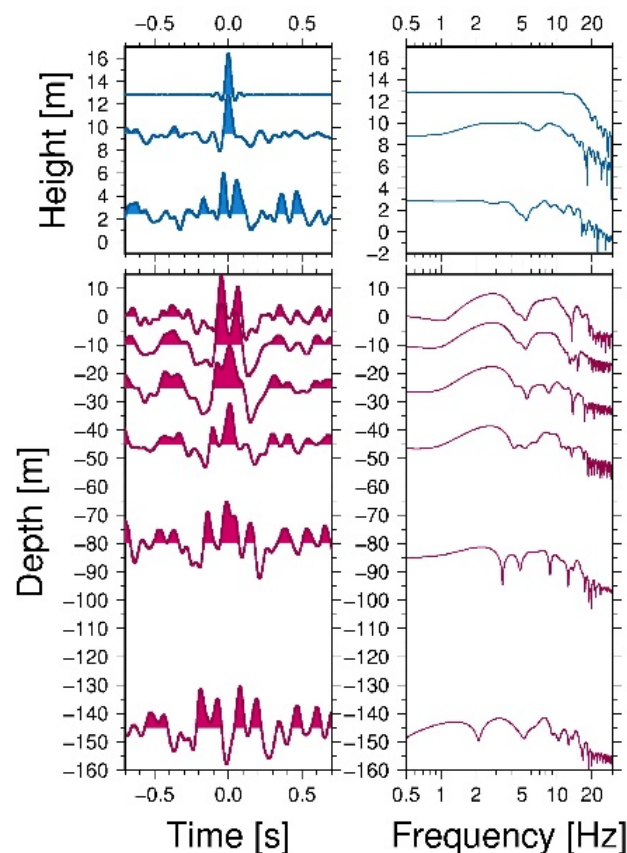


Figure 10. Deconvolved wave fields using the recordings at the top of the building as the reference and the corresponding spectra of deconvolved wave fields for the same events as for Fig. 7 for the building-downhole installation (blue lines: building sensors, magenta lines: downhole sensors) in Bishkek, event BI-2015-2, Table 1.

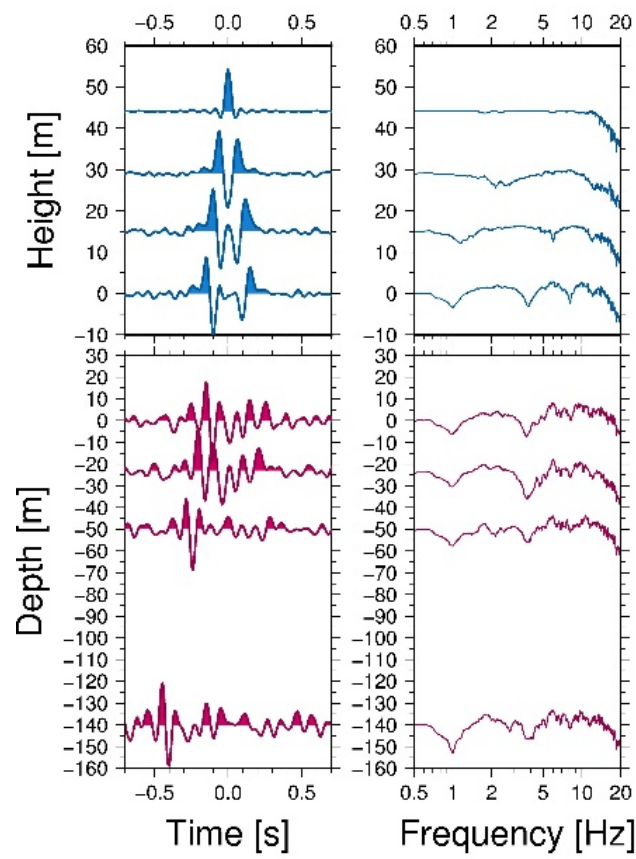


Figure 11. Same as Figure 10 but for the Istanbul vertical array for event IS-2015-1, Table 2.

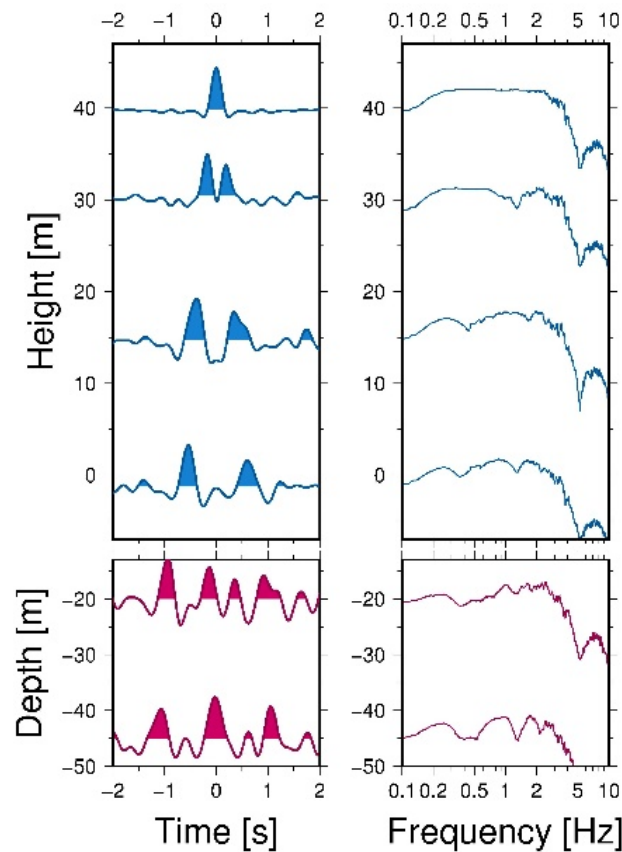


Figure 12. Same as Figure 10 but for Mexico City vertical array, event MC-1993-2, Table 3.

5.2 Estimation of the energy being radiated back from the building to the soil

The deconvolved wave fields are stacked for one horizontal component (Bishkek: transverse component, Istanbul: x-direction, see Fig. 5a and 5b) for all events for the test sites in Bishkek and Istanbul and are shown in Figure 13a and 13b, respectively. Since the buildings have not suffered any damage until now, the dynamic characteristics can be assumed to be constant, and thus, the results are stacked. Please note that the new dense installation of SOSEWINs in Istanbul was finalized in September 2015 and hence, for three earthquakes only the recordings at the top and bottom of the building are available. Moreover, the downhole sensor at 50 m depth suffered some malfunctions in November 2013, hence the recording of the two 2013 events are missing for this sensor. The dynamic characteristics of the Jalapa building in Mexico City have changed during the considered time period. Between the 1993 earthquakes and the events in 1997-1998, the Jalapa was damaged by a M_w 6.5 earthquake in 1994 and a M_w 7.5 earthquake in 1995, and was retrofitted in 1996-1997. For this reason, the results of the deconvolved wave fields are stacked for different time periods in which the structure is assumed to have the same dynamic behavior. The results are shown in Figure 14a (1993 events after stacking), 14b (1997-1998 events after stacking) and 14c (MC-1999-2 event). The comparison of the deconvolved wave fields for the first two time periods (Fig. 14a and b) shows the change in the dynamic characteristics of the Jalapa building, i.e., the increase in the shear wave propagation velocity and, hence, the fundamental frequency in the transverse direction. After the 1998 event, another M_w 6.9

event occurred before the MC-1999-2 earthquake (Table 3), which caused structural damage, leading to a decrease in the shear wave velocity and the fundamental frequency.

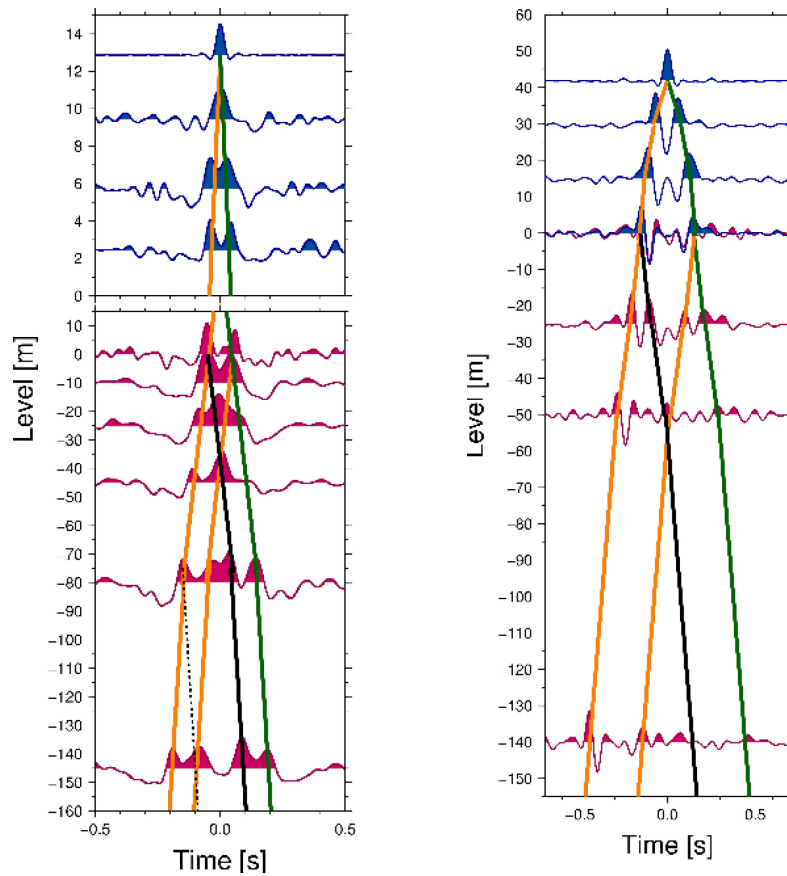


Figure 13. Deconvolved wave fields (blue lines: building sensor, magenta lines: downhole sensors) obtained after stacking the results of all analyzed events for one horizontal component (Bishkek: transverse direction; Istanbul: x-direction) using the recordings at the top of the building as reference. Orange, black and green lines correspond to upward propagating waves, downward propagating waves reflected at the Earth's surface and the wave field radiated back from the building to the soil, respectively. a) Bishkek VA, stacking of results of all events in Table 1; b) Istanbul VA, stacking of results of all events in Table 2. Please note the different vertical and horizontal scales that are used for the different test sites.

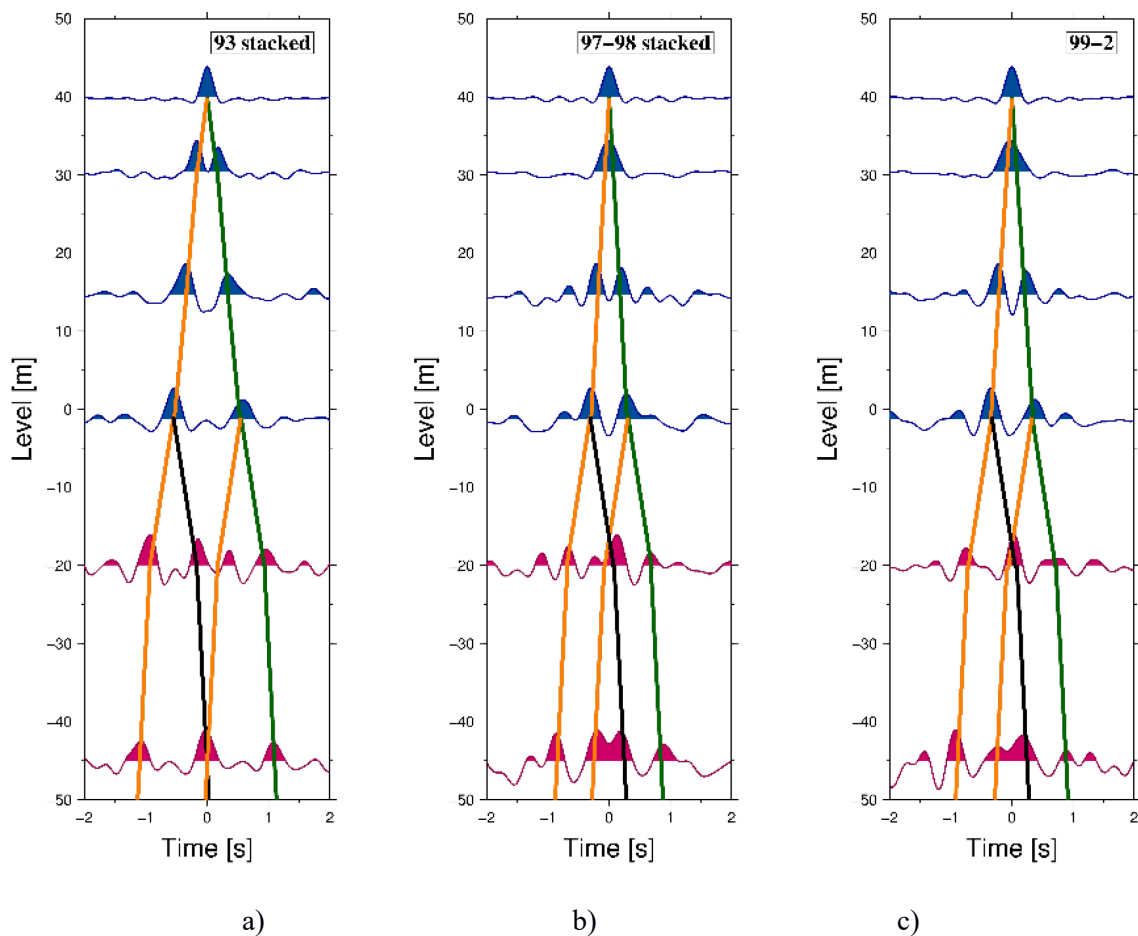


Figure 14. Deconvolved wave fields (blue lines: building sensor, magenta lines: downhole sensors) obtained after stacking the results of events of different time periods for the Mexico City vertical array (transverse direction) using the recordings at the top of the building as reference. Orange, black and green lines correspond to upward propagating waves, downward propagating waves reflected at the Earth's surface and the wave field radiated back from the building to the soil, respectively. a) Events of 1993b) events of 1997-1998, c) event of 1999, Table 3.

For the three test cases, the different up and down-going waves contributing to the wave fields are marked by lines (e.g., Trampert et al. 1993) of different colors. The upward propagating waves can be identified at the deepest sensors (first peak in the acausal part marked by the first orange line), they propagate through the soil up to either the first impedance contrast or to the Earth's surface where a part of the energy is radiated back into the soil (black lines). The other part of the wave field is transmitted either to the adjacent soil layer or into the building layer. The remaining part propagates through the building up to the building's top (orange lines) where the wave field is reflected and propagates back down to the Earth's surface (green lines). When reaching the Earth's surface, one part of the wave field is reflected back into the building, whereas the other part is transmitted into the soil (green lines). This latter part of the wave field is the one of major interest in this study. For the test cases in Bishkek and Mexico City, the downward propagating waves can be clearly identified down to the deepest sensor (Bishkek: at -145m, Mexico City: at -45m). For the test site in Istanbul, the peak associated with the downward propagating waves being radiated back from the building to the soil can be identified univocally in the deconvolved wave field down to 50 m depth.

Differently from the simple case where the sensors are installed in a homogenous layer and hence one upward and one downward propagating wave is obtained in the deconvolved wave field, for all three test cases, the structure of the soil is more complex, as is the resulting deconvolved wave field. In order to better understand the wave propagation in the building-soil system and hence, the more complex deconvolved wave field, numerical simulations (comparisons of deconvolved wave fields of real and synthetic data) and the estimation of the analytical Transfer functions have been carried out.

The numerical simulations for the building-soil structure were performed using the Wang (1999) approach, based on a matrix propagator method which is stabilized numerically by inserting an additional numerical procedure into the matrix propagation loop. The simulations are carried out using sampling rates and generate a signal frequency band similar to that used with the real data. For this purpose, the buildings were assumed to behave as a shear beam and an additional layer for the building was added on the top of the soil layers. It is worth mentioning that assuming a building behaves as a pure shear beam is a very simplified model. Most buildings, such as for example the B22 building, do not behave as a pure shear beam, but as a combination of a shear and a bending beam (Petrovic et al., 2017). The scope of this study is not to find the model which describes the building's dynamic behavior in the best way, but, to model the building-soil structure in a simple way to make the interpretation of the real data results easy. The correct positions of the peaks in time (defined by the velocity profile) and not the correct amplitude of the peaks (defined by the attenuation) are hereby of interest. For this reason, for the quality factor Q_s , an approximated value ($Q_s=10$ for Bishkek and Istanbul and $Q_s=20$ for Mexico City) is used. Studying the attenuation through the building-soil layers is beyond the scope of this study.

The deconvolution approach is also applied to the synthetic seismograms obtained by the numerical simulation. The deconvolved wave fields of the synthetic data (gray lines) are shown together with the results of the real data (blue lines: building sensors, magenta lines: downhole sensors) in Figure 15 (a: Bishkek, b: Istanbul) and 16 (Mexico City, a: 1993 events after stacking, b: 1997-1998 events after stacking and c: MC-1999-2 event). For the test cases in Istanbul and Mexico City, two different simulations are used, namely the one including a building layer and the one without the building layer. It was observed that when considering only the model including the building layer (as for the case in Bishkek), the wave field reflected at the Earth's surface was not identified and the discrepancy between the real and synthetic data results was large. Two aspects contribute to this discrepancy. On the one hand, the building is not a continuous layer and as for the Istanbul vertical array, the downhole installation is not below the building's basement, but is shifted some tens of meters. Since there is no building layer above the borehole, more energy is being reflected at the Earth's surface. The second aspect that explains the Mexico City test case is the Fresnel zone. Reflections do not take place at a single point, but over an area. This area is larger than the building's footprint, and hence for this case, energy is also being reflected at the Earth's surface and recorded at the downhole sensors. The results of the synthetic data for both models are plotted one above the other in Figs. 15b and 16.

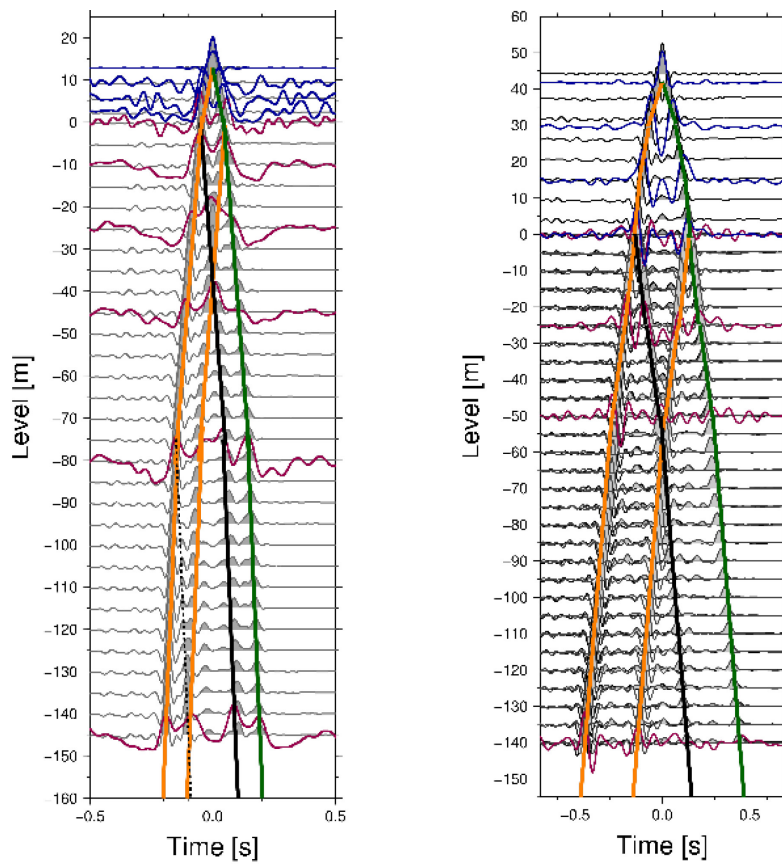


Figure 15. Comparison of the deconvolved wave fields (blue lines: building sensor, magenta lines: downhole sensors) derived from real data obtained after stacking (as shown in Fig. 13) and the synthetic data (gray lines) obtained from numerical simulations. Orange, black and green lines correspond to upward propagating waves, downward propagating waves reflected at the Earth's surface and the wave field radiated back from the building to the soil, respectively. a) Bishkek VA; b) Istanbul VA. Please note the different vertical and horizontal scales that are used for the different test sites.

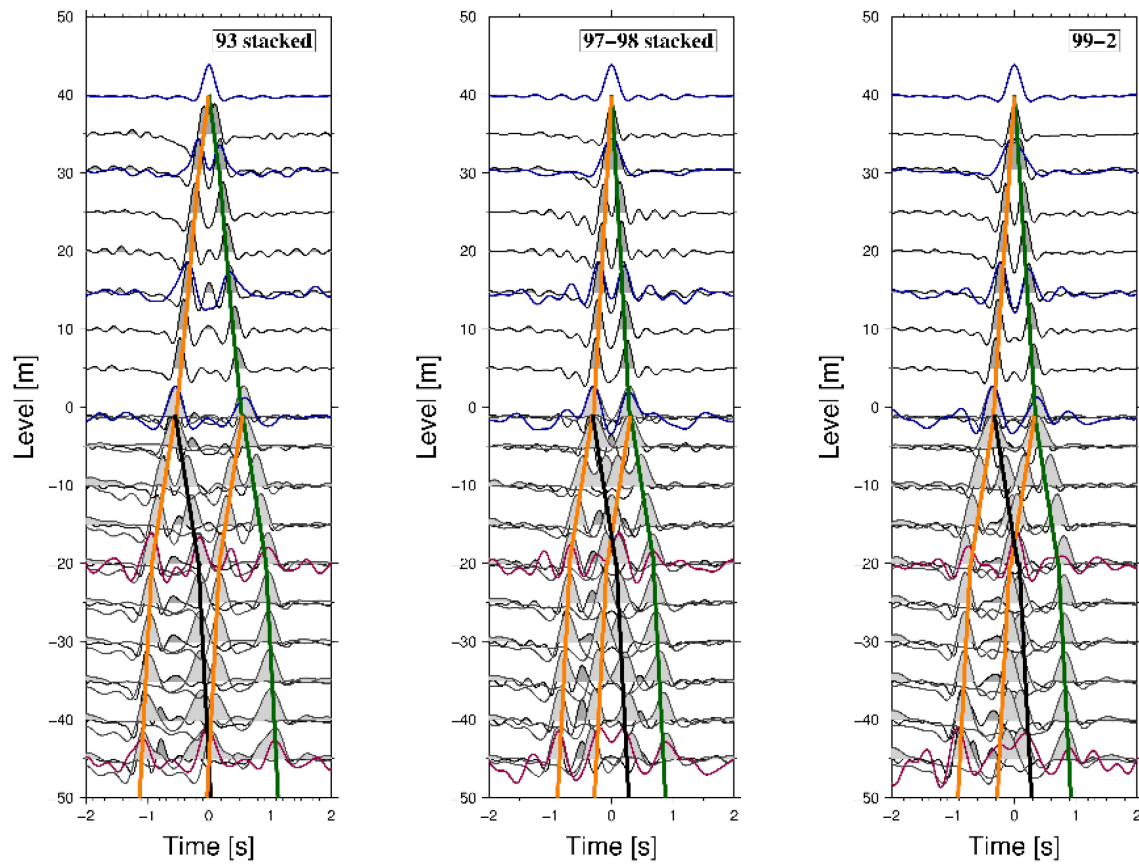


Figure 16. Same as Figure 15 but for the Mexico City vertical array. a) Events of 1993, b) events of 1997-1998, c) event of 1999, Table 3.

When comparing the results of the real and synthetic data, the similarity between the results for all three test cases is clearly visible. For the Bishkek test case, simply a better separation of the single peaks in the results of the synthetic data (probably due to different frequency bandwidths used for the analyses) and a discrepancy in the propagation velocities between -145 m and -85 m can be observed. For the Istanbul test site, it can be seen that the deconvolved wave field of the real data set is dominated by peaks with inverted polarity that propagate from the building down to the soil with the same velocity and which are not observed in the results of the synthetic data set. As analyzed and discussed in detail in Petrovic et al. (2017), these peaks with inverted polarity are due to the excitation of the second bending mode and are projected to downhole sensors, since the recordings at the top of the building are used as the reference. Note that, in this case, modeling the building as an additional layer is a too simple model and hence, the contribution of the second bending mode cannot be seen in the results of the synthetic data. For the Mexico City test case, the agreement between synthetic and real data is very good, showing that the simplified model of building layers is sufficient in this case.

For the Bishkek test case, when considering the building and the soil layer above 75 m depth, the building-soil system can be modeled by two layers, while for sensors installed below 75 m depth a three-layer model is assumed. In Istanbul, when considering the soil down to 50 m depth, a two layer system (one for the building and one for the soil) is used. For Mexico City, we examined one building layer for the Jalapa building and two soil layers (0 m to 20 m and 20 m to 45 m).

The derivation of the analytical transfer functions for the sensor at the bottom of the downhole installation for both models (two and three-layer) can be found in the Appendix of Petrovic and Parolai (2016). When considering the two-layer model, the two peaks in the acausal part (orange lines in Figs. 13-16) can be explained as follows: the first one is related to the upward going wave, while the second one must be taken into account when the recordings at the roof (affected by multiple reflections in the building that have to be removed) are back-projected to the borehole. To reconstruct the seismic input correctly, both peaks have to be considered.

The peak related to the part of the wave field that is radiated back from the building to the soil (green lines) overlaps with another peak corresponding to a wave which arrives at the same time. It is related to the part of energy that is missing in the recordings on the top of the building since it was reflected back at the Earth's surface. In order to reconstruct correctly the wave field that is related to the part of ground motion that is radiated back from the building into the soil layers, the relative contributions of these two peaks have to be considered. This is obtained from the terms $0.5(1 - r)$ (back-radiated wave field) and $r^2/[2(1 + r)]$ (wave field missing in the roof's top registration), with r being the reflection coefficient.

After the identification of the phases, the seismic input and the part of the wave field being radiated back from the building to the soil are estimated by the constrained deconvolution for the three test cases. In Figure 17, the spectra of the reconstructed seismic input (blue lines) at a certain depth and the separated wave field being radiated back from the building to the soil for two depths (red and green lines) are shown exemplarily for Bishkek and Istanbul, in each case for one earthquake (a: BI-2015-2, Table 1; b: IS-2015-1, Table 2) and for one earthquake in each of the three considered time periods for Mexico City (c: MC-1993-2, d: MC-1997-1, e: MC-1999-2, Table 3).

For the test sites in Bishkek and Istanbul, the spectra of the downward propagating waves are dominated by the peaks of the first (Bishkek, Fig. 17a) or the three first (Istanbul, Fig. 17b) bending modes in the considered direction. For Mexico City, the spectra of the reconstructed downward propagating waves show two peaks at the frequencies of the first two bending modes in this direction for the shown earthquake before the retrofitting (Fig. 17c), whereas the two events after the retrofitting show additionally also a peak at the frequency corresponding to the first torsional mode. Moreover, due to the fact that the dominant frequencies of the soil and the transverse direction of the building are very close (e.g., Meli et al. 1998), the peak of the first bending mode in the transverse direction and the resonance frequency of the soil (shown in the seismic input) are very close.

The velocity spectra of the seismic input and the wave field radiated back from the building to the soil are integrated (Bishkek: over a frequency range of $f=1-10$ Hz, Istanbul $f=0.1-15$ Hz, Mexico City: $f=0.1-5$ Hz) in order to estimate the spectral energy. The selection of the frequency band was based on that of the spectra of the recording at the roof and is the same as the one used for the joint deconvolution. For the Bishkek vertical array, the energy that was radiated back by the building down to -145 m and -10 m corresponds to 10% and 40%-50% (the range corresponds to different events which were analyzed), respectively, of the energy of the seismic input at 145 m depth. At 145 m depth, there is almost no variation of the estimated spectral energy for different events, thus, only one value is given. For Istanbul, the energy associated with the downward propagating wave field at 25 m and 50 m depth is estimated to be around 10-15% of the energy of the reconstructed seismic input at 50 m depth for both levels for the analyzed events. For Mexico City, the energy belonging to the wave field radiated

back from the building to the soil is estimated as 70-90% (at -20 m) and 25-65% (at -45 m) of the reconstructed seismic input at 45 m depth.

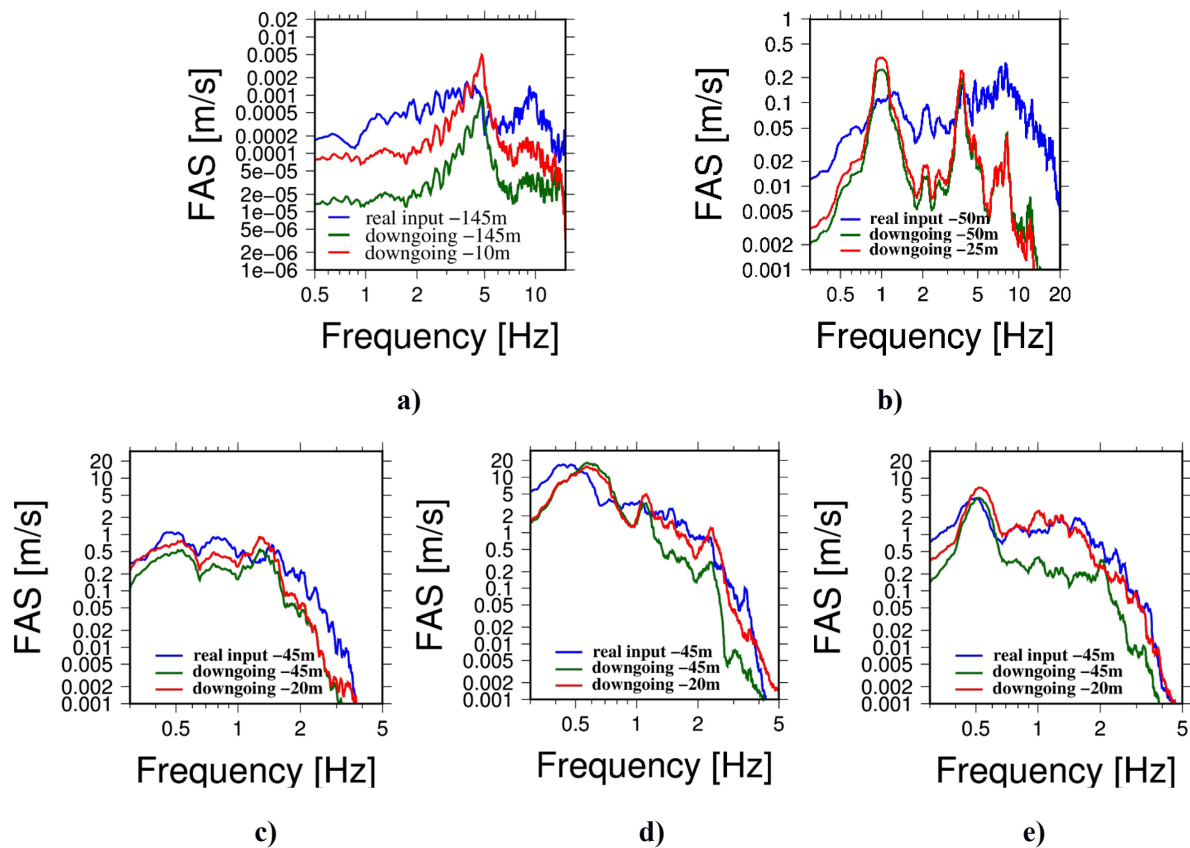


Figure 17. a) Bishkek: Input spectrum at -145 m (blue), spectrum of down-going waves radiated back from the building reconstructed at -145 m (green) and at -10 m (red) for event Bi-2015-2 (Table 1). **b) Istanbul:** Input spectrum at -50 m (blue), spectrum of down-going waves radiated back from the building at -50 m (green) and at -25 m (red) for event IS-2015-1 (Table 2). **c) - e) Mexico City:** Input spectrum at -45 m (blue), spectrum of down-going waves radiated back from the building at -45 m (green) and at -20 m (red) for events MC-1993-2 (c), MC-1997-1 (d) and MC-1999-2 (e) (Table 3).

6 Discussion and conclusion

In this study, the analysis of wave propagation through three different building-soil structures was performed by the application of the joint deconvolution (Petrovic and Parolai, 2016). The three different test cases consider different building construction types and shear wave velocity profiles of the buildings and underlying soil (and impedance contrasts between the buildings and the uppermost soil layer). The wave field associated with the seismic input (after removing the downward propagating waves) and the one associated with the wave field being radiated back from the building to the soil is separated by the constrained deconvolution approach. Finally, for all three test cases, the energy being radiated from the building back to the soil was estimated, concluding that the energy being radiated

back is not negligible and possible interactions between buildings located close to each other should be taken into account.

Interestingly, when considering the spectra of the reconstructed downward propagating waves, these spectra are dominated by peaks at the fundamental frequencies of the buildings in all three test cases. For the Bishkek vertical array, a clear peak is observed at 5 Hz (corresponding to the first bending mode in the transverse direction). The spectra of the reconstructed down going waves for the Istanbul vertical array are dominated by three peaks at frequencies corresponding to the first three bending modes in the x-direction ($f_1=1$ Hz, $f_2=3.84$ Hz, $f_3=7.5$ Hz). For the Mexico City test site, the spectra of the downward propagating waves are dominated by different peaks before and after retrofitting. For the considered event before the retrofitting, the spectra show peaks at frequencies corresponding to the first two bending modes ($f_1=0.5$ Hz and $f_2=1.3$ Hz). After the retrofitting, the spectra show not only peaks at frequencies corresponding to the first two bending modes (MC-1997-1: $f_1=0.6$ Hz, $f_2=2.4$ Hz; MC-1999-2: $f_1=0.5$ Hz, $f_2=2$ Hz) but also a peak at a frequency corresponding to the first torsional mode (MC-1997-1: $f=1.2$ Hz, MC-1999-2: $f=1.1$ Hz).

For the Bishkek and the Istanbul test cases, the variation between the events of the amount of energy being radiated back from the buildings to the soil compared to the seismic input energy is very small for different events that have been analyzed. This is probably due to the fact that only weak motion events of a similar magnitude range and epicentral distance have been considered. For Mexico City, there is a larger variation of the energy being radiated back from the building to the soil compared to the seismic input energy for different events. This is consistent with the fact that the range of magnitudes and epicentral distances vary more for this test case and the dynamic properties of the building have changed due to damage and retrofitting over the different period considered. Analyzing the interactions of a building in which changes in the building construction have been performed, i.e., retrofitting, is similar to analyzing different buildings. For the Istanbul test site, the energy being radiated back from the building to the soil compared to the seismic input energy is the same (10-15%) for both considered depths. This is probably due to the fact that there is no impedance contrast between the two sensors installed at 25 and 50 m depths. For the test cases in Bishkek and Mexico City, the shear wave velocity increases with depth for the considered sensors and hence, the amount of energy being radiated back decreases.

The proportion of the observed wave field being radiated back from the building to the soil correlates inversely with the impedance contrasts. The Jalapa building has been damaged and retrofitted between the events in 1993 and 1997, leading to an increase of both the shear wave velocity through the building (from 70 to 140m/s) and the effective density. Thus, the impedance contrast has decreased (from 0.3 to 0.6) followed by an increase of the amount of energy being radiated back from ~45% (MC-1993-1, MC-1993-2) to 55-65% (MC-1997-1, MC-1997-2 and MC-1998). The test cases in Bishkek and Istanbul have a higher impedance contrast compared to the Mexico City test case, less energy is being radiated back in this case. However, it is worth mentioning that different from Mexico City and Istanbul, for the Bishkek test case the energy being radiated back is considered at -145m (at ~50m depth for the other test cases).

The energy being radiated back from the building to the soil compared to the seismic input energy is estimated to be largest for the Mexico City test case. This is consistent with previous studies, where the soil-structure effects of the Jalapa building, which is constructed on soft soil, have already been

confirmed. Moreover, the installation in Mexico City is the only one where the downhole installation is located directly below the building.

As summarized in the introduction, studying soil-structure interactions and site-city soil effects has found increasing interest over the last decades, especially when considering the use of 2D and 3D numerical simulations. Analyzing earthquake recordings from buildings and downhole installations provides the opportunity to learn about such interactions from real data and to better understand the ongoing processes, including wave propagation through building-soil layers. In this study, it was shown that downhole recordings are rich in information that on the one hand put questions on the standard uses, but on the other hand highlight the active role of built structures in shaping the wave field. Moreover, the obtained results suggest that a full comprehension of the wave field in the borehole recordings is necessary for improving studies of non-linearity in structures.

The interactions between the buildings and soil could not be identified in detail in these experiments and, therefore, more complicated 3D vertical arrays (multiple borehole-building network installations) are necessary. These installations would make it possible, first, to understand how the interactions are occurring, and second, to try to guide these interactions in order to minimize the effect of the input ground motion on the structures. Moreover, extensions to studies of building-building-interactions and site-city effects are required.

Acknowledgments

The authors would like to thank Tobias Boxberger, Dino Bindi, Marco Pilz and Stefan Mikulla for the installation of the Self-Organizing Seismic Early Warning Information Network (SOSEWIN) in the CAIAG Institute in Bishkek, and in the B22 building in Istanbul. The authors thank Messrs. Ahmet Korkmaz and Nafiz Kafadar of KOERI, Istanbul, for their efforts in maintaining the permanent installation at the B22 building. Moreover, we thank Vila-Murià for taking care of the Jalapa network and for sharing the data set (events from 1996 onwards) with us. This research was supported by the Global Change Observatory Central Asia and the Plate Boundary Observatory Turkey of the GFZ, and the MARsite project. Kevin Fleming kindly revised our English.

References

- Bard PY, Chazelas JL, Gueguen P, Kham M, Semblat JF (2008) Site-city interaction. *Assesing and Managing Earthquake Risk, Springer, The Netherlands*: 91-114
- Bard PY, Gueguen G, Wirgin A (1996) A note on the seismic Wave field radiated from large building structures into soft soils. *11th World Conference on Earthquake Engineering*
- Bertero M, Boccacci P (1998) Introduction to inverse problems in imaging. Bristol: IOP Publishing
- Bindi D, Parolai S, Picozzi M, Ansal, A (2010) Seismic input motion determined from a surface-downhole pair of sensors: a constrained deconvolution approach. *Bull Seism Soc Am* 100:1375-1380
- Bindi D, Petrovic B, Karapetrou S, Manakou M, Boxberger T, Raptakis D, Pitilakis KD, Parolai S. (2015) Seismic response of an 8-story RC-building from ambient vibration analysis. *Bulletin of Earthquake Engineering*, 13, 7:2095-2120
- Boutin C, Roussillon P (2004) Assessment of the urbanization effect on seismic response. *Bull Seismol Soc Am* 94:251-268
- Cardenas M, Bard PY, Gueguen P, Chavez-Garcia FJ (2000) Soil-structure interaction in Mexico City. Wave field radiated away from Jalapa Building: data and modelling. *12th World Conference on Earthquake Engineering; Auckland, New Zealand, January 30 – February 4, 2000*
- Cardenas-Soto M, Chavez-Garcia FJ (2007) Aplicación de la interferometría sísmica para obtener la respuesta de edificios y depósitos de suelo ante movimientos Fuertes. *XVI Congreso Nacional de Ingeniería Sísmica, Ixtapa-Zihuatanejo, Guerrero, 2007* (in Spanish)
- Céspedes I, Huang Y, Ophir J, Spratt S (1995) Methods for estimation of subsample time delays of digitized echo signals. *Ultrasonic Imaging* 17:142-171
- Chavez-Garcia FJ, Cardenas-Soto M (2002) The contribution of the built environment to the free-field ground motion in Mexico City. *Soil Dyn Earthq Eng* 22:773-780
- Chazelas JL, Abraham O, Semblat JF (2001) Identification of different seismic waves generated by foundation vibration: centrifuge experiments, time-frequency analysis and numerical investigations. *4th Int. Conf. on Recent Advances in Geotechnical Earthquake Eng. And Soil Dynamics, San Diego*
- Cheng MH, Kohler MD, Heaton TH (2015) Prediction of wave propagation in buildings using data from a single seismometer. *Bull Seism Soc Am* 105:107-119
- Colombi A, Roux P, Guenneau S, Gueguen P, Craster RV (2016) Forests as a natural seismic metamaterial: Rayleigh wave bandgaps induced by local resonances. *Sci Rep* 6:19238
- Ditommaso R, Mucciarelli M, Gallipoli MR, Ponzo FC (2009) Effect of a single vibrating building on free-field ground motion: numerical and experimental evidences. *Bull Earthquake Eng* 8:693-703
- Faccioli E, Paolucci R, Vanini M (1996) Studies of site response and soil-structure interaction effects in a tall building in Mexico City. *11th World Conference on Earthquake Engineering, Acapulco, Mexico, June 23-28, 1996*

Fleming K, Picozzi M, Milkereit C, Kühnlenz F, Lichtblau B, Fischer J, Zulfikar C, Özel O, SAFER and EDIM working groups (2009) The Self-organizing Seismic Early Warning Information Network (SOSEWIN). *Seismological Research Letters* 80:755-771

Guéguen P, Bard PY, Chávez-García FJ (2002) Site-City seismic interaction in Mexico City-like environments: An analytical study. *Bull Seismol Soc Am* 92:794-811

Guéguen P, Bard PY, Oliveira CS (2000) Experimental and numerical analysis of soil motions caused by free vibrations of a building model. *Bull Seismol Soc Am* 90:1464-1479

Guéguen P, Colombi A (2016) Experimental and numerical evidence of the clustering effect of structures on their response during an earthquake: A case study of three identical towers in the city of Grenoble, France. *Bull Seismol Soc Am* 106:2855-2864

Isbiliroglu Y, Tabora R, Bielak J (2015) Coupled Soil-structure interaction effects of building clusters during earthquakes. *Earthquake Spectra* 31: 463-500

Jennings PC (1970) Distant motions from a building vibration test. *Bull Seismol Soc Am* 60:2037-2043

Kanai K (1965) Some new problems of seismic vibrations of a structure. In: *Proceedings of the 3rd world conference on earthquake engineering, Auckland and Wellington, New Zealand*

Kanamori H, Mori J, Anderson DL, Heaton TH (1991) Seismic excitation by the space shuttle Columbia. *Nature* 349:781-782

Kham M, Semblat JF, Bard PY, Dangla P (2006) Seismic site-city interaction: main governing phenomena through simplified numerical models. *Bull Seism Soc Am* 96:1934-1951

Kitada Y, Kinoshita M, Iguchi M, Fukuwa N (1999) Soil-structure interaction effect on an Npp reactor building. Activities of Nupec: Achievements and the current status, M. Celebi and I. Okawa (Editors), Proc. *UJNR workshop on soil-structure interaction, Menlo Park, California, 22-23 September*, paper no. 18

Mazzieri I, Stupazzini M, Guidotti R, Smerzini C (2013) SPEED-spectral elements in elastodynamics with discontinuous Galerkin: a non-conforming approach for 3D multi-scale problems. *Int J Numer Meth Eng* 95:991-1010

Mehta K, Snieder R, Grazier V (2007a) Extraction of near-surface properties for a lossy layered medium using the propagator matrix. *Geophys J Int* 169:2171-280

Mehta K, Snieder R, Grazier V (2007b) Downhole receiver function: a case study. *Bull Seism Soc Am* 97:1396-1403

Meli R, Faccioli E, Murià-Vila D, Quaas R, Paolucci R (1998) A Study of site effects and seismic response of an instrumented building in Mexico City. *Journal of Earthquake Engineering* 2:89-111

Murià-Vila DM, Rodriguez G, Zapata A, Toro AM (2001) Seismic response of a twice-retrofitted building. *ISET Journal of Earthquake Technology* 38:67-92

Murià-Vila DM, Tabora R, Zapata-Escobar A (2004) Soil-structure interaction effects in two instrumented tall buildings. *13th World Conference on Earthquake Engineering, Vancouver, B.C., Canada, August 1-6, 2004*, paper no. 1911

- Nakata N, Snieder R (2014) Monitoring a building using deconvolution interferometry. II: Ambient-vibration-analysis. *Bull Seism Soc Am* 104:204-213
- Newton C, Snieder R (2012) Estimating Intrinsic Attenuation of a Building Using Deconvolution Interferometry and Time Reversal. *Bull Seism Soc Am* 102:2200-2208
- Oth A, Parolai S, Bindi D (2011) Spectral analysis of K-NET and KiK-net data in Japan, Part I: Database compilation and peculiarities. *Bull Seism Soc Am* 101:652-666
- Paolucci R (1993) Soil-structure interaction effects on an instrumented building in Mexico City. *European Earthquake Engineering* VII 3:895-908
- Parolai S, Ansal A, Kurtulus A, Strollo A, Wang R, Zschau J (2009) The Ataköy vertical array (Turkey): insights into seismic wave propagation in the shallow-most crustal layers by waveform. *Geophys J Int* 178:1649-1662
- Parolai S, Bindi D, Ansal A, Kurtulus A, Strollo A, Zschau J (2010) Determination of shallow S-wave attenuation by down-hole waveform deconvolution: a case study in Istanbul (Turkey). *Geophys J Int* 181:1147-1158
- Parolai S, Bindi D, Ullah S, Orunbaev S, Usupaev S, Moldobekov B, Echtler H (2013) The Bishkek vertical array (BIVA): acquiring strong motion data in Kyrgyzstan and first results. *Journal of Seismology* 17:707-719
- Parolai S, Wang R, Bindi D (2012) Inversion of borehole weak motion records observed in Istanbul (Turkey). *Geophys J Int* 188:535-548
- Petrovic B, Parolai S (2016) Joint deconvolution of building and downhole strong-motion recordings: evidence for the seismic wave field being radiated back into the shallow geological layers. *Bulletin of the Seismological Society of America* 106:1720-1732
- Petrovic B, Dikmen SU, Parolai S, Safak E (2016) Studying the soil-structure interaction by joint deconvolution: The Ataköy (Istanbul, Turkey) vertical array. *ACE2016 – 12th International Congress on Advances in Civil Engineering, Istanbul, Turkey*
- Petrovic B, Dikmen SU, Parolai S (2017). A real data and numerical simulations-based approach for estimating the dynamic characteristics of a tunnel formwork building: preliminary results, *Bulletin of Earthquake Engineering*. <https://doi.org/10.1007/s10518-017-0250-3>.
- Picozzi M, Parolai S, Mucciarelli M, Milkereit C, Bindi D, Ditommaso R, Vona M, Gallipoli MR, Zschau J (2009) Interferometric Analysis of Strong Ground Motion for Structural Health Monitoring: The Example of the L'Aquila, Italy, Seismic Sequence of 2009. *Bull Seism Soc Am* 101:635-651
- Pianese G, Petrovic B, Parolai S, Paolucci R (2018). Non-linear seismic response estimation of buildings by a combined Stockwell Transform and deconvolution interferometry approach, *Bulletin of Earthquake Engineering*, DOI: 10.1007/s10518-018-0307-y
- Rahmani M, Todorovska MI (2013) 1D system identification of buildings during earthquakes by seismic interferometry with waveform inversion of impulse responses – method and application to Millikan library. *Soil Dyn Earthq Eng* 47:157-174

Raub, C., M. Bohnhoff, B. Petrovic, S. Parolai, P. Malin, K. Yanik, R. F. Kartal, and T. Kilic (2016). Seismic-wave propagation in shallow layers at the GONAF-Tuzla site, Istanbul, Turkey, *Bull Seismol Soc Am* 106:912-927.

Semblat JF, Kham M, Bard PY, Gueguen P (2004) Could “site-city interaction” modify site effects in urban areas? *13th World Conference on Earthquake Engineering Vancouver, B.C., Canada*

Semblat JF, Kham M, Gueguen P, Bard PY, Duval AM (2002) Site-city interaction through modifications of site effects. *7th Conference of Earthquake Engineering, 2002, Boston, United States*

Semblat JF, Kham M, Bard PY (2008) Seismic wave propagation in alluvial basins and influence on site-city interaction. *Bull Seismol Soc Am* 86:2665-2678

Snieder R, Şafak E (2006) Extracting the building response using seismic interferometry: Theory and application to the Millikan library in Pasadena, California. *Bull Seism Soc Am* 96:586-598

Sorensen MB, Oprsal I, Bonnefoy-Claudet S, Atakan K, Mai PM, Pulido N, Yalciner C (2006) Local site effects in Ataköy, Istanbul, Turkey, due to a future large earthquake in the Marmara Sea. *Geophys J Int* 167:1413-1424

Stockwell RG, Mansinha L, Lowe RP (1996) Localization of the Complex Spectrum: The S Transform. *IEEE Trans Signal Process* 44:998–1001

Tamim NSM, Ghani F (2010) Techniques for Optimization in Time Delay Estimation from Cross Correlation Function. *International Journal of Engineering & Technology* 10:69-75

Tikhonov AN, Arsenin VY (1977) Solution of ill-posed problems. Washington: Wiston/Wiley

Trampert, J., Cara, M. & Frogneux, M., 1993. SH propagator matrix and Qs estimates from borehole- and surface-recorded earthquake data, *Geophys. J. Int.*, 112, 290–299 Wang R (1999) A simple orthonormalization method for stable and efficient computation of Greens functions. *Bull Seismol Soc Am* 89:733-741

Wirgin A, Bard BY (1996) Effects of building on the duration and amplitude of ground motion in Mexico City. *Bull Seismol Soc Am* 86:914-920.